Andreas Öchsner
Holm Altenbach *Editors*

Machining, Joining and Modifications of Advanced Materials

Springer

Advanced Structured Materials

Volume 61

Andreas Öchsner · Holm Altenbach
Editors

Machining, Joining and Modifications of Advanced Materials

Springer

Editors
Andreas Öchsner
Griffith School of Engineering
Griffith University
Southport, QLD
Australia

Holm Altenbach
Institut für Mechanik
Otto-von-Guericke-Universität
Magdeburg
Germany

Preface

The idea of this monograph is to present the latest results related to mechanical and materials engineering applied to the machining, joining, and modifying modern engineering materials. The contributions cover the classical fields of casting, forming, and injection molding as representatives of manufacturing methods. Additive manufacturing (rapid prototyping and laser sintering) is treated as a more innovative and recent technology which opens the possibility for the manufacturing of shapes and features which are not possible to achieve based on traditional methods. Water jet cutting is treated as an innovative cutting technology which avoids the heat increase as in the case of classical mechanical cutting. As a different technology for separation of materials, the laser cutting technology is introduced. Classical bonding and friction stir welding approaches are treated as joining technologies. In many cases, forming and machining technologies require a post-treatment to achieve a required surface quality or to equip the component with a protective layer. This area is covered based on laser treatment, shot peening, and the generation of protective layers.

The 9th International Conference on Advanced Computational Engineering and Experimenting, ACE-X 2015, was held in Munich, Germany, from June 29 to July 2, 2015, with a strong focus on computational based and supported engineering. This conference served as an excellent platform for the engineering community to meet with each other and to exchange the latest ideas. This volume contains 18 revised and extended research articles written by experienced researchers participating in the conference. Well-known experts present their research on casting, forming, injection molding, and laser-based methods.

The organizers and editors wish to thank all the authors for their participation and cooperation which made this volume possible. Finally, we would like to thank the team of Springer-Verlag, especially Dr. Christoph Baumann, for the excellent cooperation during the preparation of this volume.

March 2016
Andreas Öchsner
Holm Altenbach

Contents

Experimental and Numerical Analysis of the Effect of Ribs and Beds in Sheet Metal Parts with 90° Bend

Alfonso Campos, Alejandro Escamilla and Orión Gutiérrez

Abstract Sheet metal forming processes are deformation processes in which force is applied to a blank of sheet metal to modify its geometry rather than to remove any material. Bending is one of the most common die-forming methods. It can be defined as a forming operation in which the metal is deformed or bent along a straight axis, normally bending operations are made in U-die or V-die. Corner beads may often be used to impart rigidity bending which might otherwise be too flexible and weak. In a right-angle bent sheet, the bend is usually a weak point. By the use of stiffening ribs, the overall rigidity is increased. However, how many? This paper aims at the numerical and experimental investigation of increasing bending strength when stamping in right-angle bent sheet a rib or bead in different depth and separation between each and other. The cross-sectional of bead is V, in steel sheet of gage No. 16 (U.S. standard).

1 Introduction

Metal working or metal forming [1–3] is a manufacturing process in which the change in shape of the work piece is not accompanied by an extensive amount of metal removal as the principal method of altering the shape. If we consider the surface to volume ratio, the metal working process is classified as massive or bulk

A. Campos (✉) · A. Escamilla · O. Gutiérrez
Unidad Profesional Interdisciplinaria en Ingeniería y Tecnologías Avanzadas,
Av. Instituto Politécnico Nacional # 2580, Col Barrio La Laguna Ticomán,
07340 Gustavo A. Madero, Mexico D.F., Mexico
e-mail: ing_campos@hotmail.com

A. Escamilla
e-mail: aescamin@hotmail.com

O. Gutiérrez
e-mail: gutierrez.orion@gmail.com

and sheet metal processes. In sheet metal, the starting material is a rolled sheet, the work piece has a large surface to volume ratio, conscious world, the sheet metal parts have already replaced many expensive cast forming processes because causes large changes in shape but small changes in thickness and the elastic recovery is usually significant. Suchy [3] established that, in today's practical and cost-conscious world, sheet-metal parts have already replaced many expensive cast, forged, and machined products, by the relative cheapness of stamped.

However, functionality of the part is also important; it must sustain the anticipated amount of work cycles, while performing all its intended duties without any unusual wear or failure.

Boljanovic [4] classifies sheet metal in two categories, the first one involves the cutting of material by subjecting it to shear stresses, and the second one involves partial or complete plastic deformation of the work material. Bending, consists of uniformly straining flat sheets or strips of metals around a linear axis. The metal on the outside of the bend is stressed in tension beyond the elastic limit, and on the inside of the bend it is compressed. There are various bending methods, which include stretch forming, also called wrap forming, roll forming, forming with high pressures, rubber forming, to name but a few. In die work, the majority of bending operations can be divided into four types: V-die bending, U-shape bending, wipe bending, rotary bending.

The process of bending it's made with industrial presses with an average production of 40–160 cycles per minute, however, in order to build the specimens we will design a framework to implement the V-die bending of 90° and then applied the corner bead using a universal testing machine. In order to avoid a decrement in the thickness of the V-die bending, in the radius of the punch and the die has to be added the sheet metal thickness in other way the radius of this bending will be weaker than the rest of the specimen affecting the experiment. It is extremely necessary that the punch and the die settle down in the sheet metal so there is a relation between the punch and the die with the sheet metal (see Fig. 1).

The sheet-metal parts are not characterized by, like forged or casting parts. Sturdiness of a sheet metal part is often aided by the inclusion of beads and ribs, namely long narrow depressions embossed in the sheet. In a right-angle bent sheet, the bend is usually a weak point. By the use of stiffening ribs, the overall rigidity is incrementing but the literature states an rigidity increase of 100–200 % [5]. However it is not established to a certain accuracy what is the value of the increase by stamping the ribs.

In this paper we describe the process to develop a sheet metal piece, in order to implement a corner bead, and by means of a framework, to determine the displacement generated for the load. The computational validation for the same conditions is performed based on ANSYS® 15 and SolidWorks® 2014.

$$r_P$$

$$|\leftarrow L/2 \longrightarrow| \leftarrow L/2 \rightarrow|$$

$$t$$

$$P/2 \qquad P/2$$

$$r_2$$

$$r_D$$

$$r_p = r_P + t$$

$$L$$
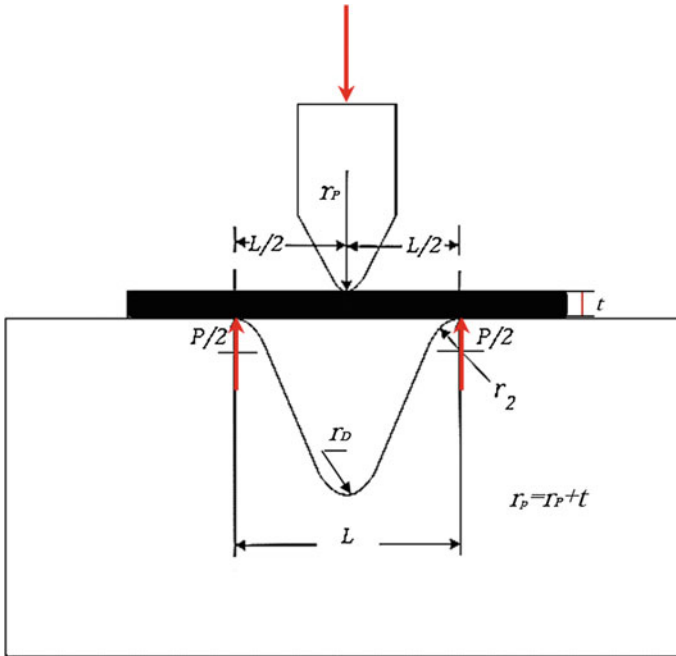
Fig. 1 V bending process

2 Development

We used an AISI 1018 sheet metal in order to determinate the increment of the sheet with a 90° bend, the following experimental procedure was established:

1. Cutting sheet metal pieces of 80 mm of length and 45 mm of width.
2. V-die bending of 90°.
3. Rib bending.
4. Load implementation and displacement measurement.
5. Finite element analysis with ANSYS® 15 and SolidWorks® 2014.
6. Analysis of experimental and computational results.

3 Experimental Analysis

By means of a framework, there are a control piece with the 90° bend (see Fig. 2a) and a second one with the corner bead (see Fig. 2b) manufactured in order to compare the results and establish an accurate percentage of increased strength, applying the load on 16.5 mm from the front face of the piece (see Fig. 3) with a
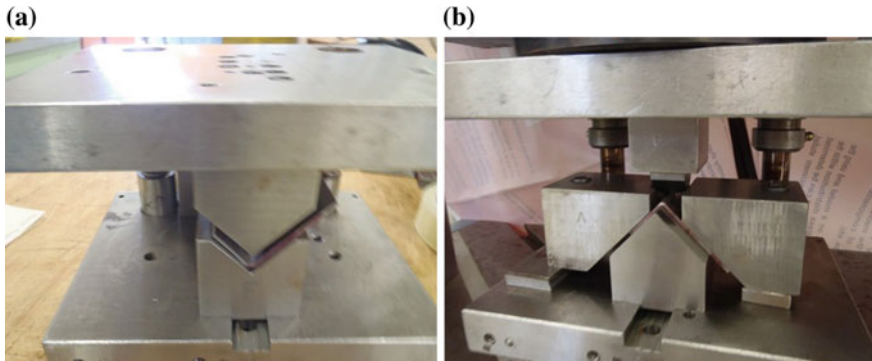
Fig. 2 a Sheet metal piece with 90° bend. **b** Array of the frame work for the corner bead
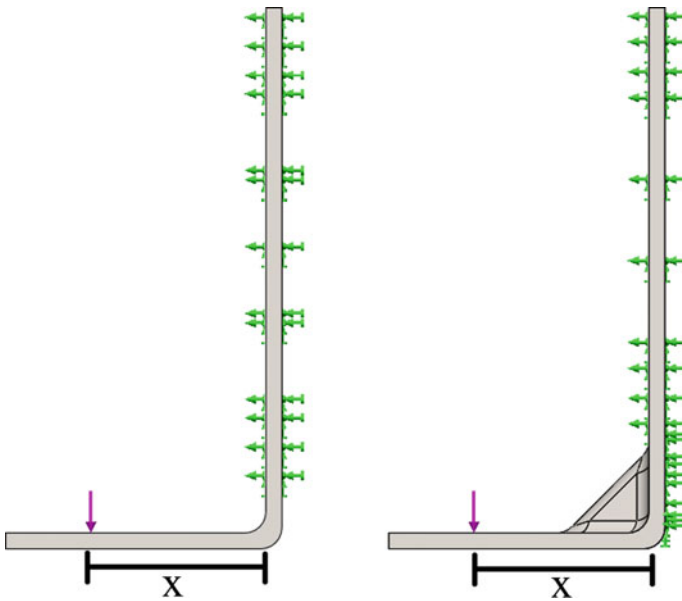
Fig. 3 Application of the load

hydraulic universal testing machine (Training Course WEW 300D). The framework is similar to an industrial die, basically formed by a die set, punch and a die holder. For the die holder, there were two plates machined and perfectly aligned by means of two bushings with the respective guidepost with a press fit of H7/p6 [6]. The components that have direct contact with the sheet metal part are the die holder and the punch, manufactured with an AISI4140 [7] thermal treated steel in order to achieve a 48–50 Rc hardness. The design of the framework includes two bending processes, the first one for the V-die bending of 90° and the second one for the
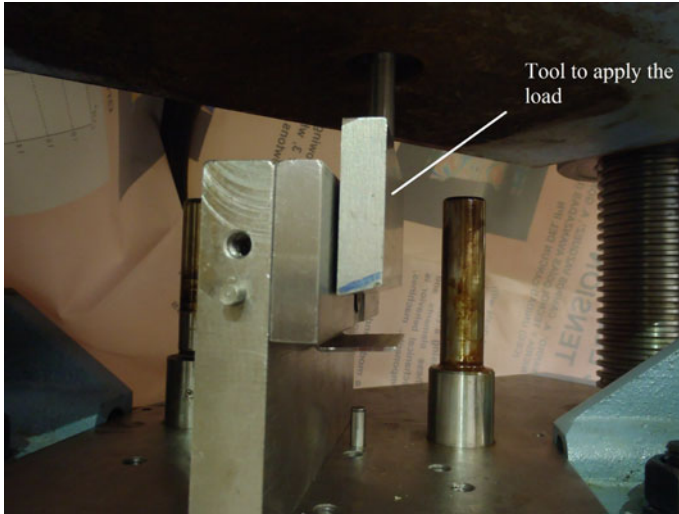
Fig. 4 Array of the framework to apply the load

corner bead. By means of the bottom plate with a slot machined to fix another plate in a perpendicular position to hold the specimen, the load it is applied. The design of the framework contains the V-die bending of 90°, the rib bending and also the load implementation in order to minimize the time between every test.

The load application needed an extra tool that joins to the test machine (see Fig. 4) and that presses on the specimen. For the specimen with the 90° bending, the graphical representation of the load-displacement curve was obtained (see Fig. 8 in Appendix 1). This representation illustrates the displacement generated for a load of 900 N. For the specimen with the corner rib a load of 1200 N was applied generating the respective load-displacement graph (see Fig. 9 in Appendix 1). The load applied to the specimens was determined experimentally and the increment between the two loads is one of the proofs that there is actually an increased strength of the sheet metal piece. Because of the corner bead, the second specimen withstands a large load.

4 Computational Analysis

By means of FEA in SolidWorks® 2014 [8] the experiment for the sheet metal piece with the 90° bending was recreated (Fig. 6a), initially with a standard mesh of 3 mm. A mesh convergence study was performed to obtain more accurate results and the mesh density was adjusted to 2.0 mm with a mesh size on the bends of 0.5 mm. The results were graphically post-processed (see Fig. 10 in Appendix 2) and the same
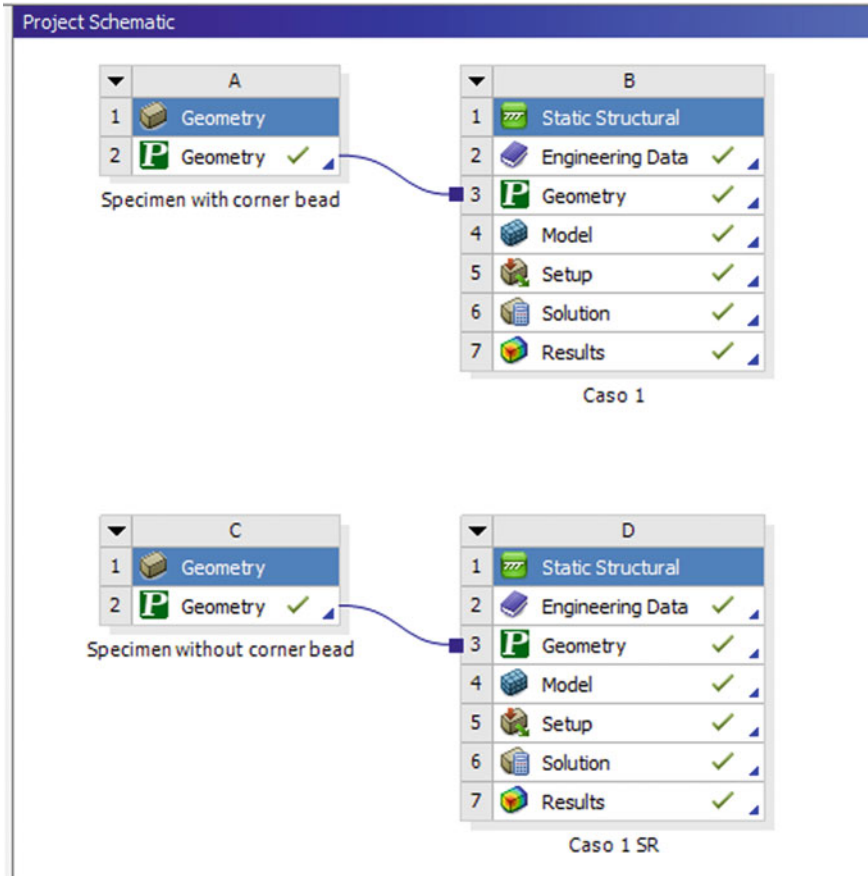
Fig. 5 ANSYS workbench intefaz for the computational analysis

process was generated for the specimen with the corner bead (see Fig. 11 in Appendix 2).

In order to compare the results of the FEA in SolidWorks, there was a complementary analysis developed in ANSYS. [9]. For the purpose, the SolidWorks Part file was imported in the '.x_t' format. Inside the Workbench interface, a static structural analysis (Fig. 6b) with the exported geometry, properly linked for every specimen, was generated (see Fig. 5). For both specimens, a 2.0 mm mesh size and a face sizing on the bends of 0.5 mm was applied, i.e. the same mesh size as in SolidWorks, in order to plot the results of both specimens (see Figs. 12 and 13 in Appendix 2).

5   Analysis of the Results

In the experimental results (Fig. 7a), the load–displacement graph for the specimen without the rib bead presents a non-linear behavior (see Fig. 8 in Appendix 1) and the initial displacement occurred with a load of 250.0 N, with a final load of 950.0 N, approximately. The second specimen (Fig. 7b) with the initial displacement generated for a 300.0 N load presents also a non-linear behavior (see Fig. 9 in Appendix 1), with a final load of 1200.0 N. This load presents a 0.5245 mm deformation which is to be compared with a similar displacement in the specimen without the rib bead, that is generated by a load of 700.00 N and represents a 41 % of increased strength.
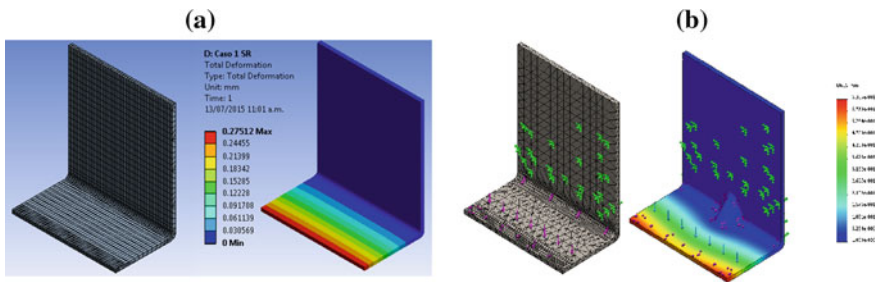
Fig. 6 Computational results
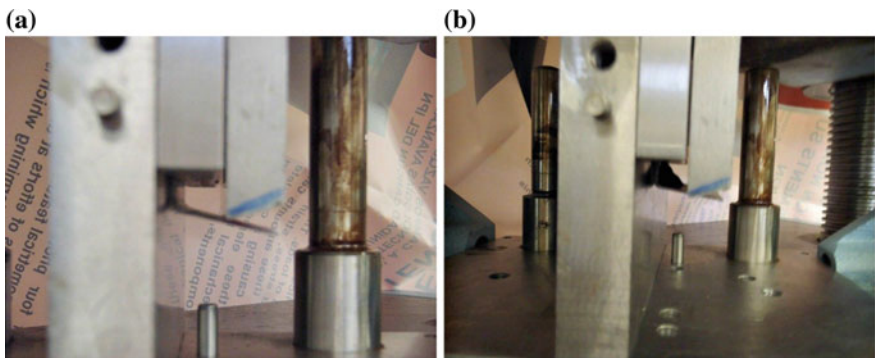
Fig. 7 Experimental results

6   Conclusions

The experimental and computational results indicate that there is a proportional behavior between the load and the strain, even with the corner bead. Furthermore, the increment on the strength of the specimen with the corner bead becomes more representative with a higher load. More experimental testing is required to compare and improve the mesh in both software packages (SolidWorks and ANSYS) in order to approximate to the real strain. A decrease of 25 % was observed in the strain with the corner bead in SolidWorks and a decrease 34 % in the strain with the corner bead in ANSYS.

Finally the machine used for the experimental analysis has a capacity of 300,000 N. This exceeds the needed capacity which could result in a variation of the displacement measured. Thus, the future work would needed a machine with a lower capacity.

Appendix 1

See Figs. 8 and 9.
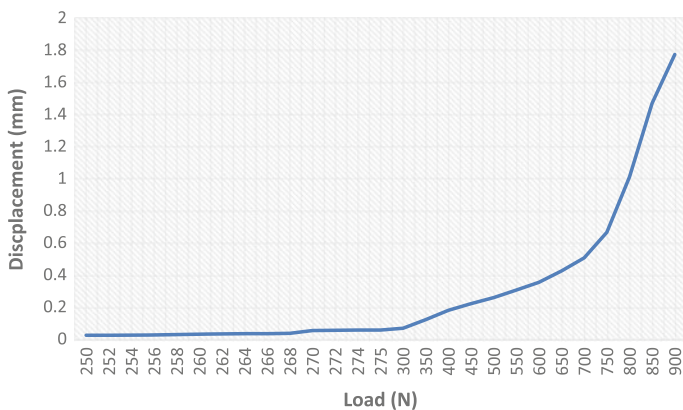
Fig. 8 Displacement in specimen without corner bead
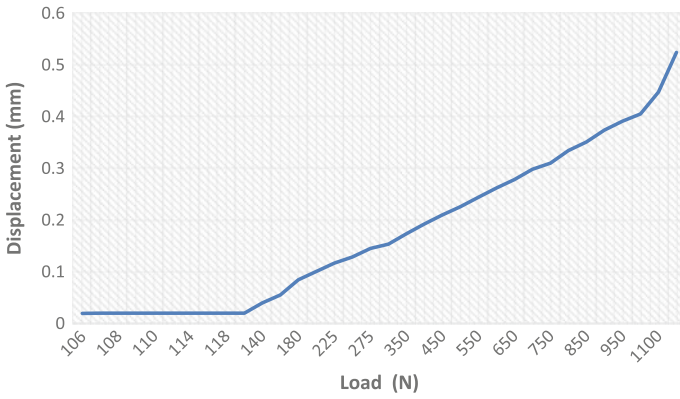
Fig. 9 Displacement in specimen with corner bead

Appendix 2

See Figs. 10 and 11.
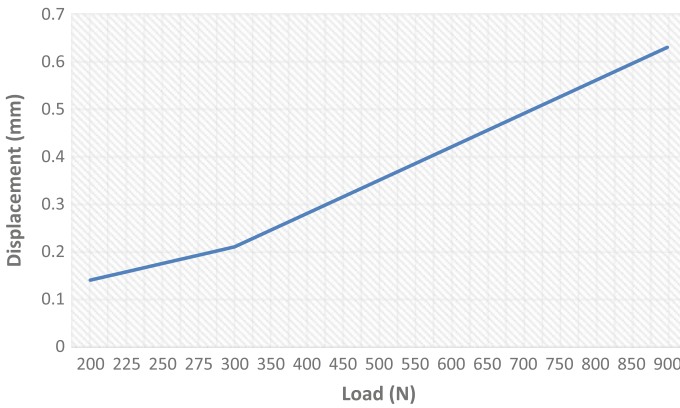
Fig. 10 Displacement in specimen with corner bead calculated by SolidWorks® 2014
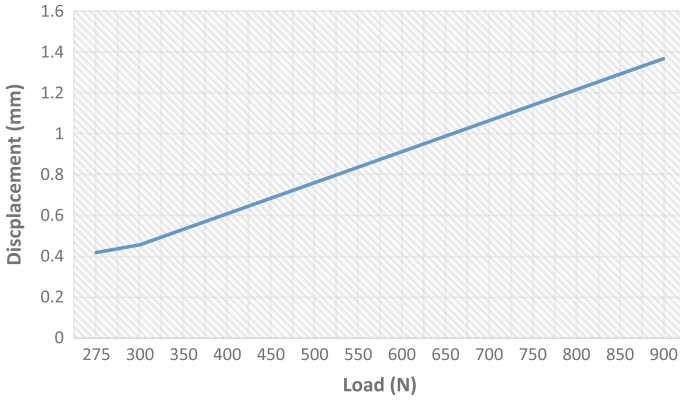
Fig. 11 Displacement in specimen without corner bead calculated by SolidWorks® 2014

Appendix 3

See Figs. 12 and 13.
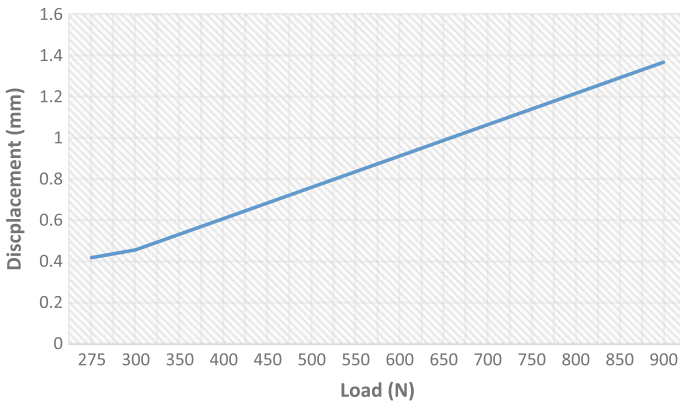
Fig. 12 Displacement in specimen without corner bead calculated by ANSYS® 15
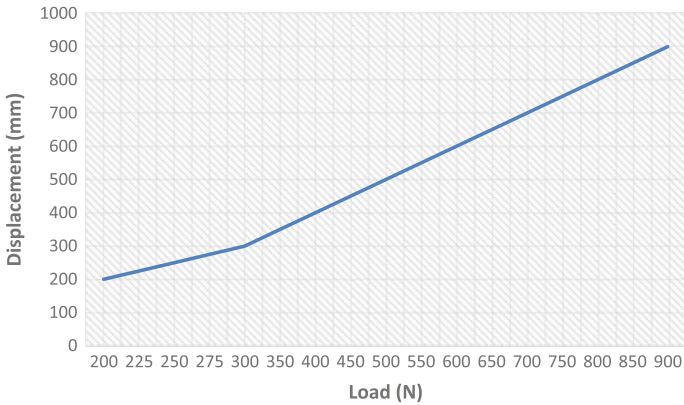
Fig. 13 Displacement in specimen with corner bead calculated by ANSYS® 15

References

1. Hosford, W., Caddell, R.: Metal Forming: Mechanics and Metallurgy, New York, USA (2014)
2. Hu, J.: Mechanics of Sheet Metal Forming, Great Britain (2002)
3. Suchy, I.: Handbook of Die Design, New York, USA (2005)
4. Boljanovic, V.: Sheet Metal Forming Process and Die Design, New York, USA (2013)
5. Nee, D.: Fundamentals of Tool Design, USA (2010)
6. Chevalier, A.: Guide du dessinateur industriel, Paris, France (2004)
7. A.I.a.S. Institute: American Iron and Steel Institute [En línea]. Available: http://www.steel.org/. Accessed 15 May 2015
8. CADArtifex: SOLIDWORKS 2015: A Power Guide for Beginner and Intermediate Users, USA (2015)
9. Huei-Huang, L.: Finite Element Simulations with ANSYS Workbench 15, USA (2014)

Effect of Boron Nitride Coating on Wear Behavior of Carbide Cutting Tools in Milling of Inconel 718

Halil Caliskan, Bilal Kursuncu, Sevki Yilmaz Guven, Abdullah Cahit Karaoglanli, Mustafa Sabri Gok and Akgun Alsaran

Abstract Boron nitride based tribological coatings promise hope in tribological applications thanks to their excellent lubrication and heat resistance properties. However, the applicability of these coatings on cutting tools in machining applications is not well known and it needs to be revealed. Therefore, in this study, a boron nitride (BN) coating was deposited on carbide milling tools. Inconel 718 was used as workpiece material in face milling tests to determine the wear behavior of the BN coated carbide tools. Surface roughness and tool wear was recorded in relation with cutting length. Wear mechanisms on the coated carbide tools were determined using scanning electron microscopy in combination with energy dispersive spectroscopy. Abrasive and adhesive wear was found as main failure mechanisms on the worn tools. Approximately two times longer tool life was obtained with the BN coated carbide tools.

Keywords Boron nitride coating · Carbide tool · Wear · Inconel 718 · Milling

H. Caliskan (✉) · B. Kursuncu · A.C. Karaoglanli · M. Sabri Gok
Bartin University, 74100 Bartin, Turkey
e-mail: hcaliskan@bartin.edu.tr

B. Kursuncu
e-mail: bkursuncu@bartin.edu.tr

A.C. Karaoglanli
e-mail: karaoglanli@bartin.edu.tr

M. Sabri Gok
e-mail: msabrigok@bartin.edu.tr

B. Kursuncu · S.Y. Guven
Suleyman Demirel University, 32100 Isparta, Turkey
e-mail: sevkiguven@sdu.edu.tr

A. Alsaran
Ataturk University, 25240 Erzurum, Turkey
e-mail: aalsaran@atauni.edu.tr

1   Introduction

Inconel 718 superalloy is widely used in high temperature applications such as gas turbines in aviation and aerospace industries [1] since the material has high oxidation and corrosion resistance and it preserves their mechanical properties at high temperatures [2, 3]. Despite these superior properties of Inconel 718, its high wear resistance, deformation hardening and low thermal conductivity cause its machinability to decrease, and Inconel 718 is, therefore, called as difficult-to-cut material [4].

Selection of a suitable cutting tool material has great importance to obtain high performance in machining of Inconel 718 superalloy due to the elevated cutting temperatures and Cr and Ni elements in its chemical composition which make the cutting process difficult [5, 6]. Coated carbide tools are usually substituted for the uncoated one in milling operations of Inconel 718 superalloy due to the fact that thin hard coatings provide superior properties to these tools such as high wear resistance, thermal insulation and/or lubrication. Cutting speeds are restricted for uncoated sintered carbide tools in milling operations of Inconel 718 due to the elevated temperatures [7, 8]. Coating application allows also higher cutting speeds to be used. Different coating layers are deposited on carbide tools for dry and MQCL milling operations of Inconel 718 superalloy in literature, i.e, single layer TiN, TiCN and multilayer $TiCN/Al_2O_3/TiN$ and TiN/TiAlN [8–10]. The diffusion wear mechanism is efficient in milling operations of Inconel 718 with sintered carbide tools due to high cutting temperatures [11]. The diffusion wear can be retarded by low thermal conductivity of the deposited hard coatings and also by low friction coefficient between the coating and chip interface, which reduces cutting temperature relatively.

Boron based tribological hard coatings attract the attention of researchers to be used in tribological applications thanks to their lubrication and heat resistance properties [12, 13]. Due to the limited information on boron nitride coated tools' performance in literature, it is necessary to reveal the applicability of boron nitride coating in milling operations of Inconel 718 superalloy. The goals of this study are to check the wear mechanism of BN coated carbide tools, to measure the lifetime of the tools and to compare the surface roughness of Inconel 718 after milling operations for both coated and uncoated carbide tools.

2   Experimental Set-up

2.1   Workpiece Material

Inconel 718 superalloy was used as workpiece material with dimensions of $150 \times 100 \times 50$ mm and the hardness of ~ 48 HRC. The material is widely used in aerospace and nuclear industry due to its high temperature strength and high corrosion resistance [1]. The chemical composition of the workpiece material is presented in Table 1. Some mechanical properties of Inconel 718 are also given in Table 2.

Table 1 Chemical composition of Inconel 718 (wt%)

C	Si	Mn	S	P	Ni	Cr	Al	Ti	Nb	Mo	Cu
0.046	0.16	0.18	0.008	0.011	51.34	17.89	0.57	0.99	5.04	3.14	0.031

Table 2 Mechanical properties of Inconel 718

Yield strength (MPa)	Tensile strength (MPa)	Elongation (%)
1072	1032	0.14

2.2 Cutting Tools and Machine Tool

Uncoated cemented carbide cutting tools (R390-11 T3 08M-KM H13A, Sandvik Company) were used in cutting tests. The tools were positioned on the cutter, supplied from Sandvik Company, with the ISO number of R390-025A25-11L. The tool holder has the cutting diameter of 25 mm and teeth number of 2. In this study, on the purpose to avoid the effect of run-out phenomenon and to maintain constant cutting conditions, only a single tooth was mounted on the cutter during milling tests. Milling operations were carried out on a three-axis Falco VMC 850 CNC vertical machining center.

2.3 Boron Nitride Coating

The boron nitride coating was deposited onto the uncoated carbide tools using a physical vapor deposition (PVD) system (VAKSIS, Turkey) in the Metal Forming Center of Excellence in Atilim University, Turkey. Sintered h-BN was used as target material. The deposition process was carried out in radio frequency magnetron power in a mixture of nitrogen and argon atmosphere. The hardness of the BN coating was measured as 1740 HV using a Fischerscope H100C nanoindenter under a maximum load of 5 mN.

2.4 Cutting Tests

The cutting parameters used in milling tests of Inconel 718 superalloy are given Table 3. The tool wear condition was evaluated using a stereo zoom microscope aided with imaging software. After several cutting distances, the milling tests were stopped and cutting tools were removed from the cutter and mounted to the microscope to measure the wear depth on the cutting tools. Wear images were taken from the flank face of the tool as the dominant wear type is observed as notch wear. The notch wear of 0.8 mm were stipulated as the criterion for tool rejection

Table 3 Cutting conditions

Cutting speed, V_c	30 m/min
Feed rate, f_z	0.05 mm/tooth
Axial depth of cut, a_p	0.1 mm
Radial depth of cut, a_e	15 mm
Workpiece material	Inconel 718
Lubricant	Dry cutting

Fig. 1 Experimental set-up

according to face milling standard (TS ISO 8688-1). Analysis of wear mechanisms was performed using a stereo zoom microscope and then scanning electron microscopy (SEM) (MAIA3 TESCAN) in combination with energy dispersive spectroscopy (EDS). Surface roughness of the machined workpiece was measured with a stylus-type instrument (Mitutoyo Surftest SJ-310). An image of the experimental set-up is given in Fig. 1.

3　Results and Discussion

3.1　Tool Lifetime

Milling tests on Inconel 718 were carried out in dry conditions. Both the BN coated and the uncoted tools were worn by notch wear in the tests. Therefore, the notch wear depth was recorded during the tests. A comparison of lifetime of the BN coated and

Fig. 2 Comparison of cutting tool lifetime
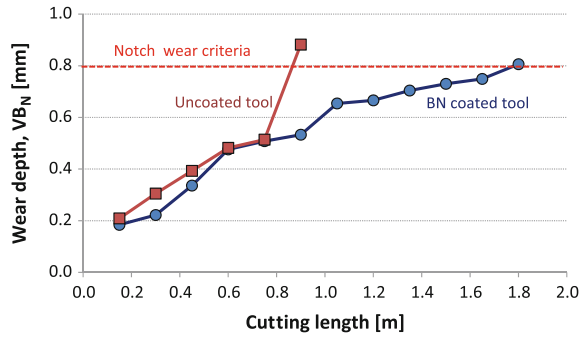
the uncoated carbide tools as a function of cutting length is given in Fig. 2. As seen from the figure, the BN coating increased the wear resistance and thereby the lifetime of the uncoated tool. The BN deposited coated carbide tool showed approximately a two times longer tool life than the uncoated one. At the initial stage of milling tests, the tools showed almost the same wear depth, and after 0.8 m of cutting length, the uncoated tool reached to the failure zone with a swift increase in wear depth.

3.2 Tool Wear Analysis

Optical microscope images of worn cutting tools are given in Fig. 3. Notch wear, flank wear and build-up edge formation are clearly seen on both the coated and the uncoated tools after milling tests of Inconel 718 superalloy. The notch wear formation is attributed to abrasion mechanism together with oxidation phenomenon at the area where the tool and workpiece material contact finished. Especially the abrasive wear mechanism was dominant on the tool owing to hard carbide particles included in chemical composition of Inconel 718 together with the friction at the tool flank face—the workpiece material interface for both the BN coated and the uncoated carbide tools [11, 14].

In order to perform a detailed investigation on the wear mechanism on the cutting edge, SEM equipment in combination with EDS was used. SEM images of the BN coated and the uncoated tools are given in Figs. 4 and 5, respectively. The dominant failure type for both tools is seen as notch wear as a result of high temperature at the cutting edge in machining of Inconel 718. Oxidation of the cutting tool material at high temperature weakens the cutting edge, and then the abrasive particles in the workpiece lead to abrasive wear of the weak edge. Regular flank wear, chipping and build-up edge formation were also observed for both tools. However, these mechanisms were more severe in the uncoated tool. We can explain the reason of these wear mechanisms in such a way that intermittent cutting in milling operation causes the cutting tool to be exposed to cycling load. These loads lead to stress concentrations at the cutting edge, and thus small fractures occur at the cutting edge and finally the chipping is formed. The reason of build-up edge
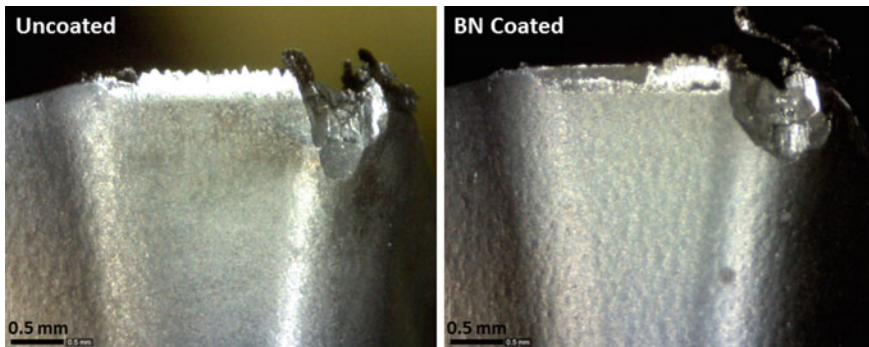
Fig. 3 Tool wear images of worn cutting tools
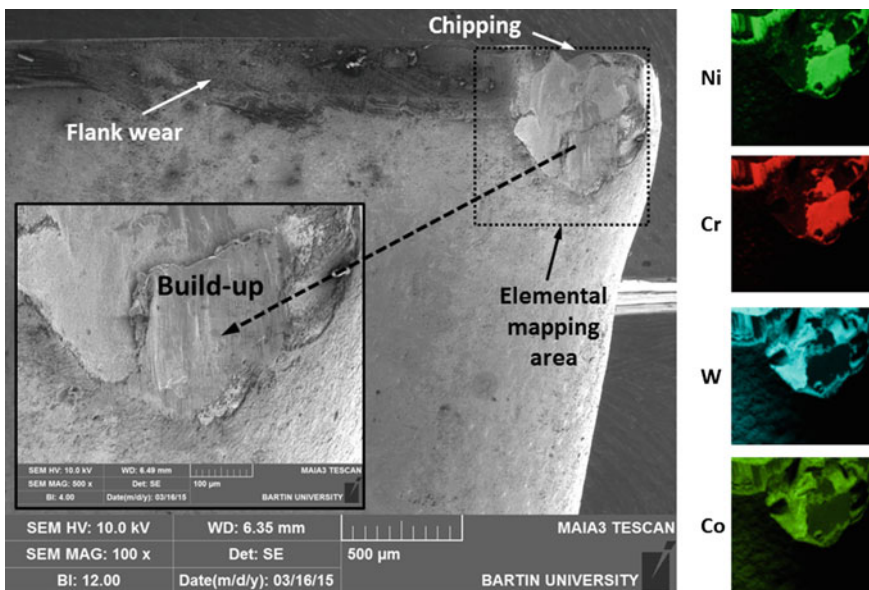
Fig. 4 SEM images and elemental mapping of the worn BN coated tool

formation can be attributed to high cutting temperatures together with high cutting forces. The hardness of the workpiece material at the cutting zone was reduced at high temperatures, and thus sticking/welding of the material on the cutting edge causes adhesive wear [2, 14, 15]. The build-up edge formation is confirmed also by elemental mapping as seen in Fig. 4. Ni and Cr elements confirm the existence of the workpiece material Inconel 718 at the cutting edge, on the other hand W and Co is coming from the carbide cutting tool material. When compared to the uncoated tool, the lower amount of notch wear and build-up formation is thought to be obtained by BN coating's lubricant property.
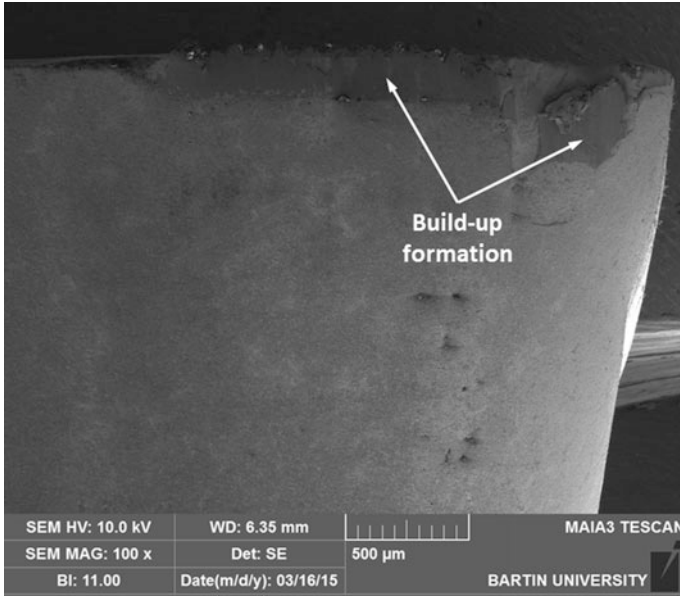
Fig. 5 SEM images of the worn uncoated tool
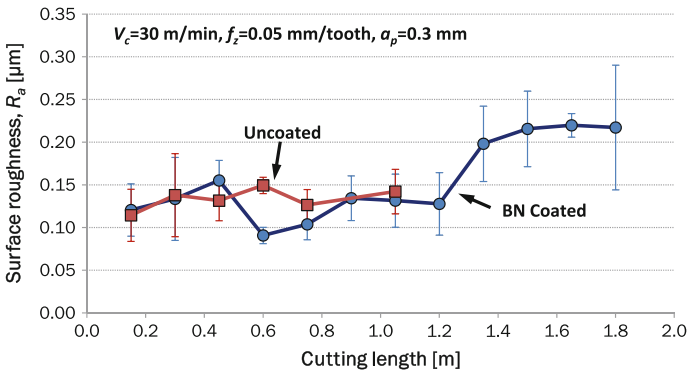
Fig. 6 Surface roughness data of the machined Inconel 718 as a function of cutting length

3.3 Evaluation of Surface Roughness

The surface roughness of the workpiece material machined by the BN coated and the uncoated tools are compared in Fig. 6. The roughness of the machined surface was observed to be lower than 0.25 µm for both the uncoated and the BN coated tools after milling process. The surface roughness obtained with the BN coated tools was almost lower than the uncoated one. The roughness of the machined

surface of Inconel 718 superalloy during milling process was seen to be not significantly affected by tool wear. The surface roughness was similar in the steady state wear region (up to 1.2 m), while a higher roughness (R_a of ~ 0.22 μm) was obtained with the BN coated carbide tool after the cutting length of 1.2 m. The increase in the roughness can be attributed to the increase of build-up edge formation and the damage of the cutting edge [16].

4   Conclusions

In this research, the influence of the BN coating on the wear behavior of carbide cutting tools in face milling of the Inconel 718 superalloy was investigated. Also, the roughness of Inconel 718 superalloy was investigated during milling tests. The main results can be summarized as follows:

– The BN coated tools outperform uncoated carbide tools by ~ 100 % in terms of maximizing the tool life, which is a promising result for using the BN in milling process of Inconel 718 superalloy.
– The main wear modes on the BN coated and the uncoated tools were abrasion and adhesion wear. Dominant tool failures were notch wear, flank wear, build-up edge and chipping.
– The BN coating has no significant effect on the surface roughness of Inconel 718 in milling tests.

References

1. Tian, X., Zhao, J., Gong, Z., et al.: Effect of cutting speed on cutting forces and wear mechanisms in high-speed face milling of Inconel 718 with Sialon ceramic tools. Int. J. Adv. Manuf. Technol. **69**, 1–10 (2013)
2. Ucun, İ., Aslantas, K., Bedir, F.: An experimental investigation of the effect of coating material on tool wear in micro milling of Inconel 718 super alloy. Wear **300**, 8–19 (2013)
3. Heuler, P., Affeldt, E., Wanhill, R.J.H.: Effects of loading waveform and stress field on high temperature fatigue crack growth of Alloy 718. Materialwiss. Werkstofftech. **34**, 790–796 (2003)
4. Benghersallah, M., Boulanouar, L., Lecoz, G., et al.: Dry high speed milling of nickel-based superalloy. Mechanika **19**, 223–228 (2013)
5. Thomas, A., El-Wahabi, M., Cabrera, J.M., et al.: High temperature deformation of Inconel 718. J. Mater. Process. Technol. **177**, 469–472 (2006)
6. Zetek, M., Česáková, I., Švarc, V.: Increasing cutting tool life when machining Inconel 718. Procedia Eng. **69**, 1115–1124 (2014)

7. Liao, Y.S., Lin, H.M., Wang, J.H.: Behaviors of end milling Inconel 718 superalloy by cemented carbide tools. J. Mater. Process. Technol. **201**, 460–465 (2008)
8. Zhang, S., Li, J.F., Wang, Y.W.: Tool life and cutting forces in end milling Inconel 718 under dry and minimum quantity cooling lubrication cutting conditions. J. Clean. Prod. **32**, 81–87 (2012)
9. Li, W., Guo, Y.B., Barkey, M.E., et al.: Effect tool wear during end milling on the surface integrity and fatigue life of Inconel 718. Procedia CIRP **14**, 546–551 (2014)
10. Li, H.Z., Zeng, H., Chen, X.Q.: An experimental study of tool wear and cutting force variation in the end milling of Inconel 718 with coated carbide inserts. J. Mater. Process. Technol. **180**, 296–304 (2006)
11. Ezugwu, E.O., Wang, Z.M., Machado, A.R.: The machinability of nickel-based alloys: a review. J. Mater. Process. Technol. **86**, 1–16 (1998)
12. Ulrich, S., Ye, J., Stüber, M., et al.: Cubic boron nitride based metastable coatings and nanocomposites. Thin Solid Films **518**, 1443–1450 (2009)
13. Uhlmann, E., Fuentes, J.A.O., Keunecke, M.: Machining of high performance workpiece materials with CBN coated cutting tools. Thin Solid Films **518**, 1451–1454 (2009)
14. Ucun, İ., Aslantas, K., Bedir, F.: The performance of DLC-coated and uncoated ultra-fine carbide tools in micromilling of Inconel 718. Precision Eng. **41**, 135–144 (2015)
15. Gu, J., Barber, G., Tung, S., et al.: Tool life and wear mechanism of uncoated and coated milling inserts. Wear 225–229, Part 1:273–284 (1999)
16. Devillez, A., Le Coz, G., Dominiak, S., et al.: Dry machining of Inconel 718, workpiece surface integrity. J. Mater. Process. Technol. **211**, 1590–1598 (2011)

Fused Deposition Modeling of PCL/HA/MMT Biocompatible Polymer Nano-composites

R.H. Abdul Haq, M.S. Wahab and M.U. Wahid

Abstract This paper presents the development of a biocompatible polymer nano-composite material for the additive manufacturing (AM) process. The material was prepared by the mechanical of polycaprolactone (PCL), montmorillonite (MMT) and hydroxyapatite (HA) using a single screw extruder nanomixer. The amount of MMT material varied from 2 to 4 (wt%) and the HA was fixed at 10 (wt%). Then, the blended material was crushed and fed into a single a screw extruder to produce a filament of 1.8 mm in diameter. The material was characterized on mechanical properties, biocompatibility and manufacturability a fused deposition modeling machine. The results show an improvement in tensile and flexural properties by increasing the MMT. The SEM image shows the bulk formation of apatite layers on the composite surface which confirmed the bioactivity of the material. The material also was successfully produced on the Fused Deposition Modeling for rapid production such as implant components.

Keywords Additive manufacturing (AM) · Fused deposition modeling (FDM) · Polymer Nano-composite (PNC) · Biocompatible polymer · Polycaprolactone (PCL)

R.H. Abdul Haq · M.S. Wahab (✉)
Advanced Manufacturing and Material Centre,
Faculty of Mechanical and Manufacturing Engineering,
Universiti Tun Hussein Onn Malaysia, 86400 Parit Raja,
Batu Pahat, Johor, Malaysia
e-mail: saidin@uthm.edu.my

R.H. Abdul Haq
e-mail: haq@uthm.edu.my

M.U. Wahid
Polymer Engineering Department, Faculty of Chemical Engineering,
Universiti Teknologi Malaysia, 81310 UTM Skudai, Johor, Malaysia
e-mail: uzir@utm.edu.my

1   Introduction

Medical practice today has been concerned with the existence of implant devices created from polymers. According to a report from worldwide orthopedic market 2004–2005, the estimated global market for orthopedic devices such as fracture repair, spinal implant and reconstructive devices is in the range of US$25–30 billion [1]. In fact, it leads to stimulate research focused on producing medical product especially from raw polymer. There is a great effort to produce implant materials from polymers instead of metal. Since metal has many disadvantages such as the presence of corrosions, fatigue failure of metal alloys, and release of metal ions such as nickel or chromium which may cause loosening of the implant, polymers are widely chosen as to replace metal. One of the biocompatible polymers that is getting a higher demand nowadays is polycaprolactone (PCL). Polycaprolactone (PCL) is a semicrystal-line polyester and highly processible as it is soluble in a wide range of organic solvents. It has a relatively low melting point (55–60 °C) and glass transition temperature −60 °C. The more important characteristic is that it has the ability to form miscible blends with a wide range of polymers has stimulated extensive research into its potential application in the biomedical field. PCL has had major acceptance in the tissue engineering field. The properties of PCL which possesses superior viscoelastic and rheological properties over other biopolymers make it easy to be manufactured and manipulated into a large range of scaffolds.

Scaffolds for tissue engineering have become a large focus of research attention and can be fabricated in a wide variety of ways. A biomaterial which lends itself very well to scaffold fabrication is PCL. PCL is an incredibly versatile bioresorbable polymer and by way of its superior rheological properties it can be used by almost any polymer processing technology to produce an enormous array of scaffolds.

From the past decades, injection moulding methods are used for making bone implants for humans. These implants need custom made process since every person has a different pattern and size of bone. To produce the implant using injection moulding, actually was very costly and also consumed a lot of time especially because each pattern of implants needed its own mould. So, in order to solve this problem, a different method can be used in order to make the process simpler and faster. This is where the additive manufacturing (AM) technique comes into action.

Fused deposition modelling (FDM) is one of the AM techniques that can be used for this process. The basic principle of the FDM process offers a great potential for a range of other materials including metals, ceramics, and composites to be developed and used as long as the new material can be produced in feedstock filament form of required size, strength, and properties [2]. In order to predict the success or failure of the flow for newly developed composite materials in the FDM process, it is necessary to investigate the main flow parameters namely temperature, velocity, and pressure drop on the flow behaviour of the composite in the liquefier head [3]. So it is a big challenge to actually employ a new type of composite material for

FDM. Apart from that, with the recent introduction of portable 3D printers, it makes it more popular as it is easy to use and user friendly compared to other types of the AM process. But typically the part produced is not strong enough, or some other material property is not suitable for the application.

2 Methodology

Materials—The biodegradable material used in this study was polycaprolactone (PCL), medical grade of BGH600C in pellets form supplied by Shenzen BrightChina Industrial Co, China. The type of MMT used in this research is Nanomer I.34TCN (modified montmorillonite) nanoclay in a powder form supplied by Nanocor Inc, America. It is specifically designed for extrusion compounding. Hydroxyapatite (HA Fluka, 3.16 kg/cm^3) was purchased from Sigma Aldrich. The specific surface area of the powder, measured by N, absorption (according to the Brunnauer-Emmet-Teller) method was found to be 33.05 m^2/g, and the particle size is 57.5 nm. Then, the materials were blended at various composition as in Table 1.

Sample preparation—The PCL which is in resin form is mixed manually with MMT powder and also HA powder. These uniformly dry-mixed batches are melt-blended in a single screw extruder nanomixer (L/D = 30) with a screw speed of 20 rpm. The temperature profile of the extruder is set at 70, 78, 77 and 70 °C at the fed zone, metering zone and die, respectively. The extruded blends will be cooled in water bath and subsequently, fed to a pelletizer.

Filament preparation—A single screw extruder machine was used for filament fabrication which have been set along with a water bath and also a roller puller machine as shown in Fig. 1.

The Wanhao Duplicator 4, a 3D printing machine was used as an experimental machine in order to run the newly developed filament wire. The machine is 245 × 260 × 30 mm in size and 15 kg in weight. The machine can achieve a high accuracy as far as 0.2 mm with 30 % strength of injection parts.

Mechanical properties evaluation—Flexural test will be carried out using a Lloyd machine according to the ISO 178 standard, three point bending system. Cross-head

Table 1 Blend formulation of PCL with MMT and HA

Designation	PCL (wt%)	HA (wt%)	MMT (wt%)
P100	100	0	0
P9M2	97	0	2
P9M3	97	0	3
P9M4	94	0	4
P8M2HA10	92	10	2
P8M3HA10	90	10	3
P8M4HA10	88	10	4
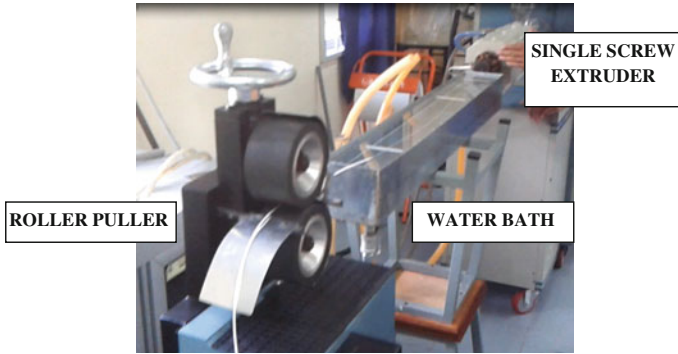
Fig. 1 Layout of the experiment conducted in producing the filament

speeds of 5 mm/min was used with a span of 50 mm. The calculation for flexural modulus and strength are as stated in Eq. 1.

$$\text{Flexural Modulus} = \frac{L^3 m}{4bd^3} \tag{1}$$

where

L Support span (mm)
m Slope of the tangent to the initial straight-line portion of the load-deflection curve (N/mm)
b Width of the beam tested (mm)
d Depth of the beam tested (mm)

The tensile test was carried out according to ISO 527 on a Lloyd machine. A crosshead speed of 50 mm/min was used.

Simulated Body Fluid—In vitro test was carried out following the Kokubo method [4]. The SBF was prepared by dissolving the reagents $NaCl$, $NaHCO_3$, KCl, $K_2HPO_4 \cdot 3H_2O$, $MgCl_2 \cdot 6H_2O$, $CaCl_2 \cdot 2H_2O$ and Na_2SO_4 into distilled water and buffered with Tris (hydroxyl-methyl-amino-methane, $NH_2C(CH_2OH)_3$) and hydrochloric acid (HCl) to pH 7.4 at 37 °C. The solution of SBF contained an ion concentration similar to that of human blood plasma. Each specimens was immersed in 200 ml of SBF and the solution was placed in an incubator for 1 and 3 days at a temperature of 37 °C.

Surface analysis—Morphological study of SBF specimen was analyzed by using a JOEL JSM-638OLA SEM-EDX microscope. In order to avoid charging during electron irradiation, the composite sample was covered with a thin layer of gold in FISON SEM coating system, using a covering time of 120 s at 80 mA.

3   Result and Discussion

The elastic modulus of PCL/MMT composites and PCL/MMT/HA composites is shown in Fig. 2. In the case of PCL/MMT there is a slight increment of the elastic modulus reinforced with 2 wt% MMT. However the value of elastic modulus decreases as the wt% of MMT increases. It was found that overall the improvement of elastic modulus is minor as the highest elastic modulus recorded is 146.43 MPa compare to PCL where the value is 144.15 MPa. In the case of the PCL/MMT/HA composite, the elastic modulus of 2 wt% increased rapidly from 144.2 to 155.6 MPa. These values were higher when compared to PCL/MMT indicating that the HA structure was affecting the interfacial adhesion between PCL and MMT. However, the elastic modulus of PCL/MMT/HA decreases as the amount of MMT increases to 3 wt%. This is because the loading is mainly bound by the matrix in the case of reinforced composites. When certain particles disperse in the matrix, it impedes the movement of molecular chains in the matrix [5]. This explains why the PCL composite containing 10 wt% HA and 2 wt% MMT was higher than the pure PCL. But as the amount of filler increases the modulus decreases due to the presence of large agglomerates forming defects acting as crack initiation sites. The trend obtained is in agreement with studies reporting on HA as filler in polymer composite. The poor strength properties resulting may be attributed to the agglomeration of HA particles in the composite which insufficiently dispersed in the matrix [6]. It was also reported that agglomeration of HA particles either in the condensed state or the intermediate state may not be sufficient to improve the mechanical properties [7].

Figure 3 shows the flexural modulus of the PCL/MMT and PCL/MMT/HA composite respectively.

It can be seen that, PCL/MMT/HA shows a better flexural modulus result when compared to PCL/MMT composite. The PCL/MMT composite shows an increase in flexural modulus as the amount of MMT is increased from 2 to 4 wt%. The
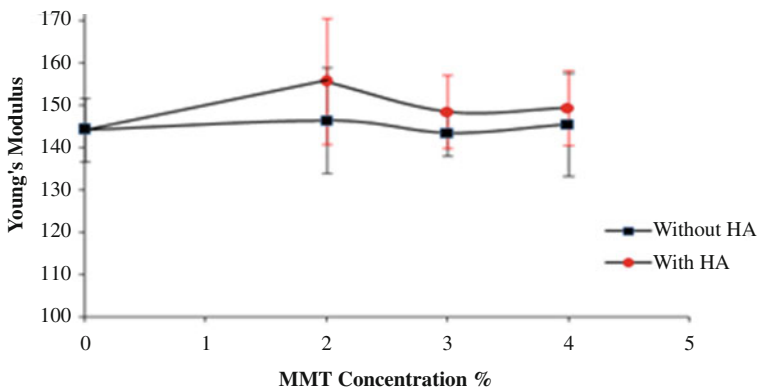
Fig. 2 Elastic modulus of PCL/MMT/HA and PCL/MMT composite (n = 3)

Fig. 3 Flexural modulus
of PCL/MMT/HA
and PCL/MMT composite
(n = 3)
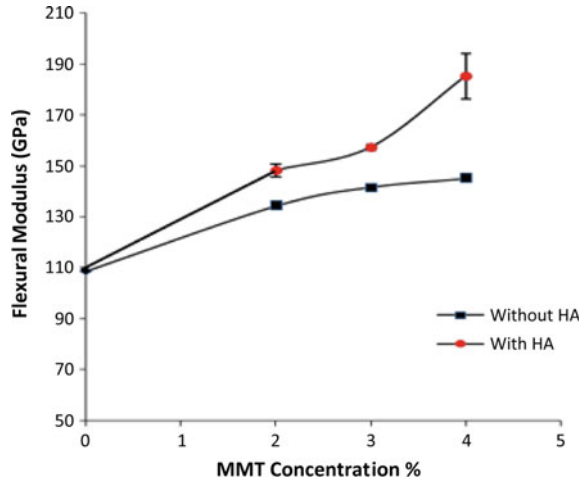
highest flexural modulus for the PCL/MMT composite is marked at 141.56 MPa
higher than pure PCL for which it is obtained at 108.88 MPa. More promising
results for the flexural modulus are shown by PCL/MMT/HA composites. The
values increase as the amount of MMT is increased. The highest result of flexural
modulus is 185.10 MPa. The modulus of the composites clearly reveals that HA
was effectively reinforced with PCL blends and demonstrates the stiffening effect of
HA particles. The increment of modulus is expected, as it is well known that HA
has a higher rigidity than the polymer. A similar trend is observed and reported by
other studies [8, 9]. The trend is also consistent with previous studies which
investigated on the effect of HA on PE composites [10]. Thus it is believed that the
increase in the modulus is due to the HA particle which is wetted by the polymer
surrounding it restricting the mobility and deformability of the matrix by hindering
the movement of polymer molecules.

A morphological study on SBF sample is shown in Fig. 4 after 3 days of
immersion. It was observed that the bulk formation of apatite layer were result from
the ion exchange occurs during immersion.

The tree-like shape of apatite layers grows rapidly within 3 days on
Hydroxyapatite contained in the composite, demonstrating the high in vitro
bioactivity of the composite. As the time increases, these apatite layers grew in size
and formed a layer to completely cover the entire composite. Thus, it is suggested
that the bone-like apatite layer may promote bone bonding with living tissue.

Furthermore, EDX analysis of the trees-like layer formed on the surface shows
the presence of C, Ca, O, and P. It is believed that the carbon (C) found in the layer
maybe the carbonate containing apatite. This was in agreement with findings
reported by others researchers [11].

Table 2 shows the result of filament fabrication testing. The P8M3H10 com-
posite is chosen to be fabricated as a filament for FDM. A better result was gained
as the composite was extruded with the help from a water bath and also a roller
puller. A filament with 1.7 ± 0.05 mm is successfully produced as the spindle
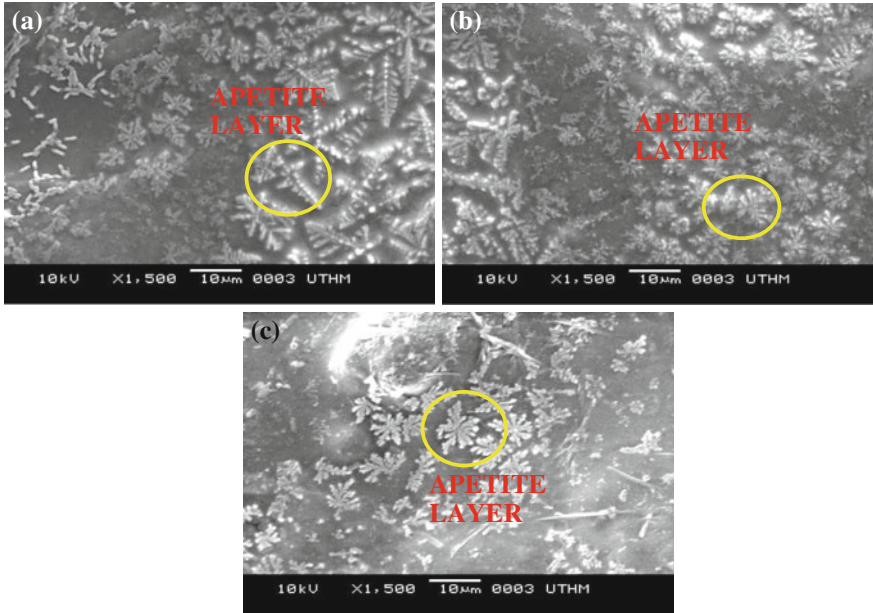
Fig. 4 The SBF result of PCL/MMT/HA composites after 3 days

Table 2 Extruder machine conducted with water bath and roller puller

No.	Puller speed (%)	Spindle speed (Hz)	Heater 1 (°C)	Heater 2 (°C)	Heater 3 (°C)	Heater 4 (°C)	Comment
1	3.5	3.5	80	110	110	80	Small diameter
2	3.0	3.5	80	110	110	80	Small diameter
3	2.0	3.5	80	110	110	80	Big diameter, curly
4	2.5	3.5	78	110	110	78	Inconsistant and curly
5	2.5	3.0	78	114	113	79	Consistant with ±0.05 mm

speeds were set at 2.5 Hz while the roller puller was set at 2.5 %. The characteristic of these composite are the main issues that need to be addressed.

This scenario shows that a better understanding of the properties of the composites is essentials such as its viscosity, melt flow characteristics and melting temperature will helps to decrease the problem in extruding the composites. Although PCL does have a low melting temperature which is suitable for the FDM process the solidifying of this polymer should be seriously taken a note as it is also important in order to run this material on FDM machine.

In the surface morphology analysis, the effect of nozzle temperature (TN) and platform temperature (TP) on samples was investigated. Figure 5 shows the result on the morphology for the samples categorized in different regions.
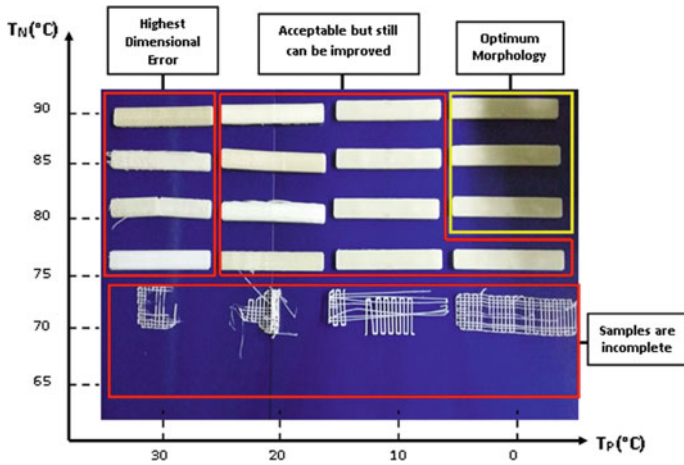
Fig. 5 FDM surface morphology
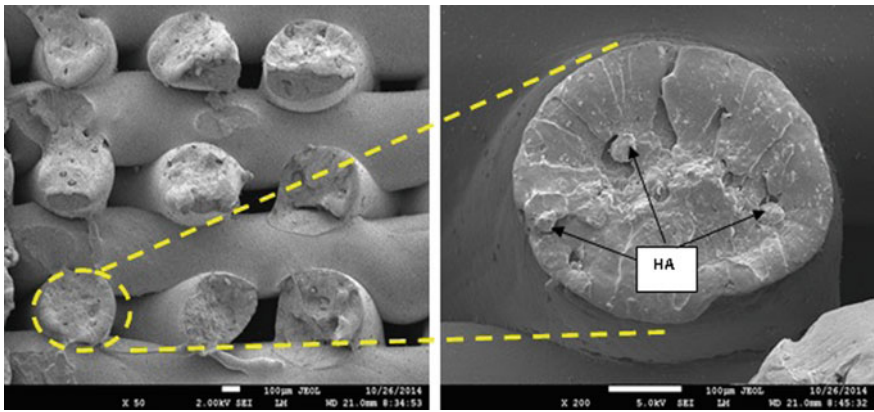
Fig. 6 SEM images of the fracture surface

It can be seen that, when the T_N is set at 65 and 70 °C, the samples seem to be either unable to be produced or incomplete. This may due to the T_N which is low and the filaments are unable to flow out from the nozzle. As the T_N is raised to 75 °C the samples are able to be produced. However, there are high dimensional errors on the samples produced as the T_P increased.

Figure 6 shows the SEM images of the fracture surface. The agglomeration of HA in samples can be seen clearly and is one of the reasons that causes earlier failure which leads to cracking.

4   Conclusion

It can be conclude that the addition of MMT and HA does actually help in increasing the elastic and flexural modulus of PCL composites. It is obvious that both the elastic and flexural modulus of PCL/MMT/HA composites gives a better result when compared to PCL/MMT as it produces higher values. But overall it seems that the differences are in a minimal range. SEM micrographs reveal the formation of the apatite layer covering the composites surface. The properties of the composites are comparable to the cancellous bone properties and suitable to be used in biomedical applications. It has also emerged from this study that HA particle loadings guarantee the growth of the apatite layer as well as needed by the fracture part of bone during healing progression.

From this experiment also a filament or wire 1.7 ± 0.05 mm in diameter were successfully fabricated. In order to get the filament the temperature at the extruder machine has to be set to 78, 114, 113, and 79 °C along with the roller puller speed should be set at 2.5 %. The main problem with Polycaprolactone is its solidifying process which is very slow compared to other polymers. The water bath and roller puller does actually help in producing the required size filament. But there are few things that should be given serious attention such as the spindle speed, the melting temperature and also the speed of the roller puller. All these parameters have to be carefully set in order to achieve a positive result. As part of that the temperature in the water bath also has to be kept cool because of the properties of the polymer which takes more times to solidify.

References

1. Streicher, R.M., Schmidt. M., Fiorito, S.: Nanosurfaces and nanostructures for artificial orthopedic implants. Nanomedicine (Lond.) **2**(6), 861–74 (2007)
2. Justin, T., Jan, H.B.: FDM systems and local adaptive slicing. Mater. Des. **20**, 77–82 (1999). doi:10.1016/S0261-3069(99)00012-6
3. Masood, S.H., Song, W.Q.: Development of new metal/polymer materials for rapid tooling using fused deposition modeling. Mater. Des. **25**, 587–594 (2004)
4. Kokubo, T.: Apatite formation on surfaces of ceramics, metals and polymers in body environment. Acta Mater. **46**(7), 2519–2527 (1998)
5. Chen, B., Sun, K.: Poly (3-caprolactone)/hydroxyapatite composites: effects of particle size, molecular weight distribution and irradiation on interfacial interaction and properties. J. Polymer Testing **24**, 64–70 (2005)
6. Ramirez, C., Albano, C., Karam, A., Domingueical, N., Sanchez, Y., Gonzalez, G.: Mechanical, thermal, rheological and morphological behaviour of irradiated PP/HA composites. Nucl. Instrum. Methods Phys. Res. B. **236**, 531–535 (2005)
7. Wang, M.: Developing bioactive composite materials for tissue replacement. Biomaterials **24**, 2133–2151 (2003)

8. Fang, L., Gao, P., Leng, Y.: Processing of hydroxyapatite reinforced ultra high molecular weight polyethylene for biomedical applications. Biomaterials **26**, 3471–3478 (2005)
9. Liu, Y., Wang, M.: Fabrication and characteristics of hydroxyapatite reinforced polypropylene as a bone analogue biomaterial. J. Appl. Polym. Sci. **106**, 2780–2790 (2007)
10. Lim, K.L.K., Mohd Ishak, Z.A., Ishiaku, U.S., Fuad, A.M.Y., Yusof, A.H., Czigany, T., Pukanszky, B., Ogunniyi, D.S.: High-density polyethylene/ultrahigh-molecular-weight polyethylene blend. II. effect of HA on processing, thermal, and mechanical properties. J. Appl. Polym. Sci. **100**, 3931–3942 (2006)
11. Gu, Y.W., Khor, K.A., Cheang, P.: In vitro studies of plasma-sprayed hydroxyapatite/Ti-6Al-4V composite coatings in simulated body fluid (SBF). Biomaterials **24**, 1603–1611 (2003)

Forming Temperature Investigation of Aluminum and Aluminum/Silicon Carbide Using Image Texture Features

Ahmad E. Eladawi, Tamer O. Diab and Hammad T. Elmetwally

Abstract The processing of aluminum composites plays a significant factor in develop the usage of such composites. The analysis of microstructure of the deformed composites specimens gives a degree of understanding of the effect of deformation process conditions. In recent years, the advent of high-speed, general-purpose, digital computers and vision systems has made image analysis easier and more flexible. Computer vision technology has maintained tremendous vitality in many fields. One of the common techniques employed by computer vision is the texture features techniques. Texture is related to qualitative properties of surfaces, but due to its complexity and great variety, there exists neither a unique definition of texture nor an accepted computational representation of it. Image texture analysis is useful in a variety of applications and has been a subject of intense study by many researchers. In the present work, the effect of forming temperature on the forming behavior of aluminum and aluminum reinforced by 10 wt% SiC was studied by using image texture features after using the compression test which was done at an elevated temperature range of 300–550 °C and a constant strain rate of 0.024 s^{-1}. The current study used a computer vision technique with Sum and Difference Histogram Matrices (GLSDM) to investigate the forming temperature of aluminum and aluminum/silicon carbide (Al and Al/Sic). The relationships between each GLSDM texture feature and the operation temperatures are discussed and the correlation coefficients are obtained. The results showed that some texture features have high correlation coefficients with high sensitivity to changes in temperature.

A.E. Eladawi (✉)
Mechanical Engineering Department, Benha University, Banha, Egypt
e-mail: Ahmadeladawi@yahoo.com

T.O. Diab
Electrical Engineering Department, Benha University, Banha, Egypt
e-mail: tamer.omar1971@gmail.com

H.T. Elmetwally
Mechanical Engineering Department, Beni-Suef University, Beni Suef, Egypt
e-mail: mmgzmhammad@gmail.com

1 Introduction

Metal-matrix composites (MMCs) based on Al are recognized as important structural materials because of its superior properties such as high specific strength, high-temperature resistance, and a reduced thermal expansion coefficient [1, 2]. Different microstructure defects are produced during the hot deformation process of the metal matrix materials due to the presence of the ceramic reinforcement material. The shape and the amount of these defects depend on the deformation conditions. Varma et al. [3] evaluated the microstructure and the fracture surface of aluminum reinforced with different particles sizes of SiC produced during tensile testing.

Humans obtain the vast majority of their sensory input through their visual system, and an enormous effort has been made to artificially enhance this sense. Eye-glasses binoculars, telescopes, radar, infrared sensors, and photo-multipliers all function to improve our view of the world and the universe. Even radio telescopes, which have been thought of as big ears, capture and amplify electromagnetic radiation, which is simply light at a different frequency, and therefore could be considered as "big eyes". It was a logical step to apply computers to this task [4]. Texture can be regarded as a similarity grouping in an image [5–7].

Texture is related to qualitative properties of surfaces, but due to their complexity and great variety, there exists neither a unique definition of texture nor an accepted computational representation of it. Image texture analysis is useful in a variety of applications and has been a subject of intense study by many researchers. The local statistics or property repetitions over the textured region is the texture element or primitive texture. Texture possesses both local and global meaning, as illustrated by Raghu and Yegnanarayana [8], which is characterized by an invariance of certain local attributes distributed over a region of an image. The previous definitions demonstrate that, the definition of texture is formulated by different people depending upon the particular application and that there is no generally agreed upon definition. Some are perceptually motivated, and others are driven completely by the application in which the definition will be used [9]. One of the widely accepted definitions of texture was given by Pichler et al. [10]. According to Pichler, a texture is an optical pattern that contains a large number of elements (spatial variations in intensity or wavelength), each visible to some degree. As texture is an important image feature for describing properties of objects in images, which are partitioned from other parts in images according to certain significant criteria [11].

The texture of an image can be quantitatively evaluated using some properties and various statistical and structural methods that have been developed to study

these features. Statistical methods gained preference over structural methods, as most image textures do not follow a specific grammar or rule, which is essential for the successful implementation of structural methods. The statistical methods are of different orders based on the number of gray values considered for analysis and the type of relationship used. The statistical methods involve the calculation of properties based on the gray tones of the specimens. The earliest approach towards higher-order statistics was developed by Haralick et al. They used an approach known as gray level co-occurrence matrix (GLCM) for the calculation of various features based on the matrices and successfully employed it to the classification of images of land seat.

A typical vision technique, which can be used to study the texture features of machined parts, should satisfy three stages, which are: image acquisition, feature extraction and texture classification.

2 Sum and Difference Histogram Matrices (GLSDM)

GLSDM is a method was introduced in 1986 by Unser [12] to calculate Haralick texture features with a significantly reduced computing time and memory constraints. GLSDM is a second-order statistics (SOS) that estimates properties of two pixels occurring at specific locations relative to each other. It can be defined as the likelihood of observing a pair of gray values occurring at the endpoints of a dipole (or needle) of random length placed in the image at a random location and orientation. These are properties of pairs of pixel values [13]. SOS texture features take into account the specific position of a pixel relative to another [14].

Before building any matrix, the parameters θ (direction of pixel pairs) and d (distance between pixel pairs) should be specified. The direction θ can be selected from four different values of 0, 45, 90, and 135, the distance depends on the resolution of the texture [15].

The gray level Difference Matrix (GLDM) computes features based on the subtraction of pairs of gray levels in an image, for any given distance, but, the gray level Sum Matrix (GLSM) is similar to GLDM, but, it computes features based on the summation of pairs of gray levels in an image, for any given distance. To deal with the features of the GLSDM, consider that Ms(i) and Md(j) are the GLSM and GLDM matrices, where: i, j are the elements of the two matrices respectively, and n is the number of elements in these matrices; Brief descriptions and the mathematical equations of the collected texture features are listed in Appendix 2.

3 Experimental Work

Pure aluminum powder was used as a matrix material and silicon carbide was used as a hard additives. Aluminum powders were supplied by the ALGOUMHORIA Company for Chemicals Trade and Medicals, Cairo, Egypt. Hard materials were supplied by the ALHARAM Company for grinding wheels, Cairo, Egypt. The aluminum powders had an average grain size ranging from 80 to 250 μm. The silicon carbide particles had a grain size of 38 μm. All samples were compacted on a computer controlled servo-hydraulic universal testing machine (Model UH—500 kNA, Schematize™, Japan). The universal testing machine had a maximum load capacity of 50 tons. The machine also had a controlled electric muff furnace with a maximum temperature of 1300 °C, which was used to heat the specimen to the required temperatures.

Compression tests were performed using a computer controlled servo-hydraulic universal testing machine (Schematize™, Japan), which had been modified to carry out uniaxial compression over a load capacity of 50 tons and a maximum ram speed of 50 mm/min. Each specimen was compressed between two grinded plates.

All specimens were firstly heated to the required test temperature by a radiation furnace enclosing the test rig. The specimens were maintained at the required temperature for 5 min. before deformation to ensure the uniform temperature distribution within the specimens. A thin layer of the burned oil with graphite was painted to the plates to reduce the friction effect. The use of this material minimized specimens barreling which is produced due to any frictional constraint between the sample and the plates. The specimens' were compressed to 60 % of their initial height. The load–stroke data was generated within the temperature range 300–550 °C and a strain rate of 0.024 s^{-1}.

All samples were prepared for microstructure inspection in the following sequence based on the Ref. [16]. All samples were etched using kelle's reagent (2 ml HF (48 %) + 3 ml HCl (conc.) + 5 ml HNO_3 (conc.) + 190 ml H_2O). Each sample was immersed in the etchant for 30 s, washed in a stream of warm water and blow dried. A JENAVERT incident-light research microscope with a high resolution digital camera was used for capturing the images. Figures 1 and 2 illustrate some used samples surfaces with different forming temperatures.

Temp = 400   Temp = 450   Temp = 550
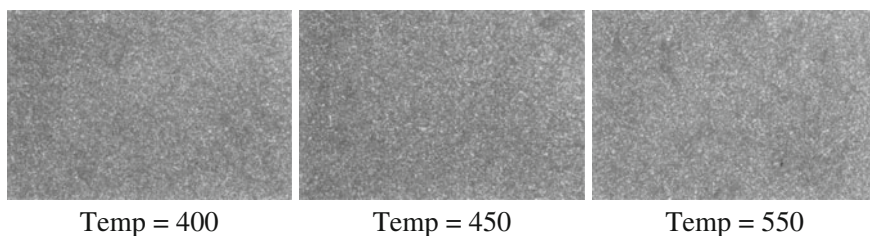
Fig. 1 Surfaces of Al samples with different temperatures

| Temp = 350 | Temp = 450 | Temp = 550 |
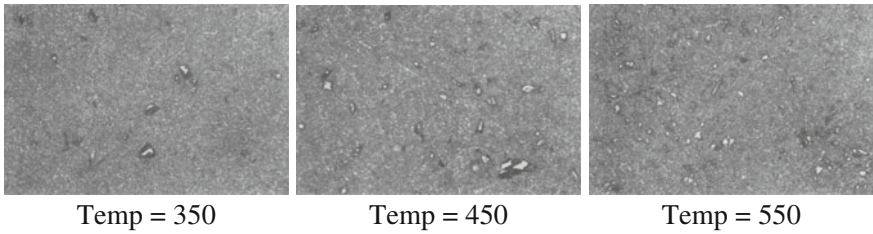
Fig. 2 Surfaces of Al/SiC samples with different temperatures

4 Used Software

This work used the image processing capabilities of MATLAB to deal with images and analyzing image data. MATLAB is a high-performance language for technical computing, programming, visualization, and simulation tool which is widely used for many scientific fields like engineering, physics, and mathematics. MATLAB is more powerful than in many competitive languages in the market because it is used friendly, and the tools and functions integrated within serve many different engineering and scientific disciplines.

Through this work, an interface named "TempGL software" was created to deal with the relationship between the features and changes in temperature through the experimental work. Figure 3 represents a sample of the interface.

The interface gives the option to open a selected image and calculates its properties as illustrated in Fig. 3. The interface gives the texture features values for the opened image.

The calculated data was used in MS Excel to get the resulting curves for every feature in different cases according to changes in temperature.

Fig. 3 Interface of TempGL program
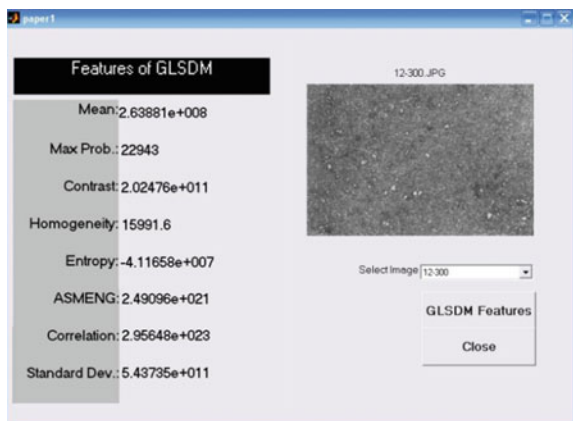
5 Results and Discussions

The results showed that the changes in structure cause changes in the texture features values and its sensitivity according to the changes in temperature. Figures 4 5, 6, 7 and 8 represent these results. Temperature values are represented in the horizontal axis in every curve.

5.1 For Al

From the resulting curves, 5 texture features have high sensitivity (More than 90 %) to changes in temperature through the experimental work. The sensitive feature can be illustrated in the next curves.

The correlation coefficients for these features are illustrated in Table 1.

Fig. 4 Mean/Temperature curve for Al

$R^2 = 0.8178$
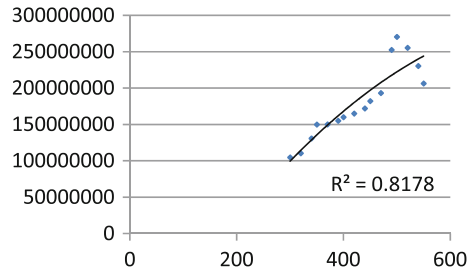
Fig. 5 MaxP/Temperature curve for Al

$R^2 = 0.9404$
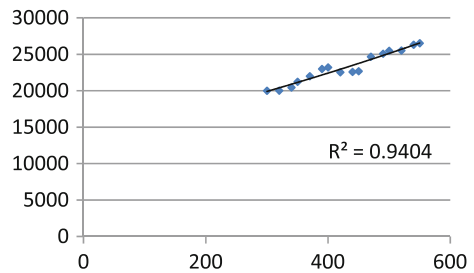
Fig. 6 ASME/Temperature curve for Al

$R^2 = 0.9781$
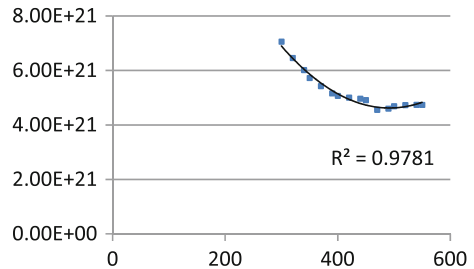
Fig. 7 COR/Temperature curve for Al

R² = 0.9452
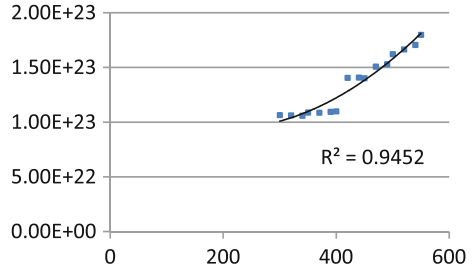
Fig. 8 SD/Temperature curve for Al

R² = 0.9758
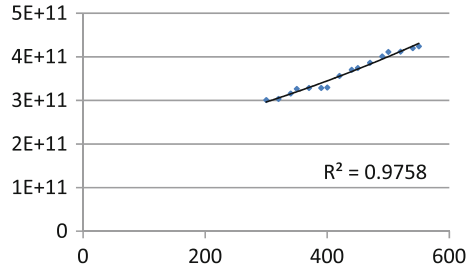
Table 1 Correlation coefficients of texture features of Al samples

Texture feature	Mean	Max probability	Angular second moment/energy	Correlation	Standard deviation
Correlation coefficient	0.904	0.97	0.989	0.972	0.988

5.2 For Al/SiC

From the resulting curves, 4 texture features are highly sensitive (More than 90 %) to the changes in temperature through experimental work. The correlation coefficients for these features can be illustrated in the Table 2.

The sensitive features can be illustrated in the next curves (Figs. 9, 10, 11 and 12).

The previous curves and tables give the next observation:

- For Al, the angular second moment/Energy is the highest sensitivity feature for the change in temperature, and standard deviation feature is the next, then, correlation feature, maximum probability feature and finally, mean feature.

Table 2 Correlation coefficients of texture features of Al/SiC samples

Texture feature	Mean	Homogeneity	Correlation	Standard deviation
Correlation coefficient	0.935	0.90	0.923	0.935

Fig. 9 Mean/Temperature
curve for Al/SiC
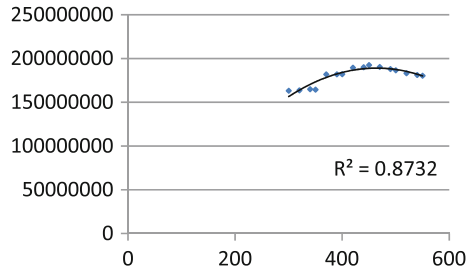
Fig. 10 Hom/Temperature
curve for Al/SiC
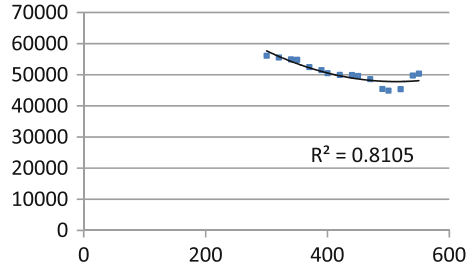
Fig. 11 COR/Temperature
curve for Al/SiC
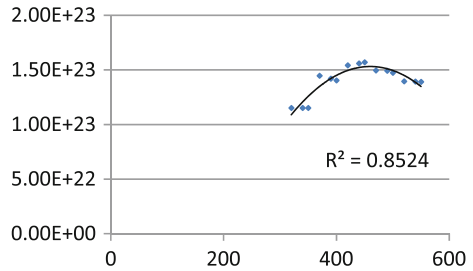
Fig. 12 SD/Temperature
curve for Al/SiC
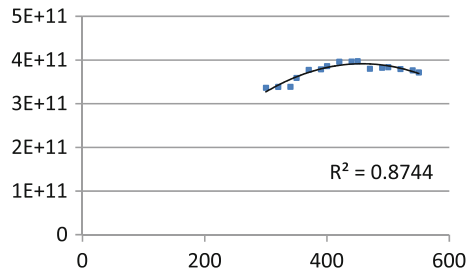
- For Al/SiC, mean and standard deviation features are the highest sensitivity features for the change in temperature, and correlation features are next, then the homogeneity feature.
- It can also be seen that there are texture features which have good correlations with the two cases simultaneously as mean, correlation and standard deviation features.
- For two cases, the high sensitivity curves give the ability to observe the trend of every case depends upon changes in temperature.
- The change in the structure of the material for two cases changes the topography of the surface texture, and so, the intensity of the gray levels, so, this can be observed through the type and values of sensitivity features.
- The contrast and entropy features are demonstrate poor sensitivity in the two cases and it cannot be depended upon them to study the changes in the temperature. Collective charts of correlation coefficient values for these features will be introduced in Appendix 3.

6 Conclusions

Processing of aluminum composites play a significant factor in develop the usage of such composites. In the present work, the effect of forming temperature on the forming behavior of aluminum reinforced by 10 wt% SiC were studied by using image texture features after using the compression test which was done at elevated temperature range of 300–550 °C and a constant strain rate of 0.024 s^{-1}. Image texture analysis is useful in a variety of applications and has been a subject of intense study by many researchers. Image texture can be quantitatively evaluated using some properties and various statistical and structural methods that have been developed to study these features. This paper studied the relationship between GLSDM features and changes in preparation temperatures of Al and Al/SiC materials. Image processing was executed to help in getting these relations. The results showed that 5 texture features have high correlations with changes in temperature in Al case, but 4 features in Al/SiC case. For Al, angular second moment/Energy feature has the highest sensitivity for temperature changes with 0.989 correlation coefficient, and standard deviation, max probability and mean features have 0.988, 0.970 and 0.904 correlation coefficients respectively. For Al/SiC, mean and standard deviation features have the highest sensitivity for temperature changes with 0.935 correlation coefficient, and correlation and homogeneity features have 0.923 and 0.90 correlation coefficients respectively. These results give the ability to study other temperature changes in other cases for the same materials.

Appendix 1

This appendix illustrates the used abbreviations and symbols through this paper.

1. Abbreviations		2. Symbols	
Sum and difference histogram matrices	GLSDM	Aluminum	Al
Gray level co-occurrence matrix	GLCM	Aluminum/Silicon carbide	Al/SiC
Second-order statistics	SOS	Direction of pixel pairs	θ
Gray level difference matrix	GLDM	Distance between pixel pairs	d
Gray level sum matrix	GLSM	GLSM matrix	M_s
Maximum probability	MaxP	GLDM matrix	M_d
Contrast	CON	Previous matrices elements	i, j
Homogeneity	HOM	Previous matrices elements number	n
Entropy	ENT	Mean	μ
Angular second moment/energy	ASM/EN		
Correlation	COR		
Standard deviation	SD		

Appendix 2

The table illustrates the different texture features as definitions and equations [17]:

Feature	Definition	Equation
μ	The pixel value is weighted not by its frequency of occurrence by itself (as in a regular mean equation), but by the frequency of its occurrence in combination with a certain neighbor pixel value	$0.5 * \sum_{i=0}^{n-1} i * M_s(i)$
MaxP	MaxP calculates grey-level, which has the maximum probability	$\max_{i=0}^{n-1} M_s(i)$
CON	A measure of the amount of local variation in the image	$\sum_{j=0}^{n-1} j^2 * M_d(j)$
HOM	It is expected to be large if the grey levels of each pixel pair are similar	$\sum_{i=0}^{n-1} \sum_{j=0}^{n-1} \frac{M_d(j)}{1+j^2}$

(continued)

Feature	Definition	Equation
ENT	It measures the randomness of a grey level distribution. It is expected to be high if the grey levels are distributed randomly throughout the image	$-\sum\limits_{i=0}^{n-1} M_s(i) * \ln(M_s(i)) - \sum\limits_{j=0}^{n-1} M_d(j) * \ln(M_d(j))$
ASM/EN	Uniformity and it can be considered as the opposite of entropy	$\sum\limits_{i=0}^{n-1} M_s(i)^2 \sum\limits_{j=0}^{n-1} M_d(j)^2$
COR	It is a measure of gray level linear dependence between the pixels at the specified positions relative to each other	$0.5\left(\sum\limits_{i=0}^{n-1} M_s(i) * (i-2\mu)^2 - \sum\limits_{j=0}^{n-1} j^2 * M_d(j)\right)$
SD	It relies on the mean and the dispersion around the mean of cell values	$\sqrt{0.5\left(\sum\limits_{i=0}^{n-1} M_s(i) * (i-2\mu)^2 + \sum\limits_{j=0}^{n-1} j^2 * M_d(j)\right)}$

Appendix 3

This appendix illustrates two collective charts of correlation coefficient values for poor sensitive features in Al and Al/SiC cases, as in Fig. 13.
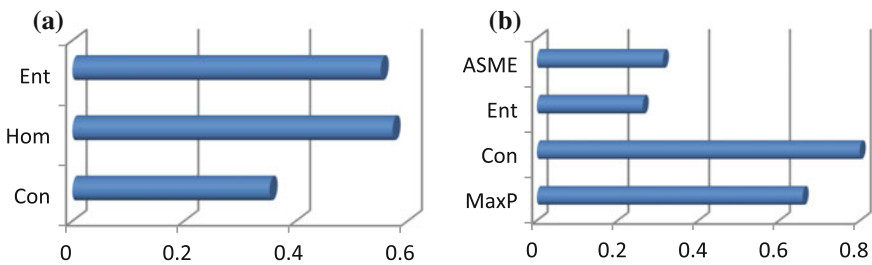
Fig. 13 Correlation coefficients of poor sensitive feature for Al and Al/SiC cases: **a** Al, **b** Al/Sic

References

1. Park, D.H., Ko, B.C., Yoo, Y.C.: Evaluation of hot workability of particle reinforced aluminum matrix composites by using deformation efficiency. J. Mater. Sci. **37**, 1593–1597 (2002)
2. Vedani, M., Gariboldi, E.: Hot forming related properties of Al-based particulate composites. Metall. Sci. Technol. **19**, 33–36 (2001)

3. Varma, V.K., Kamat, S.V., Kutumbarao, V.V.: Tensile behavior of powder metallurgy processed (Al-Cu-Mg)/SiCp composites. Mater. Sci. Technol. **17**, 93–101 (2001)
4. Parker, J.R.: Algorithms for Image Processing and Computer Vision. Wiley, New York (1997)
5. Rosenfeld, A., Kak, A.C.: Digital Picture Processing, vol. 1. Academic Press, New York (1982)
6. Ferro, C.J.S., Warner, T.A.: Scale and texture in digital image classification. Photogram. Eng. Remote Sens. **68**, 51–63 (2002)
7. Pratt, W.: Digital Image Processing. Wiley, New York (1991)
8. Raghu, P.P., Yegnanarayana, B.: Segmentation of Gabor-filtered textures using deterministic relaxation. IEEE Trans. Image Process. **5**, 1625–1636 (1996)
9. Tuceyran, M., Jain, A.K.: Texture Analysis, Handbook of Pattern Recognition and Computer Vision. World Scientific Publishing Co., Singapore (1993) (Chen, C.H., et al.)
10. Pichler, O., Teuner, A., Hosticka, B.J.: A comparison of texture extraction using adaptive Gabor filtering, pyramidal and tree structured wavelet transforms. Pattern Recognit. **29**, 733–742 (1996)
11. Park, B., Lawrence, K.C., Windham, W.R., Chen, Y.R., Chao, K.: Discriminant analysis of dual-wavelength spectral images for classifying poultry carcasses. Comput. Electron. Agric. **33**, 219–231 (2002)
12. Unser, M.: Sum and difference histograms for texture classification. IEEE Trans. Pattern Anal. Intell. **8**, 118–125 (1986)
13. Chen, C.H., Pau, L.F., Wang, P.S.P.: Pattern Recognition and Computer Vision, pp. 207–248. World Scientific Publishing Co., Singapore (1998)
14. Clausi, D.A.: An analysis of co-occurrence texture statistics as a function of gray-level quantization. Can. J. Remote Sens. **28**, 45–62 (2002)
15. Palm, C.: Colour texture classification by integrative co-occurrence matrices. Pattern Recogn. **37**, 965–976 (2004)
16. Ganesan, G., Raghukandan, K., Karthikeyan, R., Pai, B.C.: Development of Processing Maps for Al/15 % SiCp composite material. Mater. Sci. Eng. **369**, 230–235 (2004)
17. Gadelmawla, E.S., Eladawi, A.E., Abouelatta, O.B., Elewa, I.M.: Investigation of the cutting conditions in milling operations using image texture features. J. Eng. Manuf. **222**, 1395–1404 (2008)

Application of Artificial Neural Network to Predict the Effects of Severe Shot Peening on Properties of Low Carbon Steel

Erfan Maleki, Gholam Hossein Farrahi and Khalil Sherafatnia

Abstract Mechanical failures in most cases originate from the exterior layers of the components. It is considerably effective to apply methods and treatments capable to improve the mechanical properties on component's surface. Surface nanocrystallization produced by severe plastic deformation (SPD) processes such as severe shot peening (SSP) is increasingly considered in the recent years. However, artificial intelligence systems such as artificial neural network (ANN) as an efficient approach instead of costly and time consuming experiments is widely employed to predict and optimize the science and engineering problems in the last decade. In the present study the application of ANN in predicting of SSP effective parameters has been investigated and evaluated. The Back propagation (BP) error algorithm is used to network's training. In order to train the ANN, experimental tests on AISI 1017 mild steel specimens were conducted and the data was gathered. Testing of the ANN is carried out using experimental data not used during training. Almen intensity, residual stress, crystallite size, full width at half maximum (FWHM) and hardness were modeled. Different networks with different inputs are developed for modeling of each mentioned parameters. The Almen intensity, hardness, crystallite size, FWHM and residual stress have least mean error respectively for the accomplished modeling. The comparison of obtained results of ANN's response and experimental values indicates that the networks are tuned well and the ANN

E. Maleki (✉)
Mechanical Engineering Department, Sharif University of Technology—International
Campus, Amirkabir Square, 7941776655 Kish Island, Iran
e-mail: maleki_erfan@kish.sharif.edu; maleky.erfan@gmail.com

G.H. Farrahi · K. Sherafatnia
School of Mechanical Engineering, Sharif University of Technology, Tehran, Iran
e-mail: farrahi@sharif.edu

K. Sherafatnia
e-mail: sherafatnia@mech.sharif.edu

E. Maleki · G.H. Farrahi · K. Sherafatnia
Materials Life Estimation and Improvement Laboratory, Sharif University of Technology,
Tehran, Iran

can be used to predict the SSP effective parameters and it can be an alternative way
for calculating of parameters of this process.

1 Introduction

The majority of failures in engineering materials such as fatigue fracture, fretting
fatigue, wear and corrosion, are very sensitive to the structure and properties of the
material surface, and in most cases failures originate from the exterior layers of the
work piece. Therefore it would be considerably effective to apply an approach to
enhance the material properties on the surface of the part. In the last few decades,
ultrafine-grained materials, especially nanocrystalline (NC) characterized by crystal
grains with dimensions up to 100 nm, have attracted considerable scientific interest,
since nanostructured materials are expected to possess superior mechanical prop-
erties in simple chemical compositions fundamentally different from their con-
ventional coarse-grained polycrystalline counterparts [1–5]. Among various
methods proposed to produce ultrafine-grained materials, the severe plastic defor-
mation (SPD) technique has received the greatest attention due to its simplicity and
applicability for all classes of materials.

   The shot peening (SP) process as one of the SPD methods, is a technique which
is most widely used to totally prevent or greatly delay the fatigue failure of a
component. In this process, the surface of the part is bombarded with a multitude of
small hard spherical shots impacting at high velocity. As a result of the collision of
the shot with the surface of the component, an indentation is created which is
surrounded by a plastic deformed region followed by an elastic zone. Upon the
rebound of the shot, the recovery of the elastic zone creates compressive residual
stresses in the surface. The magnitude of these residual stresses and the depth of the
layer containing these stresses are a function of the process parameters [6–11].
Figure 1 demonstrates the plastic deformation caused by shot peening.

Fig. 1 Plastic deformation caused by shot peening
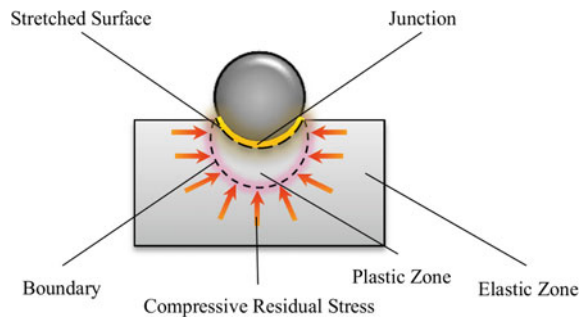
Severe shot peening (SSP) is an unconventional way to perform air blast shot peening (ABSP), and it is performed by the conventional ABSP device using peening parameters with a very high kinetic energy. It has been recently applied as a severe plastic deformation (SPD) process in order to generate a nanocrystallized layer on the surface of treated materials [12–18]. Thus, the main difference between shot peening and severe shot peening is that SSP is able to generate a nanostructured layer of material, whose depth depends on the selected parameters.

Artificial intelligence (AI) systems are widely accepted as a technology offering an alternative way to tackle complex and ill-defined problems [19]. The artificial neural network (ANN) approach as one the AI system is a well known type of the evolutionary computation methods in last decades. ANN models were widely utilized to interpret and correlate the variable relationships in complex nonlinear data sets. On the use of ANNs in modeling of shot peening process, Karatas [20] have been used ANN to predict residual stresses in the shot peened material C-1020. Delijaicov [21] have provided a model for peen forming process planning of Aluminium 7050 alloy to predict Almen displacement. In the present study, the application of ANN in modeling of the effects of SSP process on mechanical and metallurgical properties of AISI 1017 mild steel was investigated. Two different modeling approaches were accomplished in this paper. In the first modeling approach, shot diameter, SP time, coverage and projection pressure were regarded as inputs and Almen intensity, surface residual stress, crystallite size and full width at half maximum (FWHM) were considered as outputs of the networks. In the second modeling approach, the distance from the surface (depth) and Almen intensity were considered as inputs and hardness was gathered as an output of the ANNs. 12 data sets of experimental tests results from the total of 16, are used to networks training, while in the networks testing 4 different experimental data sets which were not used during training are used. Since the whole experimental results were not include in the training data sets and the performance of ANN is evaluate in a proper way.

2 Experimental Tests

The experimental data are taken from Unal and Varol [22]. In their work, the material used in the investigation was AISI 1017, a low carbon steel with the chemical composition shown in Table 1.

Rectangular plate specimens (30 × 30 mm) with a thickness of 10 mm were cut from the steel. Specimens were ground by 180–1200 grit sandpapers then polished with 6 and 1 μm diamond paste. Then heat treatment was applied to the specimens

Table 1 Chemical composition of AISI 1017 mild steel (wt%) [22]

C	Mn	P	S	Fe
0.15–0.20	0.30–0.60	Max. 0.04	Max. 0.05	Balance

annealing at 810 °C for 30 min plus furnace cooling process. Tables 2 and 3 illustrate SSP treatment conditions and their effects on mechanical and metallurgical properties of AISI 1017. In Table 3, the Almen intensity of 0 is related to not-peend specimens.

In the study by Unal and Varol [22], Almen intensity effect on the microstructure evolution and mechanical properties of low carbon steels was investigated. Nevertheless, the surface coverage was analyzed only to adjust the Almen intensities with air pressure, peening time and shot diameter and also investigated for

Table 2 Values of peening parameters and their effects on specimens [22]

Sample no.	Shot diameter (mm)	Coverage (%)	Time (s)	Pressure (kPa)	Almen intensity (mm)	Surface residual stress (MPa)	Crystallite size (nm)	FWHM (°)
1	0.28	100	45	690	0.31 A	210	82	0.120
2	0.28	200	45	690	0.31 A	210	82	0.120
3	0.58	100	25	413	0.31 A	210	82	0.120
4	**0.58**	**200**	**25**	**413**	**0.31 A**	**210**	**82**	**0.120**
5	**0.28**	**100**	**50**	**690**	**0.33 A**	**220**	**44**	**0.219**
6	0.28	200	50	690	0.33 A	220	44	0.219
7	0.58	100	25	448	0.33 A	220	44	0.219
8	0.58	200	25	448	0.33 A	220	44	0.219
9	0.28	100	50	723	0.35 A	260	39	0.243
10	**0.28**	**200**	**50**	**723**	**0.35 A**	**260**	**39**	**0.243**
11	0.58	100	20	482	0.36 A	260	39	0.243
12	0.58	200	20	482	0.36 A	260	39	0.243
13	**0.28**	**100**	**45**	**690**	**0.09 C**	**310**	**38**	**0.250**
14	0.28	200	45	690	0.09 C	310	38	0.250
15	0.58	100	40	345	0.10 C	310	38	0.250
16	0.58	200	40	345	0.10 C	310	38	0.250

Table 3 Hardness of severe shot peend specimens [22]

Sample no.	Depth (μm)	Almen intensity (mm)	Hardness (GPa)
1	0	0.00	4.82
2	0	0.33 A	8.18
3	0	0.35 A	8.85
4	**0**	**0.09 C**	**11.38**
5	**20**	**0.00**	**5.01**
6	20	0.33 A	7.89
7	20	0.35 A	8.09
8	20	0.09 C	9.75

Table 3 (continued)

Sample no.	Depth (µm)	Almen intensity (mm)	Hardness (GPa)
9	40	0.00	4.74
10	**40**	**0.33 A**	**7.09**
11	40	0.35 A	8.19
12	40	0.09 C	8.54
13	**80**	**0.35 A**	**7.21**
14	80	0.33 A	6.64
15	80	0.00	4.52
16	80	0.09 C	8.06

determining its impact on the surface roughness for 100 and 200 % values. Surface characteristics were affirmed using optical microscopy, scanning electron microscopy (SEM) and high resolution transmission electron microscopy (HRTEM). Nano hardness measurements were taken along the depth from the shot peened surface using nanoindentation methods. The experimental test results showed that the SSP process is an effective way to obtain ultra-fine grained surface layers and to obtain superior mechanical properties.

3   Artificial Neural Networks

Artificial intelligence (AI) systems such as artificial neural networks (ANNs) have found many applications in science and engineering problems in the last decade. ANN is a mathematical and numerical method in which its original idea has been inspired by human's brain. Basically the brain functions with a very dense network of neurons. The brain contains a lot of neurons connected to each other by many interconnections among them. A neuron consists mainly of the following parts: dendrite, cell body and axon [23]. Dendrite gets the signals from various other neurons to the neuron and carries them to the cell body to processing, after that an axon carries the signal from the cell body to various other neurons. Similarly, the neural units in the artificial neural network are developed as a very approximate model of the natural biological neurons [24]. Figure 2 shows an artificial neuron that is a computational and mathematical model of the biological neuron. A single neuron computes the sum of its inputs which are multiplied with a variant called the weight, adds a bias term, and drives the result through a generally nonlinear transfer function to produce a single output termed the activation level of the neuron.

An ANN model is created by interconnection of many of the neurons in a known configuration. The primary elements characterizing the neural network are the distributed representation of information, local operations and non-linear processing. ANN models have three main layers including input, hidden and output layers.

Fig. 2 An artificial neuron
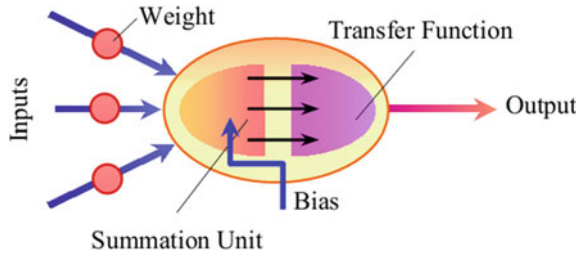
Fig. 3 Architecture of neural network
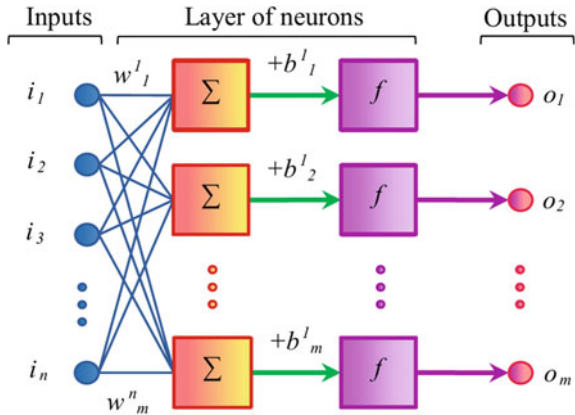
The structure of an ANN model is determined by the number of its layers and respective number of nodes in each layer and the nature of the transfer function [25, 26]. Selecting the optimum architecture of the network is one of the challenging steps in ANN modeling. The term "architecture" mentions the number of layers in the network and number of neurons in each layer. However, there is no straightforward method to estimate the optimal number of hidden layers and neurons in each layer [27, 28]. Thus trial and error methods have been used by many researchers to determine such case dependent parameters for studies involving ANN-based models [29]. Figure 3 represents the architecture of the neural network. In this network, each input consists of n parameters and each output comprises m parameters, while i, w, b, f and o represent the inputs, weight matrixes, bias vectors, transfer function in neurons, and outputs, respectively.

Mathematically, a layer k may be described by Haykin [30]:

$$u_m^k = \sum_{j=1}^{n} w_m^k i_j \tag{1}$$

$$o_m = f\left(v_m^k\right) = f\left(u_m^k + b_m^k\right) \tag{2}$$

where i_1, i_2, …, i_n are the inputs signals; w_1^k, w_2^k, …, w_m^k are the synaptic weights of neuron k; u_k is the linear combiner output due to input signals; b_k is the bias; f is the activation function and o_1, o_2, …, o_m are the output signals of the neuron. The tangent sigmoid (Tansig) (x), logarithmic sigmoid (Logsig) $\psi(x)$ and linear $\chi(x)$ transfer functions are described as follows [31]:

$$\phi(x) = \frac{2}{1 + e^{-2x}} - 1 \tag{3}$$

$$\psi(x) = \frac{1}{1 + e^{-x}} \tag{4}$$

$$\chi(x) = linear(x) \tag{5}$$

3.1 Training of ANN

The ANNs are trained with a training set of input and known output data. There is no exact available formula to decide what architecture of ANN and which training algorithm will solve a given problem and the best solution is obtained by trial and error [32]. In the present study, the feed forward error back propagation (BP) algorithm is used for ANN training that is the most common and efficient algorithm for training. The back Propagation algorithm defines a systematic way to update the synaptic weights of multi-layer feed forward supervised networks. The networks are composed of an input layer that receives the input values, an output layer, which calculates the neural network output, and one or more intermediary layers, so-called hidden layers [33]. The basis of the BP supervised learning process is the gradient descent method that usually minimizes the sum of squared errors between the target value and the output of the neural network.

3.2 Implementation of ANN

In this paper effects of the SSP process on mechanical and metallurgical properties of AISI 1017 mild steel were modeled by means of ANN. Two different modeling were accomplished in this paper and their related inputs and outputs are shown in Table 4.

It should be noted that the Almen intensity is not one of the SP process effects and actually it is one of the effective parameters of SP. But since all of the mentioned output parameters of modeling A, are affected by the parameters of shot diameter, coverage, peening time and projection pressure, they are considered in the common and same modeling approach. Figure 4, for example, represents the schematic architecture of ANN for modeling A and B: a four layer—feed forward

Table 4 Implemented modeling and their related inputs and outputs

Modeling approach	Input parameters	Output parameters
A	(1) Shot diameter (2) Coverage (3) Peening time (4) Projection pressure	(1) Almen intensity (2) Residual stress (3) Crystallite size (4) FWHM
B	(1) Depth (2) Almen intensity	(1) Hardness
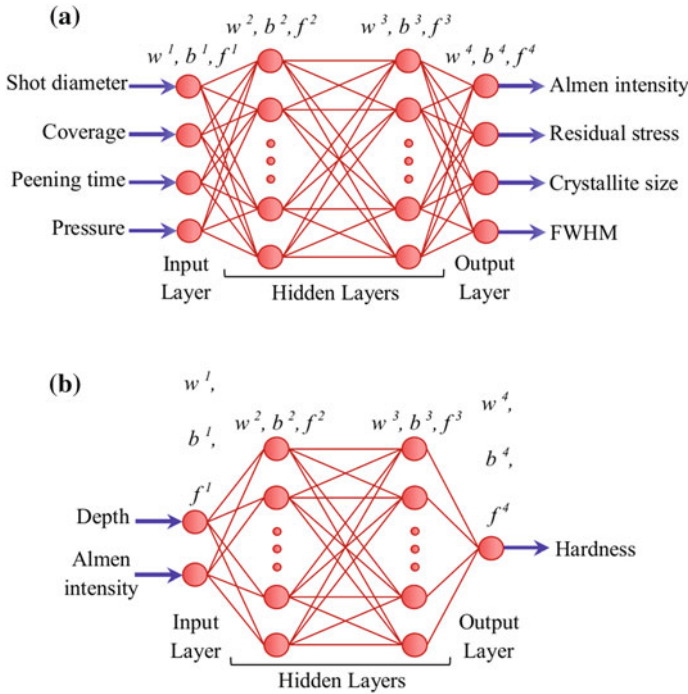
Fig. 4 Conceptual structure of implemented networks, **a** Modeling A and **b** Modeling B

with BP algorithm with full interconnection. In the considered networks, inputs are logged into the input layer to determine the outputs. In the ANN methodology, the sample data is often subdivided into training and testing sets. The distinctions among these subsets are crucial [34]. The Ripley defines the following: Training set: a set of examples used for learning that is to fit the parameters of the classifier. Testing set: a set of examples used only to assess the performance of a fully-specified classifier.

3.3 Performance Evaluation of ANN

The performance of the ANN models in predicting the severe shot peening effects on mechanical and metallurgical properties of AISA 1017 mild steel were statistically evaluated using four prediction score metrics calculated from the test dataset: coefficient of correlation (R^2), root mean square error (RMSE), mean relative error (MRE) and mean absolute error (MAE). These parameters have been determined using the following equations:

$$R^2 = \frac{\sum_{i=1}^{n} \left(f_{EXP,i} - F_{EXP}\right)\left(f_{ANN,i} - F_{ANN}\right)}{\sqrt{\sum_{i=1}^{n}\left(\left(f_{EXP,i} - F_{EXP}\right)^2\left(f_{ANN,i} - F_{ANN}\right)^2\right)}} \tag{6}$$

$$RMSE = \sqrt{\frac{\sum_{i=1}^{n}\left(f_{EXP,i} - f_{ANN,i}\right)^2}{n}} \tag{7}$$

$$MRE = \frac{1}{n}\sum_{i=1}^{n}\frac{\left|f_{EXP,i} - f_{ANN,i}\right|}{f_{EXP,i}} \times 100 \tag{8}$$

$$MAE = \frac{1}{n}\sum_{i=1}^{n}\left|f_{EXP,i} - f_{ANN,i}\right| \tag{9}$$

where $F_{EXP} = \frac{1}{n}\sum_{i=1}^{n}f_{EXP,i}$, $F_{ANN} = \frac{1}{n}\sum_{i=1}^{n}f_{ANN,i}$, n is the number of used samples for modeling, f_{EXP} is the experimental value and f_{ANN} is the networks predicted value.

3.4 Model Function Generating

After the neural network is trained successfully, for example, with four layers, the values of the four parameters of the network (i, b, w and f) for each modeling approaches A and B can be obtained. The function which correlates the inputs to the corresponding output can be calculated applying the aforementioned parameters. Finally, the model function can be determined as below (these relations are related to modeling approach B):

$$o^1 = f^1(w^1 i + b^1) \tag{10a}$$

$$o^2 = f^2(w^2 i^1 + b^2) \tag{10b}$$

$$o^3 = f^3(w^3 i^2 + b^3) \qquad (10c)$$

$$o^4 = f^4(w^4 i^3 + b^4) \qquad (10d)$$

$$G(g(1)) = o^4 = f^4(w^4 f^3(w^3 f^2(w^2 f^1(w^1 i + b^1) + b^2) + b^3) + b^4) \qquad (11)$$

where o^1, o^2 and o^3 are outputs of the first, second and third layer, respectively; o^4 is the fourth layer output which is equal to the function $G(g(1))$. The function G gets the values of two input parameters of depth and Almen intensity. Function of $g(1)$ represents the hardness.

4 Results and Discussion

In order train the network in the present study, the achieved experimental tests results on AISI 1017 mild steel have been used. The networks were trained to achieve the optimum structure (OS) in order to generate a model function (MF). Afterward by employing the obtained OS and MF, the operation of the network was tested. 12 data sets were used from the total of 16, as data sets to train the network, while in the network testing, 4 different ones (data of samples 4, 5, 10 and 13) which were not used during training are used for network testing. Therefor the whole experimental results were not used in the training phase. For investigative purposes, out of 16 samples data, 75 % data was taken for training and 25 % data was considered for testing. Several networks have been trained with different number of layers, number of neurons and rates of trainings (different structures) to find the OS of ANNs, to predict the considered output parameters, with the best performance and the highest R^2, the least RMSE, MRE and MAE. Some relevant information of the different trained networks for modeling approaches A and B are shown in Tables 5 and 6, respectively. The data shown in Table 5 are related to

Table 5 Related information of five different networks for modeling A (Almen intensity)

ANN modeling no.	Rate of training	Layers structure	Hidden transfer function	Output transfer function	R^2	RMSE	MRE (%)	MAE
1	0.095	4 × 4 × 4 × 4	Logsig	Tansig	0.0.9873	0.0081	0.8579	0.0077
2	0.095	4 × 4 × 6 × 4	Logsig	Tansig	0.99006	0.0047	0.6217	0.0044
3	0.110	4 × 6 × 6 × 4	Logsig	Tansig	0.99984	0.0029	0.3912	0.0013
4	**0.120**	**4 × 6 × 8 × 4**	**Logsig**	**Logsig**	**0.99991**	**0.0011**	**0.3380**	**0.0007**
5	0.120	4 × 8 × 8 × 4	Tansig	Linear	0.99965	0.0031	0.4333	0.0018

Table 6 Related information of five different networks for modeling B

ANN modeling no.	Rate of training	Layers structure	Hidden transfer function	Output transfer function	R^2	RMSE	MRE (%)	MAE
1	0.090	$2 \times 4 \times 6 \times 1$	Tansig	Linear	0.99155	0.0946	0.9004	0.0817
2	0.095	$2 \times 5 \times 7 \times 1$	Tansig	Linear	0.99751	0.0700	0.8215	0.0616
3	0.110	$2 \times 5 \times 9 \times 1$	Logsig	Logsig	0.99914	0.0510	0.5856	0.0421
4	**0.100**	$\mathbf{2 \times 8 \times 6 \times 1}$	**Logsig**	**Logsig**	**0.99987**	**0.0443**	**0.5078**	**0.0384**
5	0.115	$2 \times 8 \times 8 \times 1$	Tansig	Linear	0.99883	0.0628	0.6772	0.0492
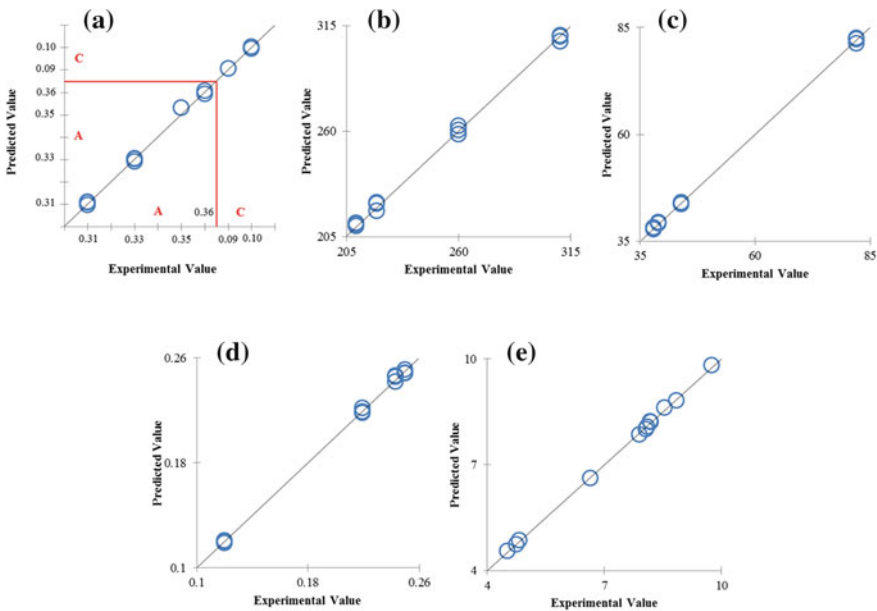
Fig. 5 Comparison of predicted and experimental values for training samples, **a** Almen intensity, **b** residual stress, **c** crystallite size, **d** FWHM and **e** hardness

Almen intensity which is one of the considered output parameters of modeling approach A. Ordinal numbers shown in the "Layer Structure" were used to indicate the total number of neurons in the input, hidden and output layers, respectively. Results of the networks were investigated and the simulations with $4 \times 6 \times 8 \times 4$ and $2 \times 8 \times 6 \times 1$ structure are selected for the modeling approaches A and B, respectively.

Figure 5 shows the predicted values in comparison with experimental values for each 12 training samples for the gathered output parameters.
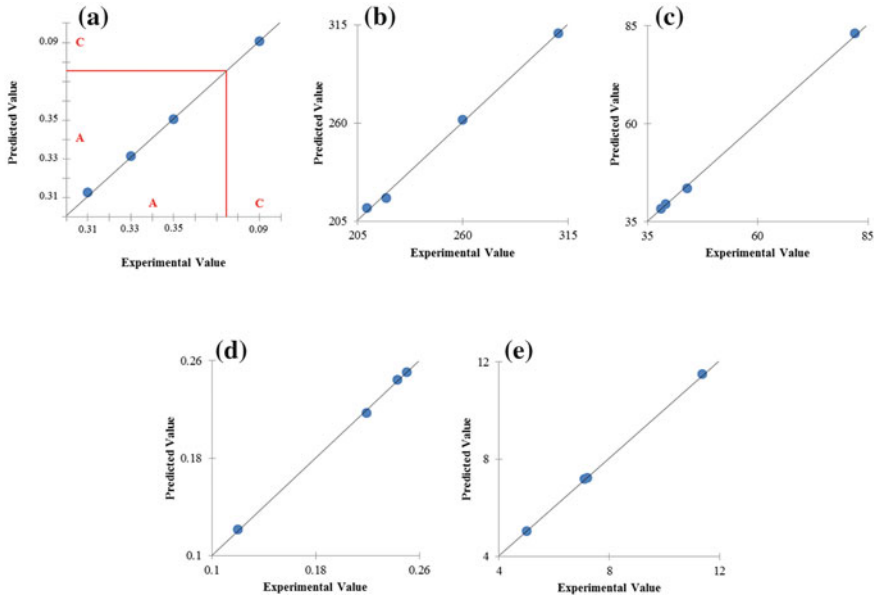
Fig. 6 Comparison of predicted and experimental values for testing samples, **a** Almen intensity, **b** residual stress, **c** crystallite size, **d** FWHM and **e** hardness

After the networks were trained, the selected networks were tested. Figure 6 illustrates the comparison of predicted and experimental values of each considered parameters for 4 different testing samples.

In Fig. 7, values of relative error (RE) for the both training and testing samples are shown.

According to the obtained values of ANN for training and testing samples, data corresponding to the used network are shown in Table 7. In the network training it is observed that the values of R^2 are more than 99.9 %. The RMSE, MRE and MAE values are very close to 0 and they are in little intervals (RMSE: [0.0011–1.9826], MRE: [0.3380–0.7326] and MAE: [0.0007–1.7467]). So it is concluded that networks are trained well and adjusted carefully. Likewise in network testing the values of R^2 are more than 99.9 % except for the residual stress modeling with a value of more than 99.8 %. Values of testing R^2 have negligible reduction. Moreover values of the testing RMSE, MRE and MAE are in tiny range (RMSE: [0.0017–1.8615], MRE: [0.5995–1.0571] and MAE: [0.0015–1.7500]) and they are acceptable. Considering the whole trained networks, modeling of Almen intensity and residual stress have minimum and maximum errors, respectively. Distributions of the Hardness from the shot peened surface to the bulk material is shown in Fig. 8; which is achieved by OS and MF of used ANN in this paper.
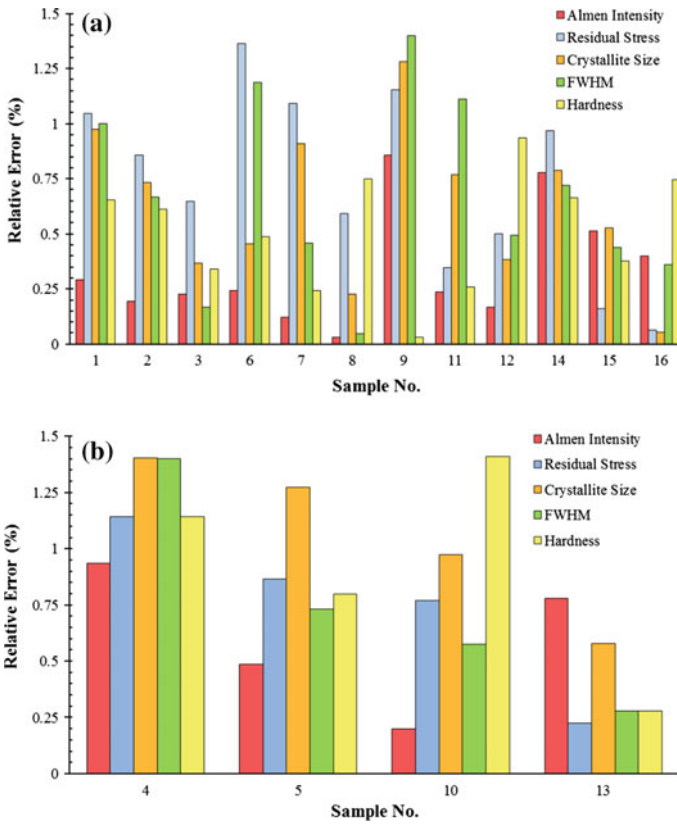
Fig. 7 Obtained values of relative error, **a** training samples and **b** testing samples

Table 7 Obtained values of R², RMSE, MRE and MAE for trained and tested network

Output parameter	Training				Testing			
	R^2	RMSE	MRE (%)	MAE	R^2	RMSE	MRE (%)	MAE
Almen intensity	0.99991	0.0011	0.3380	0.0007	0.99975	0.0017	0.5995	0.0015
Residual stress	0.99953	1.9826	0.7326	1.7467	0.99821	1.8615	0.7504	1.7500
Crystallite size	0.99986	0.3865	0.6224	0.3225	0.99958	0.6762	1.0571	0.5775
FWHM	0.99962	0.0017	0.6706	0.0014	0.99944	0.0014	0.7467	0.0013
Hardness	0.99987	0.0443	0.5078	0.0384	0.99983	0.0850	0.9071	0.0725
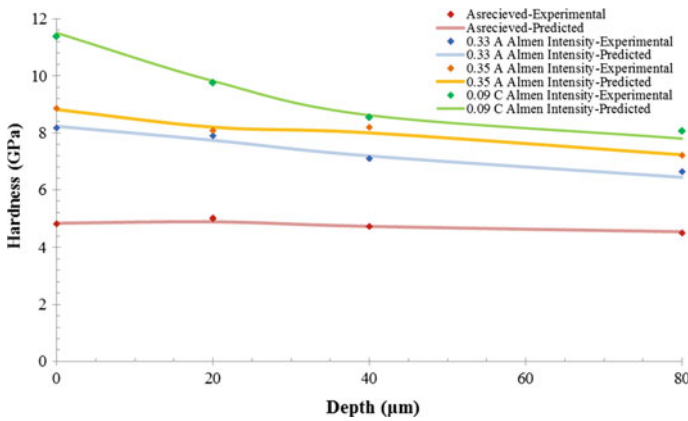
Fig. 8 Predicted values of ANNs using optimum structure and obtained model function for hardness

5   Conclusion

In the present study, application of ANNs for modeling of severe shot peening process on AISI 1017 mild steel steel were investigated. Experimental data were used to networks training and the ANN developed with Back propagation algorithm. The experimental test results showed that the SSP process is an effective way to obtain ultra-fine grained surface layers and to obtain superior mechanical properties. Almen intensity, residual stress, crystallite size, FWHM and hardness were modeled. Obtained results indicate that statistical errors, including RSME, MRE and MAE are very small. Moreover the values of R^2 for all of the regarded output parameters in implemented networks are more than 99.9 %. According to the achieved results it can be concluded that when the ANNs are tuned well and adjust carefully the modeling results are in a good agreement with the experimental results. Therefore using ANNs instead of costly and time consuming experiments decreases costs and the need for special testing facilities and the ANNs can be employed to predict and optimize SSP effects on mechanical and metallurgical properties of materials.

References

1. Valiev, R., Korznikov, A., Mulyukov, R.: Structure and properties of ultrafine-grained materials produced by severe plastic deformation. Mat. Sci. Eng. A-Struct. **168**, 141–148 (1993)
2. Morris, D.G.: Mechanical Behaviour of Nanostructured Materials. Trans Tech Publication, Switzerland (1998)

3. Nagahora, J., Kita, K., Ohtera, K.: New type aluminum alloys with higher strength. Mater. Sci. Forum **304–30**, 825–830 (1999)
4. Kulik, T.: Nanocrystallization of metallic glasses. J. Non-Cryst. Solids **287**, 145–161 (2001)
5. Valiev, R.: Nanostructuring of metals by severe plastic deformation for advanced properties. Nat. Mat. **3**, 511–516 (2004)
6. Almen, J.O., Black, P.H.: Residual Stresses and Fatigue in Metals. McGraw- Hill Book Company, New York (1963)
7. Marsh, K.J.: Shot Peening: Techniques and Applications. Engineering Materials Advisory Service, United Kingdom (1993)
8. Schulze, V.: Modern Mechanical Surface Treatment: States, Stability, Effects. Wiley, New York (2006)
9. Baker, S.: Shot Peening—A Dynamic Application and its Future. MFN Publishing House, Wetzikon (2012)
10. Gao, Y.-K., Yao, M., Shao, P.G., Zhao, Y.-H.: Another mechanism for fatigue strength improvement of metallic parts by shot peening. J. Mater. Eng. Perform. **12**, 507–511 (2003)
11. Gao, Y., Wu, X.: Experimental investigation and fatigue life prediction for 7475-T7351 aluminum alloy with and without shot peening-induced residual stresses. Acta Mater. **59**, 3737–3747 (2011)
12. Bagherifard, S., Guagliano, M.: Review of shot peening processes to obtain nanocrystalline surfaces in metal alloys. Surface Eng. **25**, 3–14 (2009)
13. Bagherifard, S., Guagliano, M.: Fatigue behavior of a low-alloy steel with nanostructured surface obtained by severe shot peening. Eng. Fract. Mech. **81**, 56–68 (2012)
14. Wen, A.L., Ren, R.M., Wang, S.W., Yang, J.Y.: Effect of surface nanocrystallization method on fatigue strength of TA2. Mater. Sci. Forum **620–622**, 545–549 (2009)
15. Roland, T., Retraint, D., Lu, K., Lu, J.: Fatigue life improvement through surface nanostructuring of stainless steel by means of surface mechanical attrition treatment. Scr. Mater. **54**, 1949–1954 (2006)
16. Li, D., Chen, H., Xu, H.: The effect of nanostructured surface layer on the fatigue behaviors of a carbon steel. Appl. Surf. Sci. **255**, 3811–3816 (2009)
17. Shaw, L.L., Tian, J.-W., Ortiz, A.L., Dai, K., et al.: A direct comparison in the fatigue resistance enhanced by surface severe plastic deformation and shot peening in a C-2000 superalloy. Mat. Sci. Eng. A-Struct. **527**, 986–994 (2010)
18. Bagherifard, S., Fernandez-Pariente, I., Ghelichi, R., Guagliano, M.: Fatigue behavior of notched steel specimens with nanocrystallized surface obtained by severe shot peening. Mater. Des. **45**, 497–503 (2013)
19. Kalogirou, S.A.: Artificial intelligence for the modeling and control of combustion processes: a review. Prog. Energ. Combust. **29**, 515–566 (2003)
20. Karataş, C., Sozen, A., Dulek, E.: Modeling of residual stresses in the shot peened material C-1020 by artificial neural network. Expert Syst. Appl. **36**, 3514–3521 (2009)
21. Delijaicov, S., Fleury, A., Martins, F.: Application of multiple regression and neural networks to synthesize a model for peen forming process planning. J. Achiev. Mater. Manufact. Eng. **43**, 651–656 (2010)
22. Unal, O., Varol, R.: Almen intensity effect on microstructure and mechanical properties of low carbon steel subjected to severe shot peening. Appl. Surf. Sci. **290**, 40–47 (2014)
23. Mukherjee, A., Schmauder, S., Ru, M.: Artificial neural networks for the prediction of mechanical behavior of metal matrix composites. Acta Metall. Mater. **43**, 4083–4091 (1995)
24. Han, J.K., Kamber, M.: Data Mining: Concepts and Techniques. Morgan Kaufmann Publishers, San Francisco (2006)
25. Özdemir, U., Özbay, B., Veli, S., Zor, S.: Modeling adsorption of sodium dodecyl benzene sulfonate (SDBS) onto polyaniline (PANI) by using multi linear regression and artificial neural networks. Chem. Eng. J. **178**, 183–190 (2011)
26. Çelekli, A., Birecikligil, S.S., Geyik, F., Bozkurt, H.: Prediction of removal efficiency of Lanaset Red G on walnut husk using artificial neural network model. Bioresour. Technol. **103**, 64–70 (2012)

27. Rezakazemi, M., Razavi, S., Mohammadi, T., Nazari, A.G.: Simulation and determination of optimum conditions of pervaporative dehydration of isopropanol process using synthesized PVA–APTEOS/TEOS nanocomposite membranes by means of expert systems. J. Membr. Sci. **379**, 224–232 (2011)
28. Rezakazemi, M., Mohammadi, T.: Gas sorption in H 2-selective mixed matrix membranes: experimental and neural network modeling. Int. J. Hydrogen Energy **38**, 14035–14041 (2013)
29. Wang, L., Yang, B., Wang, R., Du, X.: Extraction of pepsin-soluble collagen from grass carp (Ctenopharyngodon idella) skin using an artificial neural network. Food Chem. **111**, 683–686 (2008)
30. Haykin, S.: A Comprehensive Foundation. Upper Saddle River, New Jersey (2004)
31. Vogl, T.P., Mangis, J., Rigler, A., Zink, W., Alkon, D.: Accelerating the convergence of the back-propagation method. Biol. Cybern. **59**, 257–263 (1988)
32. Maleki, E.: Artificial neural networks application for modeling of friction stir welding effects on mechanical properties of 7075-T6 aluminum alloy. IOP Conf. Ser. Mater. Sci. Eng. **103**, 012034 (2015)
33. Maleki, E., Sherafatnia, K.: Investigation of single and dual step shot peening effects on mechanical and metallurgical properties of 18CrNiMo7-6 steel using artificial neural network. Int. J. Mater. Mech. Manuf. **4**, 100–105 (2016)
34. Shabanzadeh, P., Senu, N., Shameli, K., Ismail, F., Mohagheghtabar, M.: Application of artificial neural network (ANN) for the prediction of size of silver nanoparticles prepared by green method. Dig. J. Nanomater. Bios. **8**, 541–549 (2013)

The Influence of Two Different Casting Moulds on the Fatigue Properties of the Al–Si–Cu Cast Alloy

L. Hurtalová, E. Tillová, M. Chalupová, J. Belan and M. Uhríčik

Abstract The most widely used technologies for founding Al castings are sand casting and die casting (gravity casting; high pressure die casting; low pressure die casting; vacuum die casting; squeeze casting or squeeze forming). The lower cooling rate setting used for casting into a sand mould (sand casting) causes a coarse granular structure and lower values of mechanical properties. Higher cooling rate settings used for casting into a metallic mould (chill casting) causes fine-grained structures and higher values of mechanical properties. The present study provides information about the effect of casting into two different moulds on the fatigue properties of the heat treated AlSi9Cu3 cast alloy. Fatigue fracture surfaces were observed using a scanning electron microscope (SEM) after the fatigue test. The results show that the existence of casting defects and different morphologies of structural parameters (especially eutectic Si particles and Fe-rich intermetallic phases) has considerable influence on fatigue properties in both types of experimental materials. The results show that the fatigue lifetime is longer for samples casted into a metallic mould (chill casting) (average fatigue lifetime for 10^7 of cycles = 68 MPa) compared to casting the same materials into a sand mould (sand casting) (average fatigue lifetime for 10^7 cycles = 39 MPa).

Keywords Fracture surface of aluminium alloy · Fatigue properties of aluminium alloy · Sand casting · Chill casting

L. Hurtalová (✉) · E. Tillová · M. Chalupová · J. Belan · M. Uhríčik
Department of Materials Engineering, Faculty of Mechanical Engineering,
University of Žilina, Univerzitná 8215/1, 010 26 Žilina, Slovakia
e-mail: lenka.hurtalova@fstroj.uniza.sk

E. Tillová
e-mail: eva.tillova@fstroj.uniza.sk

M. Chalupová
e-mail: maria.chalupova@fstroj.uniza.sk

J. Belan
e-mail: juraj.belan@fstroj.uniza.sk

M. Uhríčik
e-mail: milan.uhricik@fstroj.uniza.sk

1 Introduction

The need for aluminium alloys with good toughness, high strength, adequate damage tolerance capability, good fatigue resistance and good corrosion resistance for use in applications in the aerospace, automotive industries as well as in commercial products led to study of the properties and structure of these materials [1]. Microstructure factors that influence mechanical properties of aluminium alloys were described in previous studies [2–4] and therefore their effects on fatigue properties were studied.

The fatigue of all engineering components is termed "fatigue lifetime". Fatigue lifetime is measured by the number of cycles that the material can withstand before fatigue damage occurs [5]. The fatigue properties of Al-casting alloys are strongly related to their microstructure [6]. The microstructure of Al-casting alloys consists mostly of eutectic (a mechanical mixture of α-phase = matrix and eutectic Si particles); α-phase and different intermetallic phases [2–4]. The Si and intermetallic (second) phases—Al_2Cu, Mg_2Si, Al_5FeSi and $Al_{15}(FeMn)_3Si_2$ are harder than the α-matrix, therefore if the localized stress level surpasses the material yield strength, there will be some deformation of the α-phase matrix while the hard phases may fracture or experience some decohesion from the α-matrix, thus forming micro-voids [7]. Previous work has shown that the most important metallurgical parameters affecting the Al-alloy's resistance to fatigue are the amount and size of casting defects (micro-porosities, oxide inclusions and shrinkage porosities), secondary dendrite arm spacing (SDAS), α-matrix, Si-particles and Fe-rich phases [6–8]. Porosity is the most common defect found in Al–Si casting alloys and is the major cause of rejection of such castings, as it often results in poor mechanical properties such as limited strength and ductility, varying fracture toughness, irregular crack initiation and crack propagation characteristics, as well as a lack of pressure tightness [9]. According to Gao [8] Si-particles size and also distribution have a significant effect, but the influence of their shape was negligible. However, according to Moreira [7], the morphology and size of the second phases are important factors causing stress concentration in the α-matrix around them. Rounded Si particles and small second phase particles cause lower stress concentration levels and delay the fatigue crack nucleation [7].

The aim of this article is to present the changes of fatigue properties in secondary AlSi9Cu3 cast alloys caused by the application of two different casting methods. This paper publishes the authors own experimental results.

2 Experimental Material and Procedures

The experimental material is the cast AlSi9Cu3 alloy (prepared from recycled aluminium scrap) delivered by the companies Uneko, spol.s.r.o. (sand casting) and Confal a.s. (chill casting). The samples for fatigue tests were extracted from circular

Table 1 Chemical composition of experimental materials

AlSi9Cu3—sand casting—Uneko, spol.s.r.o.										
Element	Si	Cu	Mn	Zn	Mg	Fe	Ni	Ti	Sn	Pb	Al
(wt%)	10.7	2.4	0.25	1.0	0.26	0.9	0.1	0.05	0.02	0.00	Remainder
AlSi9Cu3—chill casting—Confal a.s.										
Element	Si	Cu	Mn	Zn	Mg	Fe	Ni	Ti	Sn	Pb	Al
(wt%)	9.4	2.4	0.24	1.0	0.28	0.9	0.05	0.04	0.03	0.09	Remainder

bars (sand casting—ø 20 × 300 mm; chill casting—ø 18 × 150 mm). Experimental materials were not modified or grain refined. Chemical composition of both experimental materials was checked using arc spark spectroscopy and is shown in Table 1.

Samples for mechanical and fatigue tests were prepared by lathe-turning and milling operation from circular bars. The fatigue tests of sand chill samples were carried out using a rotating bending fatigue machine—ROTOFLEX operating at 30 Hz, load ratio R = −1 and at room temperature of 20 ± 5 °C. In this type of machine, a sample with a round cross section is subjected to a deal-weight load while bearings ensure rotation. A given point on the circular test section surface is subjected to sinusoidal stress amplitude from tension on the top to compression on the bottom with each rotation [10]. The fatigue tests of chill cast samples were done on the Vibrophores Amsler 50–250 HFP 5100 testing machine with the symmetrical push-pull load and at room temperature of 20 ± 5 °C.

The microstructural details were analysed using the light microscope Neophot 32 (analysis of Si-particles, pores and intermetallic phases) and using the scanning electron microscope VEGA LMU II (for analysis of the chemical composition of intermetallic phases). The fatigue fracture surface observation was done on the scanning electron microscope VEGA LMU II. The samples for metallographic analysis were prepared by standard metallographic procedures (wet ground on SiC papers, DP polished with 3 μm diamond pastes followed by Struers Op-S and etched for study at an optical microscope by standard etcher Dix-Keller and 0.5 % HF).

3 Results and Discussion

3.1 Characterisation of Microstructure

The defects, the morphology of eutectic and the morphology of intermetallic phases have an important effect on the ultimate mechanical properties of the casts. Al–Si alloys usually contain Si and sometimes Mg or Cu as the main alloying elements, together with various impurities such as Fe, Mn, Zn or Cr. These elements go into solid solution but they also form different intermetallic phases. The formation of these phases should correspond to successive reaction during solidification— Table 2 [11–13].

Table 2 Reactions occurring during solidification of AlSiXCuX alloys [14]

Reactions	Temperature (°C)
α—dendritic network	580–620
Liq. $\rightarrow$ α-phase + Si + AlFe$_5$Si	555–570
Liq. $\rightarrow$ α-phase + Si + Mg$_2$Si + Al$_8$FeMg$_3$Si$_6$	500–540
Liq. $\rightarrow$ α-phase + Si + Al$_2$Cu + Al$_5$Mg$_8$Si$_6$Cu$_2$	470–500
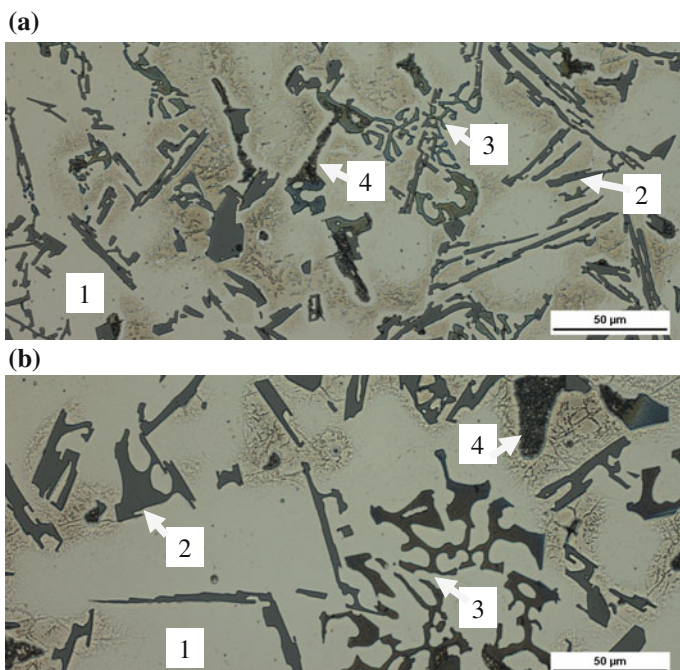
Fig. 1 Microstructure of secondary AlSi9Cu3 alloy cast into two different mould *1*—α-phase, *2*—eutectic Si-particles, *3*—Fe-rich phases, *4*—Cu-rich phases, etch. 0.5 % HF. **a** Chill casting; **b** sand casting

Typical microstructures of the experimental materials AlSi9Cu3 in as-cast state are shown in Fig. 1. The microstructure of the recycled Al–Si–Cu cast alloy consists of dendrites α-phase (light grey—Fig. 1—1), eutectic (mixture of α-matrix and dark grey eutectic Si-phases—Fig. 1—2) and variously types of intermetallic phases (Fig. 1—3, 4).

The fineness of dendrites in the material cast into a metallic mould is lower when compared to the material cast into a sand mould (Fig. 2). Eutectic Si in the untreated state in the alloy casted into the sand mould is manifested as larger needles (Fig. 1b—2) than in samples cast into the metallic mould, which influences the decreasing tensile strength. Eutectic Si in the untreated state observed in the
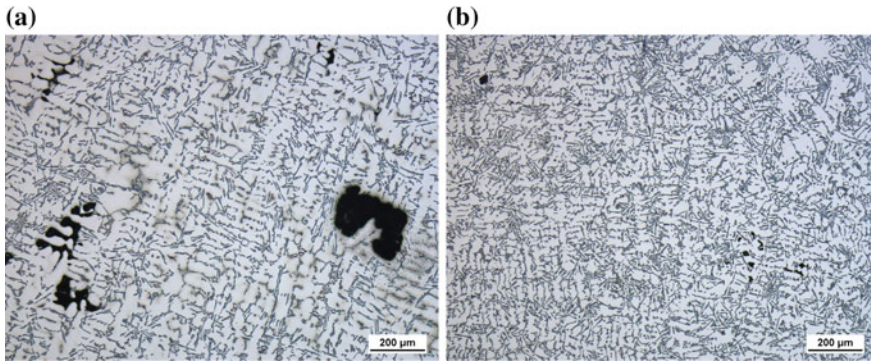
Fig. 2 Effect of casting methods on porosity in AlSi9Cu3 alloy, etch. Dix-Keller. **a** Alloy cast into the sand mould (sand casting); **b** alloy cast into the metallic mould (chill casting)

AlSi9Cu3 alloy cast into the metallic mould is manifested as little needles (Fig. 1a—2), thinner than the platelets observed in samples cast into the sand mould. The quantitative assessment results show that the average area of eutectic Si particles in alloys cast into the sand mould is 976.58 and 737.55 μm^2 in alloys cast into the metallic mould. The intermetallic phases have a greater size in the alloys cast into the sand mould in compared to alloy cast into the chill mould, too (Fig. 1).

The effect of the casting on porosity is shown in Fig. 2. Massively occurring porosity and shrinkages were observed in recycled AlSi9Cu3 cast alloys cast into the sand mould. Porosity was higher by about 10 % (see Fig. 2a) than in materials cast into the metallic mould. It influences the degradation value of mechanical properties. Materials cast into the metallic mould had almost zero porosity (Fig. 2b). This is probably related to the slower cooling rate in sand casting [15].

3.2 Fatigue Behaviour

The results of fatigue tests carried out on samples extracted from experimental circular bars are presented in the S/N (stress amplitude vs. cycles to failure) diagrams in Fig. 3. The number of cycles that the samples had to reach without breaking was 10^7 for materials cast into the sand mould, and 2×10^7 for materials cast into the chill mould. The samples that reached these numbers of cycles without breaking are defined as run-out. The range of fatigue lifetimes for 10^7 cycles was from 29 to 49 MPa from which average value of fatigue lifetime for 10^7 cycles was observed 39 MPa in material casted into the sand moulds (Fig. 3a).

The range of fatigue lifetime for 2×10^7 cycles was from 50 to 80 MPa from which average value of fatigue lifetime for 2×10^7 cycles was observed 67.5 MPa in materials cast into the metallic mould (Fig. 3b). The predicted value of fatigue lifetime for 10^7 cycles for materials cast into the metallic mould was 68 MPa
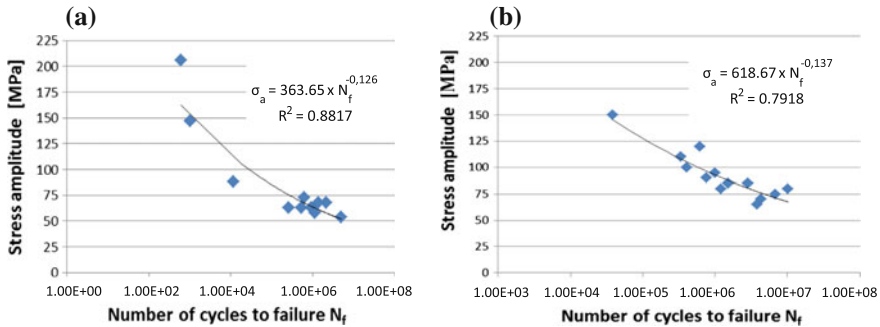
Fig. 3 Effect of two different casting moulds on fatigue properties of secondary AlSi9Cu3 cast alloy. **a** S/N fatigue data for material cast into a sand mould; **b** S/N fatigue data for material cast into a metallic mould

according to Basquin's equation obtained from the diagram (Fig. 3b). The fatigue resistance was found to be by about 43 % higher in the push-pull test than in the rotating bending test due to the different material volumes under high stress, but also due to the different casting methods that had been used for the production of the experimental samples.

3.3 Fractography Analysis of Fatigue Fracture

The process of fatigue consists of three stages [10]: crack initiation (stage I); progressive ("stable") crack growth across the component (stage II); and a final sudden fracture of the remaining cross section of the component (stage III). Stages I and II are also called the fatigue region. The features responsible for crack initiation were studied in the samples on SEM after the fatigue test. Within the fatigue test boundaries we established that high stress amplitude causes a small fatigue region and a large region of final static rupture for both experimental samples (cast into a sand mould—Fig. 4a, or metallic mould—Fig. 5a).

The SEM metallographic analysis of fracture surfaces confirmed the key role of porosity, which was the point of fracture crack initiation in both types of samples. The initiation sites were pores (casting defects) of irregular shape, near the surface of the samples, initiating the crack propagation (Figs. 4b, c and 5b, c).

The sand cast samples have more initiation sites as shown in Fig. 4b, compared to the chill casted samples that had always only one initiation site during the experiment—Fig. 5b. The initiation sites for samples cast into sand moulds were more concentrated at one point with the decreasing stress amplitude.

Stages II and III for samples cast into a sand mould: The area of the stable crack propagation (Stage II) is characterised by transcrystalline fatigue fracture of α-phase with smooth areas (Fig. 6a). The smooth areas were identified as Fe-rich phases and
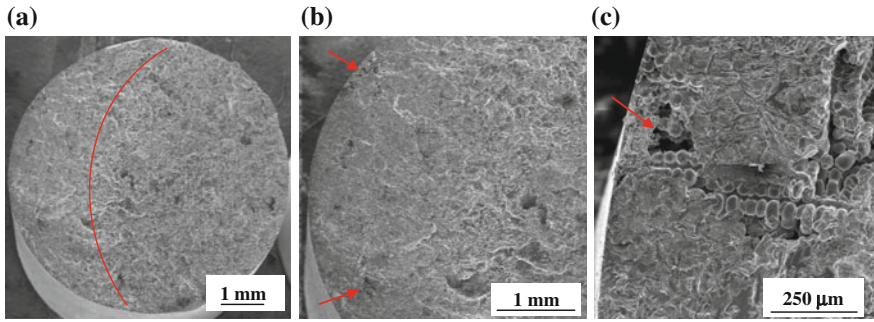
Fig. 4 Fractography analysis of fatigue fracture on samples cast into a sand mould. **a** Fracture surface of a fatigue samples; **b**, **c** the initiation sites (stage I)
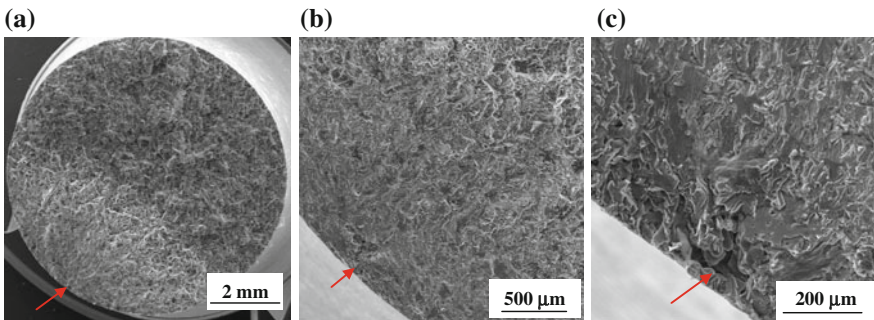
Fig. 5 Fractography analysis of fatigue fracture on samples cast into a metallic mould. **a** Fracture surface of a fatigue samples; **b**, **c** the initiation sites (stage I)

Si particles using SEM (BSE) and EDX analysis. The typical aspect of fatigue—striations—were observed only in few isolated cases in an area between Stage II and Stage III of fatigue fracture.

The last stage (Stage III) consisted of a transcrystalline ductile fracture with plastic strain ranges of Al matrix (α-phase) and transcrystalline cleavage fractures of Si particles and also brittle iron intermetallic phases (Fig. 6b). The transcrystalline ductile fracture is related to the Cu-rich intermetallic phases, too.

Stages II and III for samples cast into a metallic mould: The area of the stable crack propagation (Stage II) is characterised by transcrystalline fatigue fracture of α-phase that forms fine relieves; intercrystalline fatigue fracture of iron intermetallic phases (smooth areas) and transcrystalline fatigue fracture of eutectic silicon (Fig. 7a). The smooth areas were identified as Fe-rich phases and Si particles using SEM (BSE) and EDX analysis. The typical aspect of fatigue—striations—were observed only in few isolated cases.

Fracture surface of the static fracture (Stage III—Fig. 7b) is characterised by mixed transcrystalline ductile and cleavage fracture. The transcrystalline cleavage

(a)   **(b)**
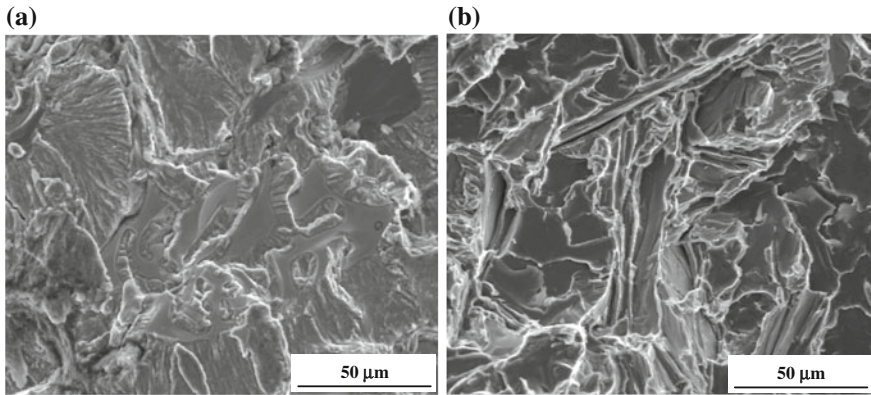
Fig. 6 Fractography analysis of fatigue fracture on samples cast into a sand mould. **a** The fatigue fracture surface (stage II); **b** the static fracture (stage III)

(a)   **(b)**
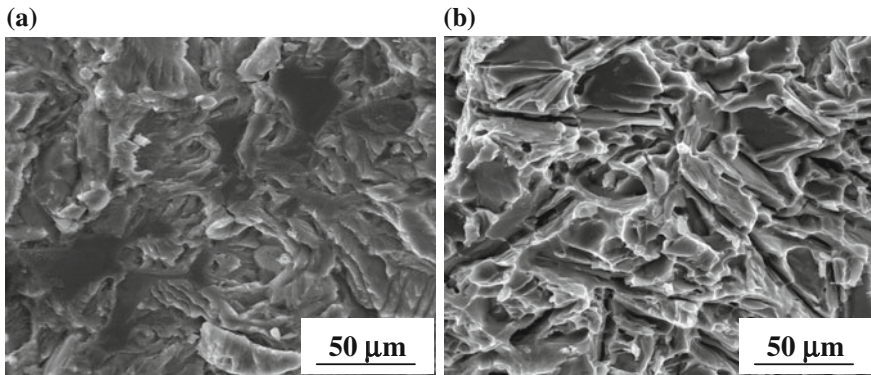
Fig. 7 Fractography analysis of fatigue fracture on samples cast into a metallic mould. **a** The fatigue fracture surface (stage II); **b** the static fracture (stage III)

fracture related to eutectic silicon occurring in platelets—in metallographic samples in form of needles, and also with brittle iron intermetallic phases. The transcrystalline ductile fracture with dimples morphology is related to matrix (α-phase) and Cu-rich intermetallic phases.

4 Conclusions

This study confirmed the negative influence of porosity, the morphology of eutectic Si particles and Fe-rich intermetallic phases on the fatigue lifetime of AlSi9Cu3 cast alloys that were cast into a sand or metallic mould without modification or grain

refinement. This work confirms that the different casting methods generate different microstructures and different amounts of porosity. The structural parameters were larger in samples cast into a sand mould and these samples had a higher volume of porosity than the samples casted into a metallic mould.

The study shows that samples cast into a metallic mould have a fatigue lifetime which is about 43 % longer for 10^7 cycles in the push-pull test (68 MPa), compared to the material cast into a sand mould during rotating bending test (49 MPa). The pores (casting defects) initiate the fatigue crack propagation in both types of samples. The hard and brittle eutectic Si particles and Fe-rich intermetallic phase causes transcrystalline and intercrystalline fatigue fracture and transcrystalline cleavage fracture; matrix with Cu-rich intermetallic phases transcrystalline fatigue fracture and transcrystalline ductile fracture.

Even though the Al cast alloy should primarily have transcrystalline ductile fracture, this study confirmed that the microstructure causes predominance of the transcrystalline cleavage fracture because of the presence of Si a Fe-rich particles (their morphology) in the microstructure.

References

1. Srivatsan, T.S., Guruprasad, G., Vesudevan, V.K.: The quasi static deformation and fracture behavior of aluminum alloy 7150. Mater. Des. **29**, 742–751 (2008)
2. Hurtalová, L., Tillová, E., Chalupová, M.: Microstructural and Vickers microhardness evolution of heat treated secondary aluminium cast alloy. Key Eng. Mater. **586**, 137–140 (2014)
3. Hurtalová, L., Tillová, E., Chalupová, M.: Optimization of eutectic Si particles morphology in secondary Al-Si cast alloys after different heat treatment. Adv. Mater. Res. **1025–1026**, 349–354 (2014)
4. Hurtalová, L., Tillová, E., Chalupová, M.: The structure analysis of secondary (recycled) AlSi9Cu3 cast alloy with and without heat treatment. Eng. Trans. **61**, 197–218 (2013)
5. Nový, F., Bokůvka, O., Trško, L., Chalupová, M.: Ultra high cycle fatigue of materials. Int. J. Eng. X **2**, 231–234 (2012)
6. Bonollo, F., Tovo, R.: Fatigue in Al casting alloys: metallurgical aspects, edited by TALAT Lecture 1254 European Aluminium Associate (EAA) (1999)
7. Moreira, M.F., Fuoco, R.: Characteristics of fatigue fractures in Al–Si cast components. AFS Trans. **2**, 1–15 (2006)
8. Gao, Y.X., Yi, J.Z., Lee, P.D., Lindley, T.C.: A micro-cell model of the effect of microstructure and defects on fatigue resistance in cast aluminum alloys. Acta. Mater. **52**, 5435–5449 (2004)
9. Fintová, S., Konstantová, V., Konečná, R., Nicoletto, G.: Porosity and fatigue behavior of cast Al-Si alloys. Mater. Eng. **15**, 29–32 (2008)
10. Bokůvka, O., Nicoletto, G., Guagliano, M., Kunz, L., Palček, P., Nový, F., Chalupová, M.: Fatigue of Materials at Low and High Frequency Loading. EDIS, Žilina (2014)

11. Tillová, E., Panušková, M.: Effect of solution treatment on intermetallic phases morphology in AlSi9Cu3 cast alloy. Mater. Eng. **14**, 73–76 (2007)
12. Skočovský, P.: Colour contrast in metallographic microscopy. Slovmetal, Žilina (1993)
13. Dobrzański, L.A., Krupiński, M., Krupińska, B.: Structure analysis of Al cast alloy. J. Achiev. Mater. Manuf. Eng. **27**, 23–26 (2008)
14. Dobrzański, L.A., Maniara, R., Sokolowski, J.H.: The effect of cast Al-Si-Cu alloy solidification rate on alloy thermal characteristics. J. Achiev. Mater. Manuf. Eng. **17**, 217–220 (2006)
15. Nicoletto, G., Konečná, R., Baicchi, P., Majerová, V.: Casting porosity and long—life fatigue strength of cast Al-alloy. Mater. Sci. Forum **567–568**, 393–396 (2008)

Mechanical Property Evaluation of Gas-Metal-Arc Welded SKD 61 Hot Work Tool Steel

S. Surapunt and T. Kanchanasangtong

Abstract The aim of this research is to study the effect of heat input on microstructure, impact and tensile strength properties of gas-metal-arc welded SKD 61 hot work tool steel by applying pulse current. Two steel plates with V groove at the connected edge, were welded under the condition of 150, 170 and 190 A of welding currents, 16–25 V of arc voltages and 1.5 mm/s of welding speed. A consumable copper-coated solid wire electrode was used in this welding process. The results showed that the martensite with retained austenite and dendrite structure of ferrite phases were found in the welded zones for all conditions. The hardness in the welded zone of three welding conditions were slightly increased with increasing heat input, and higher than that of the base metal, which resulted from martensite transformation. The absorbed energy of welded specimens during impact tests was increased with increasing heat input. The values of impact energies at the welding currents of 150, 170 and 190 A were 8.7, 10.0 and 14.0 J, respectively. Tensile strengths of all welded specimens were almost constant at 250 MPa. The tensile specimens were fractured at the heat affected zone.

Keywords GMAW process · SKD 61 steel · Heat input · Pulse current

1 Introduction

The gas metal arc welding (GMAW) process can be widely used for many types of metals, such as alloy steels, stainless steels, as well as aluminum alloys [1–4]. Despite, its wide application and advantages, the technique of pulsed current is also interesting to be applied in the gas metal arc welding process (GMAW-P) for

S. Surapunt (✉) · T. Kanchanasangtong
Department of Industrial Engineering, Faculty of Engineering,
Thammasat University, Klong Luang, Pathum Thani 12120, Thailand
e-mail: ssupacha@engr.tu.ac.th

T. Kanchanasangtong
e-mail: teerayut.k@rmutk.ac.th

providing more precisely controlled spray droplet transfer at low welding current [5–7]. By using this technique, a smaller and more precisely controlled welding pool can be obtained along the welding area. The major information of GMAW-P of these alloys concerning welding technique are available in the literature [8–12], but it still lacks of the information of metallurgical aspects for mold and die repairing. Especially for low weldability materials, such as SKD 61 hot work tool steel, undesirable microstructures, such as martensite, influenced by thermal distribution in the welded area and the heat affected zone (HAZ) are very essential factors which have effects on the material properties and increase the susceptibility to crack the steel [13]. The effect of heat input on the microstructure and hardness of the SKD 61 was investigated [14]. In this study, a detailed experimental investigation of the effect of heat input on mechanical properties and microstructure of SKD 61 hot work tool steel using gas metal arc welding with pulse current was carried out in order to evaluate mold and die repairing.

2 Materials and Method

The material used in this experiment was SKD 61, in the form of a hot work tool steel plate. The chemical compositions of the base metal and filler material are shown in Table 1. Two steel plates with dimensions of 50 mm width × 120 mm length and 10 mm thickness with groove shape at the connected edge based on welding specification were considered see Fig. 1. The experimental welding

Table 1 Chemical compositions of SKD 61 base metal and filler material

Element %	C	Si	Mn	P	S	Cu	Cr	Mo	V
Base metal	0.38	0.10	0.40	0.01	0.01	0.08	4.97	1.25	0.97
Filler material	0.42	2.80	0.40	–	–	–	8.50	–	–
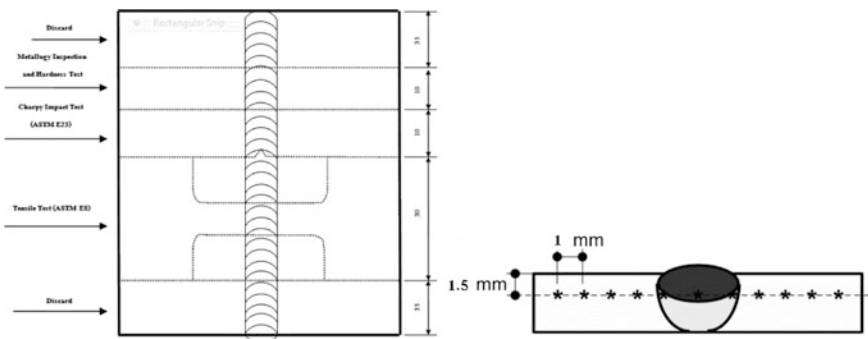
Fig. 1 Schematic illustration of the workpiece of this experiment

Table 2 Welding parameters utilized in this experiment

Parameter	Value
Specimen	SKD 61 hot work tool steel
Electrode type	MIG 600 HB
Diameter of electrode	1.2 mm
Vertex angle	90°
Shield gas	82 % Ar–18 %CO_2
Gas flow rate	13 L/min
Arc voltage	16–25 V
Welding current	150, 170, 190 A
Welding speed	1.5 mm/s

parameters were listed in Table 2. A consumable copper coated-solid wire electrode was used for filler material. The specimens were preheated at 400 °C before welding and post heated at 300 °C after welding. The sample was cut by an EDM wire-cut machine along the transverse welded bead which covered the three zones of welded zone, heat affected zone (HAZ) and base metal for microstructure investigation, hardness measurement, and tensile and impact testing.

The heat input (kJ/mm) at the welded area was estimated by using Eq. (1):

$$\text{Energy Input} = \frac{V \times A}{\text{Speed(mm/s)} \times 1000},\tag{1}$$

where V is the voltages (V) and A is the electric currents (A).

3 Results and Discussion

The values of the heat input were calculated from the arc current and arc voltage by using Eq. (1) and are shown in Table 3.

3.1 The Effect of Heat Input on Microstructures

The microstructure of the welded zone, HAZ and base metal of welded specimens are almost the same for heat inputs of 2.51, 3.01 and 3.53 kJ/mm (150, 170 and 190 A arc currents), which are shown in Fig. 2. In the welded zone, they revealed

Table 3 Heat input values calculated using Eq. (1)

Arc current (A)	Arc voltage (V)	Heat input (kJ/mm)
150	25.1	2.51
170	26.6	3.01
190	27.9	3.53
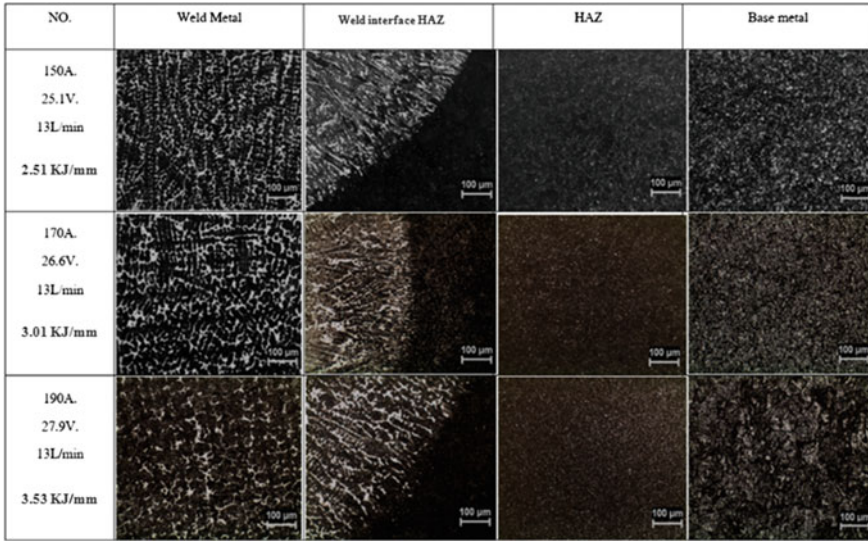
Fig. 2 Microstructures of welded zone, HAZ and base metal of welded specimens with various numbers of heat inputs

Fig. 3 Microstructure of the welded zone with 35.3 kJ/mm heat input (190 A arc current) reveals martensite with retained austenite in the dendritic ferrite phase
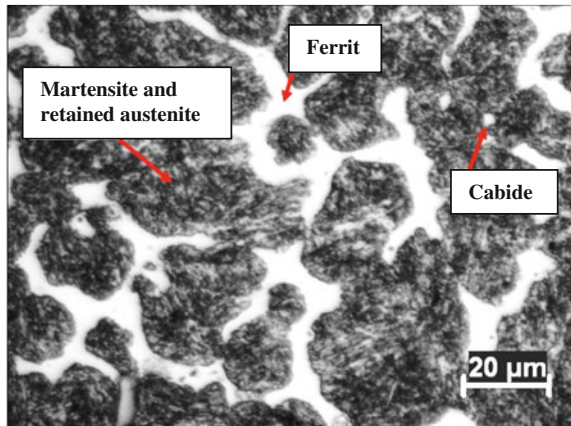
coarse grains of martensite with retained austenite in the matrix of dendritic segregation pattern of ferrite phase, and with some carbide particles as was shown in Fig. 3. At the higher welding current, the higher heat input and higher feeding speed of the filler material result in a carbon increase from the filler material, which results in a higher ratio of the martensite and ferrite phases. In the HAZ, the mixed phases of rounded martensite and a large amount of carbide particles were founded in the ferrite matrix phase. The carbide particles in the ferrite matrix phase were found in the base metal.
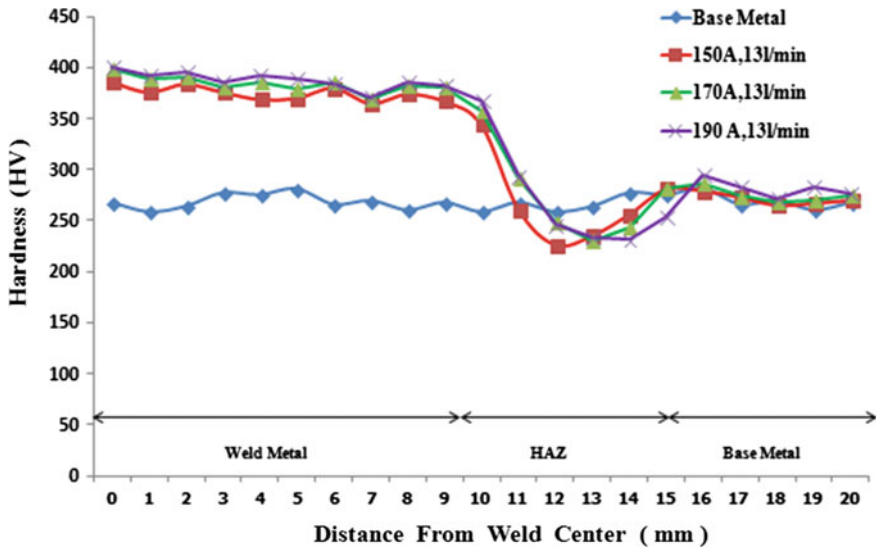
Fig. 4 Vicker microhardness (HV) profiles of base metal and welded specimens at 150, 170 and 190 A arc welding currents

3.2 The Effect of Heat Input on Hardness Properties

The hardness profiles of the welded specimens measured along the welded zone, heat affected zones and base metals are shown in Fig. 4. The average hardness values at the welded zones for the welding currents of 150, 170 and 190 A were 386, 399 and 401 HV, respectively. It was found that the hardness values slightly increased with increasing heat input which resulted from martensite transformation. The higher heat input results in the higher ratio of martensite and ferrite matrix phases as described above. In the welded zone, the hardness values were higher than those in the HAZ and the base metal. It can be ascribed as the difference of microstructures in the welded area and HAZ. In the parent metal, welding variables have no influence on the hardness profile.

3.3 The Effect of Heat Input on Impact Properties

The impact energy was measured at the welded zone of the specimen. The relationship between impact values and welding currents is showed in Fig. 5. The energy absorption at the welding currents of 150, 170 and 190 A was 8.7, 10 and 14 J, respectively. It was shown that the heat input had a large effects on the impact strength. It can be ascribed as the difference of the higher ratio of martensite and ferrite matrix phases in the welded zone.

Fig. 5 Relationship between impact energy and arc welding current
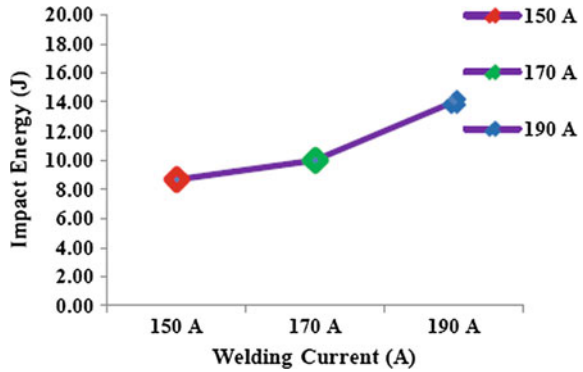
Fig. 6 Tensile load (kN) for tensile strength values (kN/cm^2) of base metal and welded alloys at 150, 170 and 190 A arc currents
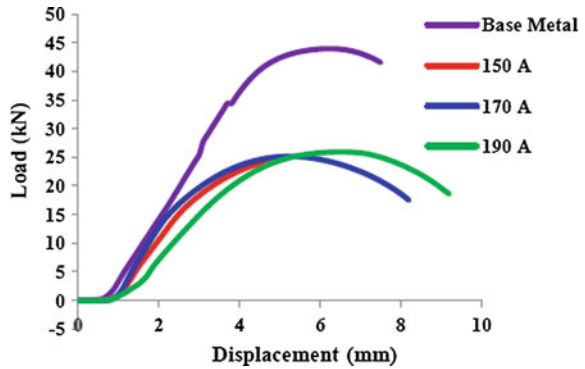
3.4 The Effect on Tensile Strength

Tensile strength values of the base metal and welded specimens with pulse currents of 150, 170 and 190 A were 440, 248.4, 251.5 and 258.0 MPa, respectively which are shown in Fig. 6. The specimens were raptured at the HAZ. The tensile strengths of welded specimens was almost the same and lower than the base metal due to the mixed phases of rounded martensite, carbide and ferrite phases in the heat affected zone.

4 Conclusion

The effect of heat input on mechanical properties and microstructure of SKD 61 hot work tool steel using gas metal arc welding with pulse current was investigated. The following conclusions are summarized in this experimental study:

1. The microstructures in the welded zone are composed mainly of martensite with retained austenite and ferrite matrix phases in the dendritic segregation pattern. In the welded zone, the heat input resulted in an increased transformation of martensite.
2. The average hardness values at the welded zones for the welding currents of 150, 170 and 190 A were 386, 399 and 401 HV, respectively. The hardness values were slightly increased with increasing heat input which resulted from the martensite transformation. In the welded zone, the hardness values were higher than those in the HAZ and base metal.
3. Impact test showed that the energy absorption of the specimens welded at 150, 170 and 190 A are 8.7, 10 and 14 J, respectively. Heat input affects on impact strength.
4. Tensile strength values for all conditions are about 250 MPa. Heat input does not affect on tensile strength.

References

1. Boughton, L.: The use of pulsed current to control metal transfer in welding. Br. Weld. J. **4**, 159–166 (1965)
2. Allum, C.J.: MIG welding-time for a reassessment. Met. Constr., 347–353 (1983)
3. Needham, J.C.: Pulse controlled consumable electrode welding arcs-general principles and operating characteristics. Br. Weld. J. **4**, 191–197 (1965)
4. Rajasekaran, S.: Weld bead characteristics in pulsed GMA welding of Al-Mg alloys. Weld. J. **78**(12), 397–407 (1999)
5. Amin, M.: Pulse current parameters for arc stability and controlled metal transfer in arc welding. Met. Constr., 272–377 (1983)
6. Stanzel, K.: Pulsed GMAW cuts cycle time by 600 percent. Weld. Des. Fabr., 85–87 (2001)
7. Jilong, M., Apps, R.: New MIG process results from metal transfer mode control. Weld. Met. Fabr., 168–175 (1983)
8. Raja, A.: Flux core stelliting by pulsed MAG welding. WRI J. **19**(3), 98–101 (1998)
9. Elliott, S.: Using synergic MIG successfully. Met. Constr., 148–151 (1985)
10. Rajasekaran, S.: Surface topography of pulsed current gas metal arc clads. Surf. Eng. **16**(6), 495–500 (2000)
11. Thompson, S.: Handbook of Mold Tool and Die Repair Welding, 1st edn, p. 224. Abington Publishing Limited (1999)
12. Vedani, M.: Microstructural evolution of tool steels after Nd-YAG laser repair welding. J. Mater. Sci. Milan **39**, 241–249 (2004)
13. Aloraier, A.: FCAW process to avoid the use of post welding heat treatment. J. Press. Vessel Pip., 394–398 (2006)
14. Kanchanasangtong, T., Surapunt, S.: Effect of heat input on microstructure and hardness of SKD 61 hot work tool steel by using gas metal arc welding. Int. Trans. J. Adv. Mater. Res., 557–559 (2012)

Investigation of Bond Strength of Spray Dried Hydroxyapatite-Wollastonite Composite Powder After Plasma Spray

F.E. Bastan, O. Karaarslan, G. Erdogan and F. Ustel

Abstract Hydroxyapatite (HA) is one of the most significant calcium phosphate bio-ceramic which is used commercially in biomedical application due to its similar structure with natural bone, bioactivity, and stability in body fluid. HA has excellent biological properties, while plasma sprayed HA coatings have poor bond strength which makes it difficult to use HA coated implants under mechanical stress. Wollastonite (CS) is a calcium silicate based bioactive ceramic which is used in thermal spraying due to its higher bond strength than HA coatings, however it dissolves quicker than HA in simulated body fluid (SBF). The aim of this work is to produce HA-CS composite powder in order to increase bond strength of the coating. In this study, commercial CS and precipitated HA mixture suspension which involved wt.20% CS was prepared for spray drying (SD) application. HA-CS composite microspheres were granulated by spray drying to supply homogeneity of coating and carry powders to the plasma easily. Afterwards, HA and HA-CS composite microspheres were coated by plasma spraying on carbon steel. Results showed that HA-CS composite coatings have higher adhesion strength, while it decomposes easier to other calcium phosphates than pure HA coating. Additionally, HA-CS coating has higher rate of porosity and un-melted particles.

Keywords Hydroxyapatite · Wollastonite · Composite powder · Plasma spraying

F.E. Bastan (✉) · O. Karaarslan · F. Ustel
Engineering Faculty, Department of Metallurgy and Materials Engineering,
Thermal Spray R&D Lab., Sakarya University, 54187 Esentepe, Sakarya, Turkey
e-mail: febastan@sakarya.edu.tr

O. Karaarslan
e-mail: onrcnkaraarslan@gmail.com

F. Ustel
e-mail: ustel@sakarya.edu.tr

G. Erdogan
Engineering Faculty, Department of Metallurgy and Materials Engineering,
Manisa Celal Bayar University, 45140 Muradiye, Manisa, Turkey
e-mail: g.erdogan@cbu.edu.tr

1   Introduction

In recent years, HA coated metallic implants have been used as bone replacement plates, hip endoprostheses and dental root implants [1] owing to the rapid osseointegration and earlier bone formation [2]. The advantages of plasma spraying such as ease of operation, high deposition rate, controlling phase, structure and porosity make it essential to coat HA on metallic substrates [3]. Besides these positive properties, plasma sprayed HA has problems like existence of amorphous and other calcium phosphate components which effect the stability of implants [4]. Moreover, the adhesion of the HA to the implant surface is poor [1, 5] and plasma sprayed HA coatings have a non-uniform structure [5].

Some solutions were suggested to overcome the adhesion problem and improving the stability of the coating. Cheang and Khor recommended to use appropriate powder size distribution and further heat treatment after coating to optimize the adhesion strength and phase structure [3, 6]. Another suggestion was to carry out hot isostatic pressing on plasma sprayed coatings [7, 8]. The adhesion strength was improved up to 31 MPa of HA coatings with less decomposition by using high velocity oxy-fuel spraying [9, 10]. Different from the above approaches, Fu et al. investigated HA/YSZ composite coatings and achieved over 40 MPa adhesive strength [11]. Li et al. studied graded YSZ/HA coatings and found higher adhesive strength than pure HA coatings [12]. Zhao et al. analyzed plasma spraying of HA/Ti composite powder and determined the adhesive strength up to 30 MPa [13].

Wollastonite ($CaSiO_3$, CS) is one of the attractive ceramic materials by the reason of its bioactivity and biocompatibility [14, 15]. Additionally, it has good strength, low shrinkage and lack of volatile compounds [16]. It has the ability to form an apatite layer on the surface [17, 18] when it is soaked in simulated body fluid (SBF) [14, 15]. As a result of the aforementioned reasons, CS was used as a powder feedstock for plasma spraying [19–22]. Plasma sprayed CS coatings have a higher adhesive strength of about 40 MPa [23–25] which is higher than plasma sprayed HA coatings. Due to the higher solution of CS in water, the HA-CS composites were considered to allow organizing of bioactivity and degradation [26]. Furthermore, the HA-CS composite was suggested to solve the brittleness issue of HA [27].

This study focuses on the investigation of HA-CS composite powder as a feedstock of plasma spraying and comparing the HA-CS coating with a pure HA coating in regards to physical and mechanical properties. Chemical precipitated HA and commercial CS powders were blended together and spray dried. Spray dried pure HA (SD-HA) and spray dried composite HA-CS were plasma sprayed on carbon steel substrates which were used in adhesion tests. The physical and mechanical properties of coatings were identified and evaluated.

2 Experimental Procedure

SD-HA was produced with chemical precipitation, filtrated and spray dried. The HA-CS composite powder was produced with the same route. As distinct from SD-HA, wt%20 commercial CS (Alfa Aesar) was added on HA precipitate before spray drying. Subsequent to spray drying, powders were heat treated in a furnace at 1000 °C to enhance density and crystallinity. Produced powders SEM micrographs, XRD patterns and size distributions are given in Figs. 1 and 2. Afterwards SD-HA and HA-CS powders were coated on carbon steel with plasma spray. Prior to plasma spraying, substrates were cleaned and sand blasted with Al_2O_3 particles to increase the surface roughness. Argon was used as a primary, hydrogen was used as a secondary plasma gas. Plasma spraying parameters are demonstrated in Table 1. Both SD-HA and HA-CS powders were sprayed with the same parameters.
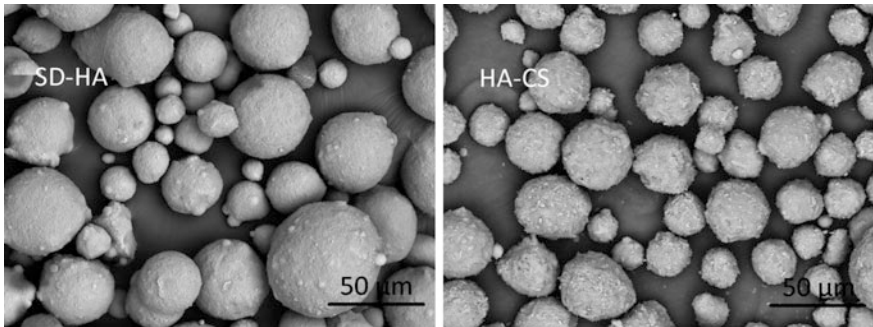
Fig. 1 Morphology of spray dried and heat treated powders (*left* SD-HA, *right* HA-CS)
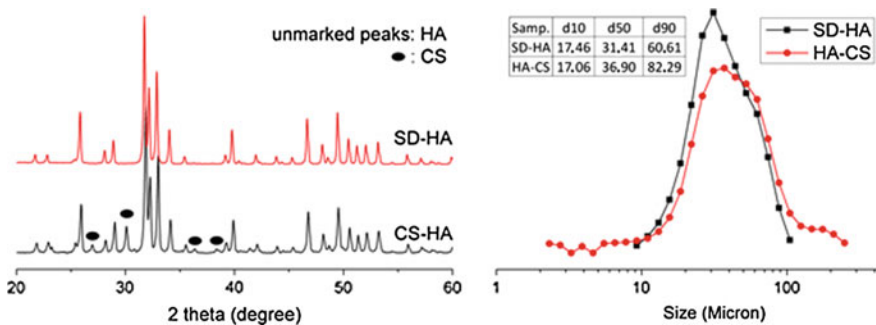
Fig. 2 XRD patterns and size distribution of spray dried and heat treated powders

Table 1 Plasma spraying parameters

Parameters	Current (A)	Ar (NLPM)	H$_2$ (NLPM)	Powd. feed (g/min)	Spr. dist. (mm)
	500	50	3	10	120

Figure 1 illustrates the morphology of spray dried and heat treated powders. It can be seen from the figure that both SD-HA and HA-CS powders have a close spherical morphology. CS particles are either on the surface or inside the spray dried HA-CS powders. However both powders were spray dried with the same parameters, SD-HA powders have higher density than HA-CS powders. XRD patterns and size distributions of spray dried and heat treated powders are demonstrated in Fig. 2. Evidently SD-HA and HA-CS powders have a similar mean size and size distribution. Although the XRD patterns of SD-HA represents the pure HA structure, HA-CS represents both pure HA and CS structure. Tensile adhesion tests were carried out to evaluate the adhesion strength of coatings according to ASTM C633-13 [28]. A stereo microscope (ZEISS) was used to investigate the surface morphology of the failure surface after the adhesion test. Laser particle size analyze (MICROTRACK) was carried out to spray dried and heat treated powders. The tensile strength test (ZWICK) was applied to determine the adhesion strength of plasma sprayed coatings. SEM (TESCAN) was used to examine the morphology of powders, surface and cross section of the coatings. The phase structure of both powders and coatings was determined with XRD (RIGAKU) analyze through a range of 20°–60° (two theta).

3   Results and Discussions

Cross section micrographs of coatings are given in Fig. 3. Both of the coatings have approximately the same thickness. The pure HA coating has less porosity than the HA-CS coating due to the difference of powder density. It is obvious that the HA-CS coating has spread splats but some of them have the same structure with spray dried and heat treated powders. It could be an indication of not to turn into the molten/semi-molten form. Melting of feedstock is a requirement to reduce porosity and to maintain the coating integrity [29]. It is suggested that the HA-CS coating structure (porosity, splat formation, phase etc.) can be improved with optimizing plasma spraying parameters. It is demonstrated in Fig. 2 that HA-CS powders have slight bigger size than SD-HA which may be the reason of porous and not to turn
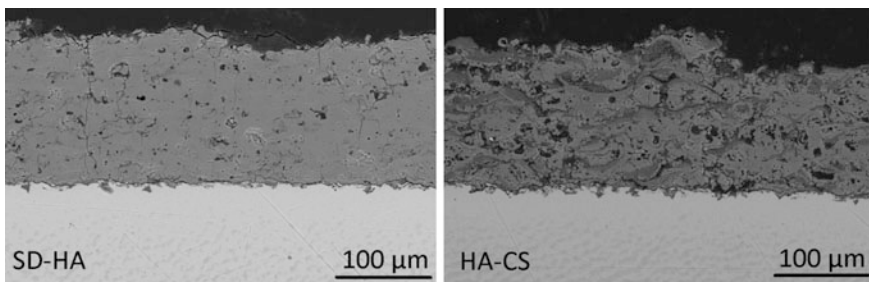
Fig. 3 Cross section micrographs of coatings

into molten/semi-molten form. This situation can be seen negatively for the integrity and porosity but exact molten particles have less crystallinity and further decomposition [6, 30].

Figure 4 shows the XRD patterns of both SD-HA and CS-HA coatings. By the nature of high temperature, plasma sprayed HA coatings have decomposed to other calcium phosphate components and amorphous phase [31, 32]. It can be seen from the figure that the pure HA coating (SD-HA) has dominantly hydroxyapatite phase. Furthermore, it has a small amount of tricalcium phosphate (TCP), tetracalcium phosphate (TTCP) and amorphous phases.

Identical to the SD-HA coating, the HA-CS coating has dominantly hydroxyapatite phase. Besides it has a higher amount of TCP, CS peaks can be seen in Fig. 4. This result indicates further decomposition of HA to other calcium phosphate components. There is a horizontal arrow in the figure to show a new peak which came into view after plasma spraying of the HA-CS composite powder. This may be due to transforming of HA-CS composite powder to a new phase because of high temperature of plasma spraying. Ryu et al. investigated HA-CS composite to produce a new type of bioactive material and found that a new phase ($Ca_{12}P_6Si_2O_{31}$), which was marked similar two theta range (between 30° and 35°) in XRD patterns, came into existence after heat treatment at 1350 °C [26].

Tensile adhesion test results are given in Table 2. The results indicate that the HA-CS coating has a higher adhesion strength than SD-HA as expected. Depending upon powder size and morphology, plasma spraying parameters, adhesive bond strength of plasma sprayed HA reaches up to 30 MPa [10, 33–37]. It can increase up to 37 MPa with decreasing of coating thickness to 50 μm [38], up to 35 MPa with HVOF spraying [10, 39] or increase up to 40 MPa with using composite powders [12, 40]. The adhesive strength of plasma sprayed CS coatings is up to

Fig. 4 XRD patterns of SD-HA and HA-CS coatings
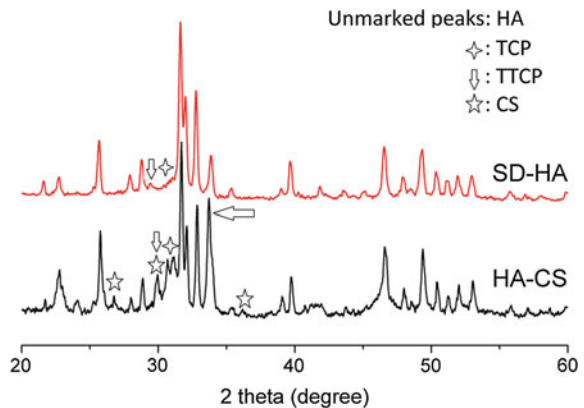
Table 2 Tensile adhesion strength of coatings

Samples	Epoxy glue	SD-HA	HA-CS
Mean Adh. Stren. (MPa)	54	31.33	38
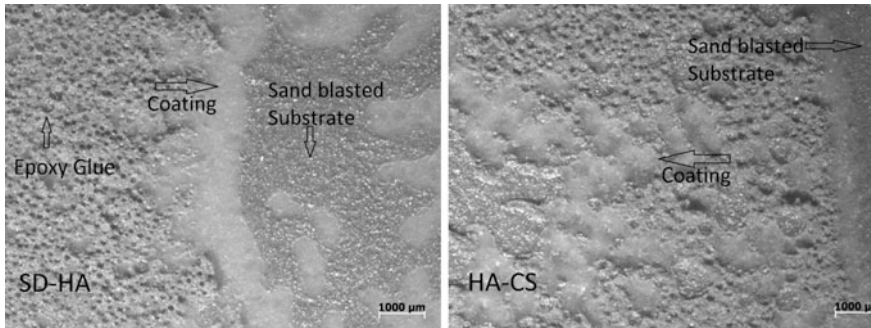
Fig. 5 Stereo micrographs of failure surfaces of coatings

43 MPa [23, 24, 41]. The achieved higher adhesive strength (38 MPa) is between the plasma sprayed HA and CS coatings strengths.

Failure surface micrographs of SD-HA and HA-CS coatings are given in Fig. 5. Both failure surfaces demonstrate a similar structure. The failure between coating and substrate is termed adhesive and the failure within the coating is termed cohesive failure [36]. A mixture of adhesive and cohesive failure can be seen in Fig. 5.

4 Conclusion

SD-HA and HA-CS powders were successfully deposited with plasma spraying. Although the HA-CS coating has further porosity and un-melted powders, it has a higher adhesive strength than SD-HA coatings. XRD results revealed that the HA-CS coating has a higher decomposition rate and it has a different structure which may be due to forming of a new phase. This composite coating might be a candidate for biomedical applications but further investigation is needed to determine the in vitro solubility, phase structure, biocompatibility of the new phase, and long term stability.

References

1. Heimann, R.B.: Thermal spraying of biomaterials. Surf. Coat. Technol. **201**, 2012–2019 (2006)
2. Cao, H., Liu, X.: Plasma-sprayed ceramic coatings for osseointegration. Int. J. Appl. Ceram. Technol. **10**, 1–10 (2013)
3. Cheang, P., Khor, K.A.: Thermal spraying of hydroxyapatite (HA) coatings: effects of powder feedstock. J. Mater. Process. Technol. **48**, 429–436 (1995)
4. Cheang, P., Khor, K.A.: Addressing processing problems associated with plasma spraying of hydroxyapatite coatings. Biomaterials **17**, 537–544 (1996)

5. Cizek, J., Khor, K.A., Prochazka, Z.: Influence of spraying conditions on thermal and velocity properties of plasma sprayed hydroxyapatite. Mater. Sci. Eng., C **27**, 340–344 (2007)
6. Khor, K.A., Wang, Y., Cheang, P.: Plasma spraying of combustion flame spheroidized hydroxyapatite (HA) powders. J. Therm. Spray Technol. **7**, 254–260 (1998)
7. Khor, K.A., Cheang, P.: Plasma sprayed hydroxyapatite (HA) coatings produced with flame spheroidised powders. J. Mater. Process. Technol. **63**, 271–276 (1997)
8. Khor, K.A., Cheang, P., Wang, Y.: The thermal spray processing of HA powders and coatings. JOM **49**, 51–57 (1997)
9. Li, H., Khor, K.A., Cheang, P.: Effect of the powders' melting state on the properties of HVOF sprayed hydroxyapatite coatings. Mater. Sci. Eng., A **293**, 71–80 (2000)
10. Li, H., Khor, K.A.: Characteristics of the nanostructures in thermal sprayed hydroxyapatite coatings and their influence on coating properties. Surf. Coat. Technol. **201**, 2147–2154 (2006)
11. Fu, L., Khor, K.A., Lim, J.P.: The evaluation of powder processing on microstructure and mechanical properties of hydroxyapatite (HA)/yttria stabilized zirconia (YSZ) composite coatings. Surf. Coat. Technol. **140**, 263–268 (2001)
12. Li, H., Li, Z.X., Li, H., Wu, Y., Wei, Q.: Characterization of plasma sprayed hydroxyapatite/ZrO_2 graded coating. Mater. Des. **30**, 3920–3924 (2009)
13. Zhao, G., Xia, L., Zhong, B., Wen, G., Song, L., Wang, X.: Effect of milling conditions on the properties of HA/Ti feedstock powders and plasma-sprayed coatings. Surf. Coat. Technol. **251**, 38–47 (2014)
14. Liu, X., Ding, C.: Morphology of apatite formed on surface of wollastonite coating soaked in simulate body fluid. Mater. Lett. **57**, 652–655 (2002)
15. Liu, X., Ding, C., Chu, P.K.: Mechanism of apatite formation on wollastonite coatings in simulated body fluids. Biomaterials **25**, 1755–1761 (2004)
16. Liu, X., Morra, M., Carpi, A., Li, B.: Bioactive calcium silicate ceramics and coatings. Biomed. Pharmacother. **62**, 526–529 (2008)
17. Abd Rashid, R., Shamsudin, R., Abdul Hamid, M.A., Jalar, A.: In-vitro bioactivity of wollastonite materials derived from limestone and silica sand. Ceram. Int. **40**, 6847–6853 (2014)
18. Ballarre, J., Seltzer, R., Mendoza, E., Orellano, J.C., Mai, Y.W., García, C., Ceré, S.M.: Morphologic and nanomechanical characterization of bone tissue growth around bioactive sol–gel coatings containing wollastonite particles applied on stainless steel implants. Mater. Sci. Eng., C **31**, 545–552 (2011)
19. Liu, X., Ding, C., Wang, Z.: Apatite formed on the surface of plasma-sprayed wollastonite coating immersed in simulated body fluid. Biomaterials **22**, 2007–2012 (2001)
20. Liu, X., Ding, C.: Phase compositions and microstructure of plasma sprayed wollastonite coating. Surf. Coat. Technol. **141**, 269–274 (2001)
21. Xue, W., Liu, X., Zheng, X., Ding, C.: In vivo evaluation of plasma-sprayed wollastonite coating. Biomaterials **26**, 3455–3460 (2005)
22. Wang, W., Liang, J., Guo, X., Xuan, F., Hong, H.: Mechanical properties and dissolution behavior of plasma sprayed wollastonite coatings deposited at different substrate temperatures. J. Therm. Spray Technol. **21**, 496–504 (2012)
23. Liu, X., Ding, C.: Characterization of plasma sprayed wollastonite powder and coatings. Surf. Coat. Technol. **153**, 173–177 (2002)
24. Liu, X., Ding, C.: Thermal properties and microstructure of a plasma sprayed wollastonite coating. J. Therm. Spray Technol. **11**, 375–379 (2002)
25. Zheng, X.B., Liu, X.Y., Xue, W.C., Ding, C.X.: Study on plasma sprayed calcium silicate coatings. Mater. Sci. Forum **475–479**, 2371–2374 (2005)
26. Ryu, H.S., Lee, J.K., Kim, H., Hong, K.S.: New type of bioactive materials: hydroxyapatite/α-wollastonite composites. J. Mater. Res. **20**, 1154–1163 (2005)
27. Encinas-Romero, M.A., Aguayo-Salinas, S., Castillo, S.J., Castillón-Barraza, F.F., Castaño, V.M.: Synthesis and characterization of hydroxyapatite-wollastonite composite powders by sol-gel processing. Int. J. Appl. Ceram. Technol. **5**, 401–411 (2008)

28. ASTM Standard C633 (2008) Standard test method for adhesion or cohesion strength of thermal spray coatings. ASTM International, West Conshohocken. doi:10.1520/C0633-13, www.astm.org. Accessed 15 May 2015

29. Tong, W., Chen, J., Li, X., Cao, Y., Yang, Z., Feng, J., Zhang, X.: Effect of particle size on molten states of starting powder and degradation of the relevant plasma-sprayed hydroxyapatite coatings. Biomaterials **17**, 1507–1513 (1996)

30. Pálka, V., Poštrková, E., Koerten, H.K.: Some characteristics of hydroxylapatite powder particles after plasma spraying. Biomaterials **19**, 1763–1772 (1998)

31. Gross, K.A., Berndt, C.C.: Thermal processing of hydroxyapatite for coating production. J. Biomed. Mater. Res. **39**, 580–587 (1998)

32. Morks, M.F., Kobayashi, A.: Effect of gun current on the microstructure and crystallinity of plasma sprayed hydroxyapatite coatings. Appl. Surf. Sci. **253**, 7136–7142 (2007)

33. Tsui, Y.C., Doyle, C., Clyne, T.W.: Plasma sprayed hydroxyapatite coatings on titanium substrates Part 1: mechanical properties and residual stress levels. Biomaterials **19**, 2015–2029 (1998)

34. Zheng, X., Huang, M., Ding, C.: Bond strength of plasma-sprayed hydroxyapatite/Ti composite coatings. Biomaterials **21**, 841–849 (2000)

35. Kweh, S.W., Khor, K.A., Cheang, P.: Plasma-sprayed hydroxyapatite (HA) coatings with flame-spheroidized feedstock: microstructure and mechanical properties. Biomaterials **21**, 1223–1234 (2000)

36. Yang, Y.C., Chang, E.: Influence of residual stress on bonding strength and fracture of plasma-sprayed hydroxyapatite coatings on Ti–6Al–4V substrate. Biomaterials **22**, 1827–1836 (2001)

37. Kweh, S.W.K., Khor, K.A., Cheang, P.: An in vitro investigation of plasma sprayed hydroxyapatite (HA) coatings produced with flame-spheroidized feedstock. Biomaterials **23**, 775–785 (2002)

38. Renghini, C., Girardin, E., Fomin, A.S., Manescu, A., Sabbioni, A., Barinov, S.M., Komlev, V.S., Albertini, G., Fiori, F.: Plasma sprayed hydroxyapatite coatings from nanostructured granules. Mater. Sci. Eng., B **152**, 86–90 (2008)

39. Li, H., Khor, K.A., Cheang, P.: Properties of heat-treated calcium phosphate coatings deposited by high-velocity oxy-fuel (HVOF) spray. Biomaterials **23**, 2105–2112 (2002)

40. Li, H., Khor, K.A., Cheang, P.: Titanium dioxide reinforced hydroxyapatite coatings deposited by high velocity oxy-fuel (HVOF) spray. Biomaterials **23**, 85–91 (2002)

41. Liu, X., Ding, C.: Plasma sprayed wollastonite/TiO_2 composite coatings on titanium alloys. Biomaterials **23**, 4065–4077 (2002)

The Hardness Variation Due to Secondary Heating in Friction Stir Welding of Small Diameter Aluminium Alloy 6063 Pipe

Azman Ismail, Mokhtar Awang, Shaiful Hisham Samsudin, Mohd Afendi Rojan and Muhammad Azrie Husainy Mohd Jasri

Abstract Friction stir welding (FSW) is a solid state joining process which utilizes the frictional heat of a high speed rotating tool to soften the adjoining sections and stirred/joined them together as one part without filler. In the FSW of pipe joining, a tool rotating at high speeds will start and stop at the same point in order to complete full weld cycle. The FSW of a small diameter pipe can cause secondary heating to occur at the start and stop point. Several pipe samples of 89 mm outside the diameter were prepared based on several specified welding parameters at a stationary position and completed the weld cycle. The Bridgeport 2216 CNC Milling Machine and a customised orbital clamping unit (OCU) were fully utilized for the sample's preparation. This present study analysed the variation in hardness due to secondary heating for a small pipe diameter. The hardness varies between 18.7 HRB minimum to 33.6 HRB maximum, yielding to lower value due to this condition.

A. Ismail (✉)
Malaysian Institute of Marine Engineering Technology, Universiti Kuala Lumpur,
Jalan Pantai Remis, 32200 Lumut, Perak, Malaysia
e-mail: azman@unikl.edu.my

M. Awang · S.H. Samsudin
Department of Mechanical Engineering, Universiti Teknologi PETRONAS,
Bandar Seri Iskandar, 31750 Tronoh, Perak, Malaysia
e-mail: mokhtar_awang@petronas.com.my

S.H. Samsudin
e-mail: shaiful_samsudin@petronas.com.my

M.A. Rojan · M.A.H.M. Jasri
School of Mechatronic Engineering, Universiti Malaysia Perlis,
02600 Pauh Putra, Perlis, Malaysia
e-mail: afendirojan@unimap.edu.my

M.A.H.M. Jasri
e-mail: azriehusainy@gmail.com

1 Introduction

Friction stir welding (FSW) is a solid state joining process which requires low heat input in order to join two metal sections together. This low heat input condition produced by FSW improved the mechanical properties of welded materials. For the FSW of pipe, a special Orbital Clamping Unit (OCU) is vitally required as the holding mechanism for the pipe during the joining process, as shown in Fig. 1.

There is not much research on pipe joining using the FSW process [1–5]. Based on previous studies [1, 2], secondary heating normally occurs during the joining of a pipe with a small diameter as shown in Fig. 2. The high rotating tool starts and stops at the same point in order to complete full weld cycle. The pipe arrangement of the previous study can be seen in Fig. 3.

The friction and plastic deformation that occurs during FSW causes heat generation which is enough to soften the aluminium [6–9]. Aluminium yields no visible change due to temperature variation but it still affects the metallurgical and mechanical properties. These properties can be assessed by hardness and tensile testing [10–15]. This present study analyses the hardness variation due to secondary heating in the friction stir welded aluminium pipe joint.

2 Experimental Setup

AA6063 pipes with an outside diameter of 89 mm and with a 5 mm wall thickness, was used in this experiment. The tool was offset about 6 mm forward from the center-line, with a dwelling time of about 30 s. These pipes were fixed onto the

Fig. 1 Orbital clamping unit for friction stir welding of aluminium pipe
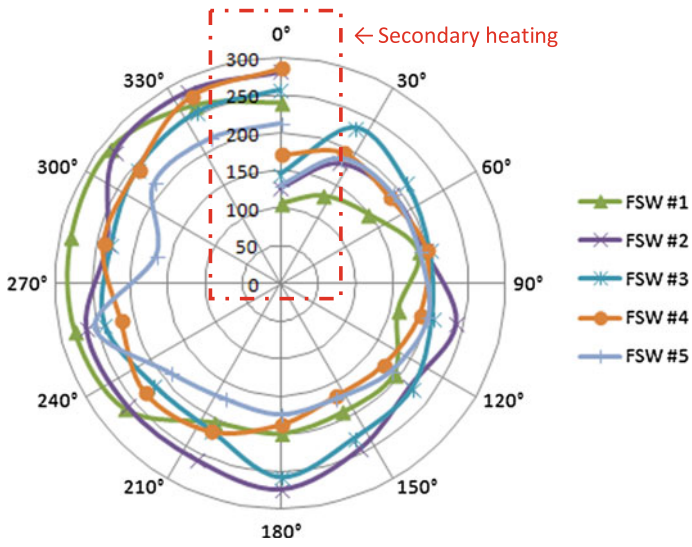
Fig. 2 Occurrence of secondary heating in small diameter pipe joining
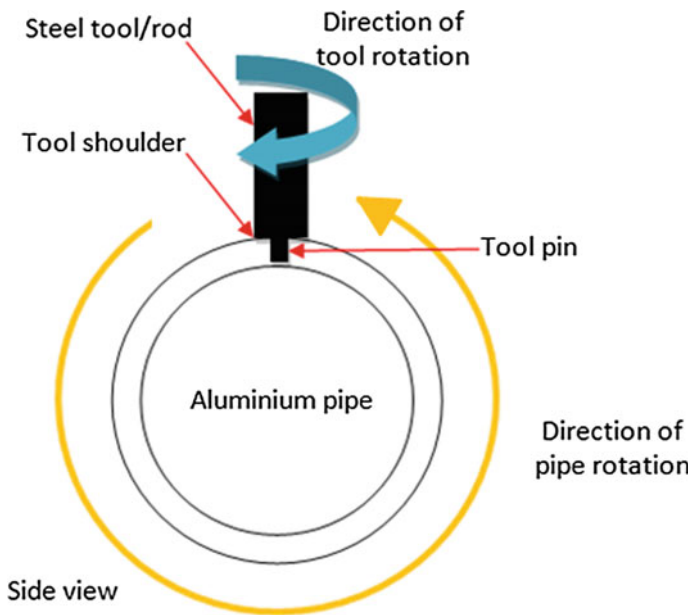
Fig. 3 Pipe positioning during the experiment setup

Table 1 Welding parameters without travel speed

FSW sample	Welding parameters	
	Rotation speed (rpm)	Travel speed (mm/s)
FSW#1	900	0
FSW#2	1200	0
FSW#3	1500	0
FSW#4	900	1.2
FSW#5	1200	1.2
FSW#6	1500	1.2
FSW#7	1500	1.8
FSW#8	1500	2.4

Table 2 Hardness testing parameters

Testing equipment	Rockwell scale	Indentor type	Load	Temperature	Type of ball
AFFRI 206 RTD	HRB	1/16″ ball	100 kg	23 °C	Steel

OCU which was already mounted to the Bridgeport 2216 CNC milling machine. The as-recorded hardness for AA6063 was 42 HRB.

The first sample, i.e. FSW#1-#3 with no secondary heating effect was made based on the welding parameters reported in Table 1. Each sample was prepared with several rotational speed settings with zero travel speed. Then, the second sample, i.e. FSW#4-#8 with secondary heating effect was prepared based on the welding parameters reported in Table 1, for a complete weld cycle. The exit hole was cross cut for sampling and these samples were hardness tested based on ASTM E18 [16], the standard testing method for Rockwell hardness and Rockwell superficial hardness of metallic materials, for hardness comparison. The hardness testing parameters are shown in Table 2.

3 Results and Discussion

Based on the results of the previous study conducted by Ismail et al. [2], the secondary heating occurred in a small diameter pipe joining by FSW process. In this FSW process, the tool starts and stops at the same point in order to complete the full weld cycle of a pipe. Figure 4 shows the exit pin hole.

The material at the starting point was still had a high temperature when the tool returned back to the same point thus introducing secondary heating at this point. This secondary heating promotes the softening (of hardness) of welded joints at this point [17]. Based on the findings at the rotational speed of 900 rpm, the high
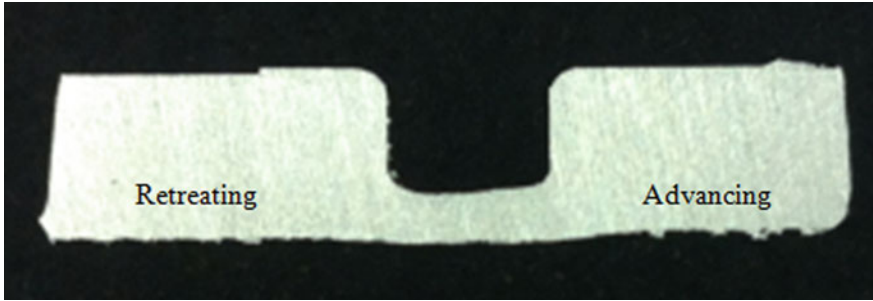
Fig. 4 The cross section of exit pin hole of FSW on pipe
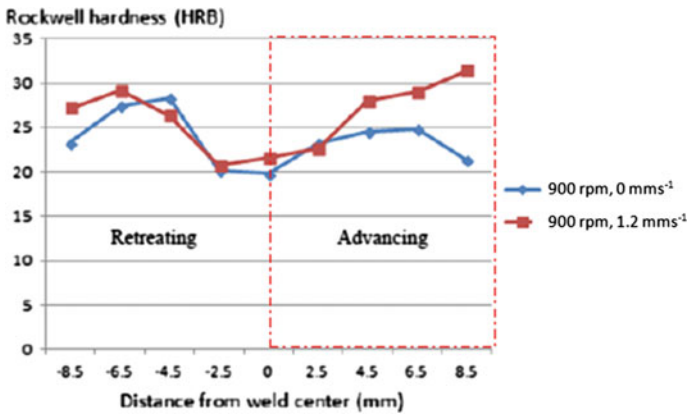
Fig. 5 Hardness due to different rotational speed of 900 rpm

hardness value was caused by an intensive stirring process. The same happened to the sample at a rotational speed of 1200 rpm. But due to excessive plasticised flow of materials at 1500 rpm, the hardness yielded a lower reading [18]. These conditions can be seen on Figs. 5, 6 and 7 respectively. The increment of rotational speed caused an increment in the stirring process causing a higher degree of plastic deformation, which affected the hardness for the lower reading [17].

With the reduction of time spent (increment of travel speed) for the high rotating tool to return to its original position, additional secondary heat input further reduced the hardness at the exit hole as can be seen on Fig. 8. Aluminium alloys underwent structural changes during FSW at an elevated temperature [19, 20].
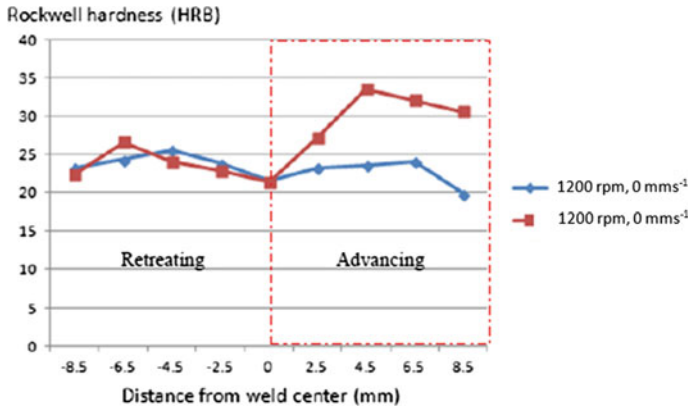
Fig. 6 Hardness due to different rotational speed of 1200 rpm
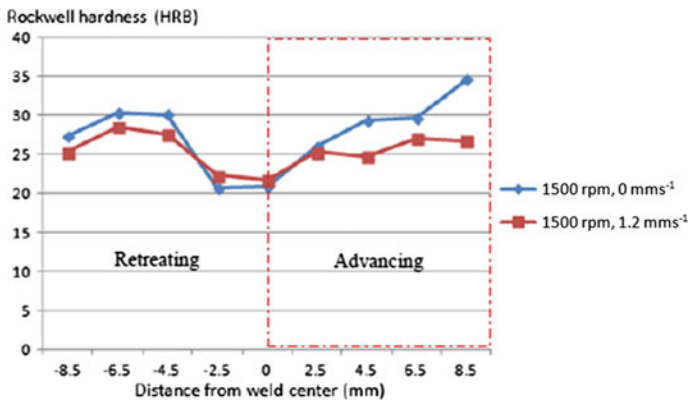
Fig. 7 Hardness due to different rotational speed of 1500 rpm
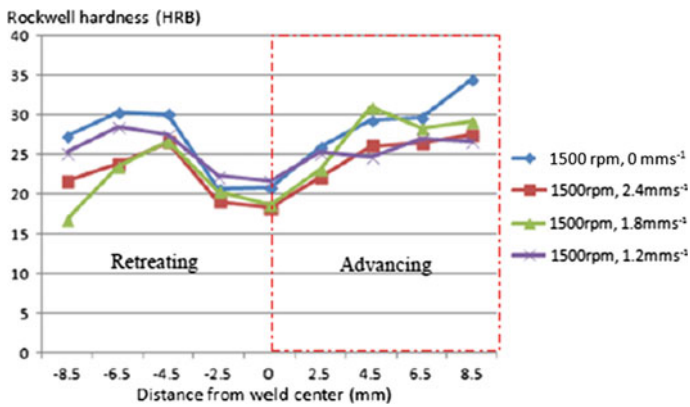
Fig. 8 Hardness due to different travel speed and fixed rotational speed of 1500 rpm

4 Conclusion

In this study, the secondary heating and hardness distributions across the friction stir welded joints were determined experimentally. Based on the results, the conclusions can be summarized as follows;

a. This secondary heating promotes softening (of hardness) of welded joints at the exit hole.
b. With the increment of rotational speed and travel speed, the secondary heating caused the reduction of hardness across the friction stir welded pipe.
c. The hardness varies between 18.7 HRB minimum to 33.6 HRB maximum.

References

1. Lammlein, D.H., Gibson B.T., DeLapp D.R. et al.: Friction stir welding of small diameter pipe: An experimental and numerical proof of concept for automation and manufacturing. Proc. Inst. Mech. Eng. Part B 1–16
2. Ismail, A., Awang, M., Samsudin, S.H.: The influence of process parameter on the temperature profile of friction stir welded aluminium alloy 6063-T6 pipe butt joint. In: Mechanical and Materials Engineering of Modern Structure and Component Design, Advanced Structured Materials, vol. 70, Springer International Publishing, Switzerland, pp. 243–249
3. Ismail, A., Awang, M.: Surface hardness of friction stir welded AA6063 pipe. MATEC Web Conf. **13**(04025), 1–5 (2014)
4. Gercekcioglu, E., Eren, T., Yildizh, K. et al.: The friction behavior on the external surface of the friction stir welding of AA6063-T6 tubes. In: The 5th International Conference on Tribology, pp. 225–228 (2005)
5. Doos, Q.M., Wahab, B.A.: Experimental study of friction stir welding of 6061-T6 aluminium pipe. IJMERR. **1**(3), 143–156 (2012)
6. Fehrenbacher, A., Duffie, N.A., Ferrier, N.J., Pfefferkorn, F.E., Zinn, M.R.: Effects of tool-workpiece interface temperature on weld quality and quality improvements through temperature control in friction stir welding. Int. J. Adv. Manuf. Technol. **71**(1), 165–179 (2014)
7. Hwang, Y.-M., Kang, Z.-W., Chiou, Y.-C., Hsu, H.-H.: Experimental study on temperature distributions within the workpiece during friction stir welding of aluminum alloys. Int. J. Mach. Tool. Manuf. **48**(7–8), 778–787 (2008)
8. Mishra, R.S., Ma Z.Y. Friction stir welding and processing. J. Mater. Sci. Eng. R, 50(1–2):1–78 (2005)
9. Threadgill, P.L., Leonard, A.J., Shercliff, H.R., Withers, P.J.: Friction stir welding of aluminium alloys. Int. Mater. Rev. **54**(2), 49–93 (2009)
10. Zhang, Z., Zhang, H.W.: Numerical studies on controlling of process parameters in friction stir welding. J. Mater. Process. Technol. **209**, 241–270 (2009)
11. Zhang, Z., Chen, J.T., Zhang, Z.W., Zhang, H.W.: Coupled thermo-mechanical model based comparison of friction stir welding processes of AA2024-T3 in different thicknesses. J. Mater. Sci. **46**, 5815–5821 (2011)

12. Peel, M., Steuwer, A., Preuss, M., Withers, P.J.: Microstructure, mechanical properties and residual stresses as a function of welding speed in aluminum AA5083 friction stir welds. Acta Mater. **51**, 4791–4801 (2003)
13. Gratecap, F., Racineux, G., Marya, S.: A simple methodology to define conical tool geometry and welding parameters in friction stir welding. Int J Mater Form **1**(3), 143–158 (2008)
14. Simar, A., Brechet, Y., de Meester, B., Denquin, A., Pardoen, T.: Microstructure, local and global mechanical properties of friction stir welds in aluminium alloy 6005A-T6. Mater. Sci. Eng., A **486**(1–2), 85–95 (2008)
15. Zeng, W.M., Wu, H.L., Zhang, J.: Effect of tool wear on microstructure, mechanical properties and acoustic emission of friction stir welded 6061 aluminum alloy. Acta Metall. Sin. **19**(1), 9–19 (2006)
16. ASTM E18, a standard testing method for Rockwell hardness and Rockwell superficial hardness of metallic materials, ASTM International
17. Liu, H, Zhang, H, Pan, Q., Yu, L.: Effect of friction stir welding parameters on microstructural characteristic and mechanical properties of 2216-T6 aluminium alloy joints. Int. J. Mater. Form. (2011). doi:10.1007/s12289-011-1048-5
18. Varun Kumar, A., Balachandar, K.: Effect of welding parameters on metallurgical properties of friction stir welded aluminium alloy 6063-0. J. Appl. Sci. **12**(12), 1255–1264 (2012)
19. www.azom.com, Aluminium and Aluminium Alloy-Heat Treatment of Alumnium and Aluminium Alloys. Accessed on 10 Apr 2015
20. Sakthivel, T., Sengar, G.S., Mukhopadhyay, J.: Effect of welding speed on microstructure and mechanical properties of friction stir welded aluminium. Int. J. Adv. Manuf. Technol. **43**, 468–473 (2009)

The Material Hardness and Tensile Strength of AA5083 Aluminum Alloy Friction Stir Welding Lap Joint with Conventional Milling Machine

M.A.H.M. Jasri, M. Afendi Rojan and M. Azman

Abstract Aluminum alloys are used in many applications in which the advantages of high strength and low weight have a significant impact, industries such as; ship building, aviation, and transportation industry [1]. Friction stir welding (FSW) is a new non-flammable welding technique particularly well suited to aluminum alloys, though this technique is also used for other materials. Friction stir welding promises joints with low defects, fine microstructures, minimum phase transformation and low oxidation compared to conventional welding techniques [2]. Experiments for tensile and deflection tests were carried out and reported in this research paper. The base material used for friction stir welding was the similar AA 50833 Aluminum alloy. The material hardness has been tested to confirm the theory that the hardness increased with increase as the rotational speed of the tool increases, but decreases after attaining marginal speed. Deflections of friction stir welded specimens and base materials were compared and they exhibited almost similar trends at different spots in the welding nugget, heat affect zone and thermal material affected zone of all the specimens [3–5].

Keywords Tensile · Lap joint · Friction stir welding · Aluminum alloy 5083 · Hardness

M.A.H.M. Jasri (✉) · M. Afendi Rojan
School of Mechatronics, Universiti Malaysia Perlis (UniMAP),
Pauh Putra, Arau, Perlis, Malaysia
e-mail: azrie@unikl.edu.my

M. Afendi Rojan
e-mail: afendirojan@gmail.com

M.A.H.M. Jasri · M. Azman
Marine Construction and Maintenance Technology Department,
Universiti Kuala Lumpur (UniKL MIMET), Jalan Pantai Remis,
Lumut, Perak, Malaysia
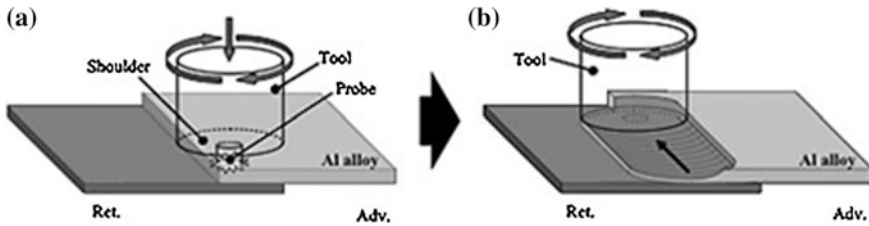
Fig. 1 The schematic diagram of FSW lap joint

1 Introduction

In 1991, an organization of experts in welding training known as the Training Welding Institute (TWI) introduce a new type of joining method which is solid state joining or more known as the Friction Stir Welding (FSW) method. The FSW method uses a rotation body movement as a tool to join two separate materials without letting the metal itself melt by the heat. The input heat is created by friction forces between the tool and materials which leads to the joining area becoming a plastic region and the two materials are blended into one material by the FSW tool, as seen in Fig. 1. It is because of the two softened material due to the raised temperature can be joined using tools by applied the mechanical pressure from milling machine. It is primarily used on aluminums that require increased weld strength without a post-weld heat treatment. Currently, there is lots of research that has been conducted on FSW to find the optimum parameters for best joining between two pieces materials. The joining type is commonly used in all joining types of welding is the butt joint. The studies consisted of making a lap joint on the two aluminum plates AA5083 with using the treaded probe by using the conventional milling machine. The specimens are welded checked to ensure the heat affected the hardness after completed welded of FSW lap joint. The FSW parameters' are selected by using heat input calculator to estimate the best heat input toward the parameters' limitation of the conventional milling machine. The jointed plate are inspected by visual welding inspection using EN ISO 5817 Standards.

2 Methodology

2.1 Base Materials

The base material used for FSW in this particular study is an aluminum alloy as the joining material. Marine grade aluminum AA5083 was selected because of its properties are valuable for the shipbuilding industry which are lightweight, a durable material, have corrosion resistance, and moderate high strength. Other than
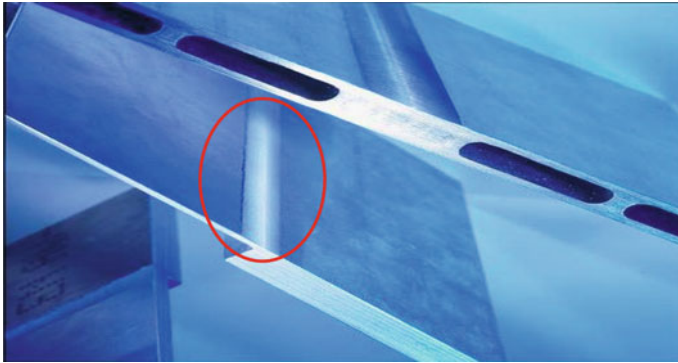
Fig. 2 Sample of joining major component structure in shipbuilding

Table 1 Chemical properties

Element	Si	Fe	Cu	Mn	Mg	Zn	Ti	Cr	Al
% Present	0.4	0.4	0.1	0.4–1.0	4.0–4.9	0.25	0.15	0.05–0.25	Balance

Table 2 Thermal properties

	SI unit
Specific heat capacity	0.9 J/g-°C
Thermal conductivity	117 W/m-K
Melting point	591–638 °C
Solidus	591 °C
Liquids	638 °C

that, as shown in Fig. 2, Aluminium Alloys 5083 commonly use in joining the plate in lots of heavy industry such as rail cars, vehicle bodies, and pressure vessels.

Tables 1 and 2 show the chemical and thermal properties which must be considered as each element may affect the material properties when joining during FSW.

The American Bureau Shipping (ABS) rules and regulations for FSW application method state that a minimum dimension of 4 mm × 150 mm × 500 mm is required for each FSW specimen. As shown in Fig. 3, the material is prepared following the minimum dimensions because of the limitation of jig installation on the milling machine.

Notes:

1 : Joint preparation and fit-up, as specified in WPS

L1 : Minimum 150 mm (6 in.)

L2 : Minimum 500 mm (20 in.)

t : Production material thickness
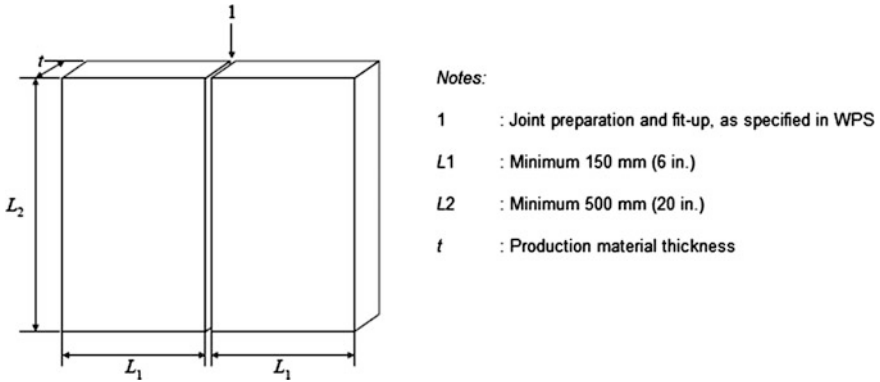
Fig. 3 The ABS minimum requirement for FSW
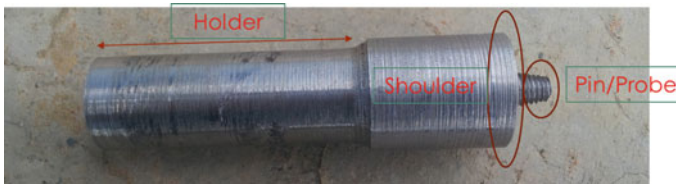
Fig. 4 Tools parameters and geometry

2.2 Tools

The tools are one of the crucial parts in FSW as they affect the material combination, the microstructure, and heat generation. During the studies, the tools parameters were selected as Mild Steel A370 cylinder bar shape. The carefully chosen geometry for the probe are cone tread to make the probe drill into the lap joint without applying additional pressure forces. The dimension of tools' shoulder are 20 mm in diameter and the probe are 5 mm in diameter as shown at Fig. 4. According to heat generation equations, the selected of tools' shoulder diameter will affect the heat generation.

2.3 Equipment

The machine preparation phase is the most crucial phase for the welding process. Therefore, to find the suitable rotation speed and travel speed to weld the aluminium plate using the FSW process, the trial and error process was undertaken. This trial and error process must meet the conditions of the tools and aluminium

Table 3 FSW parameter based on machine limitation

No.	Parameter	Set 1	Set 2
1	Rotation speed (RPM)	960	1240
2	Travel speed (mm/min)	24	32
3	Shoulder diameter (mm)	20	
4	Material	AA5083 + AA5083	
5	Tilt angle	3°	

Table 4 FSW specimen

Set	Rotation speed (RPM)	Travel speed (mm/min)
A1	960	24
A2	1240	32
B1	960	32
B2	1240	24
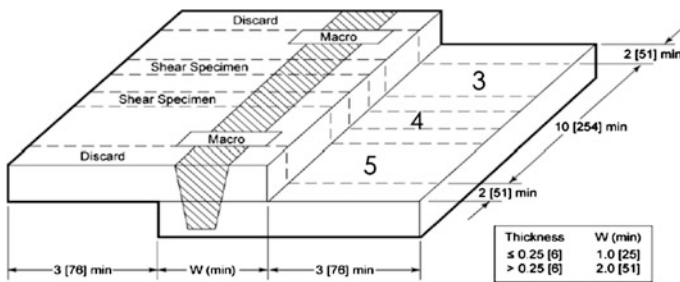
Fig. 5 The location of specimens [7]

plates welded and within all ranges of the travel speed and rotation speed calculated. Based on the analysis of the conventional milling machine, the machine can actually be converted to run the FSW process but has some of limitations on the numbering of rotation speeds and travel speeds. The parameters have been selected are shown in Table 3 below.

The FSW process requires some initial runs with the aluminium A5083 plate according the American Bureau of Shipping (ABS) regulations during the welding phase [6]. For the FSW process, the best manipulated variables were selected based on the trial and error experimental results as shown in Table 4.

After the welding, the specimens were cut into seven pieces as shown in Fig. 5. The locations are define in the Weld Procedure Qualification (WPQ) issued by American Weding Society (AWS). For the hardness testing, area Nos. 3, 4 and 5 were selected as qualified to be tested.

3   Result

3.1   Tensile Result

The tensile properties of the FSW specimens were measured in the longitudinal rolling direction at room temperature, transverse to the welding direction. As seen, the ultimate tensile strength (UTS) increases gradually with the increasing of the rotation speed of tools, up to a certain point, and then decreases by scales rate. The maximum UTS of 48.6 MPa is obtained at a rotation speed of 960 rpm and travel speed of 24 mm/min. The balance of the rotation speed and travel speed must be in the balanced ratio to ensure the strength in the UTS value range. When the travel speed beyond its peak value, the weld strength gradually decreases until the weld is no longer accepted by ISO standards [8].

It is also discovered that the FSW process softens the material to make a combination of the present alloy in each material. As seen at Fig. 6, the vibration of the FSW specimen during the tensile test shows the mixing of the elements are the proofing that the material are mixed together in solid state. It also shown in the red circle, the weld bead is able to absorb energy during elongation which causes the vibration seen in the graph.

Based on the results, the UTS results can be divided into two different categorizes, the differences of high rotation speed and low speed rotation speed. In the low rotation speed, the UTS for A1 which parameters are 960 rpm and 24 mm/min, is
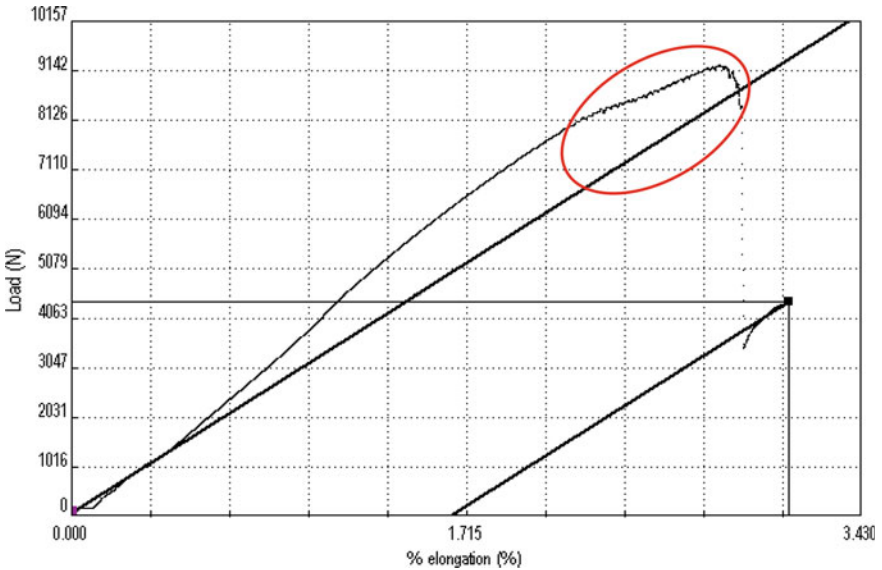
Fig. 6 UTS result for one sample of FSW specimen lap joint

Fig. 7 Tensile strength versus specimens

Tensile Strength VS Specimens

	A1	A2	B1	B2
Tensile Strength	48.6	48.38	48.48	48.57

Specimen
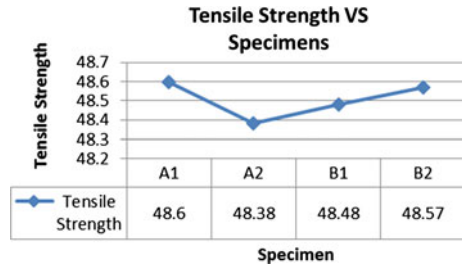
the highest, meanwhile for high rotation speed, the value of the UTS is highest for 1240 rpm and 24 mm/min based on the graph on Fig. 7.

Whenever the travel speeds are unbalanced with the rotation speeds, the decreasing of UTS are solidly proven by Fig. 7. The travel speed of 32 mm/min is the lowest in both rotation speeds, whether considering 960 rpm or 1240 rpm. The UTS can be improve by increasing the rotation speed if the travel speed of 32 mm/min still needed to be in use.

3.2　Hardness Result

The results were obtained from five different positions from each specimen as shown in Fig. 8. The hardness measurement was taken at the parent's metal section, heat affected zone (HAZ) section, and stir zone section. This is to determine the differences between the hardness of base material, the weld bead shoulder and the weld bead.

It can be observed that the position 2 and 4 are heat affected zone (HAZ) section as these positions have the most hardness in the plate. This is due to the thermal effect that annealing the microstructure of the aluminum plate while releasing the shear stress caused by the plastic material flow during the FSW process (Fig. 9) [9].

The highest hardness for the HAZ section was specimen A1 at position 2 (advancing side) with 31.2 HRB rather than the HAZ on position 4 (retreating side).

Fig. 8 The hardness position based on the thermal zone
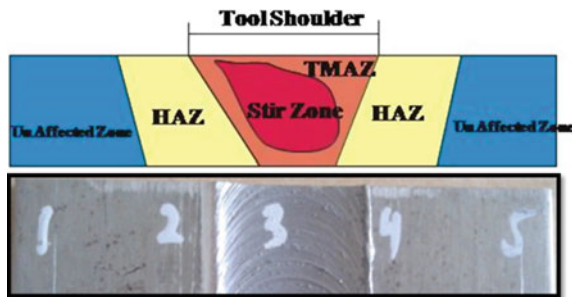
Fig. 9 HRB value VS
Position on Weld Bead

HRB vs Position on Weld Bead

Position	1	2	3	4	5
Specimen A1	28.4	31.2	29.8	29.4	28.2
Specimen A2	28.4	30.7	30.1	29.6	28.3
Specimen B1	28.3	30.8	29.6	29.8	28.4
Specimen B2	28.5	31	29.7	29.5	28.7
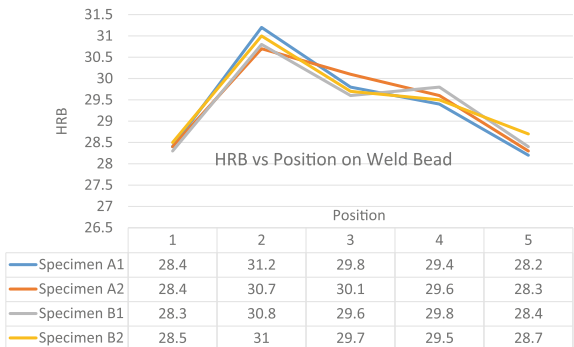
The advancing side will have a higher hardness value as the heat generated is on the advancing plate. In addition, the parent's metal has almost the same hardness because of the distance of the section from the focusing heat generation at the weld bead (i.e., position 1 and 5). At position 3, as known as the weld joint, the decreasing hardness result because the material suse the heat to transform its state from the solid to the plastic state. At this point, the focusing friction heat is exceeding the aluminum alloy heat capacity and thus the aluminum alloy changes its form [10]. Moreover, the tool's pin mixed the material together to fuse the material. Therefore, the heat cannot precede any material hardening process.

4   Conclusion

To conclude, we note that the tensile strength is dependent on the balance of rotation speed and travel speed. Therefore we can conclude that the strength of a lap joint is based on the percentage of mixing material in the joining area. The heat input that had been supplied to the jointing area of material A into material B must be exceeding the heat capacity of both materials. Besides that, the tensile strength is dependent on the balance of the rotation speed and travel speed. Therefore we can conclude that the strength of a lap joint is based on the percentage of mixing materials on the joining area. The heat input that has been supplied into the joining area of material A into material B must be exceeding the heat capacity of both materials. The maximum hardness was at the weld bead shoulders for all specimens tested and it was found that the hardness plot trend of the FSW process was same for all specimens. The heat capacity of a material also must be considered as the austenite transformation consumers a certain amount of heat to complete the process. Other than that, the travel speed as well as the heat conveyor also must be considered to avoid the excessive heat toward the material. The effect of excessive heat of heat capacity at the cross section of welding spot will nit reform its aluminum microstructure itself, but also the plate at its melting point.

References

1. Mishra, R.M., Mahoney, M.W.: Friction stir welding and processing. ASM Int. (2007)
2. Khaleed, T.: An outsider looks at friction stir welding. ANM–112 N-05-06 (July 2005)
3. Williams, S.W.: Air Space Eur. **3**(3–4), 64 (2001)
4. Dawes, J.: An introduction to friction stir welding (1995)
5. Bloodworth, T.: On the immersed friction stir welding Of Aa6061-T6: a metallurgic and mechanical comparison to friction stir welding. MSc Thesis, Vanderbilt University (2012)
6. American Bureau of Shipping (ABS): Guide for the approval of friction stir welding in aluminium (Oct 2011)
7. American Welding Society (AWS): Draft specification for friction stir welding of aluminium alloys for aerospace hardware (28 July 2012)
8. American Society for Testing and Materials (ASTM International): E18-standard test methods for rockwell hardness of metallic materials
9. Mitchell, J.: The experimental thermo-mechanics of friction stir welding. MSc Thesis, Vanderbilt University (2002)
10. Li, W., Yang, Q., Zhang, Z., Gao, D.: Effect of weld curvature radius and tool rotation direction on joint microstructure in friction stir welding casting alloys. Mater. Des. **53**, 124–128 (2014). ISSN: 0261-3069
11. Baghel, P.K.: A survey: friction stir welding of stainless steel 304. IOSR J. Mech. Civ. Eng. (IOSRJMCE) **1**(2), 22–23 (2012). ISSN: 2278–1684

Effect of Process Parameters on the Strength of Swept Friction Stir Spot Welded Plates

Mokhtar Awang, Azman Ismail and M. Aiman K. Zaman

Abstract Swept friction stir spot welding, a derivative of friction stir welding is a solid-state process for joining materials by using frictional heat generated due to rotating tool along the weld line. The main objective of this study is to investigate the strength of the swept friction stir spot welded aluminum plate by changing the welding process parameters. In this paper, the joining was done on thin aluminum alloy plates using the Octaspot™ tool path with a radius of 10 mm. The samples were welded using a CNC milling machine. The study focuses on two process parameters which are the tool rotational speed and the welding traverse speed. The samples were analyzed on their shear strength and the results show that the higher the tool speed, the higher the shear strength is. However, when the rotational speed is increased, the shear strength shows a decreased pattern. The overall results are in good agreement with other published results.

Keywords Swept FSSW · Octaspot · Process parameters · Weld strength · FSSW

1 Introduction

Swept friction stir spot welding (SFSSW) is a new joining technique that has been introduced to the manufacturing industry recently. The process of SFSSW is almost similar to friction stir spot welding (FSSW) except that the tool will move around a

M. Awang (✉) · M.A.K. Zaman
Mechanical Engineering Department, Universiti Teknologi PETRONAS,
32610 Seri Iskandar, Perak, Malaysia
e-mail: mokhtar_awang@petronas.com.my

M.A.K. Zaman
e-mail: stp.lagendallo@gmail.com

A. Ismail
Malaysian Institute of Marine Engineering Technology, Universiti Kuala Lumpur,
32200 Lumut, Perak, Malaysia
e-mail: azman@unikl.edu.my

point to create a larger contact area. Theoretically SFSSW gives better strength as compared to FSSW due to a larger joint interface produced during the welding.

There are only a few studies which aim to investigate the critical parameters of the SFSSW on the mechanical properties of the welded plate. For example, the SFSSW has been under significant development at Wichita State University (WSU) since 2005 [1]. They came out with a tool movement pattern called the Octaspot as shown in Fig. 1. An advantage of swept spot over the plunge spot is the increase in strength primarily due to the resulting increased shear area. The flow of material during the plunge and dwell of a typical spot can create an upturn of the sheet interface. The thinning of the effective sheet thickness typically correlates with the decrease in strength or at least a loss of peel strength.

They also have conducted the evaluation of SFSSW in 2.5 mm-thick aluminum 2219-T6. The purpose of the investigation was to evaluate the effects of SFSSW on tensile strength and fatigue life in 2219-T6 material with a faying surface gasket compound. Three types of welding tools were used, namely psi tool, counter-flow tool with thread and counter-flow with tapered flats. The three tools have common pin and shoulder geometries. The strength of the welded sample has been compared with the 4 spot riveted coupons which carried an average load of 16.5 kN.

The previous published results also showed that the SFSSW was capable of producing sound joints through 0.1 in. 2219-T6 with a faying surface gasket compound and surface treatment [2, 3]. Moreover, it was also shown that the strength alone was not a reliable predictor of fatigue performance. When compared to riveting, SFSSW has the potential to be much stronger while maintaining comparable fatigue properties [4–6].
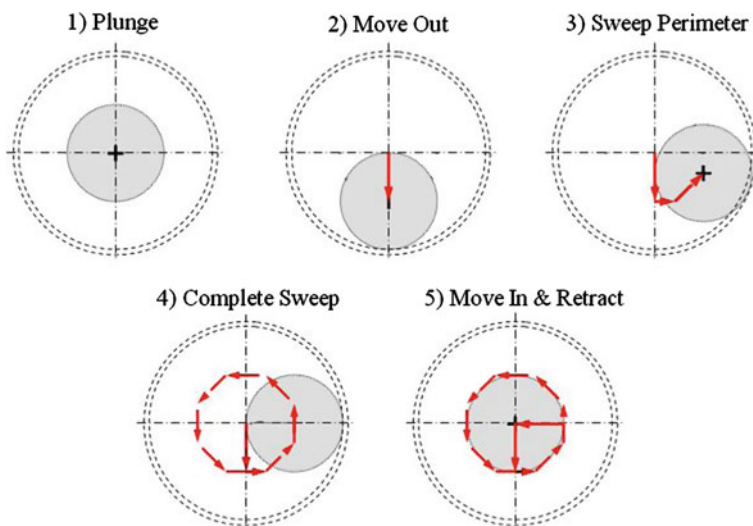
Fig. 1 Schematic of Octaspot™ swept FSSW [1]

A previous study also investigates the effect of the sealant and surface treatment on the faying surface of SFSSW. The study evaluated the ultimate strength, fatigue life and corrosion resistance of the joints. Three types of the welding tool geometry were used namely psi, threaded counter-flow and modified trivex. The results showed that psi geometry tool gave the most significant result in producing highest strength specimen compared to other tool geometry while the threaded counter-flow produced the second highest and modified trivex was the lowest.

In this paper, the effect of the process parameters on the strength of the swept friction stir spot welded plate was investigated. In addition, the strength results of the swept FSSW and FSSW joints were then compared.

2 Experimental Works

In this present study, the tool made of H-13 tool steel material was fabricated and heat treated for surface hardening. The tool geometry is shown in Table 1. In this work, aluminum alloy 6061 workpieces were cut in 30 mm by 120 mm. The welding process was done using a CNC milling machine with special fixture as in [7].

There were several welding parameters used in this setting to determine the effect of rotation and travel speed towards the strength as shown in Table 2. The plunge depth used was 1.6 mm with varying rotational and travel speed. The strength of FSSW joints are also investigated in order to compare with the SFSSW samples. Three different rotational speeds were chosen, i.e., 4000, 5000, and 6000 RPM. The traverse speed was kept constant at 50 mm/min.

A universal testing machine was used to conduct lap shear tests. The position of the welded sample on the universal testing machine is shown in Fig. 2. Lap shear

Table 1 Tool's geometry

Shoulder's diameter	Tip's diameter	Length of tip	Length of tool's holder
10.0 mm	2.0 mm	1.5 mm	70.0 mm

Table 2 Welding parameters

No.	Rotational speed (rpm)	Traverse speed (z-axis) (mm/min)	Traverse speed (y and x-axis) (mm/min)
1	2000	50	50
2	2500	50	50
3	3000	50	50
4	3500	50	50
5	3000	50	40
6	3000	50	50
7	3000	50	60
8	3000	50	70

Fig. 2 A photograph of lap shear test

tests have been conducted to measure the strength of the welded plates. It is one of the indicators to determine the strength of the welding joint especially for lap welding samples. The maximum lap shear load will be recorded for the evaluation.

3 Results and Discussion

Based on Fig. 3, it was found that the failure point of the sample is around the welding area either in the front or back of the sample. The weakest point of the welding is at the edge of the circle where most of the samples fail at that point.

Figure 4 shows the relationship between maximum lap shear load and tool traverse speed. It shows that as the welding speed is increasing, the maximum lap shear load of the welding joints also increased. Higher welding speeds are associated with low heat inputs, which result in faster cooling rates of the welded joint.

Fig. 3 Visual inspection

Fig. 4 Maximum lap shear load versus tool traverse speed
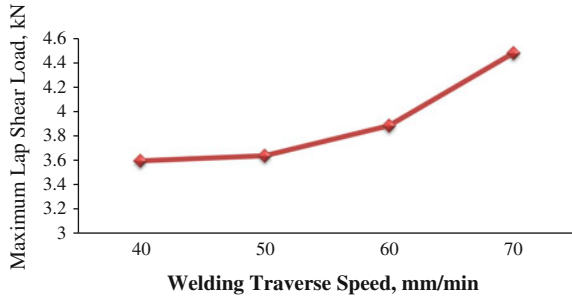
Fig. 5 Maximum lap shear load versus rotational speed
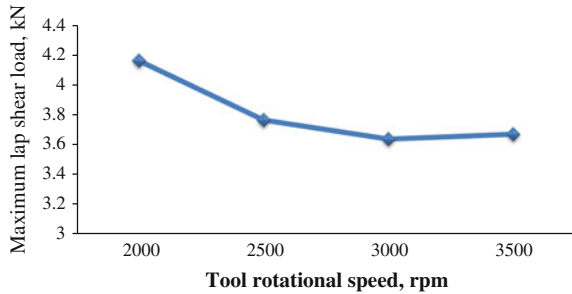
This can significantly reduce the extent of metallurgical transformations taking place during welding and hence the local strength of individual regions varies across the weld zone. The traverse speed is also associated with the heat dissipation of the welding process. Increasing the traverse speed increases the heat dissipation rate because the heated SFSSW zone is quickly brought into the cool base metal, resulting in reduced temperature and duration of thermal exposure in the HAZ. Increasing temperature can increase the rate of diffusion which may accelerate the dissolution and growth rates and therefore enhance particle coarsening.

Based on Fig. 5, as the rotational speed increases, the value of maximum lap shear load shows a decreasing trend. In FSSW, the tool rotation speed results in stirring and mixing of material around the rotating pin which in turn increase the temperature of the metal. It appears to be the most significant process variable since it tends to influence the transitional velocity. It is known that the frictional heat can be formulated as a function of rotation speed. When the rotational speed increases, the heat input within the stirred zone also increases due to the higher friction heat which in turn result in more intense stirring and mixing of materials. Therefore, as the heat increases, the strength was reduced due to the formation of defects and over aging in heat-affected zone (HAZ). Moreover, higher rotation speeds could raise the strain rate and turbulence in the material flow which could cause a tunnel defect at the weld nugget.

Figure 6 illustrates the comparison of maximum lap shear load of SFSSW and FSSW. It can be noticed that at every rotational speed, the strength of SFSSW is much higher than that of FSSW. Obviously, it is because the contact surface of

Fig. 6 Strength of swept FSSW compared to FSSW joint
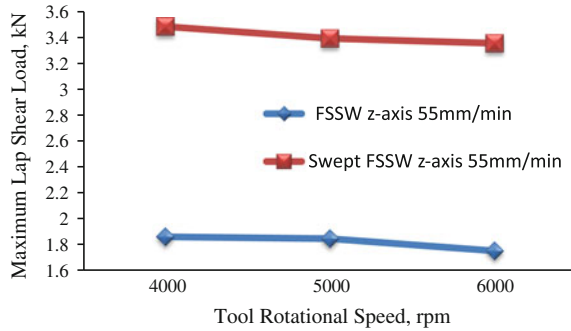
SFSSW is larger and could withstand larger shear load. The lower strength of FSSW can be also due to the flow of material during the plunge and dwell of typical spot, thus create an upturn of the sheet interface [5].

4 Conclusions

Based on the present study, several conclusions can be drawn as below:

1. With the increment of rotation speed, the strength of the joint tends to decrease from about 4.16 kN to 3.67 kN.
2. Meanwhile, with the increment of travel speed, the strength tends to increase from about 3.60 kN to the highest load of 4.48 kN.
3. A SFSSW welded joint is almost twice stronger as compared to a FSSW joint.

References

1. Jeremy, M.B.: The effect of sealant and surface treatments on faying surface of swept friction stir spot welding. Thesis, Wichita State University (2006)
2. ESAB: Friction Stir Welding Technical Handbook. LAXÅ, Sweden (2010)
3. Thomas, W.M., Nicholas, E.D., Needham, J.C., Murch, M.G., Temple-Smith, P., Dawes, C.J.: US Patent 5, 460, 317 (1995)
4. Mishra, R.S., Ma, Z.Y.: Friction stir welding and processing. Mater. Sci. Eng. **50**(1–2), 1–78 (2005)
5. Badheka, V.J.: Utilisation of a conventional milling machine for friction stir welding of commercial aluminum. Weld. Res. Abroad **56**(6), 6 (2010)
6. Smith, C.B., et al.: Effect of compliance and travel angle on friction stir welding with gaps. J. Manuf. Sci. Eng. **132**(4), 1–9 (2010)
7. Ghazanfar, B., Awang, M., et al.: Development of a new approach for incorporating tool tilting in friction stir welding. Adv. Mater. Res. **701**, 378–381 (2013)

Mechanism of Creating the Topography of an Abrasive Water Jet Cut Surface

J. Valíček, M. Harničárová, A. Panda, I. Hlavatý, M. Kušnerová,
H. Tozan, M. Yagimli and V. Václavík

Abstract The development and application of new materials brings, in connection with their technological machining, a number of new questions. Classical methods of machining are supplemented by new technologies. An abrasive water jet represents a universal flexible tool enabling the machining of all natural and artificial materials that are not damaged by direct contact with water. Great attention is paid to the study of the cut surface topography after abrasive water jet machining. The study of surface topography is important from the point of view of modelling and prediction of the topographic function of the abrasive water jet. On the basis of knowledge of the topographic function, we are able to optimise the technological parameters of the abrasive water jet machining process, which has an impact on the

J. Valíček (✉) · M. Harničárová · M. Kušnerová
Institute of Physics, Faculty of Mining and Geology, VŠB—Technical University of Ostrava,
17. listopadu 15/2172, 70833 Ostrava, Czech Republic
e-mail: jan.valicek@vsb.cz

M. Harničárová
e-mail: marta.harnicarova@vsb.cz

M. Kušnerová
e-mail: milena.kusnerova@vsb.cz

J. Valíček · M. Kušnerová
RMTVC, Faculty of Metallurgy and Materials Engineering, VŠB—Technical University of
Ostrava, 17. listopadu 15/2172, 708 33 Ostrava, Czech Republic

J. Valíček · V. Václavík
Institute of Clean Technologies for Mining and Utilization of Raw Materials for Energy,
Faculty of Mining and Geology, VŠB—Technical University of Ostrava, 17. listopadu
15/2172, 70833 Ostrava, Czech Republic
e-mail: vojtech.vaclavik@vsb.cz

M. Harničárová
Nanotechnology Centre, VŠB—Technical University of Ostrava, 17. listopadu 15/2172,
70833 Ostrava, Czech Republic

A. Panda
Faculty of Manufacturing Technologies with a Seat in Prešov, TUKE, Bayerova 1, 08001
Prešov, Slovak Republic
e-mail: anton.panda@tuke.sk

output, quality and price of the final product. The mechanism to remove material is an area which has not received much attention. In material disintegration, the mechanisms of cutting, plastic deformation, fatigue and fracture participate physically. By studying the surface topography we can better understand the process of abrasive water jet machining, specify the theory and correctly quantify the mechanism of material removal, which is the subject of this paper.

1   Introduction

The area of abrasive waterjet cutting is characterised by cut trace retardation and roughness formed in the course of abrasive waterjet cutting. The abrasive waterjet cutting technology and the accompanying phenomena occurring in the process of material cutting have been the subject of many research activities aimed at optimizing technological parameters affecting the quality of a cut. From the literature [1–25] dealing with the problems of quality of cut wall surfaces in relation to the settings of the technological process in the case of abrasive waterjet cutting technology, it follows that the study of surface quality and the development of a topography function while cutting are a very debatable issue at present. Analysis of literary sources shows that the number of authors uses statistical, empirical and mathematical models for the quantification of various influences of technological parameters of the process of abrasive waterjet cutting [1–25]. Based on the literature search, it can be stated that most of them rest on a regression analysis. Critically it can be stated that the majority of existing procedures are, from the point of view of use in operating practice, problematic, especially owing to the problematical

I. Hlavatý
Department of Mechanical Technology, Faculty of Mechanical Engineering, VŠB—TU Ostrava, 17. listopadu 15, 70833 Ostrava-Poruba, Czech Republic
e-mail: ivo.hlavaty@vsb.cz

H. Tozan · M. Yagimli
Department of Industrial Engineering, Turkish Naval Academy, 34942 Tuzla, Istanbul, Turkey
e-mail: htozan@dho.edu.tr

M. Yagimli
e-mail: mustafa.yagimli@okan.edu.tr

V. Václavík
Institute of Environmental Engineering, Faculty of Mining and Geology, VŠB - TU Ostrava, 17. listopadu 15, 70833 Ostrava-Poruba, Czech Republic

J. Valíček
VŠB - Technical University of Ostrava, 17. listopadu 15/2172, 70833 Ostrava-Poruba, Czech Republic

determination of a series of used constants, because of the concretization of inputs to the derived relations, etc.

K_{plmat} [μm] is a new technology length parameter, which extends with the increasing plasticity of the divided material, and which is determined either from three deformation parameters, according to $K_{plmatx} = \frac{Ra_x \cdot h_x}{Y_{ret_x}}$ [μm], or from deformation parameters according to $K_{plmat_x} = \frac{10^{12}}{E_{mat_x}^2}$ [μm], or from the velocity of ultrasound propagation v_{luz} [m·s^{-1}] according to $K_{plmat_x} = \left(\frac{10^4}{v_{luz}}\right)^6$ [μm], or from the modulus of elasticity in tension E_{mat} of the divided material. Physically this is a complex parameter, related both to the material mechanical properties, as well as to the technology parameters. Figure 1 shows the basic hydro-abrasive cutting of
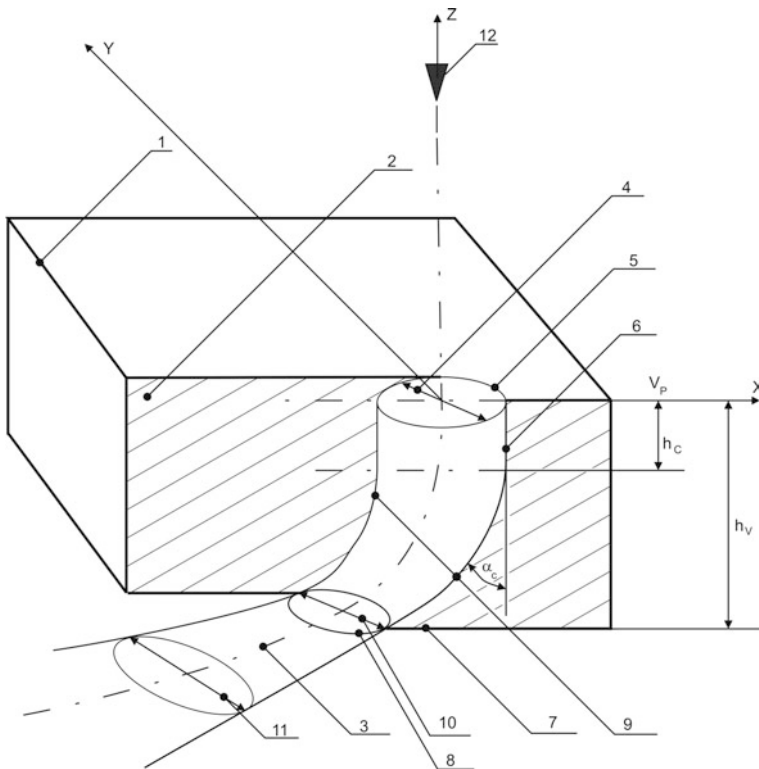
Fig. 1 Principle of hydro-abrasive division of materials and nomenclatural marking of basic technological and geometrical AWJ elements. *Legend 1* sample *top edge*, *2* cutting wall, *3* AWJ axis of symmetry, *4* AWJ flow input diameter on the cut head, *5* shape of the cut gap on the cut head, *6* cut front, cut front trace, *7* sample bottom edge, *8* shape of the cut gap on the cut heel, *9 curves* of external flow lines in the cut plane, *10* AWJ flow output diameter on the cut heel, *11* AWJ flow diameter after exit from the sample *bottom edge*, *12* AWJ output nozzle, v_p—feed direction, h_c—critical depth of the cut, h_v—depth of the sample cutting-off (sample height)

materials and nomenclatural marking of basic technological and geometric AWJ elements.

2 Identification and Prediction of Surface Roughness

Types of roughness and their distribution on the depth of the cut (Fig. 2) are predicted evolutions in dependence on the instant depth of the cut $h_{abs} = 0 - h_{lim}$ [mm] for steel grade ČSN 17 251.

Equation (1) represents the function $Ra = f(h, E_{mat}, K_{plmat})$, which enables prediction of the wall roughness in the trace of the cut, and K_{pl} is deformation surface or magnitude of reduction according to the depth:

$$Ra = (-10) \cdot \left(\frac{1 - K_{plmat}}{K_{plmat} - h}\right), \quad K_{pl} = Ra \cdot h \tag{1}$$

Equation (2) represents the actual function of the surface topography in radial direction

$Ra_{sk} = f(Ra, Ra_o)$, where Ra_o is surface roughness in the neutral plane:
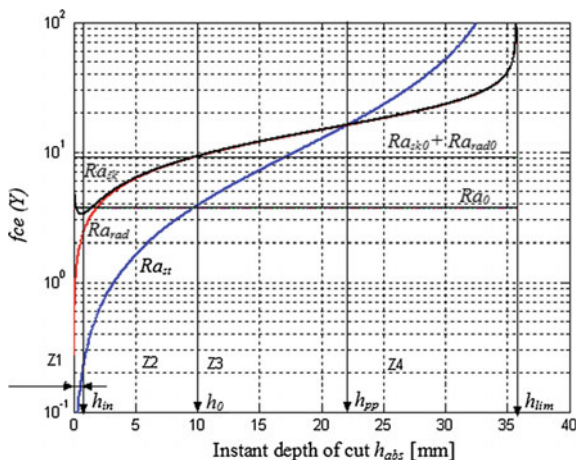
Fig. 2 Types of roughness and its distribution on the depth of the cut. *Legend Ra_{st}*—roughness in the trace [µm], *Ra_{sk}*—roughness, which is actually measured in radial direction [µm], *Ra_{rad}*—theoretical bearing roughness in radial direction [µm], *Ra_o*—roughness on neutral plane [µm], Z1 + Z2 + Z3 + Z4—main deformation zones on the depth of the cut and their depth levels: h_{in}—depth of the initiation zone Z1 [mm], h_o—depth of the elastic deformations zone Z2 [mm], h_{pp}—depth of the elastic-plastic deformations Z3 [mm], h_{lim}—depth of the plastic deformations zone Z4 and limit depth of the cut in the given material [mm]

$$Ra_{sk} = Ra - \log \left(\frac{Ra}{Ra_o} \right) \tag{2}$$

Ra_{sk} in radial plane respects the initiation zone h_{in} (Fig. 2). This initiation zone varies logically from 1 to 4 mm depending on the material, and its increased values complicate the surface quality, which must be subsequently adapted.

3 Resolution of Stress in the Cut

We used the Mohr's resolution of stress and resolution of the main flow stress σ_d (3), which act in the main stress plane, into mutually perpendicular normal components σ_x (4) a σ_y (5), applied for stress relations in normal cut planes. It is generally valid that both main minimal and also main maximal stresses act in the main stress plane. The main stress plane is always perpendicular to the origin of external forces. Normal stress components act in the planes revolved by a certain angle which is why the magnitudes vary between the limit values of the main stress. We then added to the normal stress components σ_x and σ_y another normal component σ_{nh}, which acts in the direction of rotation or deepening of the trace of the cut. From the viewpoint of technology it is possible to define on the basis of the performed analyses individual components in the following manner: the component σ_x is responsible for material disintegration and deepening; the component σ_y comprises the increasing tangential stress and friction with the increasing depth of the cut and is responsible for retarding of the trace and its revolving into the direction opposite to the movement of the nozzle; the component σ_{nh} (6) is responsible for material disintegration in the direction of trace, which at the same time gets elongated due to retardation and revolving into the opposite direction. More detailed characteristics of the mentioned normal stress components is described below.

The original main stress plane, represented by perpendicular setting of the nozzle in direction of the axis Z, revolves in the trace of the cut with an instant depth under the angle δ = function (h) (7). It follows from the theory of elasticity and strength, that the main flow stress σ_{md} is equal to the sum of mutually perpendicular normal stresses $\sigma_{md} = \sigma_x + \sigma_y$. It is in principle equal to the measured material contractual strength Rm, which must be overcome by external forces in order to achieve a disintegration of the material structure in the stressed area. As it is evident from Fig. 3, evolutions of the normal components σ_x and σ_y are mutually completing each other in dependence of the instant depth h. Sum component of the main stress in the cut σ_{md} is constant, because it is given by the sum of sinus and cosine projections of revolving planes and normal vectors of forces in relation to the axes X and Y. The normal component σ_x decreases with the depth of the cut h according to the function $\cos(\delta)$ right to zero value $\sigma_x = 0$ at the moment of achieving the

maximum technological depth h_{tech} and maximum angle of curvature of the trace of the cut $\delta_{max} = 90°$. On the other hand the normal component σ_y increases with the depth of the cut h according to the function $\sin(\delta)$ right to the maximum value $\sigma_y = \sigma_{md} = Rm$ at the moment of achievement of the maximum technological depth h_{tech} and maximum angle of curvature of the trace of the cut $\delta_{max} = 90°$. At the same time both normal components σ_x and σ_y vary in positive values and therefore according to the sign convention they initiate tensile stress in the stressed material.

Since we know that compression stress also acts particularly in the plastic area of material forming, we used a differential expression and we associated it to the instant depth of the trace of the cut. This differential normal component is in diagram in Fig. 3 marked as $\sigma_{nh} = \sigma_x - \sigma_y$ and it illustrates very well a transition into negative values of compressive stressing of material in the cut after transition into plasticity. The normal component σ_{nh} is from technological perspective in negative (compressive) values significant by the fact, that it indicates a steep increase in surface deformation on the cut walls with high roughness and big curvature of the trace of the cut in combination with higher power load and with drop of output.

Discrete values of σ_{nh}, as well as of other normal components σ_x and σ_y (or σ_n upon request), can be for the examined depths either read directly from the
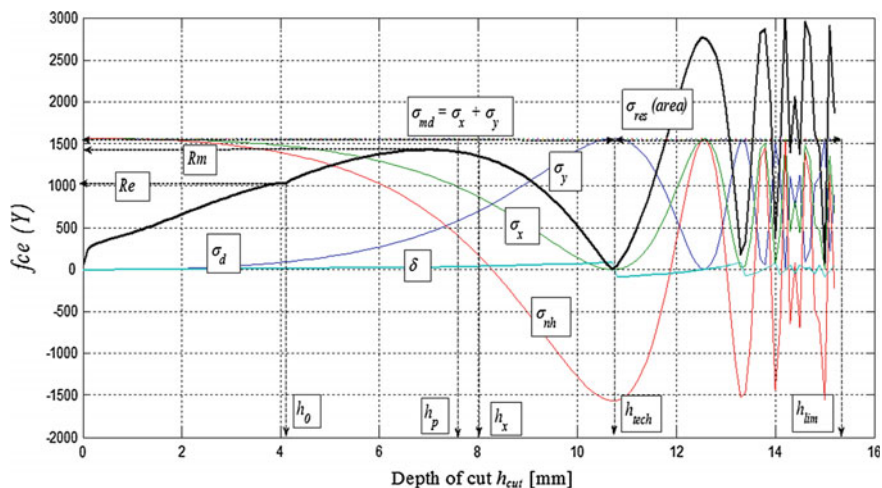
Fig. 3 Stress analysis, steel CSN 13 180, $Emat = 256,466$ MPa. *Legend* σ_{md}—main max. flow stress given by the sum of the components $\sigma_{md} = \sigma_x + \sigma_y$ [MPa], σ_x—normal component related to the axis x [MPa], σ_y—normal component related to the axis y [MPa], σ_{nh}—normal component related to the instant depth h [MPa], Rm—material contractual tensile strength [MPa], Re—material yield strength [MPa], σ_{res} (area)—area of residual stresses [MPa], h_o—depth of the neutral plane in the cut [mm], h_p—depth of material plasticity in the cut [mm], h_x—chosen depth [mm], h_{tech}—technically achievable depth of the cut limited by the curvature $\delta_{max} = 90°$ [mm], h_{lim}—limit depth of the cut limited by the parameters K_{cut} and T_{cut} [mm]

progressive values from the diagram in Fig. 1, or they can be calculated according to the discrete values of the angle of curvature using the equations contained in the algorithm. For example at the chosen depth $h_x = 8$ mm (for the analyzed material in Fig. 3 the value δ_x is 42°) according to the required thickness of division in the given material, or for the state on the depth position of the neutral plane h_o (for the analysed material in Fig. 3 the value h_o is 4.1 mm and the value δ_o is 14°), or at the limit of plasticity in the half of the limit depth $h_p = h_{lim}/2$ (for the analysed material Fig. 3 the value $h_p = 7.6$ mm, $\delta_p = 38°$). At the moment of achievement of the maximum technological depth h_{tech} and the maximum angle of curvature of the trace of the cut δ_{max} is 90°, when $\sigma_y = /+/\sigma_{md}$, i.e. at the value of the maximum tension, and $\sigma_x = 0$ is $\sigma_{nh} = /-/\sigma_{md}$, i.e. it is equal to the value of the maximum compression due to fact that at this moment it acts by full compression in the trace, which was already formed perpendicularly to the direction opposite to the shifting of the nozzle. It is therefore a confirmation of the correctness of the solution on the new manner of resolution of stress in the cut. Equations (3)–(7) and Fig. 3 present a decomposition of the main stress σ_{md} to the normal components σ_x and σ_y, angle δ represents curvature of the trace of the cut due to decomposition of the forces in the cut. σ_{res} is residual stress in the cut (8).

$$\sigma_d = \left(\left(\frac{K_{plmat}}{Ra \cdot h} \right) \cdot \left(\frac{Ra \cdot h \cdot Y_{reto} \cdot V_{obj}}{Y_{ret}} \right)^{0.25} \right)^{0.5} \tag{3}$$

where Y_{reto} is trace retardation in the neutral plane h_o, V_{obj} is deformation volume.

$$\sigma_x = \sigma_m - \sigma_m \cdot \left(\sin\left(\frac{\delta \cdot 3.14}{180} \right) \right)^2 \tag{4}$$

$$\sigma_y = \sigma_m - \sigma_m \cdot \left(\cos\left(\frac{\delta \cdot 3.14}{180} \right) \right)^2 \tag{5}$$

$$\sigma_{nh} = \sigma_x - \sigma_y \tag{6}$$

$$\delta = \arctan\left(\frac{Y_{ret}}{h} \right) \cdot \frac{180}{3.14} \tag{7}$$

$$\sigma_{res} = E_{mat}^{0.5} \cdot \sin\left(tg\left(\frac{Ra}{K_{plmat}} \right) \right)^2 \tag{8}$$

On the basis of topographic parameters of the surface it is possible to construct an equivalent of the forming diagram σ_d = function (h), and by expression of the relation for proportionate deformation $\varepsilon = f(h)$ it is possible to construct also an equivalent of the forming diagram $\sigma_d - \varepsilon$ according to Fig. 4, which is most often measured on the tensile testing machines in specialised laboratories and workshops. It is possible to evaluate the main material parameters, the diagram can be

completed with use of the function δ by the branch of the so called real flow stress σ. The value of the proportionate deformation $\varepsilon_{fr} = 0.04$ and appropriate ductility $T_{ad} = 4\ \%$ at the moment of achievement of the σ_{fr} indicates a steel with high brittleness at its high strength Rm.

4 Conclusions

The paper presents a mechanism of forming of the surface topography by hydro-abrasive division. Stress resolution in the cut was made. Furthermore, on the basis of the topographic surface parameters and with use of their inherent laws concerning relations it is possible to construct an equivalent diagram of deformation $\sigma_d = f(h)$ (seen in Fig. 4), which is usually measured on tensile testing machines in specialised laboratories and workshops. This method could be used in the future as a predictive method for identification of stress-deformation parameters of materials. In the case of cutting and division of technologies by the AWJ technology, it is in principle a flexible disintegration tool which contrary to the fixed tools is governed
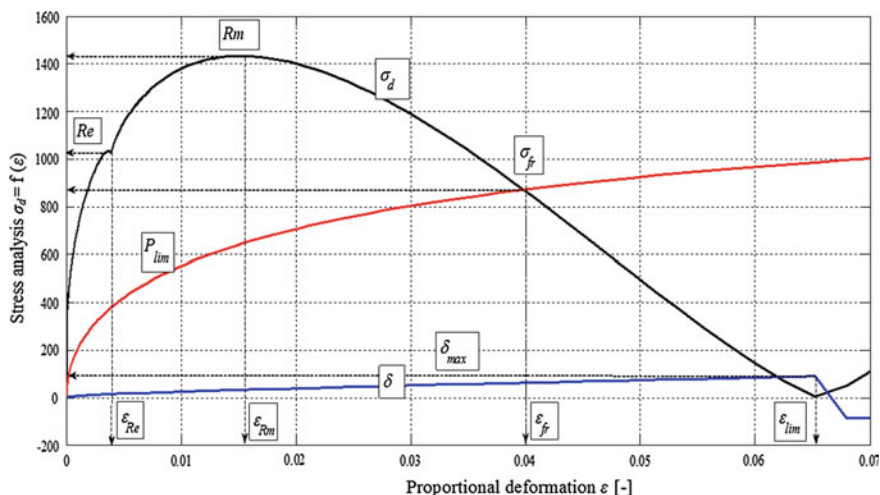
Fig. 4 Stress analysis, σ_d—ε, steel CSN 13 180, $E_{mat} = 256{,}466$ MPa. *Legend* σ_{fr}—stress at the moment of destruction of material structure in the sample [MPa], p_{lim}—evolution of the limit state of stress in the material core [MPa], δ—angle of curvature of the trace of the cut according to the depth of the cut h [°], δ_{max}—angle of curvature of the trace of the cut according to the depth of the cut [°], ε—proportionate deformation [−], ε_{re}—proportionate deformation at the yield strength (yield strength corresponds in depth to h_o) [−], ε_{rm}—proportionate deformation at the limit of contractual strength Rm [−], ε_{fr}—proportionate deformation at the moment of destruction of the material structure [−], ε_{lim}—proportionate deformation at the $\delta_{max} = 90°$ [−]

by different physical-mechanical laws both from the viewpoint of the mechanism of formation of a new surface, and from the perspective of its final topography.

References

1. Institute of Geonics AS CR, V.V.I., Valicek, J., Borovicka, A., Hloch, S., Hlavacek, P.: Method for the Design of a Technology for the Abrasive Waterjet Cutting of Materials. U.S. Patent 9073175, 7 July 2015
2. Kolahan, F., Khajavi, A.H.: Modeling and optimization of abrasive waterjet parameters using regression analysis. Int. J. Aerosp. Mech. Eng. **5**, 248–253 (2011)
3. Hashish, M.: Optimization factors in abrasive waterjet machining. J. Eng. Mater. Technol. **113**, 29–37 (1991)
4. Hashish, M.: A modeling study of metal cutting with abrasive water jets. J. Eng. Mater. Technol. **106**, 88–100 (1984)
5. Hashish, M.: A model for abrasive—waterjet (AWJ) machining. J. Eng. Mater. Technol. **111**, 154–162 (1989)
6. Hashish, M.: Visualization of the abrasive—waterjet (AWJ) machining. Exp. Mech. **28**, 159–169 (1988)
7. Kovacevic, R.: Monitoring the depth of abrasive waterjet penetration. Int. J. Mach. Tool. Manuf. **32**, 725–736 (1992)
8. Wang, J.: Predictive depth of jet penetration models for abrasive waterjet cutting of alumina ceramics. Int. J. Mech. Sci. **49**, 306–316 (2007)
9. Lemma, E., Chen, L., Siores, E., Wang, J.: Optimising the AWJ cutting process of ductile materials using nozzle oscillation technique. Int. J. Mach. Tool. Manuf. **42**, 781–789 (2002)
10. Chakravarthy, P.S., Babu, R.N.: A hybrid approach for selection of optimal process parameters in abrasive water jet cutting. Proc. Inst. Mech. Eng. B J. Eng. Manuf. **214**, 781–791 (2000)
11. Engin, C.I.: A correlation for predicting the abrasive water jet cutting depth for natural stones. S Afr J Sci **108**, 1–11 (2012)
12. Chen, F.L., Siores, E., Patel, K.: Improving the cut surface qualities using different controlled nozzle oscillation techniques. Int. J. Mach. Tool. Manuf. **42**, 717–722 (2002)
13. Selvan, M.C.P., Raju, N.M.S., Sachidananda, H.K.: Effects of process parameters on surface roughness in abrasive waterjet cutting of aluminium. Front Mech. Eng. **7**, 439–444 (2012)
14. Valicek, J., Hloch, S., Kozak, D.: Surface geometric parameters proposal for the advanced control of abrasive waterjet technology. Int. J. Adv. Manuf. Tech. **41**, 323–328 (2009)
15. Valicek, J., Hloch, S.: Using the acoustic sound pressure level for quality prediction of surfaces created by abrasive waterjet. Int. J. Adv. Manuf. Tech. **48**, 193–203 (2010)
16. Valicek, J., Hloch, S.: Optical measurement of surface and topographical parameters investigation created by abrasive waterjet. Int. J. Surf. Sci. Eng. **3**, 360–373 (2009)
17. Hlavacek, P., Valicek, J., Hloch, S., et al.: Measurement of fine grains copper surface texture created by abrasive waterjet cutting. Strojarstvo **51**, 273–380 (2009)
18. Hloch, S., Valicek, J.: Prediction of distribution relationship of titanium surface topography created by abrasive waterjet. Int. J. Surf. Sci. Eng. **5**, 152–168 (2011)

19. Hloch, S., Valicek, J.: Topographical anomaly on surfaces created by abrasive waterjet. Int. J. Adv. Manuf. Tech. **59**, 593–604 (2012)
20. Valicek, J., Cep, R., Rokosz, K., Lukianowicz, C., et al.: New way to take control of a structural grain size in the formation of nanomaterials by extrusion. Materialwiss. Werkstofftech **43**, 405–411 (2012)
21. Valicek, J., Hloch, S., Samardzic, I., et al.: Influence of traverse speed on surface irregularities created by the abrasive waterjet. Metalurgija **51**, 43–46 (2012)
22. Hloch, S., Valicek, J., Samardzic, I., et al.: Classification of technical materials according to classes machinability for hydroabrasive cutting. Metalurgija **51**, 125–128 (2012)
23. Vikram, G., Babu, N.R.: Modelling and analysis of abrasive water jet cut surface topography. Int. J. Mach. Tool. Manuf. **42**, 1345–1354 (2002)
24. Thomas, D.J.: Characteristics of abrasive waterjet cut-edges and the affect on formability and fatigue performance of high strength steels. J. Manuf. Process **11**, 97–105 (2009)
25. Kusnerova, M., Valicek, J., Hloch, S., et al.: Derivation and measurement of the velocity parameters of hydrodynamics oscillating system. Strojarstvo **50**, 375–379 (2008)

Injection Moulding Versus Rapid Prototyping—Thermal and Mechanical Properties

Pavel Koštial, Ivan Ružiak, Svetozár Malinarič, Zora Jančíková and Vladimír Rusnák

Abstract This paper is devoted to the comparison of the influence of injection moulding (IM) on heat transport phenomena and the mechanical properties of materials, with rapid prototyping (RP). The tested materials included ABS and polyurethane (PU). The results show decrease of both mechanical properties and thermal transport phenomena in the case of RP samples.

1 Introduction

High performance polymers are commonly and widely used in advanced technologies and cover large varieties of applications such as micro and nanoelectronics, civil and military transportation, defence, etc. It is important for these technologies to design tailor-made high tech materials by focusing on molecular structure/processability/properties relationships of high performance polymers, such as heterocyclic polymers known for their outstanding thermal properties and their good mechanical behaviour, or even functionalized polymers or inorganic polymers. Rapid prototyping (RP) fabrication techniques are currently widely used in various industrial and medical fields, providing substantial advantages in regards to

P. Koštial · Z. Jančíková (✉) · V. Rusnák
VŠB—TU Ostrava, 17. listopadu 15, 708 33 Poruba, Ostrava, Czech Republic
e-mail: zora.jancikova@vsb.cz

P. Koštial
e-mail: pavel.kostial@vsb.cz

V. Rusnák
e-mail: vladimir.rusnak@form-composite.sk

I. Ružiak
Technical University of Zvolen, T.G. Masaryka 24, 96001 Zvolen, Slovak Republic
e-mail: ruziak@tuzvo.sk

S. Malinarič
Constantine the Philosopher University, Trieda Andreja Hlinku 1, Nitra, Slovak Republic
e-mail: smalinaric@ukf.sk

development time and costs in comparison with more traditional manufacturing processes. This paper presents a new method used for the fabrication of high-intensity focused ultrasound transducers using RP technology. To fabricate microstructures using a rapid prototyping system, a new integral stereolithography (SL) system is developed in [1]. The dynamic mask generator consists of a high pressure mercury lamp, collimating lens, shutter, parabolic concentrator, digital micro-mirror device and its control, lens and computer. Experimental investigations were carried out to research the UV light intensity distribution in the imaging plane, as well as to investigate the relationship of UV light intensity with the position in the imaging plane and gray-scale of pattern. Cast polyurethane resins (PUR) filled with modified bentonites were prepared in [2]. The effect of the amount and type of modified bentonites, as well as the type of used resin, on the mechanical and processing properties of composites containing 1.5–4.5 wt% of nano-filler were studied. The addition of modified bentonites to the polyurethane resin resulted in an increase of tensile strength by 40 % and Charpy impact resistance by 70 %. However, the decrease in Rockwell hardness by 18 % was also observed. The paper [3] presents the development of a 3D printer that shapes the parts layer by layer by depositing the material on a predefined position. The development is presented from the engineering point of view. The construction steps, the control and the actuator solutions are presented. The ABS plastic was analysed for its material properties. The 3D printer evolved from prototype to pre-production phase.

Polydimethylsiloxane is a translucent and biologically inert silicone material used in sealants, biomedical implants and micro-scale lab-on-a-chip devices [4]. Furthermore, in membrane technology, polydimethylsiloxane represents a material for separation barriers, because it has high permeability for various gases. The facile handling of two component formulations with a silicone base material, a catalyst and a small molecular weight crosslinker makes it widely applicable for soft-lithographic replication of two-dimensional device geometries, such as micro-fluidic chips or micro-contact stamps. Two major processes are currently being used to produce prototypes, namely machining and rapid prototyping. Machining is generally more accurate and precise, but it is difficult to produce objects with certain complicated features. In contrast, rapid prototyping can produce objects with complicated features, which allows materials to be used more efficiently. However, due to the uneven shrinkage and residual stresses within rapid prototyping products, their accuracy is usually uncertain. The study [5] attempts to integrate these two manufacturing processes and develop a hybrid rapid prototyping system in order to overcome the disadvantages associated with each process and to develop new applications. In this work, various three-dimensional (3D) scaffolds were produced via micro-stereolithography (m-SLA) and 3D printing (3DP) techniques. Work [6] demonstrates the advantages and disadvantages of these two different rapid prototyping methods for the production of bone scaffolds. Compared to 3DP, SLA provides the means to produce smaller features with a better dimensional resolution and accuracy. The permeability of these structures was evaluated experimentally and via numerical simulation utilizing a newly derived Kozeny-Carman based equation for intrinsic permeability. Papers [7, 8] are devoted to the rapid prototyping technology

application in some specific cases, with the accent on the mechanical properties of the obtained RP products.

This paper presents a comparative study of polymeric materials prepared by injection moulding (IM) as well as by rapid prototyping (RP). We have tested the strength and thermal material parameters, such as thermal conductivity, diffusivity and specific heat capacity.

2 Experimental Procedure

Two 3D printers, the Fortus 360mc and a uPrint SE Plus were used for the samples preparation. A PC and white colour was used to manufacture the tensile specimens with the Fortus 360mc 3D printer, using BASS as a supporting material and the other 3D printer, uPrint SE Plus, used P430 ABSplus as its material, in a blue coloured version with supporting material SR-30 SS to manufacture the tensile specimens.

The filaments of molten PC and ABSplus were applied at an angle of 45° and the formation of the next layer used a fibre perpendicular to the previous direction of the fibres, which is −45. As the name suggests, it is a copolymer consisting of three monomers, including C3H3N acrylonitrile, butadiene C4H5 and styrene C8H8. These three monomers form two distinct copolymeric phases, from which the resulting ABS is formed. The first phase is a harder styrene-butadiene copolymer and a softer second phase is represented by the styrene-acrylonitrile copolymer.

The typical features of ABS materials are that they are opaque, have good mechanical properties, toughness, excellent processability, chemical resistance and glossy hard surfaces, but they are inferior in resistance to weather and light conditions, when it is necessary for the higher resistance of material to add different types of stabilizers, pigments and absorbers. At the same time, we can increase the strength of the material by the addition of glass reinforcements.

The determination of specific heat capacity, diffusivity and thermal conductivity has been performed according to LCM in details described in [9].

The equipment consists of a thermally insulated chamber as described in [10]. The cover of the chamber has an opening for the pyro-electric sensor Raytek THERMALERT MID 02. The scheme of the measuring system is presented in Fig. 1.

The measured samples must have an area of about $(10 \times 10 \times 2)$ mm^3 and must be finely ground. Matt black spray-paint is applied on all sides of the samples in order to ensure they have the same emissivity. The sample is heated above room temperature in a thermostat. After the removal from a thermostat, the sample is quickly placed into the measuring chamber which will be closed. The time dependence of the temperature decay caused by sample cooling in predominantly convective and partly radiative mode is measured. The following software treatment allows determining the specific heat capacity, diffusivity and thermal conductivity from one cooling curve.
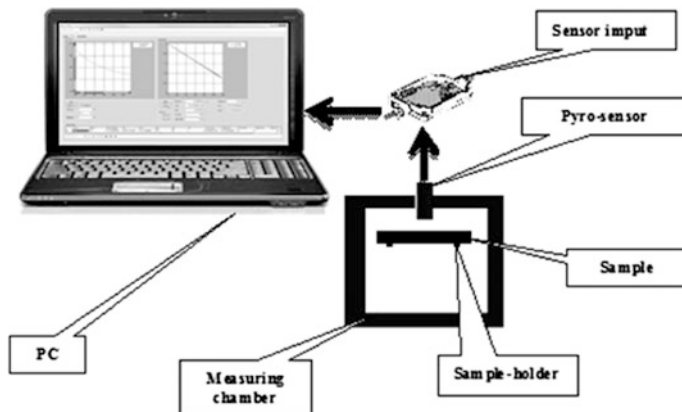
Fig. 1 Scheme of the apparatus

First of all, we have measured the same (RP) ABS sample by the *LCM* method and, subsequently, by using the *Netzsch* laser equipment *LFA* 427. The relative difference between both measurements of diffusivity was 4.1 %, which is a very decent result.

The results of the mechanical testing of both materials under investigation are presented in Figs. 2, 3 and Table 1. An analysis of mechanical properties of materials has shown that P430 ABSplus has about 44 % lower relative strength than in the case of the material prepared by injection moulding. A detailed inspection of the P430 ABSplus shows a slight increase in breaking strength. The worse mechanical results obtained for the polymer P430 ABSplus are probably due to a faster deposition of fibres and their worst sintering. We can see lots of air capsules here (Fig. 4). Furthermore, the material produced by PC RP technologies on the 3D printer Stratasys Fortus 360mc show a loss of strength of only ∼11 %, compared to the material prepared by injection, which is an excellent result. On the other hand, RP PC breaks near the yield point.

The measured results of the thermal properties of the RP—ABS material show that the specific heat capacity has increased by 8.7 %, the coefficient of diffusivity has decreased by 17.5 % and the thermal conductivity has decreased by 11 % compared to the material prepared by injection moulding, as seen in Table 2. When comparing the densities, the material P430 ABSplus has 12 % lower density than the material prepared by injection moulding. This could probably be a result of an excessive number of air cavities in the RP samples appearing during rapid and incomplete sintering in the printer (Fig. 4).

The measured results of the thermal properties of PC materials suggest that the specific heat capacity of the material prepared by RP has decreased by 7 %, the coefficient of thermal diffusivity has decreased by 7 %, and thermal conductivity has decreased by 9 %, compared to the material prepared by IM, as shown in Table 2. The comparison of densities shows their decrease for both kinds of the tested RP

Fig. 2 Comparative tensile tests for (IM) ABS (*solid line*) and (RP) P430 ABSplus (*dashed line*)
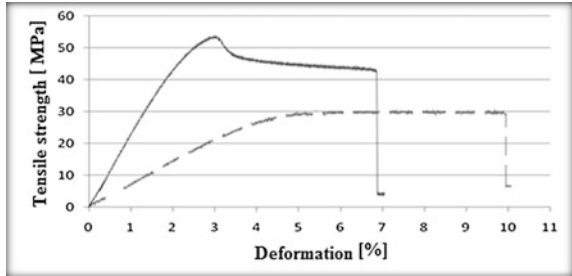
Fig. 3 Comparative tests of (IM) PC (*solid line*) and (RP) PC (*dashed line*)
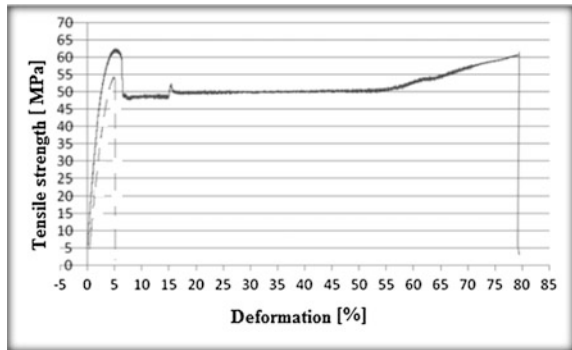
Table 1 Comparative data of the strength for IM and RP samples

Sample	Tensile strength (MPa)
P430 ABSplus (RP)	30.01 ± 0.57
ABS (IM)	53.64 ± 0.35
PC (RP)	55.14 ± 0.82
PC (IM)	62.32 ± 1.48

Fig. 4 Macro picture of RP ABS structure
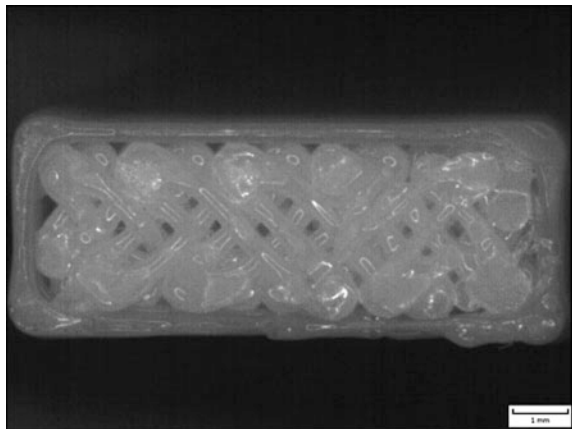
Table 2 Specific heat capacity, diffusivity, thermal conductivity and density for samples prepared by RP or IM

Sample	c_p (J kg^{-1} K^{-1})	a (mm^{-2} s^{-1})	k (W m^{-1} K^{-1})	ρ (kg m^{-3})
RP-P430 ABSplus	1516.11 ± 45.31	0.109 ± 0.004	0.154 ± 0.000	935.4
IM-ABS	1384.75 ± 37.80	0.132 ± 0.003	0.173 ± 0.01	1059.7
RP-PC	1271.3 ± 113.00	0.141 ± 0.005	0.196 ± 0.03	1104
IM-PC	1184.5 ± 73.91	0.152 ± 0.014	0.22 ± 0.01	1209.5

samples. Sensitivity limit of the used method (thermal properties measurements) is approximately 5 %, it means that measured results are close to this edge.

3   Conclusions

We can finally draw following conclusions:

- RP produces samples with worse mechanical parameters (strength).
- RP lowers the values of both thermal conductivity and diffusivity and increases specific heat capacity.
- RP lowers the sample density.

References

1. Xu, G.S., Hu, S.Q., Pan, H., et al.: Research of a novel integral stereolithography system for microstructures. In: 2nd International Conference on Intelligent Computation Technology and Automation Proceedings, pp. 880–883 (2009)
2. Oleksy, M., Oliwa, R., Zawila, B., et al.: Polyurethane compositions for rapid prototyping containing bentonites modified with silsesquioxanes. Polimery **57**, 463–469 (2012)
3. Valentan, B., Pogacar, D., Brajlih, T., et al.: Development of a 3D printer for thermoplastic modelling. Materiali in Tehnologije **46**, 589–594 (2012)
4. Kim, Y., Maxwell, A.D., Hall, T.L., et al.: Rapid prototyping fabrication of focused ultrasound transducers. IEEE Trans. Ultrason. Ferroelectr. Freq. Control **61**, 1559–1574 (2014)
5. Lee, W.C., Wei, C.C., Chung, S.C.: Development of a hybrid rapid prototyping system using low-cost fused deposition modeling and five-axis machining. J. Mater. Process. Technol. **214**, 2366–2374 (2014)
6. Lipowiecki, M., Ryvolova, M., Tottosi, A., et al.: Permeability of rapid prototyped artificial bone scaffold structures. J. Biomed. Mater. Res. Part A **102**, 4127–4135 (2014)
7. Lipina, J., Marek, J., Krys, V.: Screw connection and its load capacity in components made by rapid prototyping technology. In: IEEE 12th International Symposium on Applied Machine Intelligence and Informatics, pp. 155–159 (2014)

8. Lipina, J., Krys, V., Sedlák, J.: Shaped glued connection of two parts made by rapid prototyping technology. Appl. Mech. Mater. **555**, 541–548 (2014)
9. Koštial, P., Špička, I., Jančíková, Z., et al.: On experimental thermal analysis of solid materials. Meas. Sci. Rev. **14**, 317–322 (2014)
10. Koštial, P., Ružiak, I., Jančíková, Z.: Patent No 303269 CS (2012)

Characteristics of Cobalt Chromium by Neodymium-doped Yttrium Aluminium Garnet; Nd:Y$_3$Al$_5$O$_{12}$ (Nd:YAG) Laser Sintering Process

Khairu Kamarudin, Md. Saidin Wahab and Mohd. Hazelin Ramli

Abstract This work reports on the results of an experimental study examining the potential of the selective laser sintering process to produce a layer of specimen by using cobalt chromium molybdenum powder. A 300 W Neodymium-doped Yttrium Aluminium Garnet; Nd:Y$_3$Al$_5$O$_{12}$ (Nd:YAG) laser machine was used in this laser sintering experiment in order to fabricate the cobalt chromium molybdenum specimen. The effects of the laser parameters such as laser power, scan speed, scan spacing, and pulse rate were investigated in this research, in which, the research started by evaluating sintered samples on a single track and continued with multiple tracks which created a single layer sintered sample. The evaluation of specimen characteristics focused on surface morphology, relative density and dimensional accuracy. There was a set power range and pulse rate applied in the single track test which was 30–75 W of laser power and 100, 150, 200, 250 Hz of pulse rate. The lasers applied in the single layer test were 55, 65, 75 W of laser power, 1, 3, 5 mm/s of scan speed and 0.5, 0.6, 0.7 mm of scan spacing. The result of the laser sintering experiment showed that laser power was inversely proportional to the porosity of the specimen, but directly proportional to the area percentage error of the specimen. While, the scan speed parameter was directly proportional to the porosity of the specimen, but inversely proportional to the area percentage error of the specimen. The purpose of this research was to find successful laser parameter conditions and create a process map for the laser sintering of cobalt chromium molybdenum powder material.

K. Kamarudin (✉) · Md.S. Wahab
Faculty of Mechanical and Manufacturing Engineering, University Tun Hussein Onn
Malaysia (UTHM), Johor, Malaysia
e-mail: khairu@uthm.edu.my

Md.S. Wahab
e-mail: saidin@uthm.edu.my

Mohd.H. Ramli
Kolej Kemahiran Tinggi Mara, Pahang, Malaysia
e-mail: hazlen@kktmkuantan.edu.my

1 Introduction

The human body is made of different functional components which allows it to adapt to different environments and perform tasks and exercises. However, not every human will be born with a fully functional human body and certain parts will age and consequently possess lower functionality, which is why artificial implants have been developed in order to replace, support and enhance the body part which requires supports or replacement. Artificial medical implants are man-made devices, in contrast to a transplant, which is a transplanted biomedical tissue. Each artificial implant has its own unique size and its shape depends on the patients body structure. There are many different manufacturing techniques applied in the implant manufacturing sector in order to fabricate the artificial implant. Among the manufacturing techniques, rapid prototyping is the one of the most well-known techniques in implant manufacturing [4]. Selective laser sintering is one of the leading commercial rapid prototyping processes which can fabricate a fully functional model or component by using the laser on layer by layer process. In the SLS process, a three dimensional model can be fabricated where the laser will generate the heat necessary for the fusible powder to create a layer by layer model from the bottom to the top [2]. The production cost and processing time of the laser sintering process are lower and faster than other manufacturing techniques [5].

This paper will discuss the effects of the different laser parameter settings on the Cobalt Chromium powder material. The discussion will be focused on dimensional accuracy, density and surface roughness.

2 Literature Review

2.1 Selective Laser Sintering of Biomaterial in Artificial Implant

In Fwu-Hsing Liu and Ruey-Tsung Lee's study, a research about selective laser sintering of bio-metal scaffolds has been done. In the study, a non-commercial selective laser sintering machine with 120 W Nd:YAG laser was developed to fabricate bone scaffolds. The biomedical material for the experiment was prepared as a slurry type and the ingredients of this biomedical material slurry were titanium powder with an average particle size of 10 μm and silica soil as a binder. In the experiment, the layer thickness was set at 0.10 mm and the laser power was adjusted from 12 to 28 W. The titanium biomedical bone scaffold with hollow shell structure was constructed within 3 h which is shown in Fig. 1. The SLS process

parameters of this bone scaffold were 100 µm of thickness layer, 15 W of laser power, 100 mm/s of scan velocity, 0.1 mm of hatching space, 1.5 J/mm^2 of energy density, 0.2 mm of laser beam size, and 16 kHz laser frequency [3].

Figure 2 shows the SEM surface image of a biomedical titanium bone scaffold. From Fig. 2, the titanium metal particles were embedded in the sintered silica matrix to form a composite structure. Besides, micro-prosity was formed, which made the surface suitable for cell attachment and growth [3].

Laser parameter:

Layer thickness-100µm

Laser power-15W

Scan velocity-100mm/s

Hatching space-0.1mm

Energy density-1.5J/mm^2

Laser beam size-0.2mm
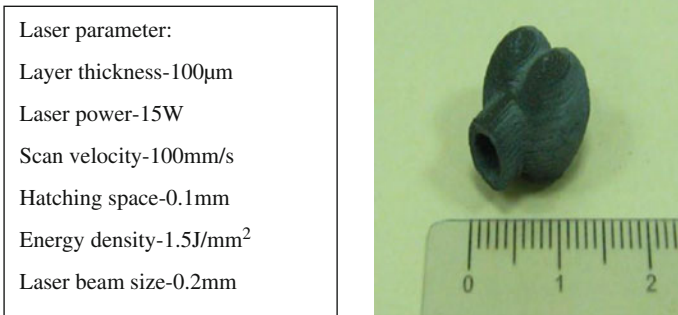
Fig. 1 Actual part of biomedical titanium bone scaffolds obtained by selective laser sintering [3]

Fig. 2 The SEM surface image of a biomedical titanium bone scaffolds after post treatment at **a** ambient and **b** 700 °C temperature [3]
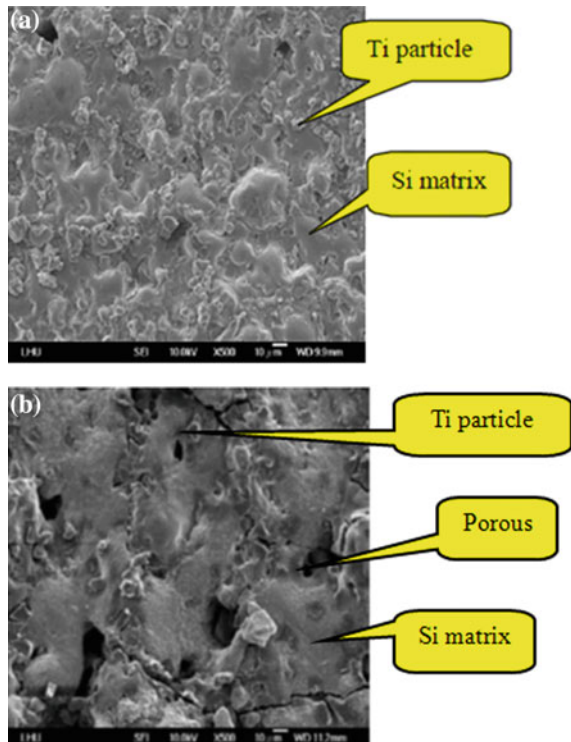
Fig. 3 Fractional density of laser sintered powders versus the ratio of laser power to scan rate. The layer thickness is 0.1 mm and the scan line spacing is 0.3 mm in the experiments [1]
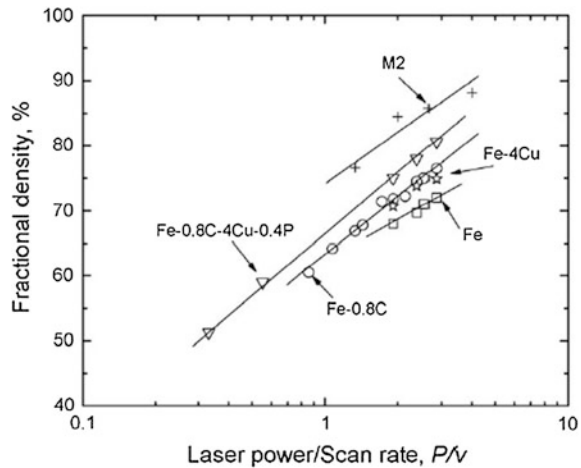
2.2   Effect of Laser Parameter in Laser Sintering Process

In a study by A. Simchi, the prepared powders were sintered by using the direct SLS layer by layer to create a rectangular test specimen with dimensions of 10 mm × 10 mm × 7 mm. The investigated laser sintering parameter conditions were laser power P = 100–215 W, scan rate v = 50–600 mms^{-1}, layer thickness w = 0.05–0.2 mm and scan line spacing h = 0.1–0.4 mm. An alternative scanning pattern from layer to layer with equal line spacing in the X and Y directions was used. The diameter (d) of the laser beam was 0.4 mm. Figure 3 one can see that the fractional density of the investigated laser power and the scan rate as a function of P/v. From Fig. 3 it show that the density is linearly proportion to the ratio of laser power to scan rate in semi-log scale [1].

3   Methodology

3.1   Laser Sintering Experiment Process

A 300 W of Nd:YAG laser machine was used for the laser sintering experiment. The laser sintering experiment was done on the cobalt chromium molybdenum powder (Co-Cr-Mo) material using the Nd:YAG laser and the powder bed had been prepared for fill up the Co-Cr-Mo powder material. The objective of the experiment is to figure out a range of laser parameters suitable for the Co-Cr-Mo powder material and fabricate a single layer of Co-Cr-Mo material specimen with different combinations of laser parameters. Thus, a number of tests and experiments were done with laser

sintering on Co-Cr-Mo to determine the range of the laser parameter which the laser sintering from a single track test and continued with the multiple track test which creating a single layer of the specimen. The laser parameters that were considered in this experiment were spot diameter, laser power and scan speed, and layer thickness.

3.2 Specimen Characteristics Analysis

All the specimen characteristics were analyzed in the aspect relative density, surface morphology and dimensional accuracy. Different types of apparatuses had been used for each analysis in order to obtain and measure the data.

3.3 Surface Morphology Analysis

Surface morphology analysis was done by using the tool maker measuring microscope. The model of the tool maker measuring microscope used for this research was the model MM-60/L3T. The measuring microscope had been equipped with a live camera and so that the picture of the surface of the specimen can be snapped. Each part of the specimen was photographed 15 times different focus depths, lengths and then all the photos of that particular part were combined to achieve a clean surface photo of the specimen. These data will be collected and analysed to compare the specimen that is being fabricated by using different combinations of laser parameters.

3.4 Relative Density

The relative density was calculated by using the relative density formula. The weight and the size (volume) of the specimen had been measured first, where the weight was measured by using the weighing and the volume was determined by using the profile projector to measure side lengths of the specimen and calculated by using the formula (1)

$$V = L * W * T \tag{1}$$

where, V is the volume, W is the width, L is the length and T is the thickness.

Once the weight and size had been measured, the density of the specimen is calculated by using formula 2.

$$\rho = \frac{m}{V}, \tag{2}$$

where, ρ is the density, m is mass, and V is the volume.

3.5   Dimensional Accuracy Analysis

A profile projector was used to analysis the dimensional accuracy of the specimen. The model of the profile projector was the vertical profile projector PJ-H3000f. A profile projector is a device that applies the principles of optics to the inspection of manufactured parts. In a profile projector, the magnified silhouette of the specimen is projected on the build in projection screen. On the screen the profile of the specimen is magnified for better ease of calculating the linear measurement.

4   Results and Discussions

The laser sintering observation starts from a single track specimen to a single layer specimen. At each stage different parameters will be considered during the laser sintering process in order to observe the effect of different parameters on the Co-Cr-Mo material in manufacturing the single track and single layer specimen. The parameters that were considered in this observation included power, scan speed, pulse rate and scan spacing which will bring some effects to the surface morphology, density, and dimensional accuracy of the specimen. Thus, the purpose of the work presented geared towards an understanding of the effect of different parameters in construction, a single layer of specimen by using the selective laser sintering process on the Co-Cr-Mo material.

4.1   Effect of Laser Parameter on Single Track Laser Sintering of Cobalt Chromium Molybdenum Powder

Figure 4 shows the process map of the single track test. In the process map there are 3 different areas that are distinguished according to the growth type of the single track specimen. Growth type I is the specimen that melts with breakage, growth type II is the specimen melting with good surface smoothness but poor integrity, while the growth type III is the specimen construct in continuous melting which means that the specimen has good integrity. In Fig. 4, the area of growth I is located at below 45 W, the area of the growth II is located at above 65 W, and the area of the growth III is located at 45–65 W.

The effect of the laser power in the laser sintering process has been clearly shown in this single track test. From the results of the single track test, it was shown that when the laser power increases, the integrity and the surface smoothness of the specimen will become better, but when the laser power had reached a certain high power level the integrity of the specimen start to become poor. Thus, the outcome of the single track test has shown that the material had its own adequate laser power range applied in the laser sintering process which can get a good integrity and
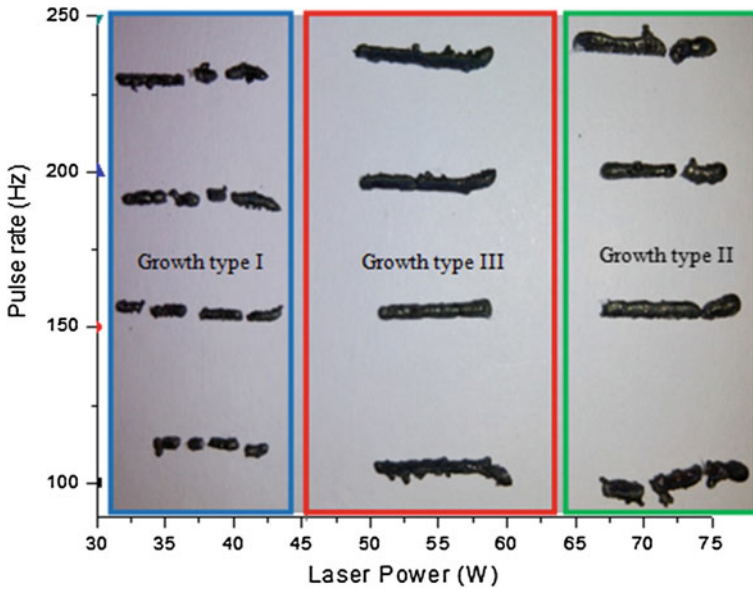
Fig. 4 Process map for single track test

surface smoothness and the adequate laser power range for the Co-Cr-Mo material is 45 W until 75 W.

4.2 Effect of Laser Parameter on Single Layer Laser Sintering of Cobalt Chromium Molybdenum Powder

The laser power ranges that were applied in this single layer test are 55, 65 and 75 W and the pulse rate of the laser will be set at 100 Hz due to the accuracy and the stability of the laser power.

4.2.1 Qualitative Observation

In the single layer specimen, there are 2 types of qualitative classification of the sintered part that had been distinguished which are listed as follows:

(a) Full melts with poor layer surface quality (see Fig. 5b): a focused, moving back and forward Gaussian beam pounding on the surface of the powder layer cause a full melting over delimited powder surface. The outcome was a sintered layer with a surface which is characterized by a poor bonding system between the track. High porosity could be observed within a layer in this category.
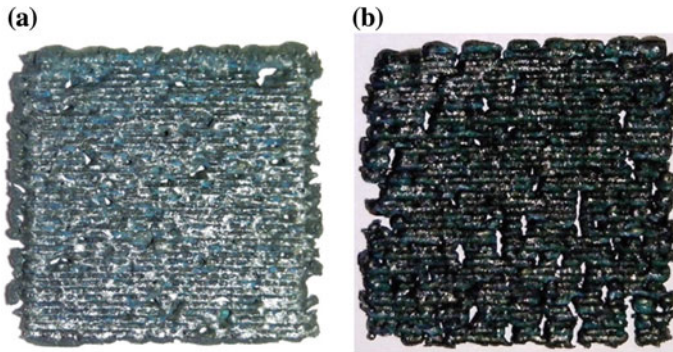
Fig. 5 Single layer specimen fabricated at 75 W laser power. **a** Good quality (0.5 mm, 60 mm/min). **b** Poor quality (0.5 mm, 300 mm/min)

(b) Full melting with good layer surface quality (see Fig. 5a): a focused, moving back and forward Gaussian beam pounding on the surface of the powder layer cause a full melting over delimited powder surface. The outcome was a sintered layer with a surface which is characterized by good melting and bonding system between track. A low porosity was observed within a layer in this category.

4.2.2 Surface Morphology of the Single Layer Specimen

The occurrence of rough and smooth surfaces has been plotted at the power/scan speed versus scan spacing map, in Fig. 6. The figures showed that most of the good surface morphology specimens were fabricated at low scan speeds which was 60 mm/min. At a low scanning speeds, the surface of the specimen had less porosity than the specimen fabricated at a high scanning speed. Considering the aspect of scan spacing, the specimen that was constructed at a low scan spacing consists of better surface smoothness. While for the specimen constructed at a high scanning speed, the shape of each track is clearly seen at the surface of the single layer specimen. Further increasing the laser power also enhances the surface smoothness of the single layer specimen. At a high laser power, the trace of the track line on the surface of the specimen was not obvious as the specimen was fabricated at low laser power. Therefore, the best surface smoothness single layer specimen was fabricated at 75 W of laser power, 60 mm/min of scan speed, and 0.7 mm of scan spacing.

4.2.3 Relative Density of the Single Layer Specimen

From Fig. 7 it can be seen that the relative density of the single layer specimen was not in a linear line and not consistent when the ratio of laser power to scan speed was increased. This is because at each different single layer specimen, there was
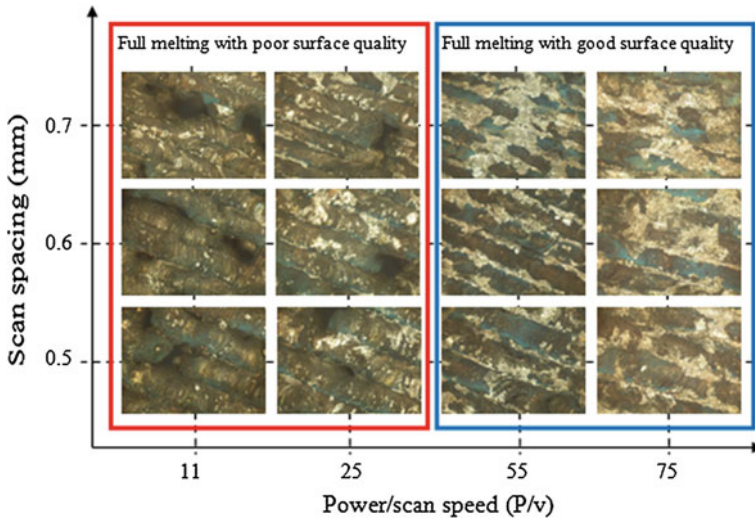
Fig. 6 Power/Scan speed versus scan spacing process map for single layer test
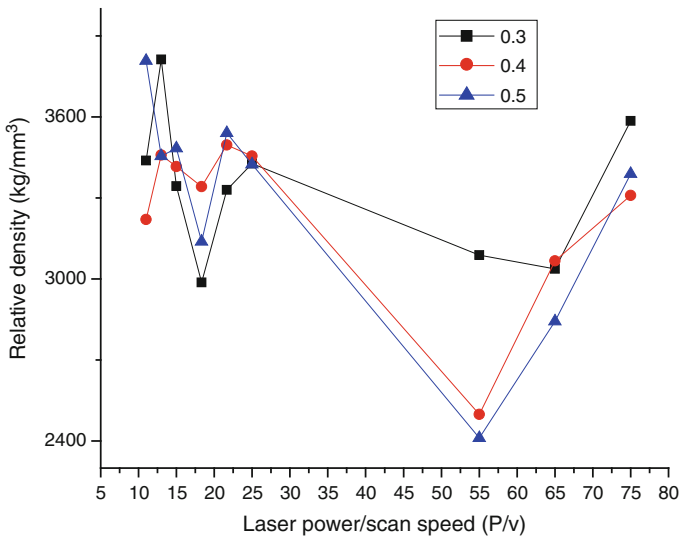
Fig. 7 Relative density of single layer specimen at 0.5, 0.6, 0.7 mm scan spacing versus the ratio of laser power to scan speed

some powder stick at the specimen and influenced the weight, which influences the relative density of the specimen. However, from Fig. 5 one case see that the average relative density of the specimen that fabricated at the scan spacing 0.7 mm are higher than the specimen that was fabricated at a scan spacing of 0.5 and 0.6 mm which the scan spacing is directly proportional to the density.

4.2.4 Dimensional Accuracy Analysis

There are 2 main laser parameters that will affect the dimensional accuracy of the specimen which are the laser power and scan speed. Figure 8 shows the relationship between the scan speed and laser power with the area percentage error of the specimen. It is shown when the scan speed increases that the percentage error will be decreased, which the scan speed is inversely proportional to the area percentage error. When the laser power increases, the area percentage error also increases, which the laser power is directly proportional to the area percentage error of the specimen.

Fig. 8 Percentage error of the single layer specimen at 0.5, 0.6, 0.7 mm scan spacing versus scan speed, laser power
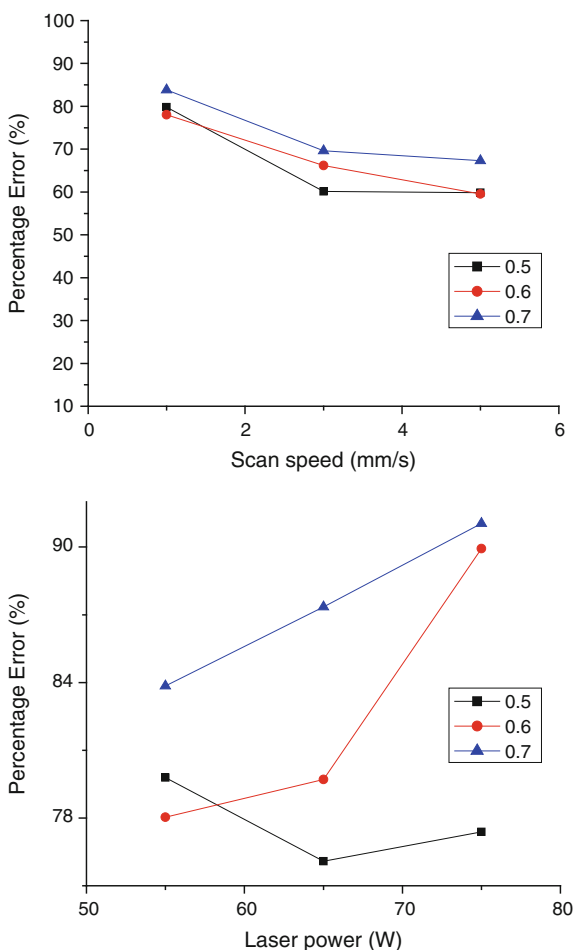
5   Conclusion

The effect of the laser power, scan speed, scan spacing and pulse rate laser parameter on the specimens' characteristics had been studied. Based on the result, the following conclusion can be drawn:

(a) The optimum laser parameters to fabricate a single layer specimen were 75 W laser power, 0.7 mm scan spacing, and 1 mm/s scan speed.

(b) The effect of the laser parameter was related to the energy density that assimilated the powder material especially the laser power parameter and scan speed parameter.

(c) The energy absorptivity changes significantly with scan speed and laser power, whereas the change in absorptivity had affected the melt pool size.

(d) At low laser powers and high scan speeds the surface smoothness and the integrity of the specimen is poor, but the area percentage error of the specimen is low.

(e) At higher laser powers and low scan speeds the surface smoothness and the integrity of the specimen is good, but the area percentage error of the specimen is high

(f) The best ranges of scan spacing to fabricate good surface smoothness are 0.3, 0.4 and 0.5 mm which is 60–70 % overlapping region of the width of the track

References

1. Agarwala, M., Bourell, D., Beaman, J., Marcus, H., Barlow, J.: Direct selective laser sintering of metals. Rapid Prototyping J. **1**(1), 26–36 (1995)
2. Dewidar, M.M., Lim, J.K., Dalgarno, K.: A comparison between direct and indirect laser sintering of metals. J. Mater. Sci. Technol. **24**(2), 227–232 (2008)
3. Liu, F.H., Lee, R.T., Lin, W.H., Liao, Y.S.: Selective laser sintering of bio-metal scaffold. Procedia CIRP **5**, 83–87 (2013)
4. Raos, P., Stoić, A.: Rapid prototyping and rapid tooling. In: An approach in Manufacturing of Medical Implant, pp. 683–686 (2005)
5. Sponaugle, C.: History of Haynes International, Inc. (2006)

Evaluation of Biomimetic Coatings on Femtosecond Laser Treated Alumina and Alumina-Zirconia Composite Surfaces

A.A. Aguiar, N.B. de Lima, F.J.C. Braga, W. Rossi, A.A. Couto and R. Baldan

Abstract The effect of texturing Al_2O_3 and Al_2O_3/ZrO_2 surfaces using femtosecond laser has been evaluated in terms of the roughness, wettability and microstructure of the substrate to increase growth efficiency and adhesion of hydroxyapatite. Femtosecond laser treatment of these materials causes phase transformation from alpha-alumina to gamma-alumina. Heat effects during femtosecond laser treatment causes the grains to be in the nanometer scale. Without heat effects, the grains are in the micrometer scale. The use of femtosecond laser permits control of the surface roughness of the alumina specimens. The higher the femtosecond laser energy, the higher is the wettability of the specimen and the total surface energy. Specimens with laser textured surfaces upon immersion in 1.5 SBF for 6 and 15 days revealed apatite layers well bonded to the substrate and without detachment. The adhesion of apatite to surfaces of specimens that were not textured with femtosecond laser was inadequate.

Keywords Al_2O_3 · ZrO_2 · Femtosecond laser · Hydroxyapatite

A.A. Aguiar · N.B. de Lima · F.J.C. Braga · W. Rossi · A.A. Couto (✉)
Instituto de Pesquisas Energéticas e Nucleares (IPEN-CNEN/SP),
05508-900 São Paulo, Brazil
e-mail: acouto@ipen.br

A.A. Aguiar
e-mail: amanda.abati.aguiar@gmail.com

N.B. de Lima
e-mail: nblima@ipen.br

F.J.C. Braga
e-mail: fjcbraga@ipen.br

W. Rossi
e-mail: wderossi@ipen.br

A.A. Couto
Universidade Presbiteriana Mackenzie (UPM), São Paulo, Brazil

R. Baldan
Universidade Estadual Paulista (UNESP), São Paulo, Brazil
e-mail: renatobaldan@gmail.com

1   Introduction

The bioactivity of a material can be evaluated from formation of apatite on its surface in simulated body fluid (SBF) solution. Hence, various studies have been done on the growth and adhesion of apatite on various candidate metallic, polymeric and ceramic materials for implants [1]. The biomimetic coating has mechanical properties that are compatible with bone structure and induces deposition of apatite on implant surfaces, resulting in rapid bone growth [2]. Another great advantage of this method resides in incorporating biologically active molecules, which regulates the cure process of a fracture with rapid bone regeneration [3, 4].

Some studies evaluated the effect of prior surface treatment of these materials on growth and adherence of apatite [5–11]. The main reason to use a prior surface activation process is to assure an efficient interfacial joint between the bio-inert material and the bioactive component to be deposited. Integration between the surface of the ceramic that is activated first and the deposited film is optimized by developing reactive species on the surface that have an affinity for the calcium and phosphorous ions in the simulated body fluid solution (SBF). The nature of the bond in this case is not just mechanical, but it also promotes improved interfacial strength. There is evidence that by adopting this procedure there are close interactions between the film and the substrate. Otherwise, the coatings obtained could behave as a brittle ceramic and fail when mechanically loaded [7].

The surface topography of bone implants influences cell reactions. Brunette [12] and Brunette et al. [13] showed the marked effect of dental implant surface topography on the orientation and migration of fibroblasts, epithelia cells and osteoblasts. Besides this, a general relationship has come about which indicates that smooth surfaces promote the formation of a fibrous tissue capsule around the implant, whereas a rough surface promotes integration with bone that is very close [14, 15]. Thus, there is considerable evidence that adhesion, migration and adsorption functions of the cells are influenced by the topography of the substrates. It is known that the formation of the mineralized matrix by osteoblasts is also influenced by the physical properties of the substrate [16].

The main surface properties that influence cell adhesion are topography and chemical reactivity. The topography of a surface markedly affects the macroscopic behavior of the material [17]. At the cell level, the biological response, its orientation, migration and cell production are directly influenced by surface topography [18]. There is evidence that adequate surface roughness at the nanometer and micrometer scale can result in successful bone-integration of implants [19]. The higher the roughness, lower is the contact angle and more wetted is the surface. The reduction in contact angle is due to the increased surface area of a rougher surface. This facilitates water to remain in the pores, contributes towards more efficient hydration, offers a more stable water film and increases the hydrophilic nature of the surface. Thus wettability of implants could become a determining factor in the protein adsorption of and consequently, on cell adhesion [20, 21]. For example, hydrophobic surfaces presumably decelerate primary interactions with aqueous

bio-systems. Thus, biomaterial surfaces with moderate hydrophilic properties improve cell growth and increase biocompatibility [22].

Few studies on laser surface modification have focused on texturing with CO_2 lasers. Texturing produces surface modifications, altering the properties of the material in a deleterious way, such as embrittlement and phase transformation. The crystalline structure affects wettability, which is an important parameter for cell adhesion. Changes in the microstructure and oxygen content on the surface have greater influence on wettability than roughness [23, 24]. It is worth mentioning that these authors used continuous CO_2 laser, which causes surface melting when the power density is more than 1.6 kW/cm^2, and does not permit the formation of very rough surfaces. At this power density, the surface roughness was 0.717 μm. By varying the power density, the following structural changes take place at the crystalline level: crystalline reordering (0.6 kW/cm^2), change in crystal structure (0.9 kW/cm^2), cell formation (1.6 kW/cm^2), uniform cell structure (1.9 kW/cm^2) and corals and dendrites (2.5 kW/cm^2). The extent to which these surface modifications alter functional groups and the fracture toughness of the material has not been evaluated.

2 Materials and Methods

Co-precipitation of aluminum, zirconium and yttrium hydroxides was done with ammonium hydroxide and the concentration of the oxides in the starting solution was maintained at 35 g L^{-1}. The precipitates were then rinsed twice: with water to remove the chloride ions (test carried out with $AgNO_3$) and with ethanol to eliminate the strong agglomerates. To achieve the latter, an azeotropic distillation treatment was also carried out using butanol as the organic solvent. After drying at 80 °C for 24 h the powders were calcined at 800 °C for 1 h and then ground in a ball mill with ethanol for 17 h. The powders were mixed in a rotating-evaporator to achieve homogeneity. Drying of the ground powders was done in a furnace at 80 °C for 24 h and finally the powders were de-aggregated in an agate mortar.

Ceramic powders of pure alumina (100A) and 85 % alumina with 15 % yttria stabilized zirconia (85A15TZP) were compacted axially using 76.4 MPa of compaction pressure in a 10 mm cylindrical die. Sintering was done in air in a box type electric furnace at 1620 °C for 3 h. The specimens were given finishing treatments that consisted of polishing with 15, 6 and 1 μm diamond paste. Biomimetic coating of the sintered specimens was done by immersion in a synthetic solution with an ionic composition similar to human blood plasma "simulated body fluid" (SBF), but with a 1.5 M concentration. The ion composition of the 1.5 M SBF solution is given in Table 1.

The solution was prepared by dissolving analytic grade NaCl, KCl, K_2HPO_4, $CaCl_2 \cdot 2H_2O$, $MgCl_2 \cdot 6H_2O$, $NaHCO_3$ and Na_2SO_4 in distilled and deionized water. The pH of all the solutions was adjusted to 7.25 at 37 °C with 0.1 M HCl and 0.05 M tris (hydroxymethyl) aminomethane (($CH_2OH)_3CNH_2$). The hydroxyapatite

Table 1 Ionic concentration of solution that was used (mmol dm^{-3})

	Na$^+$	K$^+$	Ca^{2+}	Mg^{2+}	HCO$_3{}^{2-}$	Cl$^-$	HPO$_4{}^{2-}$	SO$_4{}^{2-}$
1.5 SBF	213.0	7.5	3.8	2.3	6.3	223.0	1.5	0.75
Human plasma	142.0	5.0	2.5	1.5	27.0	103.0	1.0	0.5

Table 2 Energy (E), flux (F) and number of pulses (Np) used to texture the surface

	E (µJ)	F (J cm^{-2})	Np	Condition
100A	20	2.5	1	No heat effect
	32	4	32	Heat effect
85A15TZP	7	2.3	1	No heat effect
	13	4.3	1024	Heat effect

nucleation tests were carried out by immersion of the cylindrical ceramic specimens in 1.5 SBF. Some precautions were taken: (a) prior ultrasonic cleaning of the ceramics with acetone and drying in a furnace; (b) volume of SBF solution was 10 times more than the area of the specimen; (c) the SBF solution was renewed every 3 days and (d) tests were carried out in a bacteriological-culture at 36.5–37 °C.

Nucleation of hydroxyapatite and microstructural stability of the alumina and zirconia based substrates were evaluated as a function of the following process variables:

– Prior treatment of the surface with femtosecond laser to increase surface roughness;
– Immersion time (6 and 15 days) in 1.5 M SBF solution of substrates with smooth surfaces (without treatment) and substrates pre-treated with femtosecond laser.

Table 2 shows the femtosecond laser treatment conditions for each type of specimen, 100 % alumina (100A) and 85 % alumina +15 % zirconia (85A15TZP). After immersion, the specimens were rinsed with distilled water and dried in a furnace at 37 °C for 24 h for further characterization.

The laser treated specimens were studied using X-ray diffractometry, scanning electron microscopy, and diffuse reflectance infrared spectroscopy (DRIFT). The wetting behavior was determined by measuring the contact angle. After testing the biomimetic coating, 'micro-scratch' tests were carried out and the adhesion of the film formed after coating was determined by examining the microstructure using a SEM. Besides the conditions described above, femtosecond laser treatment at higher power (E = 109 µJ; Np = 512) was given to alumina specimens to amplify the effect of phase transformation that occurs on the surface.

3   Results and Discussion

Figure 1 shows micrographs of laser treated alumina (100A) specimens and reveals the formation of equidistant trails in those treated with high energy laser (with heat effect). The specimens treated with low energy lasers (without heat effect) revealed surface damage but without formation of trails, and the particle size was in the micrometer range.

The X-ray diffraction spectra are shown in Figs. 2, 3 and 4. These spectra revealed the following phases: α-Al_2O_3 and γ-Al_2O_3 in the alumina (100A)
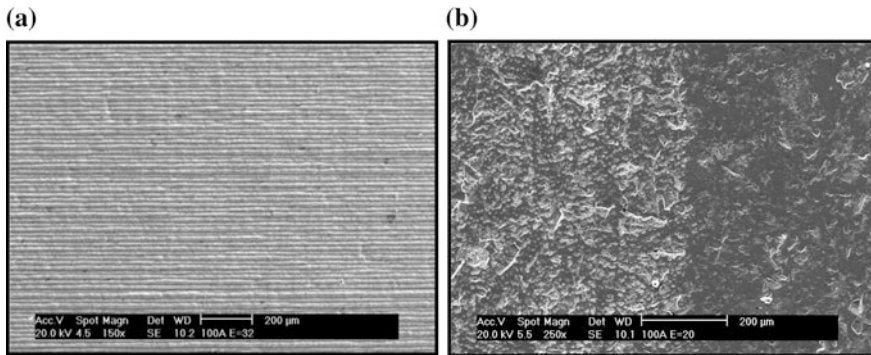
Fig. 1 Micrograph of alumina (100A) specimen surface treated with femtosecond laser. **a** E = 32 μJ; Np = 32; **b** E = 20 μJ; Np = 1
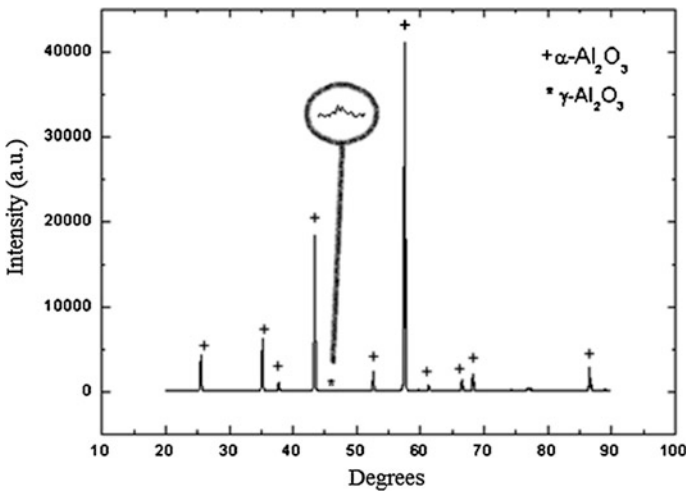
Fig. 2 Diffraction spectrum of alumina (100A) specimen textured with femtosecond laser under the conditions E = 20 μJ; Np = 1
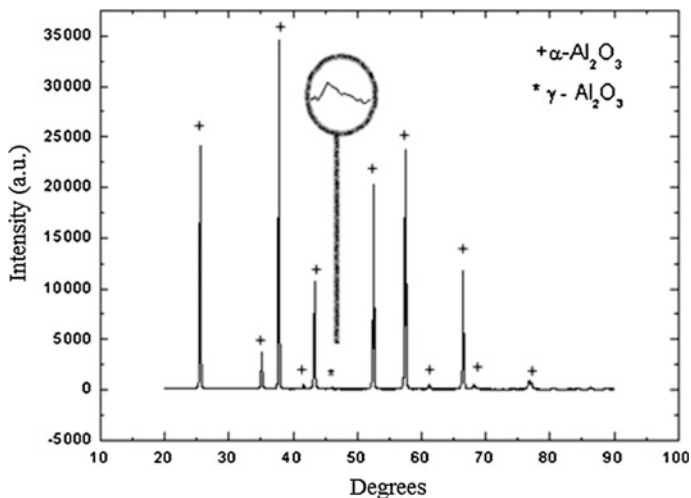
Fig. 3 Diffraction spectrum of alumina (100A) specimen textured with femtosecond laser under the conditions E = 32 μJ; Np = 32
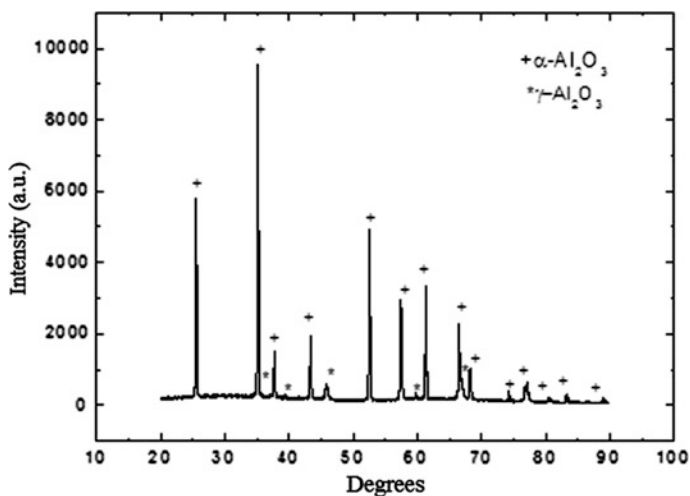
Fig. 4 Diffraction spectrum of alumina (100A) specimen textured with femtosecond laser under the conditions E = 109 μJ; Np = 512

specimens laser treated under conditions where E = 20 μJ; Np = 1 and E = 32 μJ; Np = 32. This indicates that in alumina (100A) specimens laser treated under conditions where E = 20 μJ; Np = 1; E = 32 μJ; Np = 32 and E = 109 μJ; Np = 512, partial transition of some alpha alumina to crystalline gamma alumina takes place. Figure 4 clearly shows that gamma alumina forms with peaks at the

angles 37.64°; 39.49°; 45.88°; 60.86° and 67.05° after irradiation with femtosecond laser. It can be observed that with increasing energy and number of pulses the amount of gamma phase alumina increases. This fact is important, since the transition of gamma alumina to alpha alumina is not thermally reversible and indicates that the laser texturing process provokes changes in charge equilibrium on the alpha alumina surface. The wettability results shown in Table 3 reveal that the contact angle is directly dependent on the laser energy used to treat the surface. It is worth mentioning that the specimens stop exhibiting hydrophobic behavior. That is, i.e. the value of the contact angle with water on alumina specimens that was not treated with laser was 93.47 (hydrophobic) and it shifted to 32.25 (hydrophilic) when it was treated with high-energy laser. Another factor that directly influences the contact angle is roughness (see Table 3). Higher the roughness, lower is the contact angle and the more wetted becomes the surface. The reduction in contact angle is due to increase in surface area of the specimen with higher roughness. This facilitates water to remain in the pores and contributes to significantly more efficient hydration. This results in a more stable film of water and an increase in the hydrophilic nature of the surface [20, 21]. The roughness increases with the increasing of the energy and the number of pulses.

According to Fig. 5, the comparison of the DRIFT of untreated and laser treated alumina (100A) and alumina-zirconia (85A15TZP) specimens reveals that neither showed a broad band at 3510 cm^{-1}, which is characteristic of OH groups on the surface of hydrated gamma alumina and without the presence of Lewis acid sites. Hence, the femtosecond laser treated specimens are dehydrated and therefore with higher surface energy, as per the contact angle measurement results. The broad bands around 800 cm^{-1} are characteristic of γ alumina. The bands located at 450, 500 and 630 cm^{-1} are characteristic of α alumina and the bands at 500 cm^{-1} are characteristic of tetragonal zirconia. It should be noted that after the laser treatment the γ alumina phase appears and does not induce the OH band.

An evaluation of the wettability results in Table 3 shows that the contact angle depends directly on the laser energy used to treat the surface. This phenomenon occurs both for pure alumina and the composite specimens. It is worth stating that the specimens are no longer hydrophobic as the contact angle value of water on the alumina specimens that were not laser treated shifted from 93.47° (hydrophobic) to 32.25° (hydrophilic) upon treatment with high energy laser. A large variation in the contact angle also occurs for the composite specimens, from 81.8° to 37.34°. In these cases laser treatment increases the hydrophilic nature of the materials.

Between the materials that were not laser treated, alumina presents a contact angle value higher than that of the composite, corroborating data presented by Kokubo and Takadama [25]. These authors stated that the radical Zr-OH is a more effective surface functional group to capture calcium and phosphorous present in SBF. The contact angle values of alumina and the composite are quite similar when treated with high energy laser, even though the energy used to treat the composite is lower. Since the initial contact angle value is lower (81.8° for the untreated composite and 93.47° for the untreated alumina) it can be considered that the alumina surface has been modified to a greater extent to have the same wettability values as

Table 3 Contact angle of the liquids, polar component, disperse component, total surface energy and surface roughness of untreated and femtosecond laser treated specimen 100A

Specimens	Contact angle (θ)			Polar component γ_s^P (mN/m)	Disperse component γ_s^D (mN/m)	Total surface energy γ_s^T (mN/m)	Ra (μm)
	Water	Ethylene-glicol	SBF				
85A15TZP	81.8 ± 3.82	53.96 ± 2.30	71.37 ± 3.70	4.5	32	36.5	0.06
85A15TZPE7Np1	52.65 ± 5.86	39.35 ± 5.13	51.66 ± 2.38	39.48	7.57	47.05	0.33
85A15TZPE13Np1024	37.34 ± 3.94	37.47 ± 3.09	41.9 ± 2.5	67.09	1.75	68.85	1.92
100A	93.47 ± 3.80	63.85 ± 1.70	81.95 ± 12.0	5.41	20.13	25.54	0.33
100AE20Np1	60.28 ± 1.47	57.10 ± 4.21	61.96 ± 8.86	43.18	2.54	45.72	0.53
100AE32Np32	32.25 ± 2.08	30.64 ± 9.97	39.63 ± 9.50	70.22	2.33	72.55	1.43
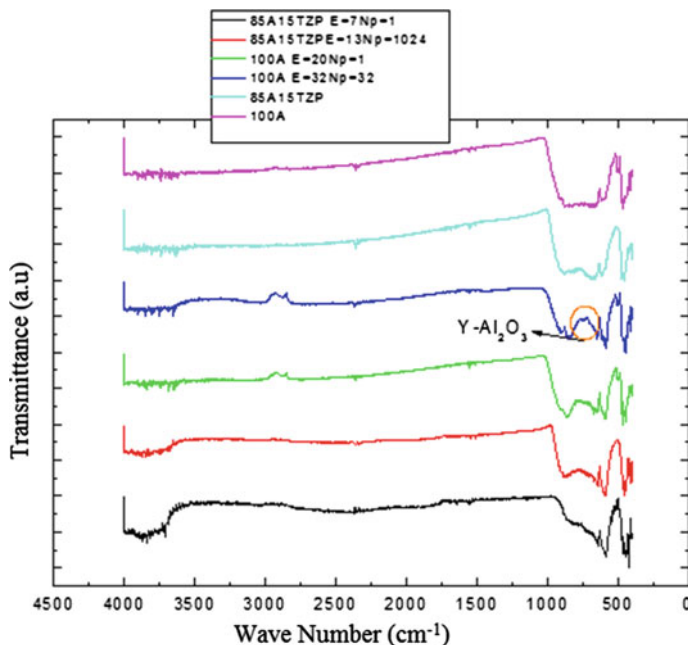
Fig. 5 DRIFT of the alumina and alumina-zirconia specimens before and after femtosecond laser treatment

the composite, and by consequence, utilizes higher laser energy. This modification of the alumina surface can be related to formation of the gamma phase, which is less stable than the alpha alumina phase, and therefore has more active radicals, thus increasing the reactivity of the Al-OH groups [26].

Comparison of the surface roughness values alongside the contact angle, reveals that improvement in wettability was not exclusively a roughness dependent phenomenon. In the case of the 85 % alumina and 15 % zirconia (85A15TZP) specimen with 0.06 μm surface roughness, the contact angle was 81.8°, whereas for the 100A specimen with 0.33 μm surface roughness the contact angle was 93.47°. By considering roughness only, one would expect the contact angle of the alumina (100A) specimen without laser treatment to be lower. Further, we observe that even though the alumina and the composites have the same roughness, their contact angles are quite different, that is 93.47° for the 100A specimen without laser treatment and 52.65° for the 85A15TZP specimen laser treated under the conditions E = 7 μJ and Np = 1. This could be attributed to the Zr-OH functional group being more effective than the Al-OH group. This explanation is however not valid when the surface roughness of the 100A specimen laser treated under conditions E = 32 μJ and Np = 32 is 1.43 μm and the contact angle of 32.25° is lower than the contact angle of the 85A15TZP specimen laser treated under the conditions E = 13 μJ and Np = 1024 (with contact angle of 37.34° and surface roughness of 1.92 μm).

This shows that laser treatment increases markedly the wettability of the 100A specimen, and this is dependent not just on increase in roughness.

As mentioned earlier, laser treatment induces transformation of α-alumina to γ-alumina which is made up of AlO_6 octahedrons and AlO_4 tetrahedrons and the most stable exposed surfaces of γ-alumina are the planes (100), (110) and (111). Theoretical calculations have shown that on the (100) surface, only five Al coordinates exist and that the surface relaxation does not change drastically the local geometry. On the (110) surface, there are Al coordinates which originate from octahedral and tetrahedral Al, where surface relaxation introduces strong geometric modifications leading to the formation of pseudo-regular tetrahedrons and planar configurations of AlO_3. Different from the (100) and (110) surfaces, the (111) surface is made up of alternating stacks of oxygen and Al atoms and is not stable when totally dehydrated, but totally stable when hydrated. Depending on the temperature and water vapor pressure, the surfaces can have a variety of OH surface groups, but when completely hydrated all the coordinated surfaces are occupied, that is the six coordinates are occupied by Al atoms. This signifies that the Lewis acid sites should not exist on a completely hydrated alumina surface [26].

It can also be seen from Table 3 that as the energy and the number of pulses increase, for both alumina and alumina-zirconia, the total surface energy increases. This signifies that laser treatment increased the surface energy in the materials. This energy quantifies the intermolecular bond ruptures that occur when the surface is created. The higher the surface energy, greater is the tendency to adsorb atoms and molecules on the surface of the material. This happens due to the fact that the higher the energy per unit of the ceramic surface area is, the greater the possibility for surface reactions to arise will be [27].

A significant increase in the polar component values of the materials, both for alumina and the composite, can be observed with an increase in femtosecond laser energy and the number of pulses. Considering that the polar component has dipole-dipole bonds, it can be said that the interaction of laser with the surface of the material promotes an increase in the quantity of polar molecules, probably Al-OH and Zr-OH. Contrary to the values of polar components of the materials, the values of dispersive components of the ceramics decrease significantly with an increase in femtosecond laser energy and the number of pulses. The dispersive component has only momentary dipole bonds, that is, bonds between non-polar molecules (similar electronegativity) [27]. Since there is a higher amount of polar molecules when the materials are laser treated, a reduction in non-polar molecules can be expected. This means that the interaction of laser with the material promotes stronger bonding between the molecules, making the surfaces more reactive. The values obtained for the polar and disperse components of SBF (γ_{SBF}^p and γ_{SBF}^d) were 38.45 and 28.7 mN/M respectively. The polar and disperse components of water and ethylene were: $\gamma_{H_2O}^p = 51$ mN/m and $\gamma_{H_2O}^d = 21.8$ mN/m and $\gamma_{e\text{-glicol}}^p = 19$ mN/m and $\gamma_{e\text{-glicol}}^d = 29$ mN/m respectively [28].

Figures 6 and 7 show small globules of apatite, smaller than 3 µm in diameter, dispersed over a layer of Ca and P on the alumina and composite specimen surfaces.
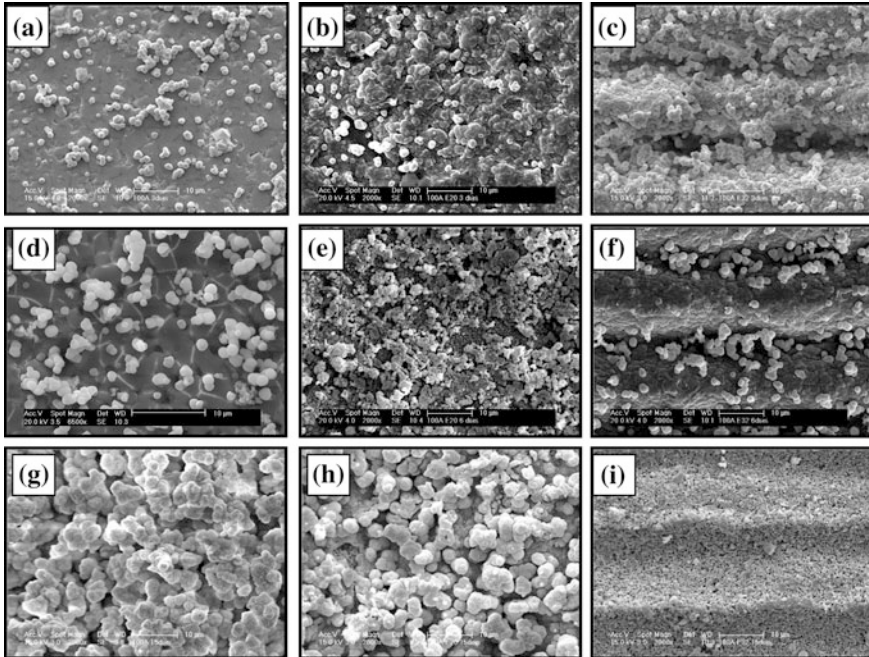
Fig. 6 Micrographs of alumina (100A) specimens untreated and treated superficially with femtosecond laser and immersed in 1.5 SBF for 3, 6 and 15 days. **a** 100A (3 days); **b** 100A E = 20 μJ; Np = 1 (3 days); **c** 100A E = 32 μJ; Np = 32 (3 days); **d** 100A (6 days); **e** 100A E = 20 μJ; Np = 1 (6 days); **f** 100A E = 32 μJ; Np = 32 (6 days); **g** 100A (15 days); **h** 100A E = 20 μJ; Np = 1 (15 days) and **i** 100A E = 32 μJ; Np = 32 (15 days)

It is worth mentioning that the layer of apatite formed is related to the topography of the samples. After 15 days of immersion in 1.5 SBF, the surfaces of the untreated and the laser treated specimens, whether alumina or the composite reveal a high density of apatite. The morphology of the apatite globules on the laser treated specimens is different from that on the specimens that were not laser treated. The apatite globules on the untreated specimen surfaces are larger and more rounded, while that on the laser treated surfaces is smaller and have a higher tendency to coalescence.

Figure 8 shows a micrograph of the micro-scratch tested alumina (100A) specimen that was not treated with femtosecond laser and then immersed for 6 days in 1.5 SBF. Each line was subject to a pre-load of 0.5 N, and the load was increased at a constant rate along a stretch of 2 mm until it reached the following values 1, 3, 5, 10, 15, 20 and 30 N. The red line indicates the presence of aluminum and the blue line the presence of calcium. These two elements were selected for analysis as there are no overlap of other rays and the presence of apatite or the matrix could be perfectly mapped. It can be seen that at the points where the analysis line did not intercept the indentation, there was a lower concentration of aluminum and more
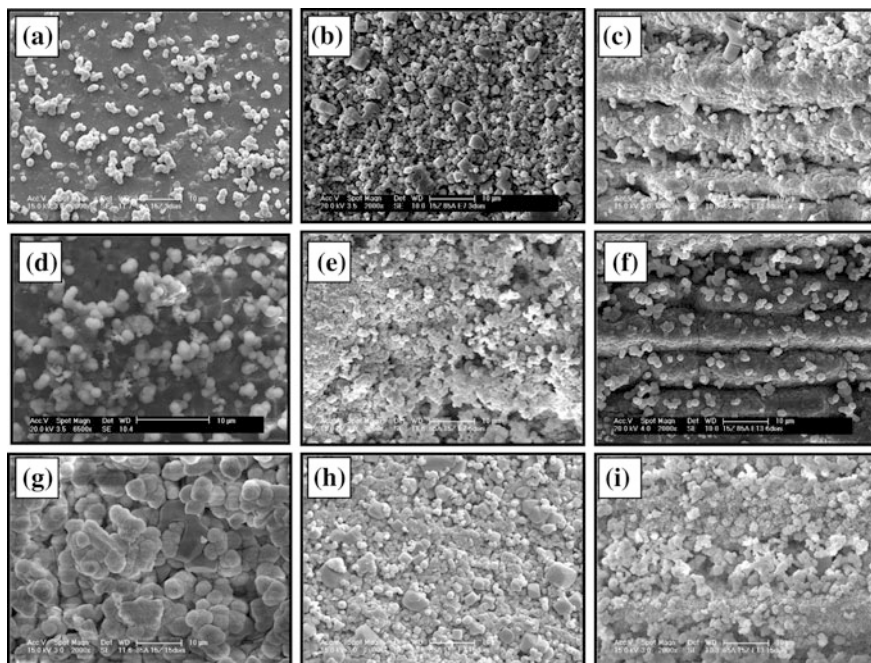
Fig. 7 Micrographs of alumina-zirconia (85A15TZP) specimens untreated and treated superficially with femtosecond laser and immersed in 1.5 SBF for 3, 6 and 15 days. **a** 85A15TZP (3 days); **b** 85A15TZP E = 7 µJ; Np = 1 (3 days); **c** 85A15TZP E = 13 µJ; Np = 1024 (3 days); **d** 85A15TZP (6 days); **e** 85A15TZP E = 7 µJ; Np = 1 (6 days); **f** 85A15TZP E = 13 µJ; Np = 1024 (6 days); **g** 85A15TZP (15 days); **h** 85A15TZP E = 7 µJ; Np = 1 (15 days) and **i** 85A15TZP E = 13 µJ; Np = 1024 (15 days)

calcium. At points where there was interception with the indentation, there was an increase in the amount of aluminum, indicating clearly that at these regions the indenter removed the apatite deposited on the alumina matrix. This effect can be observed in the 3 N indentation line, which shows weak adhesion of apatite to the specimen that was not surface treated with laser.

Figure 9a, b show the end of the indentation with a load of 30 N on specimens with: 100A E = 20 µJ; Np = 1 and 100A E = 32 µJ; Np = 32 respectively that were immersed for 6 days in 1.5 SBF. Tables 4 and 5 show the concentration of the elements as determined by EDS at regions within (area 1) and outside (area 2) the indentation. In the case where the indentation was done with the highest load (30 N), it can be seen that there is very little variation in the calcium and phosphorous contents in the two regions, indicating that there was no detachment of apatite from the matrix and showing thus strong adhesion between the components when the surface is treated with femtosecond laser and then immersed in SBF for 6 days. The alumina specimens (100A) that were not treated with femtosecond laser but immersed for 15 days in 1.5 SBF revealed weak adhesion of apatite to the
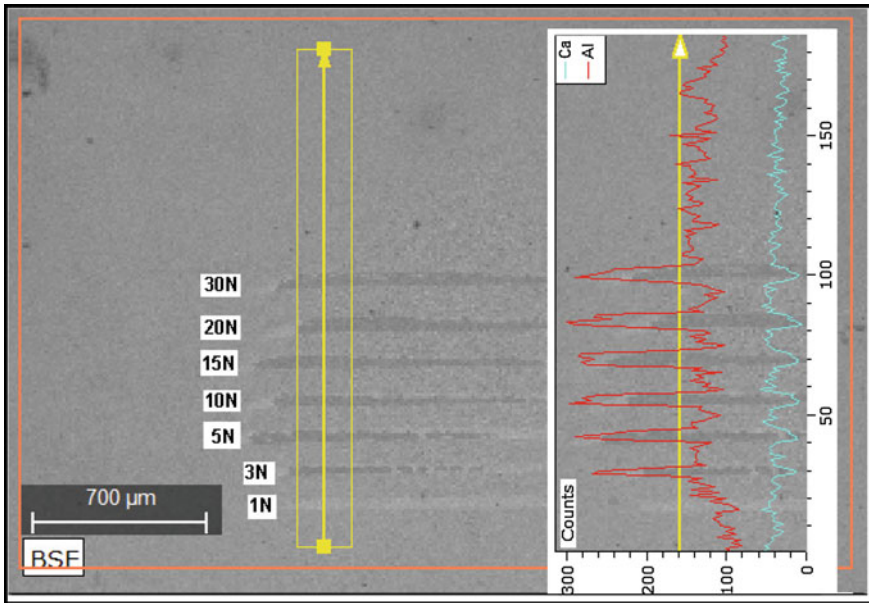
Fig. 8 Micrograph of alumina 100A specimen without femtosecond laser surface treatment immersed in 1.5 SBF for 6 days, showing adhesion behavior of the apatite layer. Detail of the aluminum and calcium concentration map at the base line for analysis
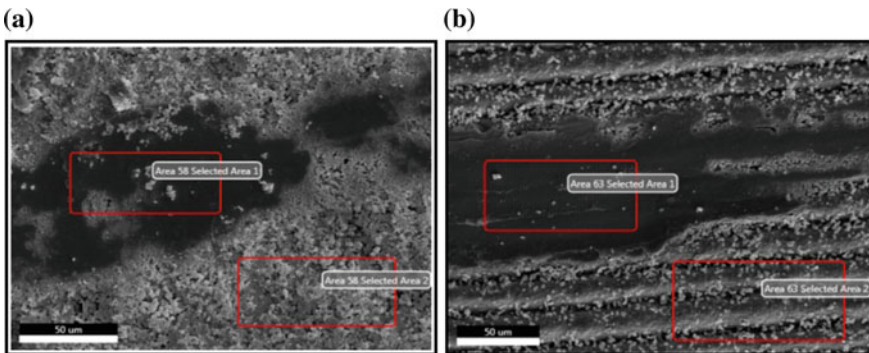
Fig. 9 Micrographs of specimens: **a** 100A E = 20 µJ; Np = 1 and **b** 100A E = 32 µJ; Np = 32 immersed for 6 days in 1.5 SBF, showing the end of the indentation with load of 30 N

matrix. This fact is evident in Fig. 10, where detachment of the apatite layer can be observed all over the specimen surface.

Figure 11 shows the end of the indentation with 30 N a load on specimen with: 100A E = 20 µJ; Np = 1 and 100A E = 32 µJ; Np = 32 that was immersed for 15 days in 1.5 SBF. Elemental analysis of the region on specimen 100A E = 20 µJ;

Table 4 EDS results in mass percent of the chemical elements Na, Al, P, Cl and Ca on specimen 100A E = 20 µJ; Np = 1 immersed for 6 days in 1.5 SBF

Element	Concentration area 1 (mass%)	Concentration area 2 (mass%)
Ca	31	28
Al	33	44
Na	7	5
P	24	20
Cl	5	3

Table 5 EDS results in mass percent of the chemical elements Na, Al, P, Cl and Ca on specimen 100A E = 32 µJ; Np = 32 immersed for 6 days in 1.5 SBF

Element	Concentration area 1 (mass%)	Concentration area 2 (mass%)
Ca	29	34
Al	50	43
Na	1.9	2
P	19	21
Cl	0.1	0
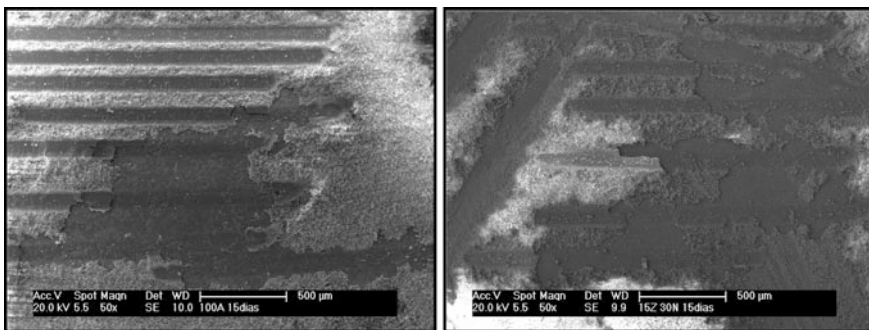
Fig. 10 Micrograph of indentations showing detachment of apatite on specimens 100A and 85A15TZP that were not given femtosecond laser surface treatment and immersed for 15 days in 1.5 SBF

Np = 1 that was micro-scratched was found to be similar to the specimens immersed in 1.5 SBF for 6 days. Table 6 shows the concentration of the elements in the region within (area 1) and outside (area 2) the indentation. Where indentation was done with a very high load, a slight difference in the calcium and phosphorous contents was observed in the two regions, indicating that there was no detachment of apatite from the matrix. This showed strong adhesion between these components when the surface was treated with femtosecond laser. On the other hand, the specimen with: 100A E = 32 µJ; Np = 32 that was immersed in 1.5 SBF for 15 days, shown in Fig. 11b, revealed regions where apatite had detached. This
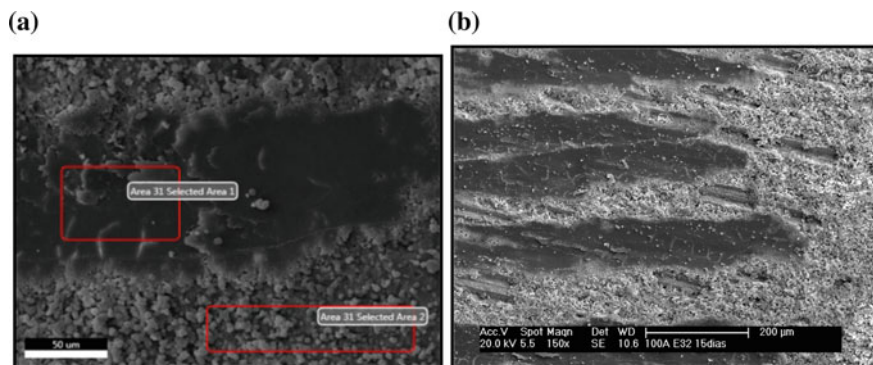
Fig. 11 Micrograph of the end of the indentation with load of 30 N on specimens: **a** 100A E = 20 μJ; Np = 1 and **b** 100A E = 32 μJ; Np = 32

Table 6 EDS results in mass percent of the chemical elements Na, Al, P, Cl and Ca on specimen 100A E = 20 μJ; Np = 1 immersed for 15 days in 1.5 SBF

Element	Concentration area 1 (mass%)	Concentration area 2 (mass%)
Ca	23	29
Al	56	42
Na	3	5
P	16	19
Cl	2	5

could be due to high surface roughness that was induced by laser treatment, compromising adhesion.

Evaluation of the adhesion test shows that the specimens that were not laser surface treated had layers of apatite weakly bonded to the substrate. Whereas the layers of apatite on specimens that had their surfaces textured earlier with laser strongly adhered to the substrate, considering that the laser induces γ-alumina formation. This is the alumina phase that is less stable compared to α-alumina, which could promote Lewis acid sites, making the textured surfaces more reactive. The composite surface treated with femtosecond laser without heat effects (85A15TZP E = 7 μJ; Np = 1) and immersed for 15 days in 1.5 SBF did not show periodic irregularities on the surface and the aluminum and calcium concentration profiles were more uniform. The specimens that were not treated with femtosecond laser did not induce conditions that were adequate for good adhesion of apatite. On the other hand femtosecond laser treatment with heat effect produced a topography that was inadequate resulting in a non-uniform layer of apatite.

4   Conclusions

The application of femtosecond laser for surface treatment is a very interesting alternative as it increases the roughness in a controlled manner with the possibility of not altering the tetragonal crystalline structure of zirconia, besides inducing the functional groups Al-OH on the surface that could facilitate the growth and adhesion of hydroxyapatite in the biomimetic process. The higher the femtosecond laser energy, higher is the wettability of the specimen surface and higher the total surface energy. The specimens without laser surface treatments that were immersed in 1.5 SBF for 6 and 15 days had apatite layers that were weakly bonded to the surface that detached easily. The specimens that had their surfaces textured with laser and immersed in 1.5 SBF for 6 and 15 days had apatite layers that were strongly bonded to the surface and did not detach.

References

1. Kokubo, T.: Novel bioactive materials. Anales de Química Int. Ed. **93**, 49–55 (1997)
2. Kim, C.Y., Jee, S.S.: Hydroxyapatite formation via bioactive-glazed alumina. J. Eur. Ceram. Soc. **23**, 1803–1811 (2003)
3. Wen, H.B., Wijn, J.R.D., Blitterswijk, C.A.V., Groot, K.D.: Incorporation of bovine serum albumin in calcium phosphate coating on titanium. J. Biomed. Res. **46**, 245–252 (1999)
4. Rosen, V., Thies, R.S.: The BMP proteins in bone formation and repair. Trends Genet. **8**, 97–102 (1992)
5. Ariasa, J.L., Mayora, M.B., Pou, J., et al.: Micro- and nano-testing of calcium phosphate coatings produced by pulsed laser deposition. Biomaterials **24**, 3403–3408 (2003)
6. Forsgren, J., Svahn, F., Jarmar, T., et al.: Formation and adhesion of biomimetic hydroxyapatite deposited on titanium substrates. Acta Biomater. **3**, 980–984 (2007)
7. Kokubo, T., Miyaji, F., Kim, H.-M., et al.: Spontaneous formation of bonelike apatite layer on chemically treated titanium metals. J. Am. Ceram. Soc. **79**, 1127–1129 (1996)
8. Uchida, M., Kim, H.-M., Kokubo, T., et al.: Apatite-forming ability of a zirconia/alumina nano-composite induced by chemical treatment. J. Biomed. Mater. Res. **60**, 277–282 (2002)
9. Cortes, D.A., Nogiwa, A.A., Almanza, J.M., et al.: Biomimetic apatite coating on Mg-PSZ/Al_2O_3 composites: effect of immersion method. Mater. Lett. **59**, 1352–1355 (2005)
10. Aguiar AA (2007) Avaliação dos tratamentos químicos e recobrimento biomimético em cerâmicas de alumina-zircônia. Dissertação de mestrado. Instituto de pesquisas energéticas e nucleares, São Paulo, Brazil
11. Sioshansi, P., Tobin, E.J.: Surface treatment of biomaterials by ion beam process. Surf. Coat. Technol. **83**, 175–182 (1996)
12. Brunette, D.M.: The effects of implant surface topography on the behaviour of cells. Int. J. Oral Maxillofac. Impl. **3**, 231–246 (1988)
13. Brunette, D.M., Cheroudi, B., Gould, T.R.L.: Electron microscopic observations on the effects of surface topography on the behaviour of cells attached to percutaneous and subcutaneous implants. In: Laney, W.R., Tolman, D.E. (eds.) Tissue Integration in Oral, Orthopaedic and Maxillofacial Reconstruction, pp. 21–31. Quintessence Publishing, Chicago (1992)
14. Cheroudi, B., Gould, T.R.L., Brunette, D.M.: Effects of a grooved titanium-coated implant surface on epithelial cells behaviour in vitro and in vivo. J. Biomed. Mater. Res. **23**, 1067–1086 (1989)

15. Inoue, T., Cox, J.E., Pilliar, R.M., et al.: Effect on the surface geometry of smooth and porous-coated titanium alloy on the orientation of fibroblasts in vitro. J. Biomed. Mater. Res. **21**, 107–126 (1987)
16. Gomi, K., Davies, J.E.: Guided bone tissue elaboration by osteogenic cells in vitro. J. Biomed. Mater. Res. **27**, 429–431 (1993)
17. Assender, H., Bliznyuk, V., Porfyrakis, K.: How surface topography relates to material's properties. Science **297**, 973–976 (2002)
18. Flemming, R.G., Murphy, C.J., Abrams, G.A., et al.: Effects of synthetic micro- and nano-structured surfaces on cell behaviour. Biomaterials **20**, 573–588 (1999)
19. Rupp, F., Scheideler, L., Rehbein, D., et al.: Roughness induced dynamic changes of wettability of acid etched titanium implant modifications. Biomaterials **25**, 1429–1438 (2004)
20. Zhu, X., Chen, J., Scheideler, L., et al.: Effects of topography and composition of titanium surface oxides on osteoblast responses. Biomaterials **25**, 4087–4103 (2004)
21. Advincula, M.C., Rahemtull, F.G., Advincula, R.C., et al.: Osteoblast adhesion and matrix mineralization on sol-gel derived titanium oxide. Biomaterials **27**, 2201–2212 (2006)
22. Janssen, M.I., Van Leeuwen, M.B., Van Coten, T.J., et al.: Promotion of fibroblast activity by coating with hydrophobins in the beta-sheet end state. Biomaterials **25**, 2731–2739 (2004)
23. Hao, L., Lawrence, J., Chian, K.S.: Effects of CO_2 laser irradiation on the surface properties of magnesia-partially stabilized zirconia (MgO-PSZ) bioceramic and the subsequent improvements in human osteoblast cell adhesion. J. Biomater. Appl. **19**, 81–105 (2004)
24. Hao, L., Ma, D.R., Lawrence, J., et al.: Enhancing osteoblast functions on a magnesia partially stabilized zirconia bioceramic by means of laser irradiation. Mater. Sci. Eng. C Biomed. Supramol. Syst. **25**, 496–502 (2005)
25. Kokubo, T., Takadama, H.: How useful is SBF in predicting "*in vivo*" bone bioactivity? Biomaterials **27**, 2907–2915 (2006)
26. Liu, X.: Drifts study of surface of ϒ-Alumina and its dehydroxylation. J. Phys. Chem. C **112**, 5066–5073 (2008)
27. Coutinho, M.P.: Influência da morfologia da superfície na molhabilidade do titânio comercialmente puro. Dissertação de mestrado, Instituto Militar de Engenharia, Rio de Janeiro, Brazil (2007)
28. Good, R.J., Van Oss, C.J.: The modern theory of contact angles and the hydrogen bond components of surface energies. In: Schrader, M.E., Loeb, G.I. (eds.) Modern Approaches to Wettability, p. 1. Plenum, New York, USA (1992)

Laser Polishing of Additive Manufactured AlSi10Mg Parts with an Oscillating Laser Beam

Jochen Schanz, Markus Hofele, Leonhard Hitzler, Markus Merkel and Harald Riegel

Abstract Powder-bed based additive manufacturing techniques, such as selective laser melting (SLM), are gaining in importance due to the opportunity to produce highly complex shapes. This offer new construction possibilities in the design. However, the surface of the produced SLM parts exhibit a high roughness which can affect the integrity and geometric tolerance. To reduce the surface roughness and to improve the mechanical properties of the outmost layer, laser polishing by re-melting the surface can be used. The present paper focus on the laser polishing of additive manufactured parts. This investigation contains measurement results of the initial and laser polished surfaces out of AlSi10Mg. The surfaces have been analyzed by roughness spectroscopy and white light interferometry. By utilizing a disk laser with a maximum power of 4 kW in combination with a 1-D scanner system, the initial surface roughness was reduced up to 92 %.

Keywords Laser polishing · Additive manufacturing · Oscillating laser beam · Surface roughness · Aluminum · High power laser

---

The original version of this chapter was revised: Affiliations of two authors were modified in the chapter. The erratum to this chapter is available at 10.1007/978-981-10-1082-8_19

J. Schanz (✉) · M. Hofele · M. Merkel · H. Riegel
Aalen University of Applied Sciences, Beethovenstraße 1, 73430 Aalen, Germany
e-mail: jochen.schanz@hs-aalen.de

M. Hofele
e-mail: markus.hofele@hs-aalen.de

M. Merkel
e-mail: markus.merkel@hs-aalen.de

H. Riegel
e-mail: harald.riegel@hs-aalen.de

L. Hitzler
School of Engineering, Griffith University, Gold Coast Campus, Southport 4222, Australia
e-mail: leonhard.hitzler@griffithuni.edu.au

1   Introduction

The fabrication of components with highly complex shapes [1] leads with conventional production processes [2] to a remarkable wastage of material, necessity of multiple processing steps and a long production time. Additive manufacturing techniques provide the opportunity to build highly complex parts in a shorter time. First additive manufacturing (AM) techniques were used to produce preliminary prototypes in the mid-1990s [3]. Through the steady development and research, AM-techniques switched from "rapid prototyping" into "rapid manufacturing" [4]. This opened the possibility of a direct manufacturing of end-use parts. At the current stage, SLM allows the fabrication of components out of a huge variation of materials. The mechanical properties were proven in investigations [5–7]. Due to the improvement of the SLM-process itself, the density of built parts reaching up to 99.9 % by improving the laser parameters and scan strategies [8–10]. The high density and the corresponding mechanical properties provide the basis to enable the application of AM-techniques for customized products and the manufacturing business which will lead to a growing market up to 20 bil. € in 2020 [11]. A negative aspect of the layer-wised SLM technique is the optical appearance and unacceptable roughness which limit the industrial uptake. The high roughness has an impact on the tolerances of the parts and represents a risk of fatigue crack initiation [12]. The local roughness of a fabricated component depends on the shape and geometry of the component as well as the orientation and positioning during the fabrication process. Inhomogeneities in the surface quality are induced by the layer-wise manufacturing procedure and its specific environmental conditions. Certain investigations demonstrated the fluctuations of the samples with different orientation and position in the process chamber [13, 14]. To reduce the roughness, different options were examined. Through an optimization of the hatch strategies [15], laser power and scan speed [16], the geometrical deviations and roughness were reduced by changing the laser exposure of each layer. Another option to improve surface quality and metallurgic properties of the built parts is laser surface remelting (LSR) of each single layer. Investigations exhibited a significant roughness improvement up to 70 % and a reduced stair-effect by 10–15 % [9] without inducing edges at the contour of the built parts [17]. The introduced possibilities to improve the surface of the parts during the SLM process is limited by the laser source, beam geometries and the direction of the treatment during the building process. Thereby, several other options were involved to improve the surface roughness of SLM parts i.e. laser ablation of single layer [18], cutting [19] chemical polishing [20] abrasive blasting [21] or mechanical polishing [22, 23]. The previously presented techniques have the disadvantages of inadequate accuracy for selective post processing, a wastage of expensive material, environmental issues or resulting forces though the abrasive and cutting processes.

Recently, laser polishing (LP) of metal parts has gained interests. LP is a high productive, full-automatable and contact-free post processing technique, which offers a similar degree of freedom in design than the SLM process itself. The

process can be used for different areas of application [24, 25]. LP can be divided into three different processes: polishing by ablating, roughness reduction by selective polishing and reduction by reallocating molten material [24]. The latter is most utilized to reduce the roughness of surface. During polishing, the surface is molten through a laser beam. In the liquid phase, the surface tension smoothens the roughness by a material flow from peaks to valleys. By laser polishing, nearly no material is lost or removed. The remelting process has an impact on the material of the boundary layer and the resulting roughness of the surface. Laser polishing and its influence has been investigated by various researcher on different materials, laser sources and varied polishing strategies [26–29]. The resulting surface topography and its roughness is influenced by the chosen parameters of the polishing process (i.e. scan velocity, track overlap, laser beam intensity, repetition rate and laser power) [26], segregations and inclusions [30]. In addition, the chosen laser source and the intensity distribution influences the polishing process as well [28, 31]. Through the melting and the fast solidification, the microstructure of the molten material is refined [26, 27, 32]. This leads to changed hardness [27, 32], corrosion resistance [33] and fatigue resistance [6, 34].

The previously presented techniques to improve the roughness of SLM parts comprise several disadvantages. However, LP of metal and alloys show promising results. Hence, LP of metal SLM parts is gaining in interest and importance through the rising market of SLM. Several investigations have been done to explore LP of AM parts, including different materials (e.g. steel, aluminum and titanium). High surface quality is achieved with the optimum laser intensity [34–36] which depends on the current surface texture [35, 37], the chemical composition and its quality [35]. Imperfections like cracks may appear with excessive laser power [38]. Marimuthu et al. [39] determined the melt pool velocity as being a significant influence factor for the roughness. The convection can be reduced by a lower heat, which simultaneously reduces the effects of the oxidation and carbonization. Heat treatment affects the oxide layer on different ways. Cabrini et al. [33] reported a decreased corrosion resistance due to an enhanced content of silicon at the surface. An improved passivity and stability characteristics in an electrolytic medium referred Pariona et al. [32]. Dependent on the material and its composition, elements with a low melting point lead to increasing enriched oxide layers with a reduced corrosion resistance and biocompatibility [40]. The remelting process caused a homogenous composition which determined a higher hardness of the surface [32, 34, 37]. The density in the remelted layer increased up to 100 % through elimination of open and closed porosity [34, 41]. Under certain circumstances the SLM process can exhibit instabilities, resulting in balling, agglomeration and waviness. Those imperfections can be influenced and eliminated by LP [41]. Various investigations were undertaken in the area of laser polishing of SLM parts, comprising different materials. The outcome of those showed promising results. An overview of the applied SLM materials, laser sources, initial roughness and reached laser polished roughness is given in Table 1.

Table 1 Overview of the undertaken investigations of laser polished SLM parts

Author	Laser source	Mode	Material	Initial roughness Ra (μm)	Roughness after LP Ra (μm)
Marimuthu et al. [39]	Solid state laser (SSL)	CW	Ti6Al4V	10.2	2.4
Perry et al. [36]	SSL	Pulsed	Ti6Al4V	0.206	0.070
Kumstel and Kirsch [35]	SSL	CW	Ti/Inconel 718	1	0.16/0.11
Alrbaey et al. [41]	SSL	CW	316L	10	1.4
Ukar et al. [38]	CO_2 + SSL	CW	1.2379 tool steel	5.32	0.36
Lamikiz et al. [34]	CO_2	Pulsed	Laserform SR100	7.5–7.8	1.2–1.3
Pariona et al. [32]	Fibre	CW	Al-1.55 wt % Fe	5.54	0.07

Table 2 Chosen parameter of the SLM building process for AlSi10Mg

	Scan speed (mm/s)	Laser power (W)	Hatch distance (mm)	Scan vector (mm)	Rotation angle increment (°)
Contour	600	350	–	–	–
Core	930	350	0.42	10	90
Final layer	850	350	0.42	10	–
Contour offset	600	350	–	–	–
Support	900	350	–	–	–

In the present study, an experimental investigation with a new high oscillating laser scanner was carried out at high laser power to achieve a reduced surface roughness of SLM built AlSi10Mg samples.

2   Methods, Material and Measurements

In the present investigation, SLM manufactured AlSi10Mg components with a size of $100 \times 30 \times 2$ mm^3 were produced in a SLM 280HL machine (SLM Solution GmbH, Lübeck, Germany) with a building chamber of $280 \times 280 \times 350$ mm^3 and a 400 W Yb-fibre-laser. The average diameter of the chosen powder was 37 μm [13]. All samples were built in a vertical position in the direction of the recoater with a slicing thickness of 50 μm and in an inert gas atmosphere employing nitrogen to prevent oxidation. The chosen parameters of the SLM process are given in Table 2.

In Table 3, a selection of the chemical composition of the parts is given [13].

The initial average surface roughness of the parts in the building direction was around $Ra = 8.7$ μm.

The laser polishing process was performed in a TRUMPF LaserCell TLC 40, using a solid state disk laser TRUMPF TruDisk 4002 (Trumpf GmbH + Co. KG, Ditzingen, Germany) with a maximum output power of 4000 W, a beam quality of 8 mm·mrad and a maximum repetition rate of 1000 Hz. The beam oscillation is done with an one dimensional scanner head (lasertronic SAO1.0x/1D Fraunhofer-Institut, Dresden, Germany) with a maximum frequency of 300 Hz. A minimal laser spot diameter of 0.43 mm was used. The used experimental setup of the laser polishing procedure is depicted in Fig. 1a.

The polishing process was performed in a process chamber with an inert gas atmosphere of argon and a maximum residual oxygen content of 40 ppm (Fig. 1b). The scanner head moved the laser beam in the traverse direction of the feed rate over the surface with the variable dimensions of 10×10 mm^2. The laser polishing with a one dimensional scanner head is shown schematically in Fig. 2.

The feeding rate of the polishing process was in the direction of the SLM building process and the tactile measurements were carried out in the building direction as well. The average initial and laser polished surface roughnesses Ra according to EN ISO 4288 [43] were detected by using tactile roughness profilometer (MarSurf M 400, Mahr GmbH, Göttingen, Germany) with a cut-off wavelength of 2500 μm

Table 3 Chemical composition of AlSi10Mg in mass-percentage

Al	Si	Mg	Fe	Ga	Na	Ti
88.946	10.496	0.3043	0.1700	0.0103	0.0170	0.0077
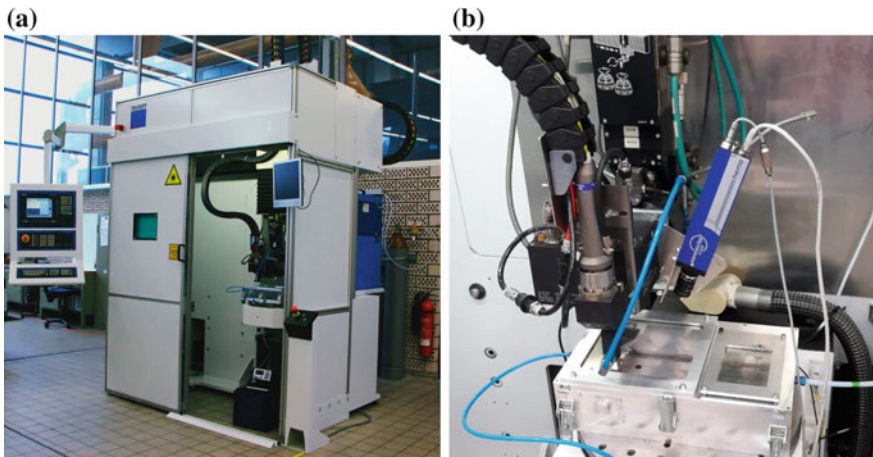
Fig. 1 Experimental setup of the laser polishing process, **a** TRUMPF LaserCell 40, **b** 1D laser scanner and process camber [42]
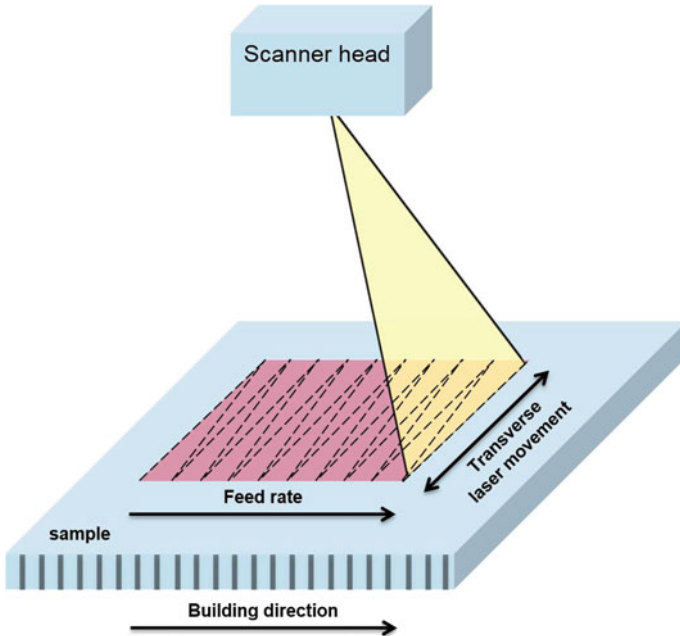
Fig. 2 Schematically function principle of laser polishing with one dimensional scanner head

(initial) and 800 µm (laser polished) [44]. For further investigations, an optical light microscopes (AxioZoom v16 Carl Zeiss Microscopy GmbH, Jena, Germany) and a white light interferometer (Zygo Zemetrics ZeGage, Zygo Corporation, Middlefield, Connecticut, USA) were utilized.

3   Results

At the beginning, suitable laser parameters have been determined to achieve a low roughness. Important parameter is the intensity of the laser spot. Through preliminary tests, a reliable pulse laser power of 1700 W in combination with a spot diameter of 1.0 mm was found as optimal laser intensity. It is desired to reach a pulse and track overlap of more than 50 % to avoid an inhomogeneous surface. The maximum the repetition rate of the laser source is 1000 Hz. Therefore, a transversal laser frequency of 10 Hz was chosen to enable a pulse overlap bigger than 50 %. The spot diameter, repetition rate and pulse duration led in combination with a transverse movement width of 10 mm at a frequency of 10 Hz to an average pulse overlap of 80 %. With a feeding rate of 40 mm/min, a high track overlap of 93 % was achieved. Figure 3 shows a comparison of tactile measurements between the initial surface and the polished surface.
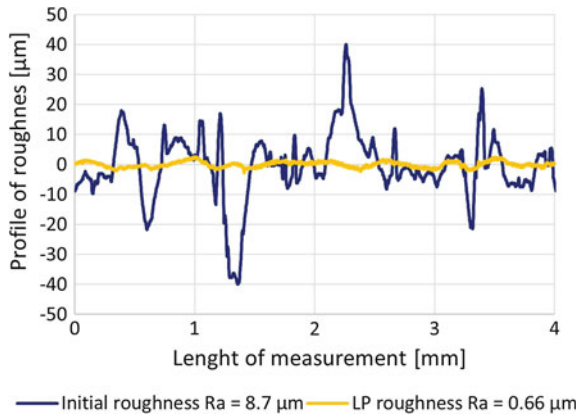
Fig. 3 Comparison between initial and laser polished surface
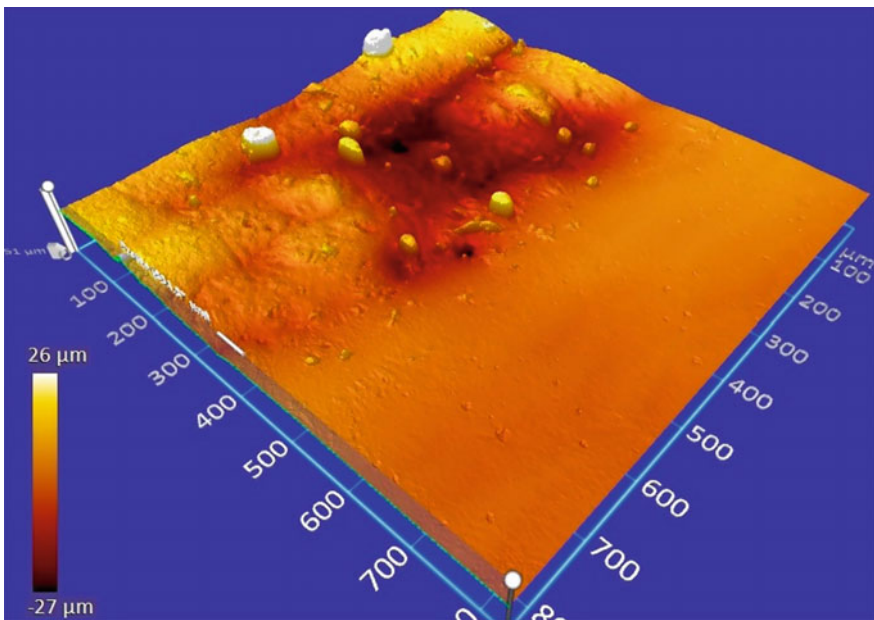
Fig. 4 Transition area of the initial and polished surface, obtained with white light interferometer

The valleys and peaks were remarkably reduced due to the laser polishing process. The polished surface exhibited still some slightly waviness and bumps over the whole section of measurements. However, the previously mentioned laser and polishing parameters led to a high reduction of the surface roughness from initially $Ra = 8.7$ µm to laser polished $Ra = 0.66$ µm. This represented a reduction of more than 92 %. To identify the varieties of the initial and the polished surface, a white light interferometer image is depicted in Fig. 4.
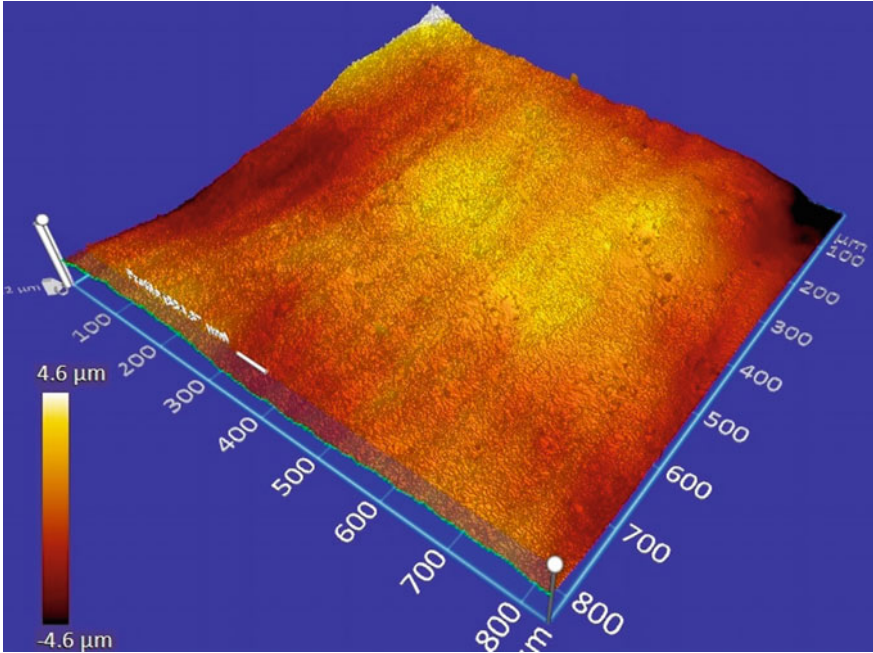
Fig. 5 White light interferometer image of the laser polished surface

The initially rough surface was smoothened through the laser remelting process. The initial roughness represented by valleys and hills of the SLM part are clearly removed. Some splatters from the SLM process were found on the initial and transient area. Pores, immersions and shadows were found in the smoothened surface. The identified are depicted in Fig. 5.

The shadows (see Fig. 4) on the surface appeared as waviness in Fig. 5 through the higher magnification. The surface exhibited unevenness, which was visible as well at the tactile measurements (Fig. 3).

4 Conclusion

Laser polishing of selective laser melted AlSi10 Mg, conducted with an oscillating laser beam, was investigated. The surface roughness was reduced by up to 92 %. The tactile measurements depicted the roughness of the initial and laser polished surface. The initial surface exhibited valleys and hills over the complete section of measurement. At the laser polished surface, slight waviness and minor bumps were still detected. The surface structure was depicted with a white light interferometer. However, laser polished surface was not completely smoothen. Several small pores,

waviness and unevenness were observed. Based on the experimental results, further investigation and optimization with the focus on improved parameters and various laser polishing strategies is recommended. In addition, the effects on the microstructure of the remelted area, its correlation to an occurring oxide layer, their causes and opportunities should be investigated.

References

1. Toyserkani, E., Corbin, S., Khajepour A.: Laser Cladding (2005)
2. Ashby, M.F.: Materials and the Environment: Eco-informed Material Choice. Butterworth-Heinemann, Amsterdam (2009)
3. Kruth, J.P., et al.: Consolidation phenomena in laser and powder-bed based layered manufacturing. CIRP Ann. Manuf. Technol. **56**(2), 730–759 (2007)
4. Kruth, J.P., et al.: Benchmarking of different SLS/SLM processes as rapid manufacturing techniques. In: International Conference on Polymers and Moulds Innovations (PMI), Gent, Belgium, 2005
5. Kempen, K., et al.: Mechanical properties of AlSi10Mg produced by selective laser melting. Phys. Procedia **39**, 439–446 (2012)
6. Brandl, E., et al.: Additive manufactured AlSi10Mg samples using selective laser melting (SLM): microstructure, high cycle fatigue, and fracture behavior. Mater. Des. **34**, 159–169 (2012)
7. Mower, T.M., Long, M.J.: Mechanical behavior of additive manufactured, powder-bed laser-fused materials. Mater. Sci. Eng. A **651**, 198–213 (2016)
8. Aboulkhair, N.T., et al.: Reducing porosity in AlSi10Mg parts processed by selective laser melting. Addit. Manuf. **1–4**, 77–86 (2014)
9. Yasa, E., Kruth, J.-P.: Application of laser re-melting on selective laser melting parts. Adv. Prod. Eng. Manag. **6**(4), 259–270 (2011)
10. Monroy, K., Delgado, J., Ciurana, J.: Study of the pore formation on CoCrMo alloys by selective laser melting manufacturing process. Procedia Eng. **63**, 361–369 (2013)
11. Wohlers, T.T.: Wohlers Report 2014: 3D Printing and Additive Manufacturing State of the Industry Annual Worldwide Progress Report. Wohlers Associates, Fort Collins (2014)
12. Yasa, E., Kruth, J.P.: Microstructural investigation of selective laser melting 316L stainless steel parts exposed to laser re-melting. Procedia Eng. **19**, 389–395 (2011)
13. Hitzler, L., et al.: Non-destructive evaluation of AlSi10Mg prismatic samples generated by selective laser melting: influence of manufacturing conditions. Materialwissenschaft und Werkstofftechnik. **5** (2016) (to be published)
14. Zhang, B., Liao, H., Coddet, C.: Effects of processing parameters on properties of selective laser melting Mg–9 %Al powder mixture. Mater. Des. **34**, 753–758 (2012)
15. Gebhardt, A., Hötter, J.-S., Ziebura, D.: Impact of SLM build parameters on the surface quality. RTejournal - Forum für Rapid Technologie (2014)
16. Calignano, F., et al.: Influence of process parameters on surface roughness of aluminum parts produced by DMLS. Int. J. Adv. Manuf. Technol. **67**(9–12), 2743–2751 (2013)
17. Kruth, J.P., Yasa, E., Deckers. J.: Experimental investigation of laser surface re-melting for the improvement of selective laser melting process. In: Proceedings of 14èmes Assises Européennes du prototypage Rapide, pp. 321–332 (2009)

18. Campanelli, S.L., et al.: Taguchi optimization of the surface finish obtained by laser ablation on selective laser molten steel parts. Procedia CIRP **12**, 462–467 (2013)
19. DMG Mori: 02 Mar 2016. Available from: http://en.dmgmori.com/technical-press/advanced-technologies/live-at-emo-2015—lasertec-65-3d—additive-manufacturing-of-a-small-turbine-casing-made-of-stainless-steel/386000
20. Łyczkowska, E., et al.: Chemical polishing of scaffolds made of Ti–6Al–7Nb alloy by additive manufacturing. Arch. Civ. Mech. Eng. **14**(4), 586–594 (2014)
21. Manfredi, D., et al.: Additive manufacturing of al alloys and aluminium matrix composites (AMCs). Light Metal Alloy. Appl. 1–32 (2014)
22. Li, Y., et al.: Vibration-assisted dry polishing of fused silica using a fixed-abrasive polisher. Int. J. Mach. Tools Manuf. **77**, 93–102 (2014)
23. Tsai, M.-Y., Yang, W.-Z.: Combined ultrasonic vibration and chemical mechanical polishing of copper substrates. Int. J. Mach. Tools Manuf. **53**(1), 69–76 (2012)
24. Willenborg, E.: Polieren von Werkzeugstählen mit Laserstrahlung. Shaker, Aachen (2006)
25. Temmler, A.: Selektives Laserpolieren von metallischen Funktions- und Designoberflächen. Shaker-Verl, Aachen (2013)
26. Schmidt, J., Scholz, R., Riegel, H.: Laserpolieren von Aluminium durch Umschmelzen mit Hochenergieimpulsen (Laser polishing of aluminum by remelting with high energy pulses). MAWE Materialwissenschaft und Werkstofftechnik **46**(7), 686–691 (2015)
27. Stein, S., et al.: Hardening and roughness reduction of carbon steel by laser polishing. In: Öchsner, A., Altenbach, H. (eds.) Design and Computation of Modern Engineering Materials, pp. 411–419. Springer International Publishing, Cham (2014)
28. Nusser, C., et al.: Influence of intensity distribution and pulse duration on laser micro polishing. Phys. Procedia **12**(PART 1), 462–471
29. Wong, T.T., Liang, G.Y., Tang, C.Y.: The surface character and substructure of aluminium alloys by laser-melting treatment. J. Mater. Process. Technol. **66**, 172–178 (1997)
30. Kiedrowski, T.: Oberflächenstrukturbildung beim Laserstrahlpolieren von Stahlwerkstoffen. Shaker, Aachen (2009)
31. Hafiz, A.M.K.B., Evgueni, V., Tutunea-Fatan, R.O.: Influence of overlap between the laser beam tracks on surface quality in laser polishing of AISI H13 tool steel. J. Manuf. Process. **14**(4), 425–434 (2012)
32. Pariona, M.M., et al.: AFM study of the effects of laser surface remelting on the morphology of Al–Fe aerospace alloys. Mater. Charact. **74**, 64–76 (2012)
33. Cabrini, M., et al.: Evaluation of corrosion resistance of Al–10Si–Mg alloy obtained by means of direct metal laser sintering. J. Mater. Process. Technol. **231**, 326–335 (2016)
34. Lamikiz, A., et al.: Laser polishing of parts built up by selective laser sintering. Int. J. Mach. Tools Manuf. **47**(12–13), 2040–2050 (2007)
35. Kumstel, J., Kirsch, B.: Polishing titanium- and nickel-based alloys using CW-laser radiation. Phys. Procedia **41**, 362–371 (2013)
36. Perry, T. L., et al.: Pulsed laser polishing of micro-milled Ti6Al4V samples. JMP J. Manuf. Process. **11**(2), 74–81 (2009)
37. Rosa, B., Mognol, P., Hascoët, J.-Y.: Laser polishing of additive laser manufacturing surfaces. J. Laser Appl. **27**(S2), S29102 (2015)
38. Ukar, E., et al.: Laser polishing of tool steel with CO_2 laser and high-power diode laser. Int. J. Mach. Tools Manuf. **50**(1), 115–125 (2010)
39. Marimuthu, S., et al.: Laser polishing of selective laser melted components. Int. J. Mach. Tools Manuf. **95**, 97–104 (2015)
40. Vaithilingam, J., et al.: The effect of laser remelting on the surface chemistry of Ti6al4V components fabricated by selective laser melting. J. Mater. Process. Technol. **232**, 1–8 (2016)
41. Alrbaey, K., et al.: On optimization of surface roughness of selective laser melted stainless steel parts: a statistical study. J. Mater. Eng. Perform. **23**(6), 2139–2148 (2014)
42. Laser Applikations Zentrum (LAZ). Aalen University of Applied Sciences. https://www.htw-aalen.de/de/facilities/97 (2016). Accessed 04 Mar 2016

43. EN ISO 4288—Geometrical product specifications (GPS)—surface texture: profile method–rules and procedures for the assessment of surface texture. International Organization for Standardization, Genève (1996)
44. EN ISO 4287—Geometrical product specifications (GPS)–surface texture: profile method–terms, definitions and surface texture parameters. International Organization for Standardization, Genève (1997)

Laser Beam Machining, Laser Beam Hybrid Machining, and Micro-channels Applications and Fabrication Techniques

Saied Darwish, Naveed Ahmed and Abdulrahman M. Alahmari

Abstract Laser beam machining (LBM) has proven its applications and advantages over almost all the range of engineering materials. It offers its competences from macro machining to micro and nano-machining of simple-to-complex shapes. The flipside of LBM is the existence of universal problems associated with its thermal ablation mechanism. In order to alleviate or reduce the inherent problems of LBM, a massive research has been done during the past decade and in turn build a relatively new route of laser-hybrid processes. The hybrid approaches in laser ablation have demonstrated much improved results in terms of material removal rate, surface integrity, geometrical tolerances, thermal damage, metallurgical alterations and many more. This chapter reviews the research work carried out so far in the area of LBM and its hybrid processes for different materials and shapes. The literature assessment is mainly classified into seven categories named as: (1) Introduction, (2) Laser Beam Machining (LBM), (3) Laser Assisted Machining (LAM), (4) Laser Chemical Machining/Etching (LCM/E), (5) Laser Assisted

S. Darwish (✉) · N. Ahmed · A.M. Alahmari
Princess Fatima Alnijiris's Research Chair for Advanced Manufacturing Technology
(FARCAMT), King Saud University, Riyadh, Saudi Arabia
e-mail: darwish@ksu.edu.sa

N. Ahmed
e-mail: anaveed@ksu.edu.sa

A.M. Alahmari
e-mail: alahmari@ksu.edu.sa

S. Darwish · N. Ahmed · A.M. Alahmari
Industrial Engineering Department, King Saud University, Riyadh, Saudi Arabia

S. Darwish · N. Ahmed · A.M. Alahmari
Advanced Manufacturing Institute, King Saud University, Riyadh, Saudi Arabia

N. Ahmed
Department of Industrial and Manufacturing Engineering, University of Engineering
and Technology, Lahore, Pakistan

Electrochemical Machining (LAECM) and (6) Under-Water Laser Ablation (UWLA) and (7) Micro-channel Applications and Fabrication Techniques. The last part of this chapter discusses the research gaps and future research directions in the context of laser and laser-hybrid ablation.

Keywords Laser beam machining (LBM) · Laser assisted machining (LAM) · Ablation rate · Under-water laser ablation (UWLA) · Material removal mechanism · Micro-channels

1   Introduction

Conventional machining (CM) is without doubt greatly applicable for a wide variety of materials. However, shaping of hard to machine materials alongside the complex geometries impose some limitations. Difficult to machine materials such as titanium and nickel alloys, superalloys, ceramics and metal matrix composites are not easy to deal with CM processes. Similarly, complex machining characteristics (3-D milling, high aspect drilling, taper free holes, crack free edges etc.) and fragile jobs (ultrathin sheets, wafers etc.) call for some competitive process. In connection, modern components and products like spinning nozzles, turbine blades and fuel injectors require high standard of machining results.

There are two common practices to accept such challenges. One is to employ non-conventional machining (NCM) processes and the other is assisting the CM process with some non-conventional machining (NCM) techniques. Laser beam machining (LBM) is much promising in this regard especially dealing with almost the whole range of engineering materials [1]. Although the process is slow but it offers great advantages over the conventional machining processes like non-contact and non-wearing tool, independence of material hardness, good surface finish and precise cut quality. Laser beam cutting is superior to any cutting method conventional or non-conventional because of material versatility, no wear or change of tool, high material utilization, production flexibility, high accuracy and edge quality.

Instead of direct material removal, however, the laser energy is also used for heating [2], melting [3] or assisting the other machining processes. In these scenarios the process is termed as laser assisting machining (LAM) [4]. It is more widely used to enrich the CM potentials especially for hard-to-machine materials. The literature is clustered with laser assisted conventional turning which majorly contribute to reduce the cutting forces, improve the tool life and process throughput. In the last decade, the trend is switching from traditional LBM to hybrid LBM by coupling some other phenomenon/process to LBM setup. The coupling process could be chemical etching [5, 6], electrochemical machining [7], ultrasonic machining [8, 9], electric discharge machining [10], water jet [11] and liquid film [12] etc. The common motive to this hybrid approach is to minimize/alleviate the

traditional LBM's drawbacks such as thermal damage, heat affected zone (HAZ), low ablation rate, cracking and melt re-deposition.

In this chapter, the competitive advantages of LBM, LAM and fluidly immersed hybrid laser machining are reviewed. The emphasis is kept to generate a clear understanding of material removal mechanisms in each regime and the impact of machining parameters on part features. The importance of micro-channels in various fields is also reviewed along with several fabrication techniques used to fabricate micro-channels. In the end, new challenges and future directions are proposed.

2 Laser Beam Machining (LBM)

Laser beam machining (LBM) is a material removal process governed by focusing a coherent beam of monochromatic light of laser on the substrate surface. The beam is generated and focused by fiber optics and/or combination of reflecting mirrors and delivered to the target through a beam delivery system. The process is energized by mishmash of different energies such as thermal, mechanical, chemical and thermo-mechanical. The material is rapidly removed in the form of tiny particles. Taniguchi defined Micromachining in terms of workpiece material removed during one cycle of removal action. Accordingly micromachining is one in which the unit removal is in sub-micron range [13]. In this research micromachining is defined as the machining of workpiece having at least one of the dimensions in microns. In view of the increasing trend toward miniaturization, micromachining becomes an important activity in the fabrication of micro parts. Various technologies such as mechanical micromachining (micro drilling and micro milling), focused ion beam micromachining, laser micromachining are being used in microfabrication. Microfluidic devices and micro-channel heat exchangers etc. are a network of complex shaped channel system meant for the flow of micro, nano and even pico liter fluid for the micro mixing and analysis used in various applications including aerospace, automotive and biomedical applications. The fabrication of microfluidic devices is very complex because of the fact that it uses wide range of materials which are not compatible with conventional photolithographic techniques.

Laser beam micro-machining works on the principle that when a high energy density laser beam is focused on work surface the thermal energy is absorbed which heats and transforms the work volume into a molten, vaporized or chemically changed state that can easily be removed by flow of high pressure assist gas jet. Laser technology uses light radiation with high energy density as a machine tool and appears as a possible efficient system for micromachining a wide range of materials without any mechanical or chemical interaction with the workpiece [14]. Laser micromachining is a relatively recent process and offers better flexibility in dimensional design of microproducts. Advancements in laser technologies like development of shorter wavelengths, shorter pulse widths, advances in the optics for the focusing systems has made laser micromachining a viable, attractive,

cost-effective and enabling technology for micro system applications. At present, laser micromachining is extensively used to produce shapes with greater complexity and lesser material damage than competing micromachining approaches.

2.1 Laser-Material Interactions

The physical processes occurring during laser-material interaction are very complex and need to be studied for proper understanding of capabilities and limitation of laser micromachining. When a laser is incident on any surface various phenomena occur such as reflection, refraction, absorption, transmission etc. Of all these the most important phenomenon in laser processing of materials is absorption of laser radiation which results in various effects such as heating, melting, vaporization and plasma formation. The extent of these effects depends upon the characteristics of laser radiation and thermo-physical properties of material. The important parameters of laser are wavelength and intensity whereas the material properties include thermal conductivity and absorptivity. The reflectivity of materials generally increases with increasing wavelength, thus the materials are stronger absorbers at shorter wavelength also Since the smallest diffraction-limited focus spot (given as $1/e^2$ the intensity diameter of the laser focus spot) is proportional to the laser wavelength, in order to micro machine smaller and smaller spots, shorter and shorter wavelengths are being used in the micromachining and hence in the recent past there is a shift towards shorter wavelengths.

The quality of micromachining also depends on laser pulse widths, the shorter the pulse width the better is the quality but at higher cost. There has been constant development in pulse times ever since the invention of laser. Few years ago nanosecond (ns) pulse times were the shortest but today picosecond (ps) and femtosecond (fs) lasers are being used and even short pulse times are obtainable in labs. Like very long distances can be expressed in light-years we can express very short times in light-distances that is the distance a light wave or a photon travels during that short time. This distance for 100 fs pulse is only 30 μm. In Fig. 1, these

Fig. 1 Overview of laser machining processes [15]
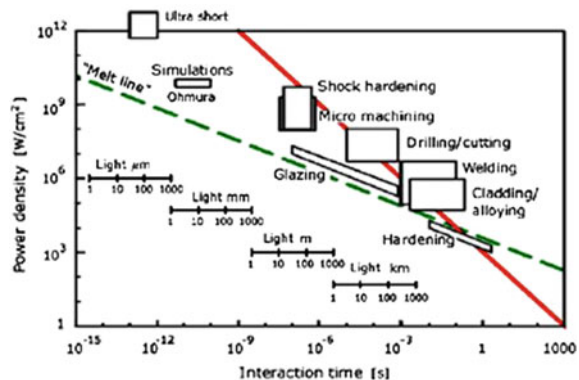
Table 1 Ultrashort pulse times for some materials

Material	Pulse length
Metals	1 ps
Ceramics	10 ps
Plastics	1 ns

light-distances are shown in relation to the laser machining processes. For very short Femtosecond pulses this distance is in the order of the wavelength of the light. The dotted line in Fig. 1 indicates the melt boundary of metal [15].

Depending upon the applications and type of material the pulse width may be selected. Chen and Liu [16] compared different pulse widths and concluded that shorter pulses produce better quality but at higher cost. For different materials this width of shorter pulses differs. A pulse is considered as ultrashort when the (thermal) diffusion depth during the pulse is in the same order or less than the skin layer depth (optical penetration depth). The optical penetration depth depends on the material and the laser wavelength. The diffusion depth depends on the material properties. Table 1 shows the ultrashort pulse times for the few materials. In general pulses shorter than 1 ps are considered as ultrashort.

2.2 Generation of Laser Pulses

Lasers can be operated either in continuous mode or in the pulsed mode. In continuous mode constant laser energy is discharged for a long time. In pulsed mode of operation, the pumped energy is stored until a threshold is reached. Once the threshold is reached, the stored energy is rapidly discharged into short duration pulses of high energy density. One of the important parameters in the pulsed laser operation is the pulse repetition rate. Pulse repetition rate is defined as the number of pulses emitted per unit time. For pulsed lasers the pulsing may be carried out in various ways: normal pulsing, Q-switching, and mode locking [17].

2.2.1 Q-Switching

In Q-switching, short and intense pulse of laser radiation is obtained by modulating the intracavity losses and thus the Q-factor of the laser resonator. A Q-value of the cavity is the measure of ability of the cavity to store the radiant energy. When the Q-value is high, energy will be stored in the cavity without significant laser radiation. If the Q-value of the cavity is lowered, the stored energy will emerge as short and intense pulse of laser beam. Thus, Q-switching involves the "switching" of Q-values of the resonant cavity leading to the emergence of short and intense pulse (high peak power) of laser radiation. Various methods of Q-switching are: rotating mirror method, electro-optic Q-switching, acousto-optic Q-switching, and passive

Table 2 Pulse frequency range of some materials

Material	Frequency (kHz)
Steels	25–45
Brass	10–25
Copper	10–25
Titanium	35–40
Hard metals	15–19
Silicon carbide	30–35
Silicon nitride	30–35
Oxide ceramics	5–10
Graphite	30–50

Q-switching. The pulse duration typically in the nanosecond range Pulse repetition rates as high as a few hundred kilo hertz can be obtained in Q-switched laser operation [17]. The technique is mainly applied for the generation of nanosecond pulses of high energy and peak power with solid-state bulk lasers.

2.2.2 Closing Frequency and Opening Time of Q-Switch

The closing frequency of the Q-switch depends on the material to be machined. Table 2 shows a range of some reference values of pulse frequency for different materials. As the opening time of the Q-switch, a constant value of 10 μs has proven to be appropriate.

2.2.3 Pulse Overlapping

As the laser beam incidents on the surface the laser pulses overlap adjacent to each other (shown in Fig. 2). In single pot area several laser pulses overlap. The overlap of each pulse cab be obtained by the following formula:

$$S_{pulse} = \frac{d - (n-1)a}{d}$$

where, n is the number of pulse, a is the distance travelled by laser in x direction and d is the beam diameter on the surface.

The corresponding effective energy per spot area can be calculated by:

$$E_{effective} = \sum_{n=1}^{N_d} \left[S_{pulse} = \frac{d - (n-1)a}{d} \right] e$$

where, N_d is the number of pulses required to scan the spot area and e is the energy of the individual pulses [18].

Fig. 2 Schematic illustrating overlap in the *x* and *y*-directions and the cylindrical volume machined per spot area [18]
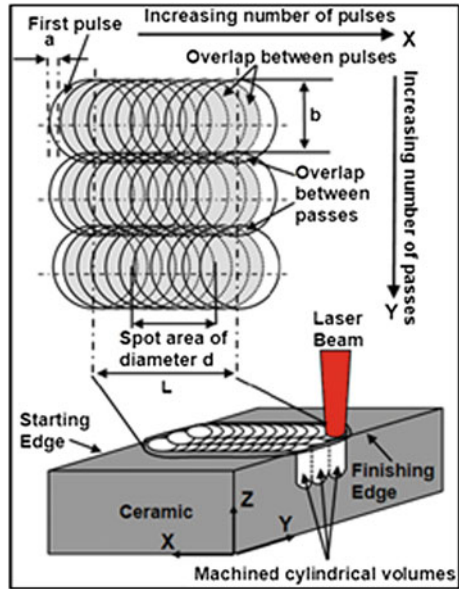
2.2.4 Function Principle of Q-Switch

With the Q-switch closed, the ray trajectory in the resonator is interrupted, no stationary waves may form so that no laser beam is generated; this means that no energy is withdrawn from the YAG rod so that it accumulates the radiated energy. The amplitude of the stationary waves formed with the Q-switch open and thus the intensity of the laser beam produced is the higher the longer the laser active medium was radiated with the Q-switch closed, i.e. the more energy has accumulated in the YAG rod. By opening and closing the Q-switch periodically, laser pulses are generated the intensity of which depends on the closing frequency and opening time of the Q-switch. Figure 3 explains this interrelation. In case of a constant closing frequency (f1 or f2, where f1 > f2), shortening the open time generates laser pulses of higher intensity, reducing the closing frequency increases the intensity level altogether.

2.3 *Physical Factors Affecting the Process*

The material removal in the laser milling is mainly a function of laser characteristics and the material properties. This dual role becomes more complex when the laser beam interacts with the material. This interaction is affected by many processes as well as material parameters.
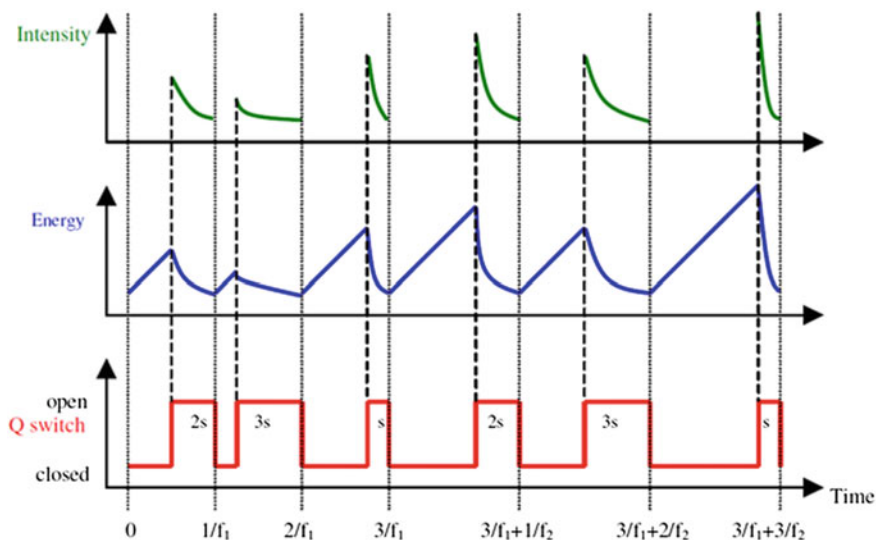
Fig. 3 Function principle of Q-switching

2.3.1 Laser Radiation Features

Laser (Light Amplification by Stimulated Emission of Radiation) is a high-energy beam of electromagnetic radiations. The light, photon, moves as a wave through space, but behaves as a particle of energy when it bumps into matter [19]. Laser radiations can be controlled and modulated by an ordered train of pulses with known pulse duration and pulse frequency. The accumulation of these pulses generates energy which is released for ultra-short time period and results, what we require, extremely high power. Moreover, when the laser beam is focused to a small spot size (100 μm or less) it significantly increases the energy density (fluence) and the power density (intensity) around the spotted zone. This extremely high intensity (10^{13}–10^{18} W/cm^2) is sufficient to cause the material melting which is not possible by conventional processes [20].

2.3.2 Substrate Material Features

The material response against laser radiation varies based upon many factors. Ablation occurs only when the material absorbs enough energy to get melted or vaporized. So the incident wavelength must be matched with the material to be worked. The higher the absorption, the efficiency could be the milling results. The thermal conductivity is another prime key which decides the energy dissipation from the laser interaction zone to the bulk material. The lower the thermal

conductivity is, the better is the expected material removal. The ablation also depends upon the associated material transition energies primarily including latent heat of vaporization and latent heat of melting.

2.4 Laser Ablation Mechanism

The ablation during laser processing refers to the material removal due to thermal and/or photochemical (non-thermal) interactions. Laser ablation mechanism is mainly affected by laser parameters, material properties and work environment. The laser–material interactions during ablation are complex and may involve the interplay between thermal and photochemical processes often referred to as photo physical processes. Figure 4 presents the various mechanisms of laser ablation [21].

During thermal ablation, the excitation energy is rapidly converted into heat, resulting in temperature rise. This temperature rise can cause the ablation of material by surface vaporization or spallation (due to thermal stresses). Thermal ablation mechanisms dominate the material removal during micromachining of metal and ceramics. Photochemical ablation is the dominant material removal
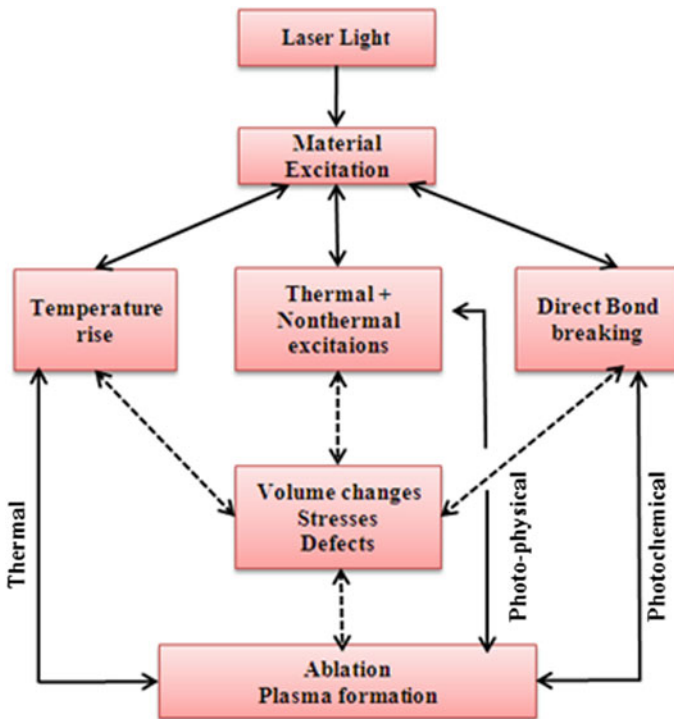

Fig. 4 Various mechanisms of laser ablation [21]

during micromachining of polymers although some of the polymers can also be effectively ablated by thermal ablation mechanism. One of the important considerations during the laser–material interaction during ablation is the thermal relaxation time (τ), which is related with the dissipation of heat during laser pulse irradiation [22]. The two important parameters that determine the ease with which the ablation can be initiated are absorption coefficient and thermal diffusivity. The large value of absorption coefficient and small value of thermal diffusivity generally provide the high ablation efficiency of a material. The ablation of material by using short pulses (pulse time shorter than thermal relaxation time) is better than the longer pulses (pulse time longer than thermal relaxation time), where the absorbed energy will be dissipated in the surrounding material by thermal processes. Ultrashort pulses produce a very high peak intensity (>1015 W/cm^2) and deliver energy before thermal diffusion occurs, thus giving high efficiency and precision to the process without significant thermal degradation (melting, spatter, recrystallization, etc.) to the surrounding region [23].

The laser ablation also depends on the optical properties of the laser beam, laser system's configuration, working parameters, plasma shield, sample position with respect to focal plane and mechanical, optical and thermal properties of the substrate material. Energy absorptions mainly influenced by two lengths. Optical absorption length $L\alpha$ which is inversely proportional to the optical absorption coefficient α. The other length is thermal diffusion length L_{th} calculated by:

$$L_{th} = 2\sqrt{D\Delta t}$$

where, D is the thermal diffusivity and Δt is the pulse length.

A thin layer of liquid phase is locally formed in the interaction zone. The recoil pressure generated squeezes up the liquid out from the interaction zone and ejects the material out. The thickness of liquid phase hl and recoil pressure P_{rec} can be found by:

$$h_l \propto (D)^{1/2}\left(\frac{\Delta H_V}{I_a}\right)^{1/4}$$

$$P_{rec} \approx 10^{-5}I_a$$

The thickness of molten layer and the recoil pressure depends on absorption of laser irradiation. As the machining depth proceeds, the distance to the surface to be ablated is increases which lowers down the irradiation absorption and ultimately results in low process efficiency [24]. When the laser radiations strikes on the substrate surface, electrons in the substrate get excited by the laser photons. This absorbs the photon energy and generates significant heat which is transferred to the close premises of the material in a picosecond interval resulting in high temperature. The temperature reaches so high that it leads the material to melting or vaporization state. The light absorption phenomenon is classically presented by the
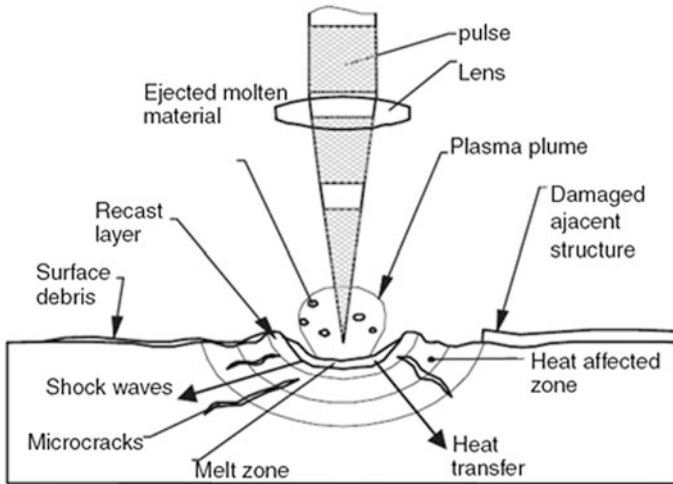
Fig. 5 Nanosecond and longer pulse laser ablation [20]

Beer-Lambert Law [25]. It states that when a light of certain wavelength is transmitted through the material, its absorption depends on the material path length and is totally independent of the incident intensity. When the materials reaches to a certain electron density, it absorbs the photon energy sufficient enough to initiate the ablation. This critical energy is termed as laser fluence threshold [20]. The laser intensity can be enhanced either by reducing the focal spot or by increasing the laser power [26]. After the substrate reaches the melting point, the melt liquid phase appears in the form of a thin layer at the localized interaction zone. The temperature of the melt liquid phase rapidly rises by the subsequent incoming pulses to reach the melt phase at evaporation state (plasma state). This yields a high pressure which is very commonly termed as recoil pressure. The recoil pressure squeezes the liquid up from the interaction zone and ejects the material out (see Fig. 5) [20]. The rapid rise of temperature further amplifies the magnitude of recoil pressure in a range of hundreds of MPa. Yilbas et al. [27] reported this pressure to 1 GPa for mild steel and stainless steel. The recoil pressure exerts the impact loading on the substrate surface that generates an elastic-plastic wave in the surface. This is more commonly known as shock wave propagation [28]. The shock wave locally dislocates the surface grains at the shock-affected region. Due to such dislocations and the impact loading of the shock wave, the target material's surface hardness gets enriched. The ejection of melt debris is another main concern of LBM which is generally derived by some assisting gas (shielding gas). Irrespective to this, the recoil pressure is considered as the main material ejecting agent [29].

2.5   Laser Beam Milling

The application of laser beam milling is equally suited for metals and non-metals. Among the metals, titanium alloy (Ti6Al4V) and nickel based superalloys (particularly Inconel 718) are mainly treated under laser. It is worth noting that the laser beam milling of nickel based superalloys is highly uncommon while cutting of nickel alloys can be very widely seen. However, laser beam milling is also widely employed on non-metals especially structural ceramics, glass, polymers and carbon fiber reinforced polymers (CFRP). Material removal rate, thermal damage, heat affected zone, taper and delamination influenced/caused by laser parameters is widely evaluated by many researchers. Numerical, mathematical and thermal models are the tools to predict their values and distributions in advance to experimental runs. Though, these estimations are well established for non-metals as compared to metals.

2.5.1   Ablation Mechanism of Laser Beam Milling

The general mechanism of laser ablation is described in the previous section. The material removal mechanism for milling is almost the same. However, it could somewhat differ by processing conditions and machined features. This difference is correspondingly included wherever it is encountered. Therefore, it is not felt necessary to include here the details.

2.5.2   Laser Beam Milling of Titanium Alloys

Alpha case (an oxygen enriched alloy layer) is commonly formed in forged titanium alloys during the manufacturing process and it reduces the service life of the material. This layer is normally removed mechanically or chemically. Laser beam milling with short pulse width can remove the alpha case layer and allows to reach the titanium alloy layer extremely smoother (R_a − 110 nm) without any surface cracks [30]. The laser pulse can also be employed in different modes particularly in two; single pulse and multi-pulse. These modes generate varying levels of fluences. The interaction of these modes at higher pulse count and varying fluences with titanium alloys shows the surface character in terms of craters, melt pools at periphery, cracks and TiO_2 layer [31]. The ablation rate under these modes varies for different materials. To explain this variation, in a study of [32] the researchers employed single shot laser pulses of 10 picosecond having 1064 nm wavelength and fluence range of 2–25 J/cm^2 on aluminum, Ti6Al4V and gold. The mechanism behind this variation was reported as the electron heat capacity and electron-phonon coupling time. Aluminum and titanium take the shortest coupling time of 4 and 7 ps while gold takes over 100 ps. In general, it is inferred that ablation depth per pulse increases with increase in laser fluence. Steel and copper also exhibit similar

behavior under these pulse and fluence ranges [33]. Biomedical implants made of Ti6Al4 V if treated under high laser fluence (140 J/Cm^2) of Nd:YAG laser can generate higher wettability characteristics than a mechanically roughened surface. In this treated way the cell attachment becomes higher and wider spread compared to any other condition and the implant shows no sign of infection [34]. Femtosecond laser treatments allow to achieve various surface textures on such biomedical implants. These textures consist of nanoscale laser-induced periodic surface structures (LIPSS), nano-pillars, micro porous columns and complex textures which are nowadays being adopted for implants due to different wettability characteristics [35]. The increase in fluence also alter the microstructure and wear resistance of implants positively in terms of surface grain size and hardness [36]. Laser re-melting (LR) is another alternative to elongate the grain size without affecting the corrosion and wear resistance properties. There is no phase transformation in LR. That is why the corrosion resistance remains unchanged. Though, as a consequent of microstructural changes the micro-hardness increases with increase in fluence. At high fluences (10 and 30 kJ/cm^2) two zones appear in titanium alloys named as melt zone (MZ) and heat affected zone (HAZ) but at low to medium fluences (0.5 and 10 kJ/cm^2), there exists three zones named as melt zone (MZ), heat affected zone (HAZ) and base metal (BM) [37]. Increase in laser fluence or laser lamp current intensity increases the laser micro-milling kerf. It has been recently reported in [38], where the laser beam micro-milling is employed to fabricate micro-channels in different aerospace alloys including titanium alloy, nickel alloy and aluminum alloy. The fabricated micro-channels in titanium alloy (Ti6Al4V) can be seen in Fig. 6.
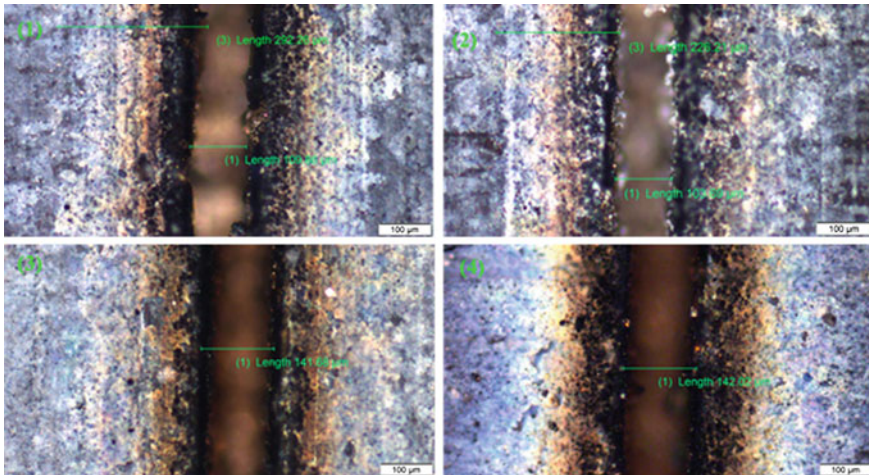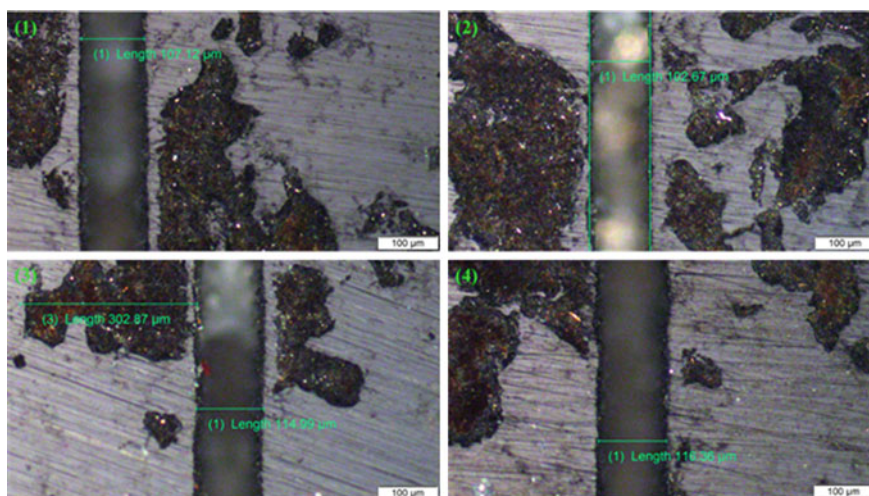

Fig. 6 Microscopic images of micro-channels machined in titanium alloy (Ti-6Al-4V) under different parametric combinations [38]

2.5.3 Laser Beam Milling of Nickel Alloys

Inconel 718 is considered as a hard-to-machine material due to difficulties of machining as a results of its extremely tough nature. Laser ablation is a competent process allowing to machine nickel alloys irrespective to their hardness. Nd:YAG, CO_2 and femtosecond lasers are generally employed to deal with nickel alloys machining. During laser cutting the influence of laser parameters on the cut quality has remained the researchers' core interest. Some of the research is dedicated towards the temperature measurements along the cut edges, circumferential and longitudinal (depth wise) directions. Heat transfer and its contribution towards microstructural alteration is also somewhat found in the literature. In general, laser beam cutting is widely attempted to cut nickel based superalloys. For the production of 3D geometrical features in nickel based superalloys the LBM is very rarely employed as per available open literature. For example, Ahmed et al. [39] fabricated 3D micro-channels in Inconel 718 by Nd:YAG laser. In another study [38], mathematical modeling of laser parameters has been presented to control the micro-channel size in nickel alloy (Inconel 718). Top views of micro-channels are shown in Fig. 7. The effect of laser parameters on geometrical and microstructural aspects are evaluated. The micro-channel's depth and width is mainly driven by the laser scanning speed.

The part quality produced by laser cutting highly depends on the surface finish of the cut section. In order to achieve a high quality cut section the excessive dross attachment and micro-cracks should be avoided. The surface roughness decreases with the increase in cutting speed. The optimal cutting speed ranges from 8 to 10 cm/s for 1–2 mm thick sheet. For the Inconel 718 having a thickness of 2 mm

Fig. 7 Microscopic images of micro-channels machined in nickel alloy (Inconel 718) under different parametric combinations [38]

and cut by Nd:YAG laser requires even low cutting speeds for the same results. However, the surface roughness of the cut section does not significantly depend on laser power for <2 mm thick sheets [40]. Laser cutting of mild steel with identical thickness and CW Nd:YAG laser parameters also yields the same inferences [41]. In addition, the oxidation reaction takes place in the kerf width forming some oxide layers. As the composition of Inconel 718 contains more reactive constituents such as chromium, nickel and niobium than the mild steel. Therefore, the heat energy caused by the oxidation reaction produces deeper grooves with higher peaks and valleys in the cut section of Inconel 718. The average surface roughness ($R_a \sim 3$ μm) can be achieved by increasing the laser power to 4 kW and an assist gas pressure of 19 bar. The increase in laser power and cutting speed however increases the taper ratio of top and bottom cut edges. However, the increase in assist gas pressure shrinks the top edge taper. There is a relationship, developed in [42], between laser parameters and kerf width depicting that the minimum kerf width of the cut section lies in the range of 0.53–0.61 mm. The recast layer thickness becomes high for high laser power but can positively be controlled by increasing the assist gas pressure and the cutting speed up to 3 cm/s. One of the common feature of laser cutting is the formation of striations on cut sections. These striations are classified into two regions. To certain penetration depth there exists a smooth and finer striation structure. The striations are straight and parallel in this region. At the second region it becomes zigzag to the bottom of the cut. This variation is explained by the divergence behavior of the laser beam along the workpiece thickness. As the beam diverges through the material thickness it becomes less intense compared to the top of the cut. The striation frequency is almost independent of power but can be controlled by cutting speed adjustments. The heights of the first region decreases while the second region heights increase by increase in cutting speed irrespective to laser power [43].

2.5.4 Laser Beam Milling of Ceramics and CFRP

Carbon fibers (CF) need approximately 98 % of energy absorption for its ablation [44]. For sublimating a single CF layer (10 μm thickness) under the area of 50 μm radius, more than 10 mJ of absorbed energy is required [26]. If the absorbed energy is too much then melting will occur and if it is too little then insufficient thermal stresses would result [45]. On the other hand, the edge remains unaffected with respect to crack, delamination and thermal damaging [46]. Quality of the CFRP strongly depends on the operating wavelength as well. The HAZ gets doubled for 1064 nm wavelength as compared to 532 and 355 nm [44]. The "perpendicular heat flow model" is helpful to achieve the minimum thermal damage in matrix materials and to understand the damage mechanism [26]. In addition to other laser oriented parameters, temperature dependent absorptivity and thermo-physical properties (conduction, convection and radiation based heat transfer) of the

material also play an important role in quality of laser beam milling in ceramics [18]. These parameters mainly affect the MRR and side tapering during 3-D machining of ceramics [47].

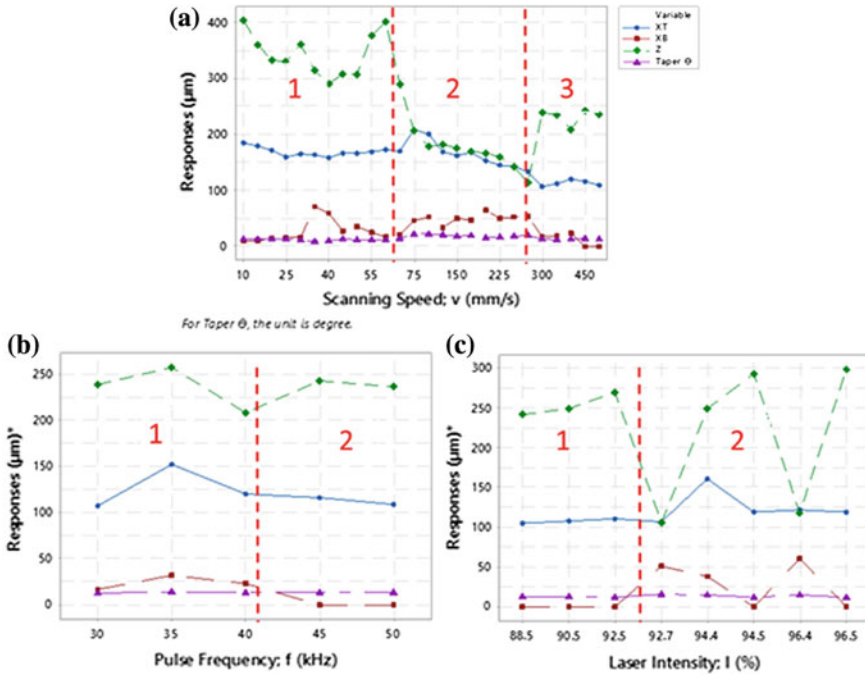### 2.5.5   Parametric Effects in Laser Beam Milling

Pulsed wave as well as continuous wave (CW) Nd:YAG and CO_2 lasers are commonly experienced in laser beam milling. Ytterbium fiber and excimer lasers are also getting popular in the last decade. Generally, the average power of 8–20 W with relatively high pulse frequency (10–80 kHz) is suitable for laser beam milling of metals and non-metals. High laser power ($\sim$500 W) is also adopted by some researchers but not in common. The only parametric difference (metals vs. no-metals) is in the pulse frequency (up to 600 kHz) and spot diameter (up to 10 µm) for non-metals. For reference, first half of Table 3 shows the detailed parametric window for laser milling. There is a lack of information in the studies about the proper reasoning of these parametric variations.

The major problems of laser beam milling are low MRR, recast layer, delamination, cracking, thermal damage and HAZ. Residual stresses, white layer and work hardening layers, as well as microstructural alterations are reported by Ulutan and Ozel [48] as the potential problems associated with laser ablation particularly on titanium and nickel alloys. Although the problems are mostly the same for metals and non-metals but their controlling and dependence is different for different materials. For example, certain metallic alloys have high viscosity in molten state due to which it is difficult to ensure clean cut. There are a number of limitations of laser machining of metals and the influence of operating parameters on productivity as well as on the quality of the machined surface. The productivity depends mainly on the frequency of the laser pulse. Aluminum alloy (AA6056) behaves differently at higher frequencies (f $\geq$ 5500 Hz) than stainless steel (X3CrNi18-10) and titanium alloy (Ti6Al4V). The surface roughness of the machined surface depends mainly on the pulse frequency and, secondarily, on sweep speed. Cicală et al. [49] obtained the lowest levels of roughness ($R_a \approx$ 2 µm) with the highest frequencies (f $\geq$ 7500 Hz) and with low sweep speeds (6 mm/s). Pulsed laser micro-polishing can be employed to reduce the surface roughness and mill scratches. High pulse frequency (4 kHz) is the key parameter to control. However, surface cracking occurs when polishing is done in air but it can be avoided by using a shielding gas. Argon gas shielding demonstrates good results. It validates a crack free surface and a reduction in average surface roughness by a factor of two for Ti6Al4V [50]. The effects of laser parameters on the micro-channel geometry has been studied in [51], as shown in Fig. 8. It is reported that the laser scan speed along with laser current intensity plays most important role during laser milling of micro-channels.

Table 3 Parametric window of LBM

Process	Work material	Investigations	Laser type	Laser parameters					Modeling	References
				Average/peak power	Wavelength	Pulse width	Frequency	Spot/beam diameter		
Laser beam milling	Metals	• HAZ • Recast layer • MRR • Cut quality • Polishing	• CW CO_2 • Nd:YVO$_4$ • Nd:YAG • Ytterbium fiber	550 W 10 W 2–8 W 30 W	532 nm 1064 nm	10 µs	10 kHz 20–80 kHz 30–50 kHz	5 mm 40 µm 70 µm 30 µm	• One-dimensional hydrodynamic model [29] • RSM based mathematical model [38]	[29, 39, 50, 51, 64–66]
	Non-metals	• MRR • Tapering • Thermal damage • Temperature fields • HAZ	• Pulsed Nd: YAG • CW Nd: YAG • CW CO_2 • Ytterbium fiber	470 W 10–23 W 20 W	1.06 µm 355 µm 532 µm 1064 nm	0.5 ms 10 ps	20 Hz 600–680 Hz 200 kHz	0.5 mm 10 µm 3 mm 32 µm 73 µm	• Thermal model • RMS based mathematical model • Heat flow model • FEA for temperature and stress fields	[18, 26, 44–47, 67, 88]
		Alumina SiC Si$_3$N$_4$ Magnesia Al/Al$_2$O$_3$-MMC CFRP Glass ABS PMMA								
Laser beam drilling/ trepanning	Metals	• Thermal distribution • Recast layer • HAZ • Hole taper • MRR • Spatter • Cracking	• CO_2 laser • Nd:YVO$_4$ • Pulsed Nd: YAG	2 kW 18 W 14 kW 400 W 10 kW 75 W	532 nm 1.06 µm	10 ns 5 ms 10 ms 120 ns	20 kHz 20 Hz 1 kHz 10 Hz	0.5 mm 300 µm 100 µm	• FEA analysis with ABAQUS • Finite Element Method (FEM) and Artificial Neural Network (ANN) • Analytical model	[29, 69–282]
		Ti6Al4V Stainless steel Nickel and cobalt based superalloy Aluminum Gamma titanium								
	Non-metals	• MRR • Hole taper • Hole circularity	• Pulsed Nd: YAG • Pico second laser		1064 nm	0.5 ms 60 ps	20 Hz 250 kHz	35 µm	• Mathematical model	[67, 68, 77, 79]
		MgO ABS PMMA Si wafer								

Fig. 8 Parametric effects on micro-channels of size $100 \times 100\ \mu m$ **a** effect of scanning speed, **b** effect of pulse frequency and **c** effect of laser intensity [51]

2.5.6 Microstructures and Micro-hardness Profiles

The observation of the microstructure clearly indicates finer grains in the laser machined regions compared to the as-received material. Figures 9 shows the microscopic images of laser machined areas at different magnifications, respectively. Before proceeding to the microstructure of laser machined regions, it is worth noting to have a glance at fundamentals of Inconel 718 and its characterization. Inconel 718 gains its high temperature strength mainly through precipitation of body-centered tetragonal (BCT) γ'', Ni_3Nb, dispersed in the γ matrix [52]. Additionally, face-centered cubic (FCC) γ', Ni_3 (Al, Ti), provides additional strength for the alloy [53]. In addition, γ'' usually precipitates at higher temperatures (720 °C) whereas γ' precipitates at lower ones (620 °C). The solvus temperatures of γ'' and γ' are about 900–920 °C [54]. γ'' particles are considered as metastable and over long term exposure to temperatures above 650 °C, transform into the stable form of Ni_3Nb, i.e., the δ phase. This phenomenon leads to the degradation of mechanical properties [52, 55, 56]. Alloying elements such as Fe, Cr, Mo, Al, and Ti also strengthen the alloy through solid solution mechanisms [56]. In addition, primary carbides, mostly Nb, and orthorhombic δ, Ni_3Nb, precipitate at grain boundaries and inhibit grain boundaries to slide at high temperatures [53].
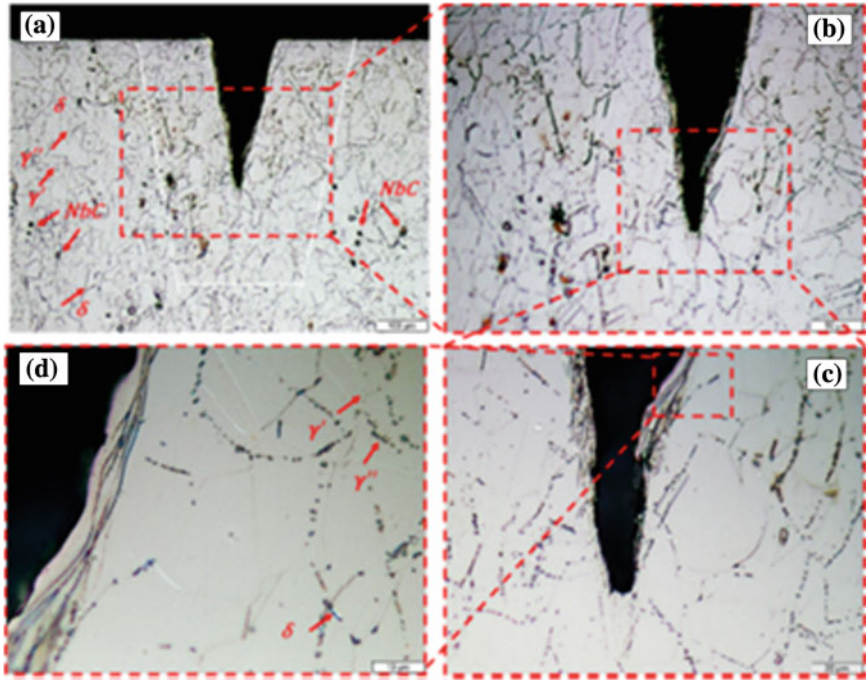
Fig. 9 Microstructures of closed vicinity of laser-machined Inconel 718 at magnification: **a** 10×, **b** 20×, **c** 50×, and **d** 100× [39]

At the first sight a significant difference in microstructure of areas close to the laser machined micro-channels is not detectable. However, paying close attention to Fig. 9a it can be seen that there are two regions divided by white lined trapezoidal shape. The area far away from the trapezoidal region contains uniform precipitations of δ, γ', γ'' and secondary carbides. Such precipitants are very rarely spread near the sub-surfaces of the channel (inside the white trapezoidal region) which are not noticeable at lower magnifications but at the higher ones as shown in Fig. 9d. As laser beam machining in air produces heat affected zone (although it is not examined in this study) to the close vicinity of machined features, therefore, the rise of temperature allows the γ' and γ'' either transform into orthorhombic δ or remains them to be less prominent and non-uniform. The low density of these precipitants at the channel's immediate sub-surfaces somewhat alter the strength properties i.e. hardness. It is validated by the micro-harness profiles discussed in the next section. Recast layer is the well-known drawback of laser beam machining as appeared at the inner surface of each micro-channel as magnified in Fig. 9c, d. This recast layer of an average thickness of 10–12 μm is the result of deposition of melt debris and adherence to the inner surface. At this surface the grain boundaries are longitudinally stretched to form lamellar structure. High temperature of melt debris allows the grains to overlap and slide along the channel's inner surface [53]. This grain's
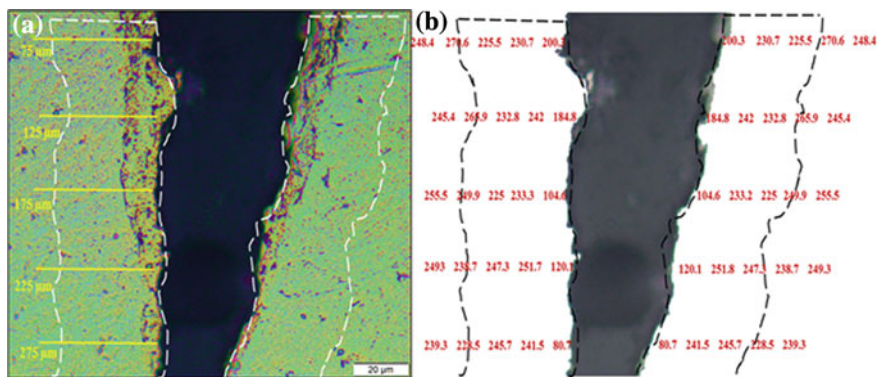
Fig. 10 Micro-hardness profile of lase-affected regions adjacent to the machined channel [39]

sliding inhibits the recast layer to loosely solidify resulting into degradation of hardness.

There is a variation in micro-hardness within the areas of ablated channels. At the edge of channel the hardness of each layer is significantly less than the hardness of base metal. The hardness profiles around the micro-channel's edges are shown in Fig. 10. The hardness values of deep layers ($\sim$100 HVA) are highly less than the hardness of upper layers ($\sim$200 HVA). This significant drop in hardness is due to the formation of recast debris at the edges of channel. However, the thickness of recast layer is not uniform throughout the depth of channel. As the ablation goes deep and deep the recast thickness becomes more and more. The average thickness of recast below the middle section of channel is found to be of 10–12 µm. This recast layer cannot be considered as the base metal rather it adhered to the base metal and solidifies with loosely packed grains with lamellar microstructure (refer to Fig. 9). High thermal energy enclosed in a narrow region causes the phase transformation at the edges and soften its neighboring areas. Phase transformation and recrystallization causes the material to become less hard but more ductile [57]. That is why the hardness of this area is soundly less than the hardness of bulk material. At a distance of 50–150 µm from the edge of channel, the hardness of each horizontal layer fluctuates within 225–260 HVA. This fluctuation can be related to the distribution and transformations of γ' and γ'' into orthorhombic δ which are believed to participate in the strength properties of nickel based super-alloys. The hardness of each layer exactly coincides with the hardness of bulk material at a distance of 200 µm from the edge of channel. Hence, it can be said that the area of 150 µm^2 around the channel symmetry becomes slightly ductile compared to the base metal.

2.5.7 Temperatures and Stress Field Distribution

Laser heating in the presence of assisting gas is usually employed to evaluate the temperature and stress field distributions. It is also used to evaluate the microstructural alterations due to laser irradiations. During laser heating, a high power (in kW) laser is generally used with relatively larger (in millimeters) spot diameters. The heat dissipates/penetrates along the three axis (x, y and z) at the same time but the distribution pattern varies for each direction. Along the x-direction (the laser movement direction) the heating cycle is more temporal and uniform than for the cooling cycle. As the heat generated beneath the spot distributes along the x-axis at one region, in the meantime the laser beam moves in the same direction to a new region. In this way the new region starts heating from some preliminary value (say half of region 1's heat) and is further heated to the peak value by the laser beam. This results in peaks and valleys in heating cycle (see Fig. 11). The valleys are in fact the average surface temperature along the x-direction. However, during the cooling cycle the temperature gradient reduces sharply due to laser spot movement. Temperature variations along the y-axis usually follows the Gaussian distribution (as of laser beam) during both the cycles. But it could be somewhat different if the laser beam follows other distributions. Along the z-axis the temperature at the surface remains maximum and decays gradually in the surface vicinity and the decay becomes sharp in the area next to the surface vicinity. During laser heating by high power, CO laser allows to achieve a crack free surface of Inconel 718 and depth of laser treated region extends almost to 50 µm below the surface. Laser heating improves the micro-hardness at the surface due to the grain refinement and high cooling rates provided by the assist gas [58]. High pressure nitrogen gas is most common in assisting gases.

The measurements of surface temperature is always considered as the tedious task. It is usually very difficult or often impossible to directly measure surface temperatures introduced by machining processes such as deep drilling. Reissig et al. [59] presented a post-mortem-method, which allows to determine maximum temperatures during machining by measuring the local vanadium concentration in
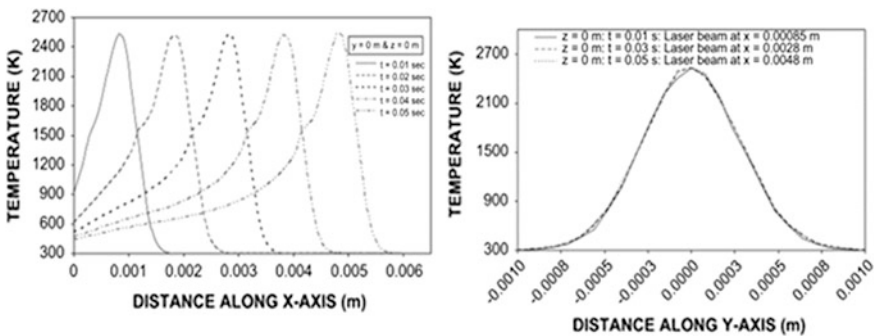
Fig. 11 Temperature distribution along the x-axis and y-axis at different heating periods [58]

transformed β-grains in Ti6Al4V. The pseudo-temperature can be detected in volumes as small as 50 nm^3 and can even be obtained directly at free surfaces. In order to investigate the complicated transient thermal phenomena in laser micro-machining, it is essential to accurately measure time-resolved temperatures of workpiece resulted from the transient laser–material interaction. While numerous analytic and numerical models have also been developed, little experimental results are available for a solid understanding of the transient thermal phenomena in nanosecond pulsed laser micromachining. Choi and Li [60] demonstrated that micro thin film thermocouples (TFTCs) can be useful in measuring the transient temperatures at micrometers away from the laser–material interaction region on the workpiece during laser micromachining, and the measured data could be utilized to validate and improve existing analytical and numerical models.

2.5.8 Laser Induced Periodic Structures

Use of high average power density or laser fluence (0.28–30 J/cm^2) and low number of overscans cause the material to become porous with high surface roughness. As the average power density increases, microscopic holes (pores) with average dimensions of 300–400 nm appear on the surface. However, by increasing the overscans (5–90) with low fluences the pores can be avoided with low surface roughness. But, for very low average power densities the surface morphology of irradiated areas comprises of ripples. The appearance of such ripples is a general phenomenon of laser ablation termed as laser induced periodic surface structures (LIPSS) [61]. This phenomenon has been detected in many different materials from metals to semiconductors. According to Fauchet [62] formation of ripples is a result of an interference between the incident laser beam and surface electromagnetic wave randomly dispersed on the surface asperities. However, stated by Fournier et al. [63], the material surface also undergoes some self-organization processes during its relaxation from a state of high non-equilibrium following the ultrafast heating by femtosecond laser. It could also be possible that the formation of ripples is the result of such processes.

2.5.9 Laser Beam Milling with Auxiliary Concepts

To challenge the traditional problems of dry laser ablation, laser beam milling is also interestingly connected with some auxiliary concepts such as combining grit blasting with laser milling. The schematic setup of laser milling assisted with grit blasting is shown in Fig. 12. Grit blasting can eject the molten material more efficiently. Under the same operating conditions as for traditional laser beam milling, this dual process allows to achieve 100 % MRR and 15 and 60 % reduction in HAZ and surface roughness respectively for mild steel, stainless steel and titanium alloys [64]. Similarly, MRR and quality of laser beam milling can be enriched by the laser-induced plasma micro-machining (LIPMM) process. When the laser beam

Fig. 12 Schematic of laser milling assisted with grit blasting [64]
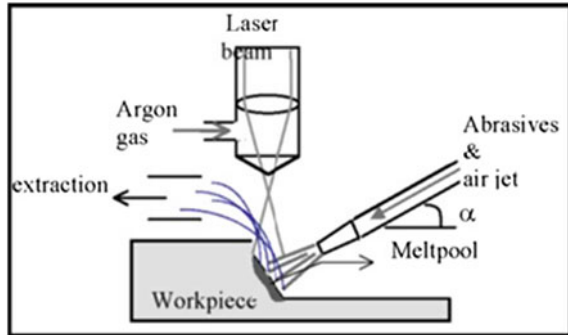
is focused, on the workpiece submerged in the dielectric, deionization of the dielectric occurs resulting in plasma spot formation. It is claimed that the process can machine, more competitively, a variety of materials including metals, ceramics and polymers [65]. Recast layer is considered as a major drawback of laser beam milling. Instead of elimination and avoidance of melt recasting, the utilization of the recast layer can be experienced in a positive sense. Lee et al. [66] adopted this technique of piling up the recast layer to synthesize the micro pins as shown in Fig. 13. Using a combination of recast layers and their successive piling-up can generate micro pin arrays of a length 603 μm in steel.

2.6 Laser Beam Drilling/Trepanning

Laser trepanning and drilling is another member of the LBM family. It allows to drill and trepan macro as well as micro holes in non-metals as well as in metals and alloys. Laser beam drilling in different types of ceramics can be seen in Fig. 14.

2.6.1 Ablation Mechanism in Laser Beam Drilling

In principle, the ablation mechanism in drilling is more or less similar to the basic mechanism of laser beam milling. However, some differences are encountered if the aim is deep drilling or through drilling. When laser radiations strikes on the workpiece surface then absorption, reflection, refraction, scattering and transmission takes place which leads to the complex understanding of the actual ablation phenomenon. Among others, the major phenomena include melting, dissociation and evaporation processes. The dissociations or decompositions in metals and ceramics contains all the three material states; solid, liquid and gas. The vaporized material develops a vapor pressure, acting in upward direction, proportional to the laser fluence and inversely to the machined depth.
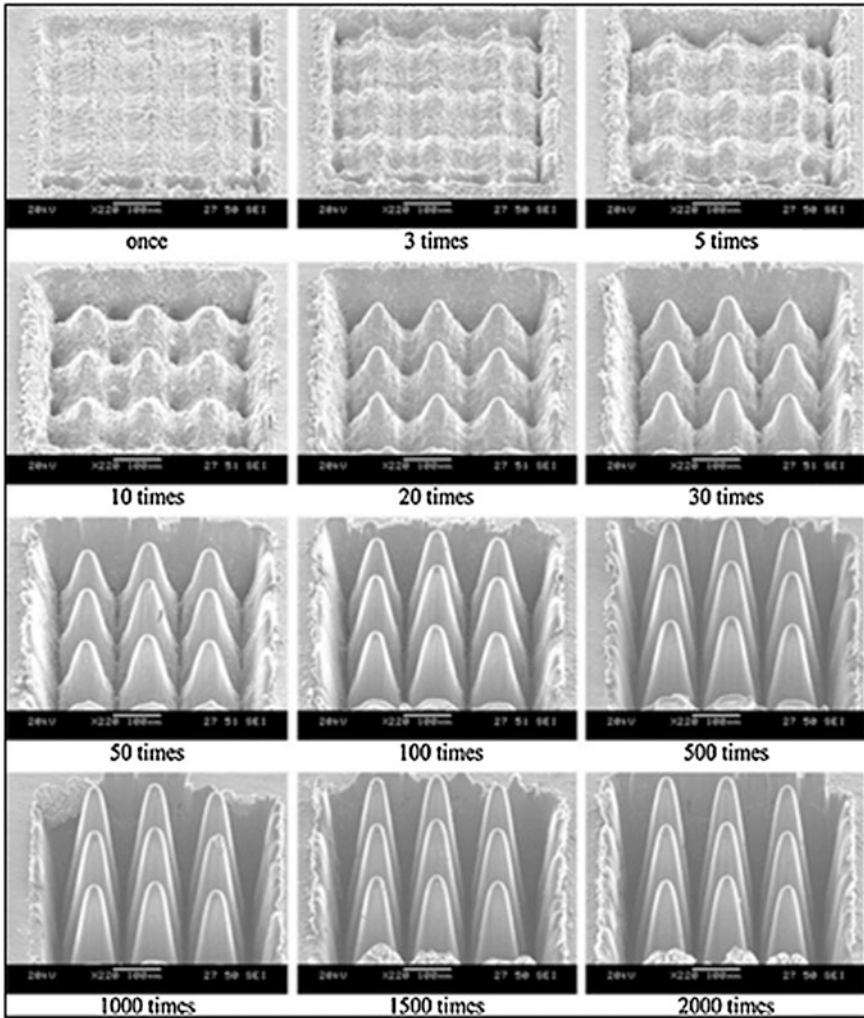
Fig. 13 Recast layer piling procedure according to the scanning repeat count [66]

$$Vapor\ Pressure = \frac{Laser\ fluence}{Machined\ depth}$$

That is why for deep machining the material removal offers more resistance [67]. As ablation depends on the energy absorption which solely varies from material to material [68], that is why the depth of machined feature does not remain the same for even same class of materials and sometimes originates side [69] and interfacial cracking [70]. The mechanism becomes different if the target is through machining, especially when the ablation reaches near the bottom of the substrate. At this point
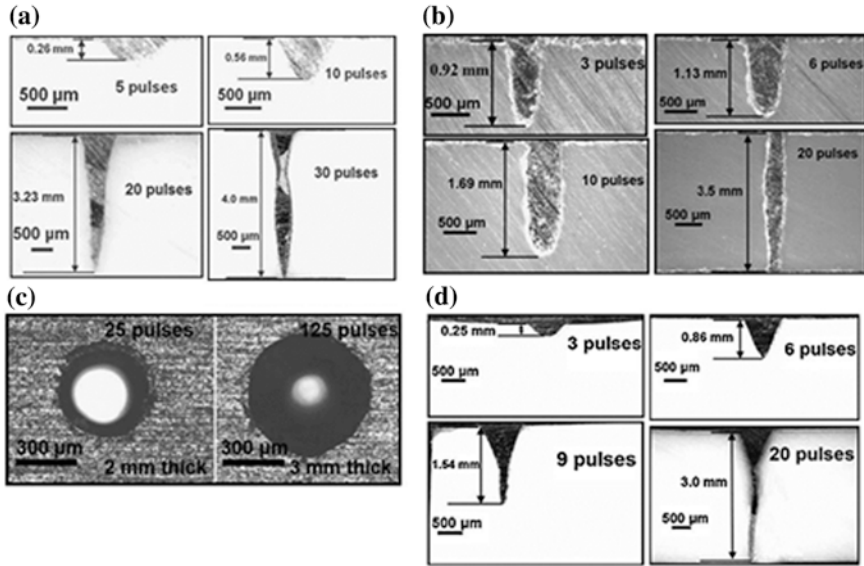
Fig. 14 Laser machining of **a** Al_2O_3, **b** Si_3N_4, **c** SiC and **d** MgO [67]

another force (gravitational force of the melt) may come into place which causes the vaporized material to flow downside instead of moving upward [71]. There is also loss of material due to vaporization. Machining of alumina is the result of combine effect of dissociation, evaporation and melt expulsion. In this case recoil pressure of the melt is the major responsible of material expulsion. Dissociation and evaporation together lead to machining in silicon nitride. The most likely reactions for the decomposition of MgO, Al_2O_3, Si_3N_4 and SiC under laser are (equation)

$$MgO \rightarrow Mg_{(s)} + O_{(g)}$$

$$Al_2O_3 \rightarrow 2Al_{(l)} + \frac{3}{2}O_{2(g)}$$

$$Si_3N_4 \rightarrow 3Si_{(l)} + 2N_{2(g)}$$

$$SiC \rightarrow Si_{(l)} + C_{(s)}$$
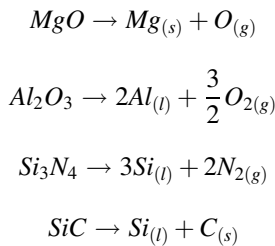
2.6.2 Parametric Effects in Laser Beam Drilling

A range of laser types (CO_2, Nd:YAG, Nd: YVO_4) are applied for drilling metals but the pulsed Nd:YAG is the only type which is commonly employed for drilling of non-metals. High laser power (in kW) and high pulse frequency (1–250 kHz) is generally required for the drilling process. However, low power can also be

employed with other parametric adjustments. In terms of wavelength there is a close match between metals and non-metals. However, the pulse width is different for metals (5 ms–10 ns) compared to non-metals (in Pico seconds). The recommended spot diameter for metal drilling is 100–300 μm and nearly 30 μm for non-metals (referenced in below half of Table 3).

The main concerns in drilling is to achieve a high aspect ratio, better circularity and low taper. However, in many applications a taper-less or reverse tapered hole is required. In connection to the laser power, assist gas pressure, number of pulses, pulse energy and standoff distance are the controllable parameters for the above said concerns. During deep hole drilling (25 mm thickness) of Inconel 718, five process parameters—pulse energy, pulse duration, pulse shape, focal position, and assist gas pressure—are crucial for the hole quality [72]. Increase in power and number of pulses and assist gas pressure increase the depth of hole (see Fig. 14) but insignificantly (20 %) affect the taper and circularity in polymeric materials [67], nickel based alloys [29] and aluminum sheets [73]. However, laser power and assist gas severely affect the drilling of small holes (2 mm diameter) and deposit high spatter around the hole [74]. The size and temperature of the melt significantly affect the hole taper and spatter deposition [75]. But, the spatter can be minimized by some anti-spatter composite coating (ASCC) [76]. The standoff distance controls the taper and circularity but majorly (80 %) contributes to the taperness [77]. The drilling quality is also very much sensitive to the consumption and flow of assist gas [78]. It directly affects the material removal capability [79], drilling speed [80] and the thermal distributions due to convective cooling by the assist gas [71]. Temperature and HAZ variations are different along the circumference than along the thickness. A handful FEA findings for metal drilling exists in literature to estimate thermal distributions and HAZ but for non-metals such modeling is not very common. Beno and Hulling [81] deduced a methodology for the temperature measurements at the edges (during cutting and drilling) of tool steel, aged Inconel 718 and Ti6Al4V. They employed a two color fiber optic ratio pyrometer which has the benefit of measurement of temperature irrespective to the work material's emissivity. The emissivity depends only on the incident wavelength not on the temperature, direction or surface structure.

In common practice scanning optics are utilized in laser drilling process. Scanning optics always shape a taper in drilled holes which is a universal problem of laser drilling. LMBT GmbH in Germany (working in the areas of biomedical optics and applied laser technology) designed a patented device (in two models; 2.1 and 2.2) with rotating optics which can resolve this problem [82]. The device allows the beam to displace angularly at a controlled speed and inclination. They achieved even the reverse taper hole in stainless steel [83]. In a similar fashion, laser helical drilling can fulfil modern drilling requirements, in which the laser beam rotates relative to work. The hole diameter in helical drilling is mainly the function of diameter of helical motion, but also influenced by the pulse energy [84]. Man et al. [85] experienced a laser micro-drilling on titanium and TiN coated titanium. Because of the difference in melting points between the TiN and Ti phases, holes of different geometry were obtained. In the TiN coated titanium specimen vase shape

holes were obtained. By applying the electrochemical dissolution technique, the vase shape holes were connected at the root of the holes and a subsurface porous network was formed. This structure is expected to enhance the fixation of dental implants [85].

2.7 Dual Beam Laser Machining

Traditionally the laser beam milling utilizes a single beam of laser in all of its process either it is cutting, milling, drilling or trepanning. Few of the researchers employed two types of laser beams to perform the same operations of laser beam milling as of single beam. One beam is normally defocused and the other is focused. In dual beam laser machining a focused CO_2 laser scribes the straight line whereas a defocused CO_2 laser beam (see Fig. 15) irradiates on the scribing line to induce thermal stresses and separates the material by fracture propagation. The defocused laser has the lower power densities and does not melt the surface but induces the steep thermal stresses during the cooling step. If thermal stresses are larger than the rupture strength, the fracture propagates along the scribing line and subsequently the material gets separated from the bulk [45]. The comparison between single laser beam and dual laser beam machining shows that dual laser offers less thermal stresses in final. It is suggested that if the distance between off-focus and focused beam is chosen closer and closer then the stresses can further be reduced [86]. The dual beam could be from two distinct sources or single beam splitting into two siblings by mirror reflection arrangements. Such arrangement is designed by Wan et al. [87] with the name of laser beam modulating device as schematically presented in Fig. 16. The design consists of an optical beam expander with a fast rotating beam chopper which splits the mother beam into two parts.

The dual beam concept is also applicable in the fracture machining element technique in which the machining is carried out in the form of removal of series of predefined shaped elements. The laser beam focuses on the work to scribe a series of groove cracks. The defocused laser originates the tensile stresses concentrated at

Fig. 15 Configuration of a laser cutting system with the dual-laser-beam method [45]
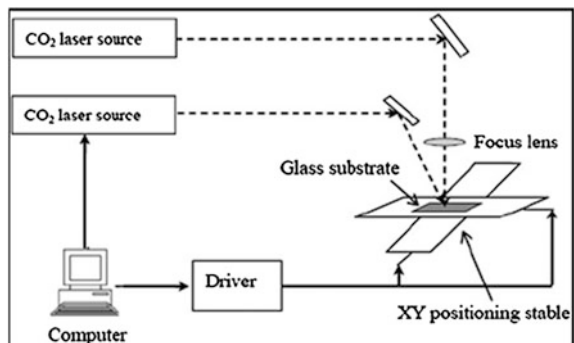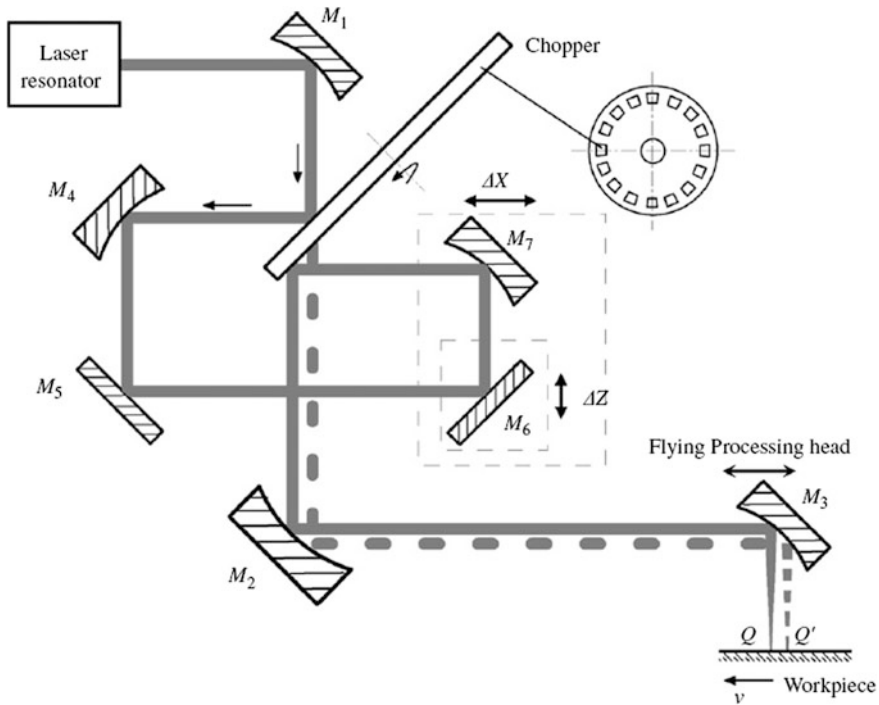
Fig. 16 Sketch of beam modulating system [87]

the tip of the groove-crack and penetration of the existing crack further propagates. The material removal is thus the result of the linkage of grove-cracks [88].

2.8 Conclusions and Remarks

Laser beam milling is an extensively used process that equally suits for metals and non-metals. Laser cutting, milling, trapenning and drilling are the famous processes. From the above discussion the following inferences could be realized:

1. There are many factors influencing the ablation mechanism. The driving forces for the ablation are still not well understood due to complex phenomena occurring at machining zone.
2. The ablation mechanism is different for laser beam milling compared to drilling. There is also a difference in mechanism for blind and through drilling.
3. Laser power, assist gas pressure, number of pulses, pulse energy, and standoff distance are the governable parameters in laser beam drilling which directly influence the circularity and taperness of the drilled holes.

4. In terms of laser parameters, the only common difference in laser beam milling and laser beam drilling is the choice of laser power. Generally, high power lasers (in kW) are employed for laser beam drilling and low power (in hundreds of watt) for laser beam milling.

5. The commonly known problems of laser beam milling are low MRR, recast layer, delamination, thermal damage and HAZ.

   (a) On the one hand, these are controlled by tuning the wavelength, spot diameter and pulse frequency. The laser power also influences but generally low power (average power of 8–20 W) with relatively high pulse frequency (10–80 kHz) is suitable for LBM of metals and non-metals.

   (b) On the other hand, some auxiliary techniques (Grit blasting, laser-induced plasma micro-machining; LIPMM) along with laser irradiations show competitive results in terms of MRR, HAZ and cut quality.

6. Thermal stresses induced by laser heating is a prevalent problem of laser beam milling. The use of a dual laser beam could be another alternative having the potential to reduce the thermal stresses.

3 Laser Assisted Machining (LAM)

LAM is a method of generally machining difficult to machine materials in which laser energy is used as an intense heating source while mechanical energy from some other process (planning, turning, milling etc.) is used to remove the material. The laser energy thermally softens the material and the cutting tool immediate behind the laser spot removes the material [90]. The material does not undergo any melting or evaporation state as in case of LBM. Indeed at the point of cutting, the high temperature generated by laser irradiations weakens the specific cutting energy which improves the machinability. For large number of materials the drop in materials strength occurs in between 500 and 600 °C [91]. A geometry of laser assisted machining (LAM) during turning is shown in Fig. 17.

3.1 Material Removal Mechanism in LAM

The LAM mechanism is very complex in nature due to the complexity of influencing parameters and their mutual interactions [93]. There are four types of parameters [91]:

 (a) Cutting parameters (speed, feed rate, depth of cut, type of tool etc.)
 (b) Tool parameters (tool type, side/rack angles, nose radius etc.)

Fig. 17 Geometry of laser-assisted machining (LAM) [92]
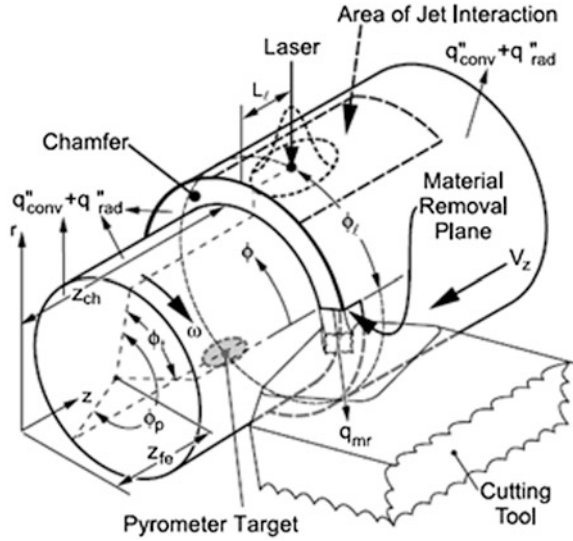
(c) Laser parameters (power, repetition rate, pulse width, spot diameters etc.)
(d) Interaction parameters (laser orientation, laser to tool distance etc.)

When work temperature increases the viscosity of the boundary particles decreases which enhances the plastic flow [90]. So, when the temperature reaches to the material's glassy phase transient temperature, the viscosity decreases and the material lattice gets mobilized. The lattice begins to slip at its boundaries. The tool cutting forces by tool cause, later on, the plastic deformation and actual material removal [94]. The mechanism becomes slightly different when dealing with metal matrix composites. This is due to the tool-particle interaction behavior. For example, TiC particle gets broken during LAM of matrix plastic deformation and embed into the matrix softened by LAM sponsorship [95].

Chip formation is an essential element of LAM and depends on several factors. The chip quantity also increases by increasing the temperature [90]. Generally, the shape of chip formed in LAM is highly irregular patterned characterized by larger fluctuations in segment height. Increase in cutting speed results in thinner chips. However, in LAM of Nickle alloys continuous ribbon-like chips are found. LAM oriented chips show more tendency to shear localization and greater strain in the primary shear zone due to the thermal softening influence [96]. There are three softening mechanisms involved in this context [97].

(a) Material yield strength reduction
(b) Material base hardness reduction
(c) Elimination of the work hardening.

3.2 Parametric Effects and Inspirations of LAM

Laser assistance is more widely practiced in conventional turning of hard-to-machine materials such as ceramics, hardened steels and metallic alloys (nickel and titanium). The turning process can be enriched in terms of tool life, cutting forces, material removal rates (MRR) and workpiece surface integrity (upper half of Table 4). However, during traditional milling and planing processes very few attempts are made regarding LAM. The focus is only converged to evaluate the reduction in cutting forces and HAZ (lower half of Table 4). There is very less attraction towards MRR and surface integrity.

3.2.1 Cutting Forces and Material Removal Rate

Cutting forces increase with an increase in feed rate during conventional turning and obeys a linear relationship. But, during LAM, the cutting forces are always lower at all feed rates and cutting speeds (see Fig. 18). It is interesting that during LAM the relationship also remains linear as the cutting forces depend upon the MRR. On average 12 % forces can be reduced during LAM of titanium beta alloys [98]. Among others, laser power is the majorly influencing parameter for heating, cutting forces and MRR. High power ranges from 1.5 to 2.5 kW are mainly reported. The laser power of 400 W or below does not impart any reduction in cutting forces in comparison with CM [99]. The cutting forces encounter in different directions and components. LAM can reduce the cutting feed forces by 22 % for ceramics [90] and hardened steels [100]. For titanium alloys, a reduction of force in x-direction up to 25 %, y-direction up to 60 % and z-direction up to 65 % can be achieved [101]. In sum of all, LAM can ensure cutting forces reduction by up to 40 % for different materials [91]. The cutting forces are commonly measured by a dynamometer or a three-component dynamic force sensor [102]. Kistler (model 9121 [95] and [103], 9255 [90]) dynamometer is proven to be good. A PCB Model 260A01 force sensor can be used to measure three-dimensional forces [98, 102]. Kim and Lee [104] examined the cutting force and preheating temperature predictions for laser-assisted milling of Inconel 718 and proved that its machinability can be enhanced by the reduction of cutting tool forces.

Reduction in cutting forces results in longer tooling life, high MRR and conclusively lowers the associated machining cost. LAM allows to achieve significantly high MRR in ceramics [94]. Hard to machine alloys (such as nickel based superalloys and titanium beta alloys) can even be machined with eight-fold high MRR via LAM [96, 98]. Due to lesser cutting forces, LAM can yield an overall cost savings of 30 % for titanium alloys [105] and about 20 % of compacted graphite iron (CGI) [103]. To reduce machining forces by LAM it is believed that the laser spot has to be as near to the tool as possible. Heat penetration increases with the increase in laser spot-to-tool distance which offers more thermal softening [102]. However, the distance between the tool and the laser spot must be sufficient to

Table 4 Inspirations of laser assisted machining (turning, milling and heating)

Process	Work material	Investigations	Machine	Tool	Laser type	Cutting force reduction	Increase in MRR	Surface roughness reduction	References
Laser assisted turning	• Al_2O_3 • Beta titanium alloy • AISI D2 • 4140 steel • AS2027 Grade Cr27 • Ti MMCs • Inconel 718 • AISI 4130 steel	• Cutting forces • MRR • Tool life • Surface integrity • Tool life • Microstructure	• FEMCO-CNC lathe • Hafco metal master lathe • Turret lathe • 3.5 hp lathe • CNC turning center • CNC lathe	• Cubic boron nitrides (CBN) • Tungsten Carbide (TC) • Carbides • Poly-crystalline-diamond (PCD) • SiAlON • PCBN	• Pulsed Nd: YAG 60 W • kW Nd:YAG • 1.5 kW CO_2 • 2 kW HDPL • 1.5 kW CW CO_2 • Ytterbium fiber	15 % 20–35 % 15 % 24 % 20 %	23.5 mm³/S 20 % 800 %	Oxide free layer 5 % 15 % 25 % 30 % Up to 0.3 µm 2.98 µm less	[92, 94–96, 98–100, 102, 103, 105, 108, 113–115]
Laser assisted milling/heating	• A2 tool steel • Ti6Al4 V • Stainless steel • Mild steel • Titanium alloy • Nickel alloy • H-13 steel • 100Cr6 • Al_2O_3 • Mullite	• Tool wear • Cutting forces • Surface integrity • Thermal distribution • Tool life • MRR • HAZ	• CNC Milling • Machining center • Deckel Maho milling machine	• TiAlN-coated tungsten carbide end mill • Cubic boron nitride (CBN) end mill • TiAlN-coated carbide insert	• 35 W CW ytterbium doped • 1.5 kW CO_2 • Rofin-Sinar 2.5 kW Nd: YAG • Rofin-Sinar CW CO_2 • 6 kW Yb:YAG laser • CW CO_2 25 W	20 % in sum 25 % in x 60 % in y 65 % in z-directions	200 %	2.98 µm less	[64, 90, 106, 109, 110, 116, 117]

Fig. 18 Effect of cutting speed on cutting forces for CM and LAM (feed = 0.25 mm/rev) [96]
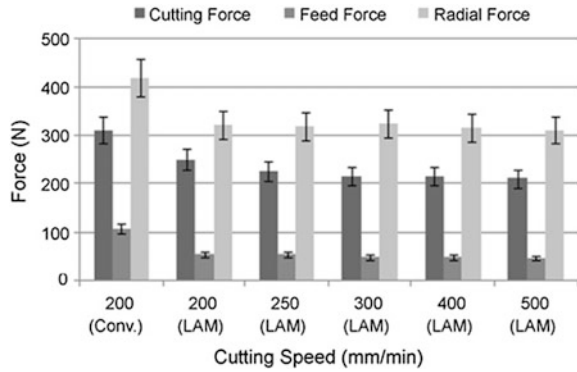
Fig. 19 Damage in the cutting tool when the laser beam is focused at a circumferential distance of 25 mm from the cutting tool [97]

prevent degradation of the tool (see Fig. 19). There is a minimum distance (45 mm) to avoid tool degradation by overheating [97]. During turning of titanium beta alloys [98], it is suggested that 208 ± 75 mm distance is safer. In laser assisted milling the distance is taken from the laser spot center to the cutting tool axis and similar number (250 mm) is nominal [106].

3.2.2 Tool Life and Surface Roughness

Tool wear is the major factor that adversely affects the work surface. If the tool life is enhanced, the tool wear would be less and consequently the resulting surface roughness could relatively be improved [94]. Tool wear is found to be widely evaluated during LAM and is always less (see Fig. 20) compared to CM. The microscopic images of tool flank wear during CM and LAM can be seen in Fig. 21. Most commonly used tools are tungsten carbide, cubic boron nitride (CBN) and

Fig. 20 Comparison of tool flank wear in conventional and laser assisted orthogonal machining: **a** 20 m/min cutting speed, **b** 30 m/min cutting speed [100]
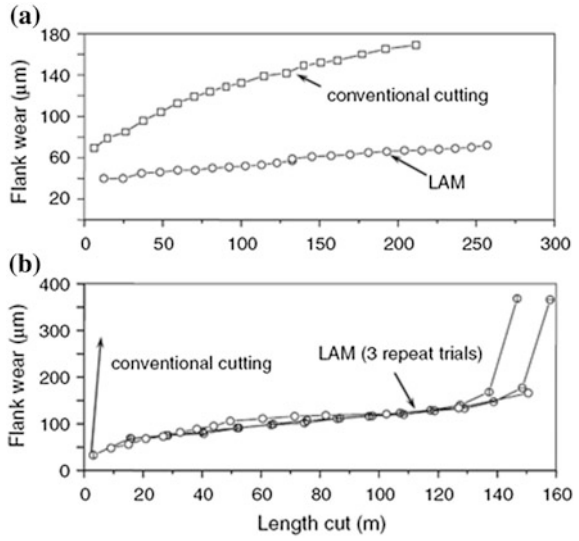
Fig. 21 Comparison of tool wear in LAM with that in conventional machining [94]
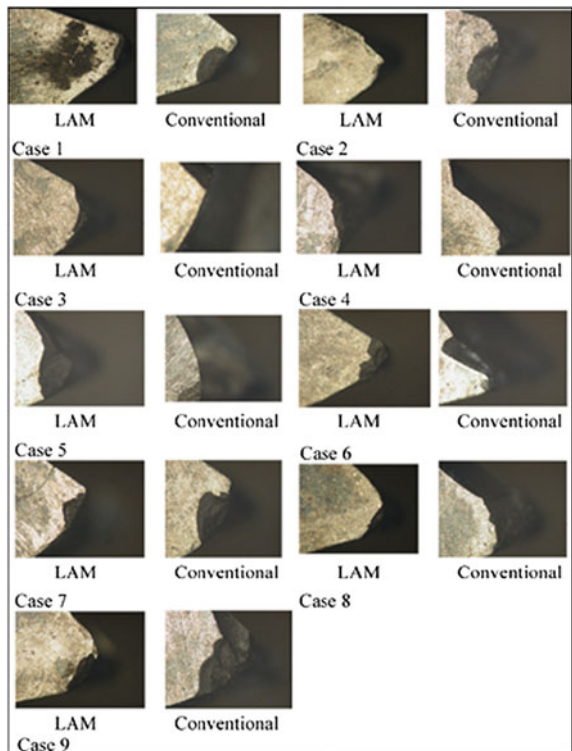
polycarbonate cubic boron nitride (PCBN). The results express a mix of belief especially for the surface finish. The reduction of the work hardening, by laser, leads to a lower notch wear that limits the threat of abrupt failure of the tool and hence the wear mode changes to flank wear, which results to a governable tool life and improved surface roughness [97]. The tool life (TC tools) can be improved in a range of 60–100 % for hardened steel [100] and CGI, respectively [103]. This improvement can be reached to 180 % for PCD tool against composites [95]. For testing the tool wear, ISO3685 standard is a scientific choice. It states that the tool life is the time it takes for the average wear on the flank to reach 300 μm or until the maximum wear on any part of the flank reaches 600 μm, whichever occurs earlier. The standard is very rarely adopted. That is why the [107]'s findings show contradiction with the other results and stated that at 150–250 °C the tool life improves maximum to 7 % but above this heating range, the tool life is shortened rather than improved.

On the other hand, laser assistance positively affect the surface finish. It allows to achieve a surface finish of R_a less than 0.3 μm for hardened steel [108] and ceramics [90]. For nickel [96] and titanium alloys, the surface roughness can be improved up to 30 % compared to conventional turning [105], however, very minor improvement (5 %) is reported for graphite iron [103]. For white cast iron and composites, the surface integrity results are reversed. The laser causes more frequent shearing of the material, and the surface profile results point to less uniformity [102]. In case of composites under LAM, roughness increases by 15 %. These contradictory results could be due to the difference of tool-particle interactions and chip formation mechanisms [95].

3.2.3   Temperature Fields Measurements and Microstructures

There are three kinds of temperature measurements and monitoring during LAM. To assure that the temperature reaches only the softening temperature, a static temperature measurement is essential [90]. Infrared thermometer or thermal camera [98] can be used to measure work surface and laser spot temperature [94]. Radiation pyrometer can also be used to record cutting zone temperatures [92]. The most widely used method of workpiece temperature measurement is the measurement via thermocouples (k or J type) [109, 110]. The micro thin film thermocouples (TFTCs) can be useful in measuring the transient temperatures at micrometers away from the laser–material interaction region on the workpiece [60]. The validation of thermocouple data can be calibrated by the study of [111]. These measurements can also theoretically be calculated by equations of transient heat transfer [102]. To predict the heat distributions, numerous techniques are seen such as Lattice Boltzman method [90], solving heat equations [112], parabolic heat conduction equation etc. [94]. Though, the transient, 3-D model is widely attempted [113]. The 3-D transient thermal model can be used to estimate the laser parameters for certain cut quality that will yield no HAZ [109].

Fig. 22 Variation of material removal temperature with laser power [92]
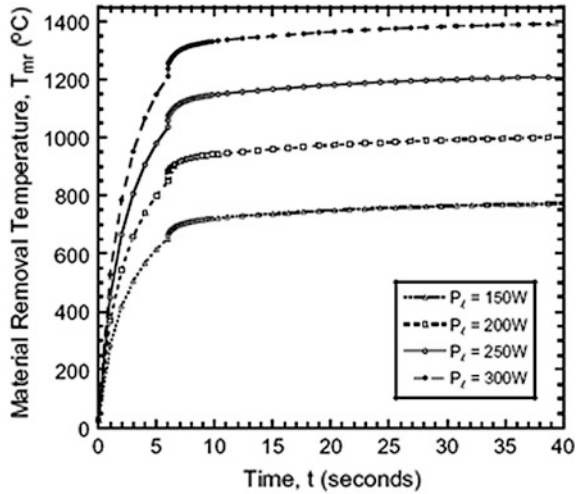
Temperature fields basically allow to understand the cutting force and residual stress phenomenon [91]. The laser power has a strong effect on LAM obeying a linear relationship with temperature variations (see Fig. 22) [92]. Cutting temperatures during CM and LAM, and the difference in temperature at the laser spot and the cutting region plotted against feed rate has also been reported in [98] as shown in Fig. 23. Depth and width of HAZ increase with increase of laser power [112]. The optimum laser power density is important to achieve the desired surface heating otherwise greater power densities can cause the plasma generation and consequently damage the surface prior to actual cutting [96]. The chemical constituents of the surface generated by LAM remain almost unchanged [90, 103] and
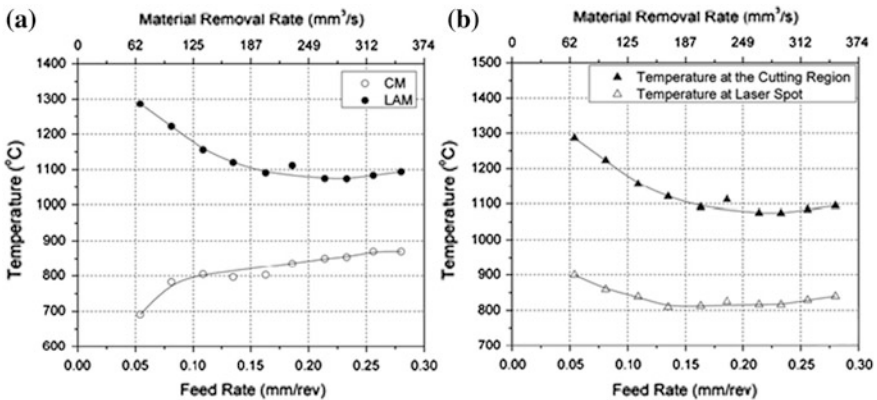
Fig. 23 Cutting temperatures. **a** During CM and LAM, and **b** difference in temperature at the laser spot and the cutting region plotted against feed rate [98]

cause no difference in microstructure [105]. In general, the higher the laser power is, the higher the hardness is near the surface of the workpiece. There appears to be no clear correlation between the depth of heat penetration and the hardness [102]. Micro-hardness shows that hardness is at maximum on the top surface and decreases towards bulk. At a depth of 150 µm the hardness approaches to that of the bulk material [110]. The hard surface layer is the result of strain hardening under high pressure and temperature conditions (during heating and machining) and afterwards the cold working action when the machined area rapidly cools down [96]. In general, LAM allows to achieve more uniform hardness and no microstructural change compared to conventional machining [108].

3.3 Conclusions and Remarks

The conventional machining processes, especially turning and milling, are aided by laser energy. The key motivation is to lower the workpiece hardness by softening the surface layers up to a certain depth by laser heating. The vital conclusions which may arise by this section includes:

1. The laser energy positively influences the LAM processes in terms of reduction in cutting forces, increase in MRR, improvement in tool life and more shiningly the surface integrity.
2. Laser assisted turning is the most widely endeavored process as compared to laser assisted milling.
3. Compared to conventional machining, the cutting forces are always lower during LAM at any feed rate value. On average, 15–35 % of cutting forces can be reduced by laser assistance for both turning and milling processes.
4. Laser power plays an important role in the reduction of cutting forces. High power ranges from 1.5 to 2.5 kW are mainly reported to reduce the yield strength of the material. The laser power of 400 W or below does not impart any reduction in cutting forces in comparison with CM.
5. The distance of the laser spot from the cutting tool is very important to avoid the melting of the tool tip. An average distance of 45 mm is considered as a safe distance.
6. In almost all the cases the surface roughness produced by LAM is lower than that of CM. A 30 % reduction in surface roughness can be achieved via LAM.
7. Overall tool wear is found to be less in LAM as compared to CM which leads to improved tool life. However, very rare conflict is there that negates the improvements in tool life.
8. LAM is capable to induce more uniform surface hardness with no microstructural alterations compared to CM.

4   Laser Chemical Machining/Etching (LCM/E)

Direct laser ablation mainly removes the material as vapor, hence, requires the delivery of a high power density within a very short interaction or pulse time. This leads to the formation of recast layers, burrs and melt droplets at the machining edge. For machining grooves even with pico-second or femto-second laser pulses this cannot be completely avoided. Laser chemical removal, that allows surface heating without surface melting or vaporizing, requires a low power density. Therefore, LBM's many drawbacks (such as detrimental thermal effects, recast or re-deposition of evaporated material) can be avoided [118]. Laser thermochemical etching of metals can be achieved in solutions of acids using pulsed or continuous wave (CW) lasers. Compared to electrochemical machining (ECM), that also allows the processing of conductive materials regardless of their hardness [119], LCM/E's aspect ratio is much smaller [120] but it has good agreement with better resolution [121] and surface roughness [122]. In comparison to direct laser ablation the MRR and aspect ratio of LCM/E are smaller but it involves little heat generation [123] and thus thermal effects do not occur [124]. Due to the required low laser power density, melting is avoided, resulting in high-precision cutting edges without burrs and debris. Furthermore, micro-cracks do not occur. Therefore, laser chemical etching is quite suitable for machining a wide range of materials not only thick samples [125] but also thin foils [126] and even wafers with high precision and ultra-smooth surface with nm level roughness [127]. The experimental setup used in laser thermochemical machining is shown in Fig. 24.

4.1   LCM/E Mechanism

The LCM/E mechanism is termed as the laser activated thermal-chemical mechanism [129]. Various phenomena are involved in LCM/E including laser energy absorption, chemical reaction, heat diffusion, hydrodynamics, and mass transfer.

Fig. 24 Experimental setup for laser thermochemical machining [128]
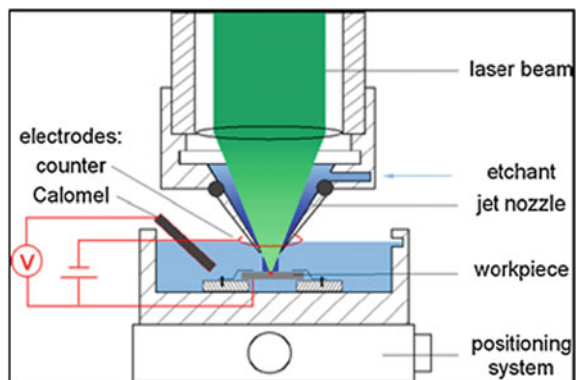
Energy absorption, chemical reaction and mass transfer are mainly found in open literature that govern the etching performance.

The reduction oxidation reaction (Redox reaction) is the fundamental phenomenon of LCM. It is driven by the temperature dependent proton activity of a redox reaction. The laser energy just supports the kinematic of dissolution and has no melting effects. The radiation wavelength has an indirect impact by variances in absorptivity of the machined material, but no direct impact. Main ingredients influencing the surface temperature of the material are the laser power, laser wavelength, and the spot diameter. In addition, reflectivity for a specific wavelength and the thermal conductivity are relevant material parameters that influence the surface temperature [128]. The processing speed is usually limited by the diffusion of anions formed during the redox reaction. The transport of reaction products is a critical phenomenon that depends on the liquid viscosity and the diffusion coefficients. Stokes-Einstein equation helps to calculate these coefficients. The dynamic viscosity of the etchant also influences the process transportation. Arrhenius-Andrade equation simplifies the viscosity calculations. The method of etchant supply plays an important role in material transportation. Commonly, a fixed quantity of etchant is provided in the horizontal positioned beaker that pose limitations. The circulation of etchant having a certain flow rate could improve material ejection. Very sparse literature is available in this regard. Stephen and Vollertsen [128] injected the etching liquid (consisting of 5.6 M phosphoric acid and 1.5 M sulfuric acid) coaxially to the laser beam directly into the irradiated area in order to improve the material ejection during nickel processing. It was evidenced that the machining quality with respect to aspect ratio, edge radius and roughness can be enhanced by increasing the velocity of the etching liquid. The etchant flow speeds ranging between 2 and 20 m/s offers competitive results. In another study the same author fabricated electron beam apertures and finishing of micro forming tools by LCM/E [124]. Li and Achara [130] achieved 300 % high MRR for stainless steel using Nd:YVO$_4$ laser with 2.6 W and high repetition frequency of 25 kHz. They employed chloride solution with varying concentrations (5–75 %). They fabricated groves and holes in 316 SS with comparably good precision, almost no HAZ and recast layer. The analysis depicted that the NaCl concentration of 50 % could offer maximum grove depth. Very common phenomena of LCM/E is the boiling of etchant upon the laser irradiation. This leads to generate the bubbles and their entrapment at the machining zone. Dealing with these etchant bubbles and their further influences on the process throughput is very rarely attempted. According to Mehrafsun and Vollertsen [131], these bubbles reduces the MRR and etching performance and also cause the machining cavity to become irregular.

4.2 Parametric Effects and Inspirations of LCM/E

Formation of nano holes and other porous structures with very fine and regular porosity in thin metal sheets enables inventions or further developments of

multitude of components such as substrate applications in fuel cell technology, microelectronics and catalytic reaction spaces in chemical reactors. Laser ablation assisted with chemical etching is a promising technique to achieve such porous structures in a wide variety of materials. 3D structures are also fabricated by some investigators through this technique even with high aspect ratio (~ 10). The process can be executed at room temperature or above depending upon the desired etch rate. The basic function of the laser energy here is to make the ground substrate ready for the initiation of chemical etching. The etching typically does not start until some pre-shapes are textured on the work surface. Therefore, the top surface is modified by the laser energy (known as photo-modification process [132]) to enable the reaction initiation [133]. Pre-holes, in common, are generated to start chemical etching.

4.2.1 Porous Structures

The laser fluence and wavelength are found as foremost parameters to control the etching performance and pore density. In order to achieve the porous layer a threshold fluence is necessary to supply. Less than this threshold there cannot be any porous layer. Higher laser wavelengths give high etching perforce. Lin et al. [134] produced a large scale and highly dense nano-holes (see Fig. 25) on stainless
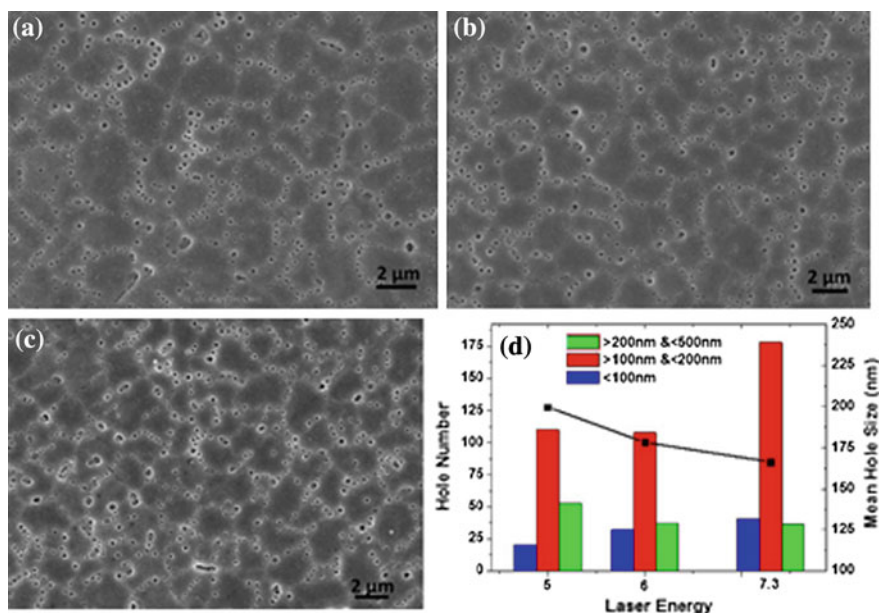
Fig. 25 Nano-holes. **a–c** Laser irradiation power 5, 6 and 7.3 W, respectively. Laser frequency 1 kHz, spot size 1.5 mm, water line height 1.5 mm and scanning speed 4 mm/s. **d** Count of nano-hole size distribution and total number under different treatment conditions [134]
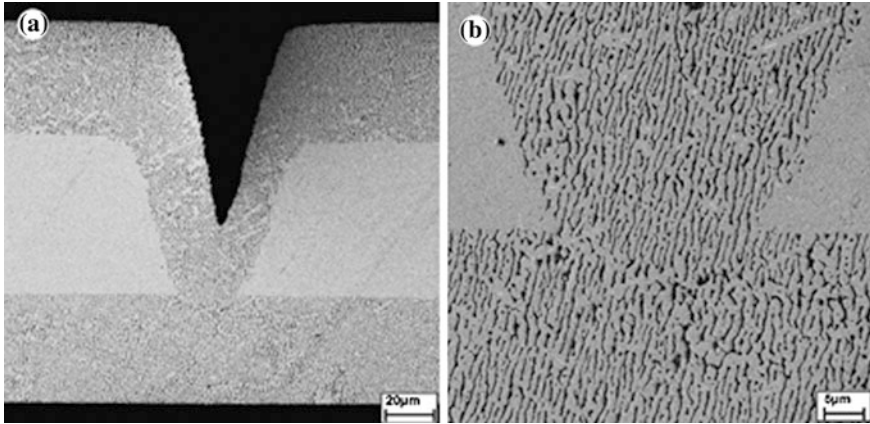
Fig. 26 Nano-porous membranes. **a** Cross-section with an embedded v-trench and **b** the magnified view affirms that mass transfer is enabled between both functional sides of the membrane [135]

steel and titanium substrates by laser assisted hydrogen etching. The water was treated as etching liquid. It was found that the nano-hole density does not increase until recrystallization of the substructures is assured. This method is applicable for a variety of materials such as Ni, NiTi, Cu_2O, etc. In the same line, Näth et al. [135] achieved nano-porous metal membranes with fine and regular porosity by the combination of the laser etching and electrochemical-etching techniques in nickel based superalloys as shown in Fig. 26. The synthesis of micro and nano porous structures with various morphologies is also supported by Al-Khazraji et al. [136]. In this study two types of lasers (CW diode and Q-switched Nd:YAG) with a wide range of wavelength (405, 530, 650, 810 and 1060 nm) were applied under 30 % diluted HF solution. A high pore density with 3 µm pore diameter can be achieved in silicon wafers. The interesting thing is that the silicon wafer remains inert in HF until the presence of holes at the surface. The laser energy absorption induces holes to initiate the chemical reaction. It was found that longer laser wavelength has a higher etching rate and this could be recognized to the higher absorption coefficient. They reported that at low laser power density (<3 W/cm^2) no porous layer was observed. Whereas, the etching rate rises to about three times when the laser power increases to 20 W/cm^2. Kumar et al. [137] also reported the surface morphologies of laser-etched silicon as a function of the laser power densities. They used four laser power densities (0.44, 0.88, 1.76 and 4.40 kW/cm^2) and found that cracks were formed at very low power density and pillar like structures were shaped at very high laser power density. Therefore, to achieve the porous structure the laser fluence should neither be too low nor be two high. Nayak et al. [138] reported the same pillar like structures in silicon and germanium surfaces. Rather than liquid, they prepared a gaseous etching environments of sulfur hexafluoride (SF6) and hydrogen chloride (HCl). Conical shaped pillars with spike top and bulb-like top

can be observed in germanium and silicon, respectively. Under the same processing conditions, the aspect ratio of silicon appeared to be higher than that of germanium.

4.2.2 3D Structures

LCM/E is considered as a rapid and direct method for the fabrication of 3D and other periodic structures with fine surface roughness ($R_a \sim 20$ nm). The 3D fabrication involves a suitable combination of laser and etchant parameters simultaneously. This includes particularly laser power, repetition rate, scan speed, etchant concentration and processing time. According to Dai et al. [139], the average surface roughness (of micro trenches) is inversely proportional to scan speed and directly to laser repetition rate. The narrow laser spot size is good to achieve sharp sidewall and small HAZ. Zhang et al. [140] observed crack free side walls of Al_2O_3 during UV laser ablation and post processing chemical etching. High laser repetition rate with low power was recommended to achieve a sidewall roughness of R_a 0.16 μm. Zimmer et al. [141] studied the influence of laser fluence, pulse number and pulse length of Nd:YAG laser on the etch rate and surface topography of fused silica. The results exhibited that the etch rate upswings linearly with the laser fluence and pulse length. The etched surfaces featured smooth, no ridge, re-deposited material or debris. Oh et al. [142] evaluated the sidewall roughness on SS foil (AISI 304, 500 μm thickness) using two types of lasers (Nd:YAG and CW Nd:YVO$_4$) and 10 % phosphoric acid as etchant. It is stated that depending upon whether a pulsed or a continuous wave (CW) laser is employed, the etch depth and surface morphology of the grooves varies significantly. Pulsed etching produces deep but rough microgrooves whereas CW etching results into shallow but smooth sidewalls. To overcome the restrictions of both processes they developed a hybrid pulse-and-CW scanning process generating deep microgrooves with smooth sidewalls.

The schematic experimental setup used to fabricate 3D photonic structures is shown in Fig. 27. Luo and Tsai [133] fabricated an array of square columns (see Fig. 28) with high aspect ratio (~ 10) on quartz glass by femtosecond laser inner modification. They employed 15 wt% hydrofluoric acid (HF) for 15 min as etching agent. In another study they achieved a 3D piled-octahedron structure by 5 wt% HF using a very low power laser (100 mW) with high repetition rate (100 kHz). However, they applied a femtosecond laser for embedded grating alone and then performed the etching in separate bath. It should be noted that the intrinsic quartz does not react with HF similar to silicon wafer (as mentioned before). In a similar study with nearly the same fundamental parameters, they also optimized the laser power and aspect ratio for the fabrication of micro-lens array [143] and V-shaped micro prism [144]. But in general, the 3D pattern's pitch and aspect ratio is mainly controlled by etching concentration and processing time. Matsuo et al. [132] fabricated various kinds of micro-channels in Pyrex glass under femtosecond laser assisted etching with the use of aqueous solution of 10 mol/dm^3 KOH. They experienced the etching at elevated temperature (80 °C) instead of room
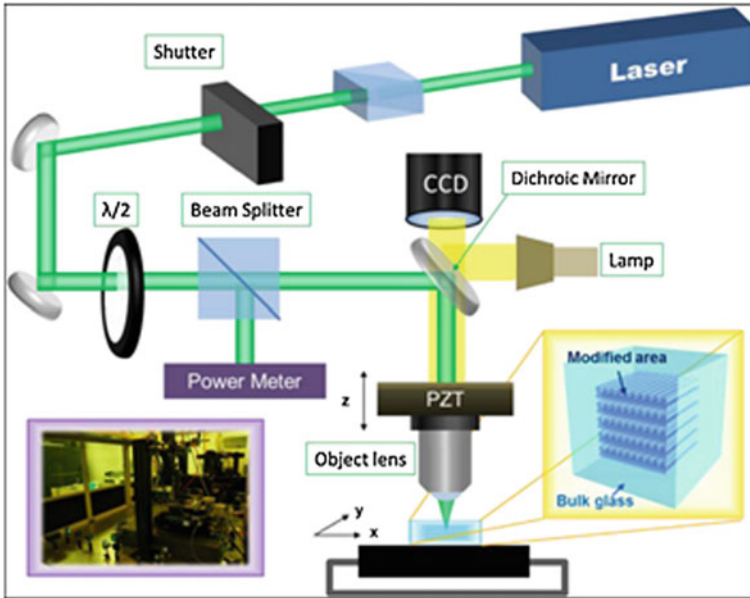
Fig. 27 Schematic diagram of 3D photonic structure fabrication [133]
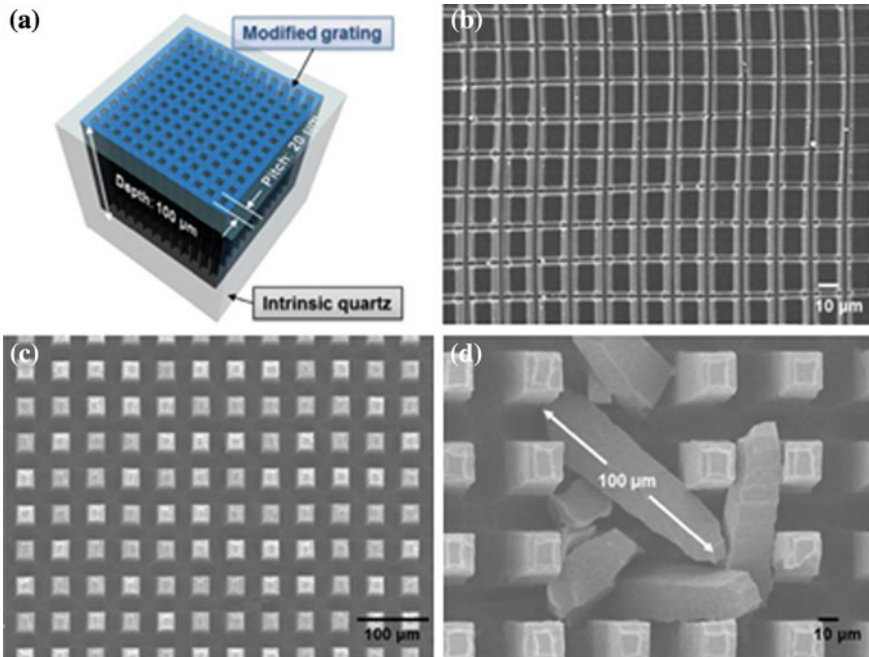
Fig. 28 Fabrication of grid photonic crystal structures inside quartz: **a** schematic diagram of the scanning pattern by femtosecond laser; **b** and **c** are SEM images of photonic crystal structures; **d** SEM image of columns with high aspect ratio [133]

temperature. The results seems to be similar as of other researchers' particularly in terms of laser parameters. The maximum etching rate recorded roughly 4 µm/min.

4.3 Conclusions and Remarks

The investigational outcomes discussed in this section have demonstrated that LCM/E is a potential candidate of machining processes to achieve high precision edges with nm level surface roughness for variety of materials. The conclusions that can easily be drawn by this section are:

1. Individually compared to ECM and LBM, this hybrid process is much superior in terms of surface morphologies, thermal damages, burrs free and re-deposited layers.
2. The machined feature and surface integrity depends on the type of etchant and its flow speed.
3. It is proven as a highly promising technique to fabricate 3D structures as well as micro-sized arrays.
4. In terms of synthesizing the porous structures for various applications, LCM/E is a competent alternative.
5. Other than positive aspects, there are two common drawbacks of LCM/E. It offers low MRR and short aspect ratio of machined cavities. Very rare in literature, high aspect ratio is achieved by this technique.
6. The major phenomena in LCM/E is the etching of substrate by chemical constituents through well-known redox reaction. The laser energy just prepares the target surface to initiate the chemical etching. That is why the MRR is low.

5 Laser Assisted Electrochemical Machining (LAECM)

There are two common etching techniques named as dry etching and wet etching. In dry etching, the material is etched/dissolved by reactive ions or vapor phase etchant. The ions are sputtered on the material to execute physical knocking of atoms as well as chemical reaction. On the other hand, wet etching requires a work sample to be immersed in chemical solution (electrolyte) and chemically dissolves the material constituents by redox reaction. Both the techniques are good for micro-pattern and microstructure fabrication on various materials [145].

LAECM process is considered as one of the wet etching processes and is a similar to LCM/E. The only difference is the chemical which is an electrolyte of certain salt solutions. The schematic diagram (see Fig. 29) shows the role of both electrolyte and laser beam. The function of the laser energy is to localize the machining zone and activate the target surface for chemical dissolution (similar to LCM/E) while the electrolyte performs the function of material dissolution, cooling
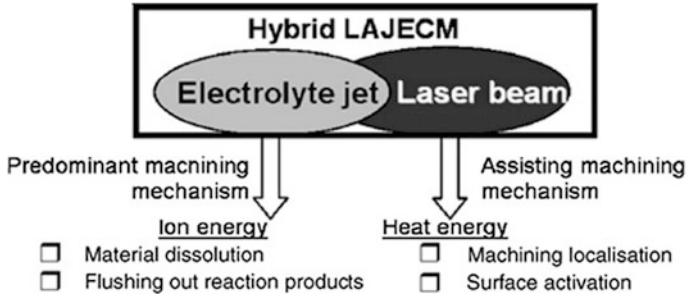
Fig. 29 Roles of electrolyte jet and laser in LAJECM [148]
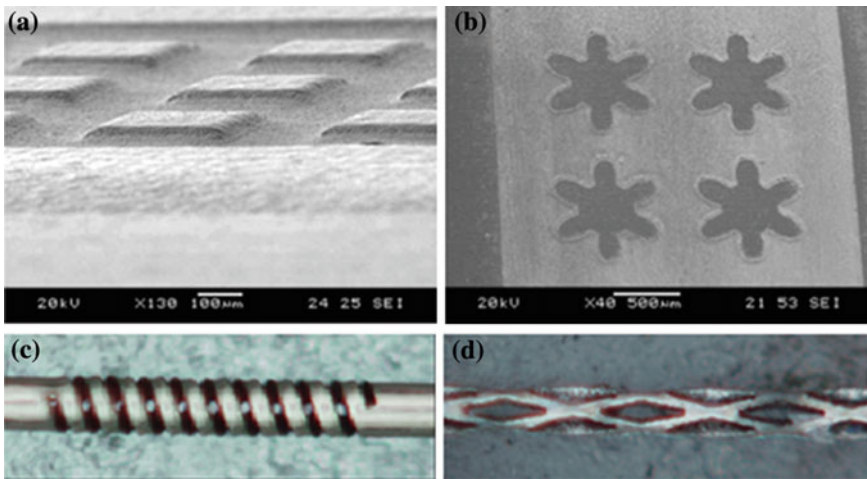
Fig. 30 Microfabrication by LAECM; **a** and **b** micro-patterns [145], **c** and **d** micro-stent with outside and inside diameters of 210 and 100 μm, respectively [147]

and transportation of debris. The electrolyte reacts with the material but the role of the laser energy is also found to be dominant by some researchers. The process is not much widely employed as per open available literature. But it offers much improved results in terms of material removal rate, surface finish, machining quality and dry laser defects. Figure 30a, b shows the micro-patterns fabricated by LAECM. Electrochemical machining (ECM) is a famous type of wet etching that is carried out, in general, in conjunction with photo-mask or micro-tool [146]. It enables to achieve microfabrication with minimal dimensional and thermal damage. In [147], Kasashima and Kurita successfully fabricated a micro stent (used in medical implants) as shown in Fig. 30c, d, having outside and inside diameters of 210 and 100 μm respectively that is still a challenge for other processes.

Long et al. [149] compared the dry laser and LAECM characteristics for silicon wafer. The low power excimer laser with varying pulse frequency was applied under
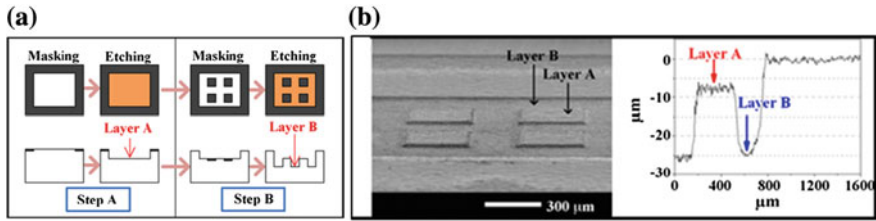
Fig. 31 Multi-step EELM for multi-layered micro-structures. **a** Schematic diagram and **b** SEM image and surface profile [151]

20 % KOH electrolyte with 1 mm layer thickness above the work surface. It was found that the etching rate and surface finish are significantly high for LAECM compared to laser dry etching. In this compound process the laser interaction is reported as the dominant factor for etching. Kikuchi et al. [150] fabricated a micro-lens array of anodic alumina by Nd:YAG laser and electrochemical techniques (anodizing, electroplating, oxidation). They used a very low power laser (0.5–1.0 mW) having a pulse width of 8 ns and 10 Hz repetition rate. A novel process for electrochemical etching of metal without a need for photo-mask is proposed by Shinet al. [151] termed as Electrochemical Etching using Laser Masking (EELM). The schematic diagram of the EELM and SEM images of the microstructures are shown in Fig. 31. This process executes in two steps; laser masking and anodic dissolution. In the laser masking step, a patterned layer on the conductive layer is formed by laser marking using a pulsed fiber laser. The laser marked area is temporarily inactive and serves as a protective mask. Afterwards, this patterned surface selectively dissolves during the electrochemical etching step. A protective layer on the surface is formed by laser marking, which is based on direct writing with a laser beam. The anodic dissolution rate of the unmarked area was substantially higher than that of the laser marked area. One year later the same team investigated the changes in characteristics of recast layer formation and the protective effect of the recast layer according to the laser masking conditions and electrochemical etching conditions [152].

Fabrication of holes by laser drilling, especially in metals, exhibits recast layer and spatter around the hole periphery. In order to avoid these potential problems, [153] proposed a hybrid process of laser drilling assisted with jet electrochemical machining (JECM-LD). In addition to cool down the work surface and transport the debris away, jet electrolyte also reacts with material. The drilled holes through laser drilling in air and laser drilling in jet electrochemical are shown in Fig. 32. The shape of the drilled holes can be explored prior to actual drilling by a 2D model presented in [154]. Drilling analysis of 321S20 stainless steel holes reveals that the laser energy (photon energy) is the main driving force while the jet electrolyte (ion energy) reduces the drilling defects. In this connection De Silva et al. [155] reported that the role of laser in LAECM is to localize the machining area. The thermal enhancement of electrochemical enables the intensification of anodic dissolution that consequently
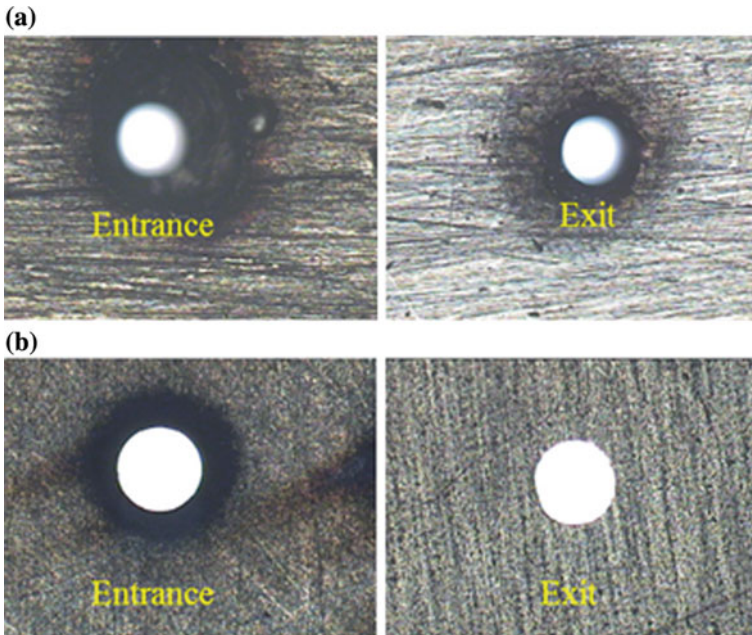
Fig. 32 Micrograph of drilled holes. **a** Laser drilling in air under 200 mJ and 10 s, and **b** drilled with JECM-LD under 200 mJ, 40 V and 20 s [153]

raise the MRR and machining precision. Temperature is the predominant determinant and it must be controlled to avoid spark generation due to electrolyte boiling. They developed a finite element model for the modelling for temperature field distributions for various alloys including stainless steel, aluminum alloy, hastelloy and titanium alloy. It was found that the modeling requires a number of assumptions due to electrolyte flow, boiling, sparking, specimen shape, energy absorption and scattering etc. The dissolution mechanism mainly depends on material's properties. That is why the surface analysis showed variations for different materials. Under the same conditions, Hastelloy exposed lowest surface roughness while titanium alloy showed highest reduction in taper (65 %) [148]. According to Pajak et al. [156] the MRR of LAECM is found to be linearly dependent on electrolyte concentration and jet velocity irrespective to the material type.

5.1 Conclusions and Remarks

Very less amount of research has been found under the category of LAECM. However, this hybrid process also has the potential to yield better results as compared to dry laser ablation. The MRR has been found to be more in the presence of

electrolyte. The machined cavities or drilled holes through LAECM exhibit low machining defects as compared to dry laser machining.

6 Under-Water Laser Ablation (UWLA)

The hybrid laser-water technology is getting popular in order to achieve minimal thermal damages and improved MRR. Underwater laser processing provides a solution to the majority of the problems of laser machining in air and other gases especially HAZ which can be substantially avoided due to the additional cooling action of the water layer/jet [157]. There are some variations in the design of laser setup, however, the most common laser setup used in UWLA is shown in Fig. 33. A massive research is available in literature attempting underwater laser processing in order to alleviate the defects around the laser cut grooves and holes. It is also widely attempted to fabricate nano particles (discussed in next section) from a variety of materials solid [158]. Several types of lasers (the same as used for dry LBM) are experimented in this regime including femtosecond, nanosecond, CO_2, Excimer and Nd:YAG laser. The crucial matter is to solely set an appropriate wavelength, pulse number, fluence, spot diameter and water film parameters to reach the desired ablation outcomes.

6.1 UWLA Mechanism

In UWLA or laser-water jet ablation the actual machining is caused by the laser energy. The function of water is to restrict the realization of undesired defects like
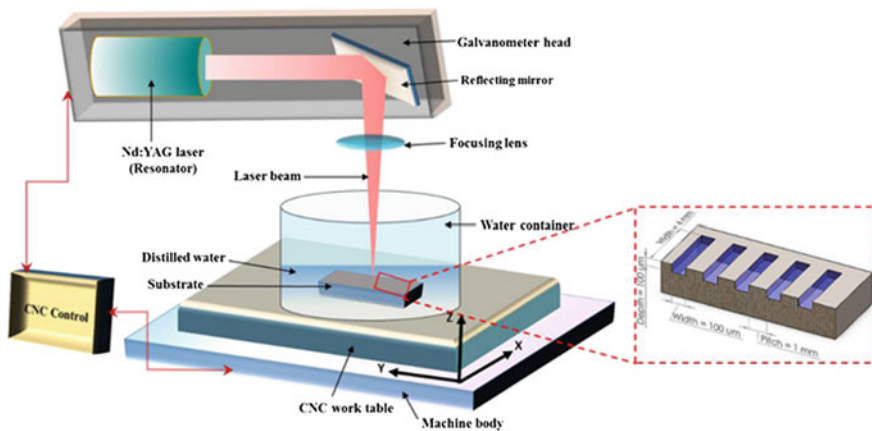
Fig. 33 Schematic diagram of laser setup used in under-water laser ablation [159]

HAZ, recast layer, spatter and cracks etc. Therefore, unlike the LAECM, the occurrence of these defects still exists in the presence of water but at low level. The material removal mainly depends on laser parameters (especially spot diameter and the focal distance) and the fluid dynamics (particularly fluid layer thickness). However, the configuration of target material with respect to incident laser beam influences the ablation performance.

6.1.1 Beam Focus

As the sample is immersed in water, so, if the laser spot is focused on the work surface the majority of the energy will be absorbed by the water instead of the work sample. It boils up and evaporates the water. This explosive evaporation of water molecules generates forces between substrate and the suspended melt particles. These forces are generally larger than adhesion forces thus propel the melt particles off the surface of the material [160]. Thus the mechanism changes from thermal phenomena in air to a more mechanical in water. Therefore, in general, the best practice is to focus the laser beam below the work surface rather than focusing on the top surface. It will bypass the high proportion of liquid layer to get boiled and impart maximum energy to the work material.

6.1.2 Water Layer Thickness

The water layer thickness above the work surface plays an important role in the ablation mechanism. It mainly decides the machined depth and kerf width [161]. The thick water layer carries away the debris more efficiently but also reduces the ablation rate. When the laser beam travels through a thick liquid film, the pulse shape does not remain uniform and/or consistent. At the laser-work interface the formation of milky suspension composed of liquid, bubbles and melt is formed that confines the plasma above target material. It scatters the laser light along with a distortion of the laser pulse and consequently the energy needs to ablate the material severely affects. A high proportion of energy is absorbed by the thick water film and thus attenuates the amount of energy to be absorbed by the work material leading to less ablation efficiency [162]. Typical water layer thickness in horizontal position is 1–2 mm [163], however, different authors experienced different thickness values like [164] maintained 6 mm layer, [165, 166] worked at 1–20 mm layer. Similarly, to ensure handful rise of ablation rate, [161] suggested 3–4 mm layer thickness for alumina. The sprayed water in the form of a thin layer could be an alternative solution to this problem [167]. On the other hand, as the energy absorbance depends on the material wavelength, therefore, the selection of incident laser wavelength, preferably, be such that it should strongly be absorbed by the target matter rather than water film. Based on this statement, Dupont et al. [160] claimed that a high ablation rate (2–15 times) for high laser intensities can be achieved if the laser

wavelength is chosen in accordance with work material's wavelength. It has been proven that the energy absorbance does not depend on the layer thickness but the incident light wavelength.

6.1.3 Splashing and Cavitation Bubbles

The water splashing and rise of temperature within the closed premises of laser beam are common phenomena [168]. The splashing generates a non-uniformity of the layer while the rise of temperature leads to ineffective cooling mechanism. A closed flowing water immersion technique ensures a controlled geometry for both the optical interfaces of the flowing liquid film and permits repeatable control of the flow-rate during machining. The splashes could somewhat be minimized due to flowing streams. In this way, however, the flow rate has its own implications and effects on precision and quality. Formation and diffusion of cavitation bubbles is another concrete phenomenon of UWLA. That is why the morphological features of UWLA machined geometries differ. These features mainly attribute by laser pulses (N) per spot and the fluence level (F). The feature differences become more evident at high pulses per spot (100–1000 pulses). Different colored lights can be observed at different E or N values. For example, reddish light is produced in the laser-work-interface at low E or N values while a brilliant white light can be seen at high values. This is called the confinement effect that is typically enhanced by the liquid environment. It results a negligible amount of melt's re-deposition but lowers the ablation rate [169].

6.1.4 Melt Ejection and Sample Configuration

The convection induced fluid motion can also be observed during under water laser processing. It helps in the transportation of debris away from the material surface. The melt ejection may also be improved by changing sample configuration from horizontal to vertical (shown in Fig. 34) and laser from vertical to horizontal. In this way the gravitational affect also adds up with fluid flow. The gravitational force itself drops down the melt debris and fluid stream that further improve the melt ejection phenomena. Even though, the thin water film could easily be maintained by this orientation. In this way the ablation efficiency is higher than in the horizontal position [170].

6.2 Parametric Effects of UWLA

Laser ablation under water is dealt with a wide range of materials in literature including metals, alloys, ceramics, glass, polymers, semiconductors and many others. The effectual material removal by laser irradiations is a fundamental concern
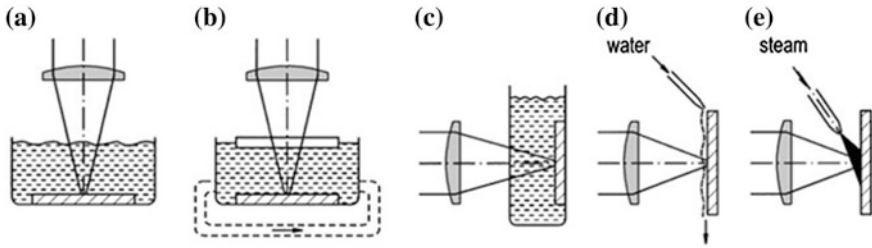
Fig. 34 Various methods for providing water at laser-material interaction zone [171]

in micro-machining. The research shows that the water environment is a great candidate for material removal by laser especially where coarse removal is required. Ablated surface attributes, geometrical aspects (width, depth and aspect ratio), melt re-deposition and HAZ are generally evaluated and compared with laser ablation in air. Nevertheless the investigations of the ablation rate is a highly common attribute. The results are entirely based on the material and the laser-water parameter settings mainly; laser fluence, pulse numbers, repetition rate, spot diameter and water layer thickness. That is why the results are not consistent in literature especially for the ablation rate. Both the high ablation and low ablation rates can be found in literature (as shown in Table 5). There are also certain materials, such as ceramics, having explicit behaviors among which thermal properties and brittleness are dominant. Such behaviors/materials lead the ablation mechanism somewhat away from the traditional ablation mechanism [172]. These behaviors are not discriminately addressed in open literature except for a few like exceptional behavior of Al_2O_3: lower etching rate, greater surface coarseness and porosity, and lesser bending strength after laser ablation in water [165, 173]. The influences of laser parameters on micro-channels geometry (width, depth and taperness) is studied in [174] as shown in Fig. 35. Among the other laser parameters, the laser scan speed significantly affect the micro-channels sizes and shapes. Laser scan speed ranging from 100 to 400 mm/s is proposed as the appropriate scanning speed during laser machining of micro-channels using water as the machining environment.

6.2.1 High Ablation Rate

Normally, for high ablation rate with UWLA the low laser power (some watts) and low-to-medium fluence range (0.1–30 J/cm^2) are more practical. In the meantime, pulses need to be short (in μs or ns) and their frequency low (<kHz) in order to achieve a high ablation rate. The authors of [163] perceived higher ablation in water than in air for SiC at a laser beam diameter of 20 μm, pulse duration of 15 ns, fluence level of 16 J/cm^2. However, they used a repetition rate of 8 kHz which is contradictory for high ablation rate as mentioned before. The reason of this high repetition was neither presented nor evaluated for any effect. Geiger et al. [165] processed different ceramics (Al_2O_3, MgO, SiC, ZrO_2, Si_3N_4) under water at two

Table 5 Ablation rate variations of different materials through UWLA

Ablation	Work material	Experimental conditions	Work position	Results	References
High ablation	• Aluminum	Pulse energy: 0–10 mJ Spot size: 10 μm Fluence: 127 J/cm^2	Horizontal	Etch grooves deeper in water than in air	[179]
	• Polyimide	Pulse duration: 20 ns Wavelength: 308 nm Fluence: <20 J/cm^2	Horizontal	Etching rate nearly same in water and air	[28]
	• Silicon	Fluence: 0–5 J/cm^2 Wavelength: 780 Pulse repetition rate: 1 kHz	Horizontal	Etching rate two times in water than in air High aspect drilling was achieved	[175, 180]
	• Steel • Al$_2$O$_3$ • SiO$_2$	Fluence: 0.1–30 J/cm^2 Spot diameter: 0.5 mm Water layer: 3–4 mm	Vertical, horizontal	Etch rate 2–15 times more in water than in air Recast layer and thermal damage was eliminated	[160, 161]
	• Al$_2$O$_3$ • Porous MgO	Wavelength 308 nm, max. pulse energy 2 J, pulse duration 50 ns Pulse repetition rate 20 Hz Fluence: 0–35 J/cm^2 Water layer: 1–20 mm	Horizontal, vertical	Etching rate is high in water than in air. The surface of Al$_2$O$_3$ remained rough and porous	[165, 166]
	• Aluminum • Brass	Wavelength: 1064 nm Pulse width: 8 ns Pulse energy: 600 mJ Pulse repetition rate: 10 Hz	Vertical	Crater depth is more in water than in air	[172]
Low ablation	• ZrO$_2$ • SiC • Si$_3$N$_4$ • Glass, • Stainless steel • Polyamide	Wavelength: 308 nm Maximum pulse energy: 2 J Pulse duration: 50 ns Pulse repetition rate: 20 Hz Fluence: 0–35 J/cm^2 Water layer: 1–20 mm	Vertical/horizontal	Etching rate is low in water than in air	[165, 166]

(continued)

Table 5 (continued)

Ablation	Work material	Experimental conditions	Work position	Results	References
	• Magnetic materials (NdFeB, ferrite)	Wavelength: 1.06 µm Pulse duration: 180 ns Pulse repetition rate: 1 kHz Water layer: 6 mm	Horizontal	Best surface finish and elimination of debris than in air. 2.5 times low ablation rate in water than in air	[164]
	• Silicon	Pulse duration: 25 ns Wavelength: 248 nm Pulse repetition rate: 10 Hz Number of pulses: 10–5000 Laser energy: 100-480 mJ	Horizontal	Machined surface is rough under water and smooth in air	[162]
	• Silicon wafer • Polycarbonate • SiC	Wavelength: 800 nm Pulse repetition rate: 1–1000 Hz	Vertical/horizontal	–	[169, 178]
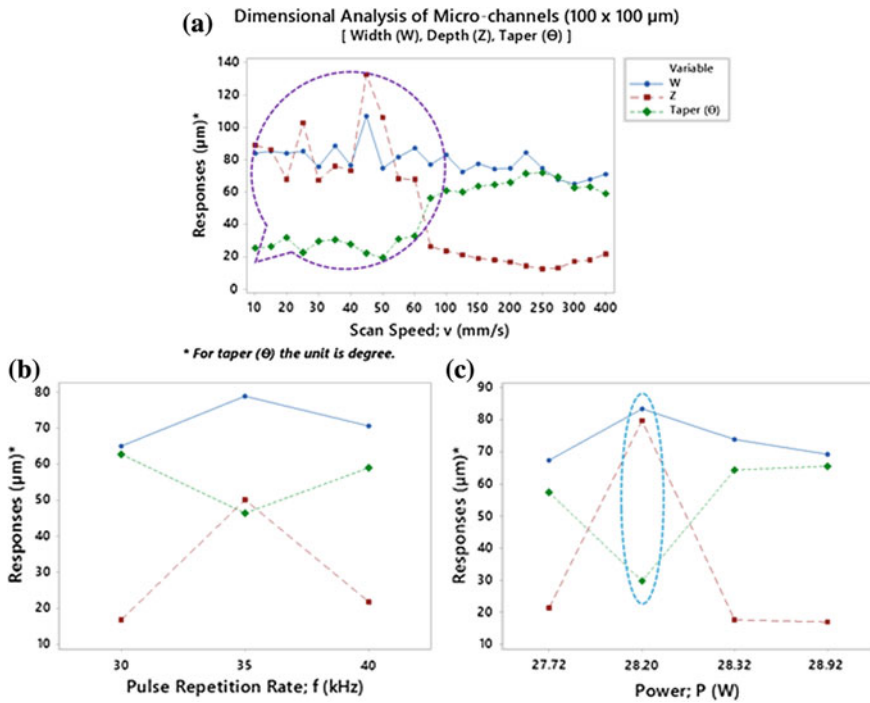
Fig. 35 Dimensional analysis of micro-channels of size 100×100 μm during under water laser machining; **a** impact of scan speed, **b** impact of pulse repetition rate and **c** impact of laser power

work configurations (Horizontal and vertical). In the horizontal position they employed 1–20 mm water level while in the vertical state 2 mm thin layer. A mix of results were obtained for the above materials. Al_2O_3 and MgO exhibited high ablation rate (2 μm/pulse) while in contrast to that the other materials showed a slightly lower ablation arte in water compared to in air. The ablation was, however, highest for both the vertical configuration having spayed water technique and horizontal with 2 mm water level. With even 10 mm water level the ablation rate was significantly high. This is totally contradicting to our prior discussion of proceeding section. They reasoned that the water level (up to some extent) does not lowers the laser energy and ablation rate if a suitable laser wavelength is chosen. As the absorption coefficient of liquid varies with the radiation wavelength. So they adjust the XeCl excimer laser's wavelength to 308 nm to which distilled water has a low absorption coefficient. In a study of Ref. [175] the authors used a 248 nm wavelength KrF excimer laser to ablate Si wafer under water thickness of 1 mm and reported the similar results. Likewise, the high ablation rate validations can be found in [160] for stainless steel, alumina, silica and in [166] for glass, stainless steel and polymers with steady results.

6.2.2 Low Ablation Rate

Some of the research portrayed the low ablation rate by UWLA as compared to dry conditions. Choo et al. [162] fabricated holes in Si. The results revealed that the ablation depth is mainly dependent on the number of pulses and the fluence level. They reported a threshold fluence of 2 J/cm^2 under water processing and 1.7 J/cm^2 for air. It means that the ablation depth is low by UWLA compared to dry ablation at certain fluence level. The experiments in [169] also exhibited almost the same results for Si wafer under very similar conditions. The only difference was the value of wavelength and repetition rate (800 nm and 1–1000 Hz by Daminelli et al. [169] while 248 nm and 10 Hz by Choo et al. [162]). All this is the story of water at still level. The water flowing at some flow rate in a closed flow is another scheme mainly applied to enhance the melt removal. But this technique also lowers the ablation rate. However, the ablation threshold in flowing water is somewhat lower as compared to water at still level. To investigate the impact of this technique on ablation threshold, Dowding and Lawrence [176] machined polycarbonate samples under various flow-rates. An average decrease in ablation threshold of 7.5 % can be acquired using turbulent flow velocity regime while laminar flow gives negligible reduction. On the other hand, a flow velocity of 3 m/s yields a minimum ablation threshold (112 mJ/cm^2).

6.2.3 Possible Reasons of Ablation Rate Variations

The above discussion reveals that the variation in ablation rate is a fact of UWLA, either positively or negatively. Few of the possible reasons of why the ablation rate varies/differs in water and air could be:

- In liquids, the temperature of confined plasma remains higher than in air [175], thus the liquid prevents the plasma expansion [177] that enriches the laser radiation energy [163] and consequently improves etching rate [178].
- The shock wave generation, originating from plasma expansion and the collisions of vapor bubbles, produces the micro-jets. These micro-jets destroy the substrate surface (especially oxide layer) [165], that results in a high ablation rate in water [163].
- The projected shock pressure in water and air environment are ~ 3 GPa and ~ 95 MPa, which means high pressure by water produces shock waves that lower the viscosity of molten material. Thus, efficient material removal and ejection rate results [172].
- The micro-bubbles carry the melt debris away more efficiently [179] that speeds up the ablation process.
- The vaporized bubbles and melt suspension scatter the laser light that lowers the machining rate in liquid.
- The water flowing direction influences the material ejection [171]. The vertically flowing water (Fig. 14d, e) assists the debris removal by its flow and gravitational effect that yields high ablation phenomena [170].

- Liquid layer thickness absorbs the high proportion of laser energy and attenuates the energy transmitted to the target surface. This lowers the ablation efficiency [162].
- Liquid's absorption coefficient depending on laser wavelength creates the difference in ablation rate [165]. Low absorption coefficient enhances the ablation performance and vice versa [175].
- Differences in ablation also occur due to material's inherent properties. For same laser-water parametric conditions some materials give high ablation [165] while some materials low ablation than in air [166].

6.3 Inspirations of UWLA

Cutting, surface craters, high aspect drilling and cavity machining are the main ablation processes performed by various researchers through UWLA. The main focus in these processes is converged to study the process capabilities in terms of thermal effects, surface quality, re-deposition, micro-structural alterations and material removal.

6.3.1 Crater Formation and Structure Characteristics

The liquid environment in laser ablation has the advantage of completely preventing charring and reduction of spatter [171] and re-deposition of melt that in combine leads to good quality microstructures [166]. The suitable pulse duration and pulse frequency is considered as necessary to avoid microstructural defects. For example, pulses over 100 μs length could not eliminate the recast layer in ceramics [181]. At further long pulse length (1 ms) and high repetition rate (over 50 kHz) the machined cavity gets wider and shallower. The recast layer is due to the re-deposition of melt particles which solidify on the surface. This abundance of re-deposition is more in air than in water. But it cannot entirely be eliminated even by UWLA. The size of re-deposited particles and their distribution across the crater periphery is significantly less in the presence of water than dry conditions. The experiments of Patel et al. [172] carried out on aluminum and brass samples by Nd: YAG laser with varying laser pulse energy under dry and wet conditions. The re-deposited particles to the material surface itself was found in both the machining conditions (dry and wet conditions). The air atmosphere generates an average particle size of 3 μm while in water the average size of re-deposited particles was 55 nm. The particle size is larger near the periphery than those away from the edge. High intensities laser pulses are capable to generate a shallow crater when irradiating metal targets. Mahdieh et al. [182] worked on crater formation in aluminum target under dry laser and wet (water) laser conditions as presented in Fig. 36. According to their research findings the crater geometry extremely depends on the laser pulse intensity, the number of laser pulses and the ambient. The higher the

pulse number is, the deeper and bigger is the creator. Similarly crater depth is linearly proportional to the pulse energy. The crater depth in water dramatically rise which strengthen the high ablation claims of UWLA. The same results are proofed for brass and aluminum by Patel et al. [172]. In addition to crater formation the presence of water also allows to generate nano-structures. These nano-structures can be characterized in various ways. The formation of such nano-structures is solely due to the re-deposition of ablated melt around the crater periphery. Figure 37 represents the needle-like nano-structures produced on brass target while crater formation through under-water laser machining.

6.3.2 Under-Water Laser Milling

Laser ablation in the presence of water is equally suited to mill three-dimensional geometries in almost all kinds of materials either it is metal or non-metal. Similar to other advantages and applications it is greatly applied to achieve good geometrical precisions, surface quality, elimination of melt re-deposition and less thermal damage. The experiments in Ref. [163] indicated that the precision and quality of machined cavities in SiC ceramics were higher by under-water laser milling compared to milling in air. They also reported that the cavity surface was free of any visible layer of oxides. The laser machining of magnetic materials (NdFeB and ferrite) under water was found to give much a much better surface finish and elimination of debris than in air [164]. Three-dimensional cavities, holes and micro-channels have also been achieved in the water ambient by Li et al. [183]. They employed the water jet on the rear side of the workpiece instead of traditional means of liquid supply on the top surface. CO_2 laser underwater machining has been found by Yan et al. [161] to result in reducing defects such as recast layer, dross, cracking and heat damages during the deep cavity machining of alumina. Different polygon cavities machined by underwater laser ablation are presented in Fig. 38. Laser beam machining under dry and wet atmospheric conditions can also be found in [159], wherein micro-channels has been fabricated in nickel alloy (Inconel 718). A comparison between dry and under-water laser machining is categorically presented as shown in Table 6.

The prediction of the temperature field, stress field and material removal were realized by numerical and thermal models. The results showed a great agreement for all the characteristics. Afterwards, they achieved deep cavities with various shapes such as square cavity, circular cavity, triangular cavity, pentagon cavity and prismatic cavity. The depth of cavity is a function of the water-layer thickness and number of laser scans. The average depth of cavity of 2 mm depth can be experienced in alumina at 60 W power with 100 scanning cycles and 10 mm/s scan speed. The kerf width mainly depends on the water layer thickness. Under-water laser milling was found to be expressively competent in terms of surface features especially sidewall and bottom surface appearance compared to machined cavities in air atmosphere. The mechanism study revealed that this was the effect of water dynamics especially the propagation of high recoil pressure that more efficiently
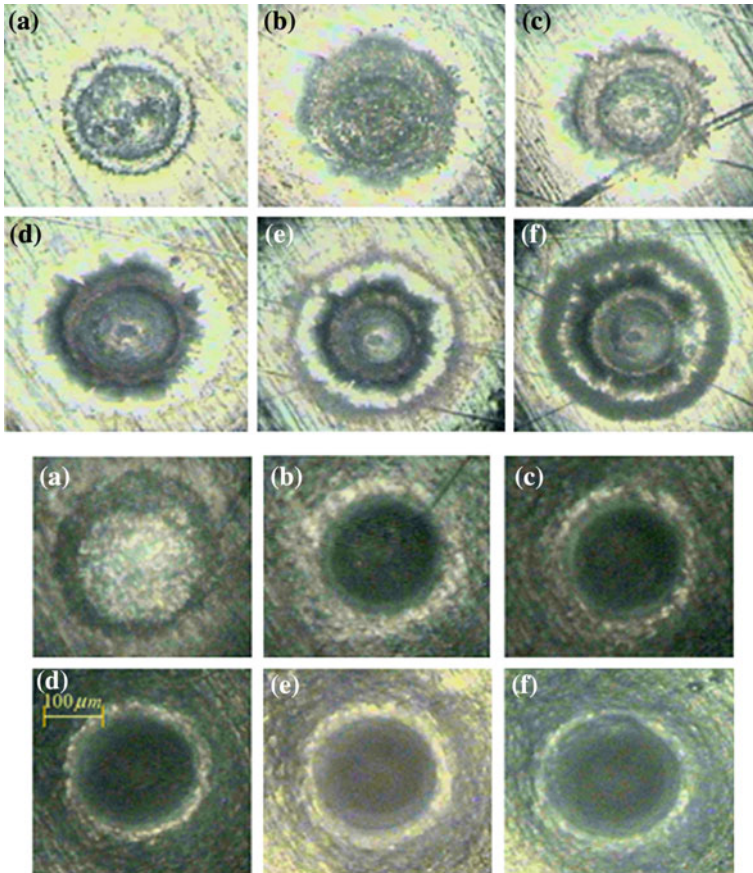
Fig. 36 Typical image of craters on an aluminum 5052 target irradiated in air (*top*) and tap water (*bottom*) by 1, 10, 20, 50, 100, and 200 pulses and they are indicated by (**a**)–(**f**), respectively [182]

Fig. 37 SEM image of the nano-structures at the crater periphery re-deposited on brass target in water [172]
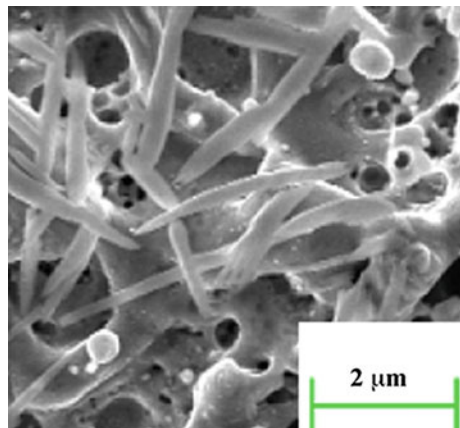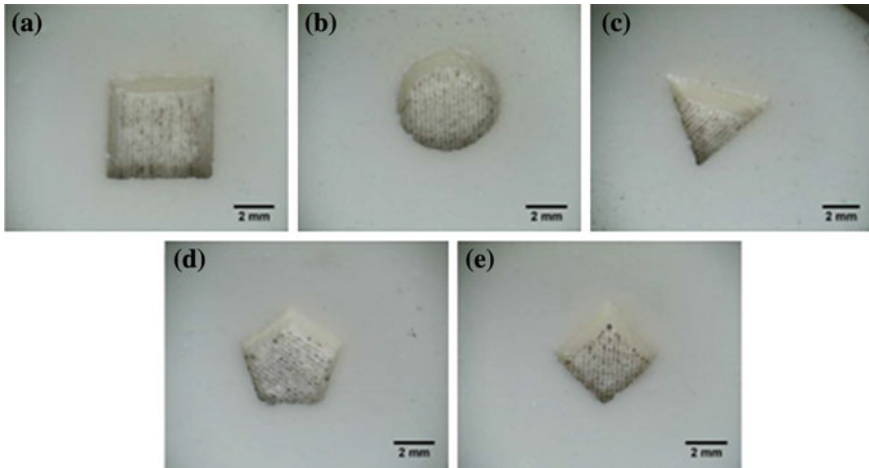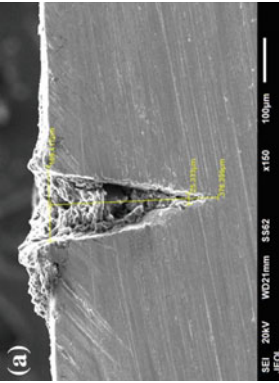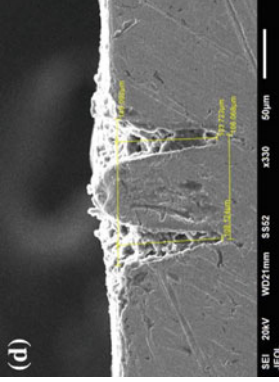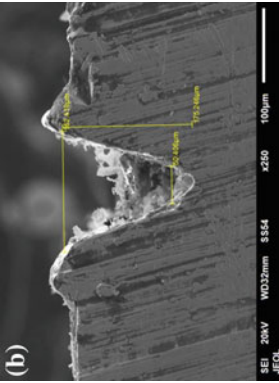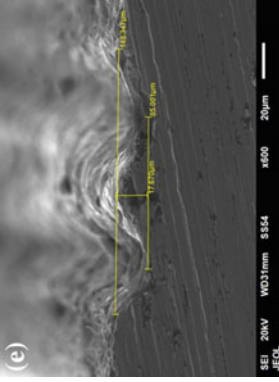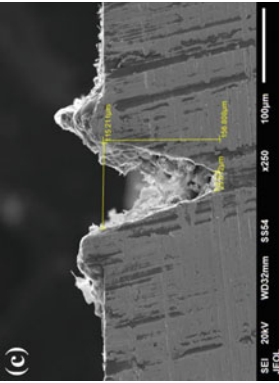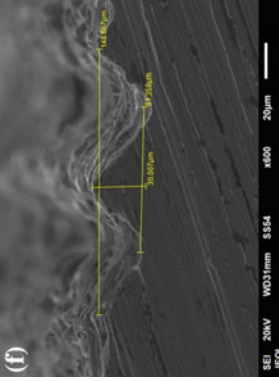
Fig. 38 Optical micrographs of laser underwater machined polygon cavities including **a** square cavity, **b** circular cavity, **c** triangular cavity, **d** pentagon cavity, and **e** prismatic cavity [161]

ejects the molten material and consequently prevents the recast formation and HAZ. In terms of ablated surface appearance of Si, opposite results were presented by Choo et al. [162]. The surface quality of the Si substrate was somewhat rough in case of water than in air. It was figured that the molten silicon rapidly solidified with a dendritic structure. The explanation is justified by the material's specific properties. In order to have more control over the underwater laser ablation process and to eliminate some of the undesired effects in cavity formation and drilling holes, the addition of solvents to the water or machining within a liquid chemical environment could be another option. For example, Voronov et al. [178] used dimethyl sulfoxide as the liquid media to process polycarbonate SiC. The ablation rate, however, was lower than that in air and water but the surface quality was good.

6.4 Under-Water Laser Drilling

Laser drilling in the presence of water is significantly viable compared to dry laser drilling. It is equally suitable for single hole as well as multi-hole arrays with good precision and quality. During the array-hole drilling the first main limitation of dry laser drilling is the hole-distance (greater than 5 mm for brittle materials such as glass and alumina) between the neighboring holes. The second main limitation is the propagation of the micro-cracks and their linkage that ultimately causes the material to be broken or at least being unstable. Low aspect ratio is also another drawback of dry laser drilling. All such factual truths can be eliminated/improved by incorporating a water environment. The authors of [184] experimentally proved that during the array-hole drilling the hole-distance of even 1–2 mm can be

Table 6 Comparison of laser beam machining results under dry and wet conditions [159]

Parameters	Laser beam machining under dry conditions	Laser beam machining under wet conditions
P = 28.2 W f = 35 kHz v = 50 mm/s		
P = 28.32 W f = 35 kHz v = 150 mm/s		
I = 28.92 W f = 40 kHz v = 400 mm/s		

achieved for brittle materials with crack free edges by using a 1 mm water layer above the work surface. Lu et al. [11] investigated the mechanism behind the quality improvements by underwater laser drilling of various metal plates including copper, aluminum, iron, stainless steel with varying thickness. They concluded that the energy required, to drill a certain hole with constant material characteristics and thickness, is lower in case of underwater drilling as compared to dry conditions. Two mechanisms were claimed to appear named as; ablation-produced impact effect and liquid-jet-induced impact effect. The later impact was considered as the main responsible for the high quality drilling results. It has also been proven that the high aspect ratio holes can also easily be achieved by this technique [183]. Kaakkunen et al. [180] investigated the effect of thin film effect in drilling of high aspect ratio (1:13) holes in silicon substrate (see Fig. 39). The depth and shape of the hole was deeper and more uniform in case of spraying water than in air atmosphere. They reasoned it due to the efficient removal of debris by the water flow. In the absence of water, the shape of hole becomes inflicted because of energy scattering by debris. The holes acquired curved shape that restricts the subsequent pulses to perform further deep ablation. The detailed mechanism of high aspect ratio etching of UWLA can be found in [179] according to which micro-bubbles generated after laser irradiation develops an upward stream in the liquid. That stream with high vapor pressure removes the debris more rapidly. In the study of Dolgaev et al. [163] drilling in SiC has been achieved by UWLA with high precision and quality results compared to those of drilling in air. The sidewall of the drilled hole was found to be free from any visible oxides.

6.4.1 Synthesis of Nano-particles

Nano-materials are of great interest due to their applications in many fields. The structural and efficacy of nano-particles (NP) depend strongly on the method applied for their synthesis. Laser ablation in liquid environment is a simple and effective technique that allows generating mass production of nano-particles from numerous materials (Ag, Au, Ni, Co and Cu-containing solid targets, brass etc.) in the form of a suspension in a given liquid [185]. The liquids could be, for example, H_2O, H_2O_2, C_2H_5OH, $C_2H_4Cl_2$, etc. This technique retains a certain flexibility in controlling the properties of nano-particles by appropriate choice of both laser parameters and the nature of the liquid. Laser ablation in liquid environment is capable of producing NP without any surface active agents or counter-ions, which is indispensable for some applications, e.g. for medical ones [186].

Semaltianos et al. [187] explained the mechanism involved during the fabrication of TiO NPs. Two types of plasma formation were reported namely (1) water plume plasma and (2) ablated species plasma (see Fig. 40). The chemical reaction took place between these two plasmas that cause adiabatic expansion and quenching of metastable phases to result in NPs. A sample of NP's produced by pulsed KrF excimer laser is shown in Fig. 41. Zhang and Lan [188] produced nano-particles of nickel (Ni) and cobalt (Co) through laser ablation in organic
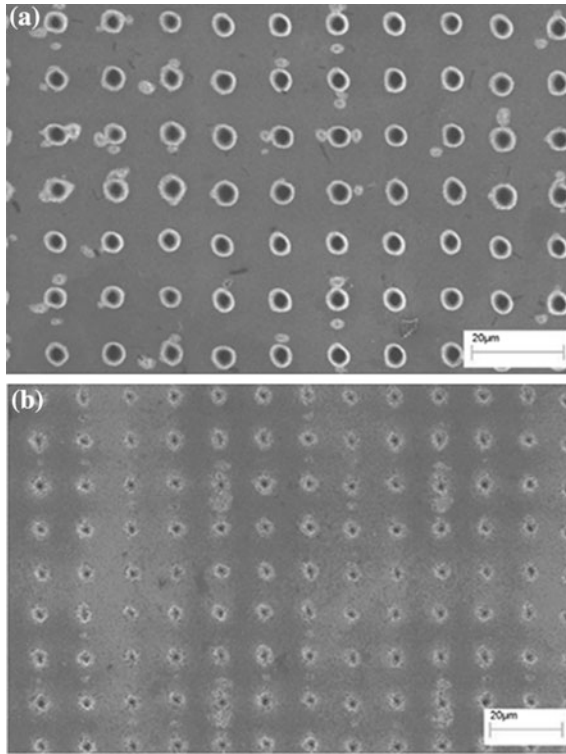
Fig. 39 The SEM photographs of the ablations made in silicon with (**a**) and without (**b**) water spray [180]

solution. Pure Ni, Ni50Co50 alloy, and Co metal plates as the targets, respectively, have been irradiated under 532 nm Nd:YAG laser in ethylene glycol. Under the same laser fluence and irradiation time, the average particle size of Ni nano-particles of 8 nm in diameter and 30 nm of Co nano-particles can be achieved. This research demonstrates that laser ablation in liquid, a one-step, non-catalyst process, can produce stable Ni and Co nano-particles. The morphology of NPs mainly depends on the laser fluence. The laser pulse energy has shown a relatively little effect on the particle size. The investigations of Piriyawong et al. [189] proved that a too high pulse energy (e.g. 5 J) could melt the adjacent NPs of aluminum that is useless if the applications require individual NPs. In contrast to this, very less energy (e.g. 1 J) may cause problem of high fragments of aluminum that could not ionized by laser beam. Therefore, they suggested the best energy of 3 J to acquire individual NPs from aluminum under water layer of 5 mm. The boundary level of their energies (1 and 5 J) offered less uniform but smaller sized particles (22 and 27 nm respectively). While the optimum level of energy (i.e. 3 J) offers more uniform, spherically shaped particles but with largest size (48–100 nm).

Mahfouz et al. [191] explained the ablation of Ni targets in water by laser impact (532 nm, 40 mJ/pulse, 10 Hz and 8 ns duration) focused on massive samples (∼2 mm diameter) that generate colloids with fine nano-particles. The amount of metal released in the solution increases first linearly with time, but slows down after 8 min of impact. This decreases the ablation efficiency. The reason behind could be the related to the abundance of nano-particles. The interaction rate of NPs with the incoming laser beam becomes high and that could lower the laser power on the metal surface or modify the surface properties which diminishes the ablation efficiency. The size distribution of the nano-particles thus produced can be in the range 3–5.3 nm in diameter, with a tendency for the size to be smaller for larger number of laser shots. Because of the nickel and oxygen reaction, in fact, nickel oxide nano-particles are produced, rather than nickel nano-particles. Gondal at el. [192] applied a pulsed laser ablation (PLA) technique in 3 % H_2O_2 aqueous solution to synthesize nano-sized nickel oxide (NiO) particles. This work demonstrates that
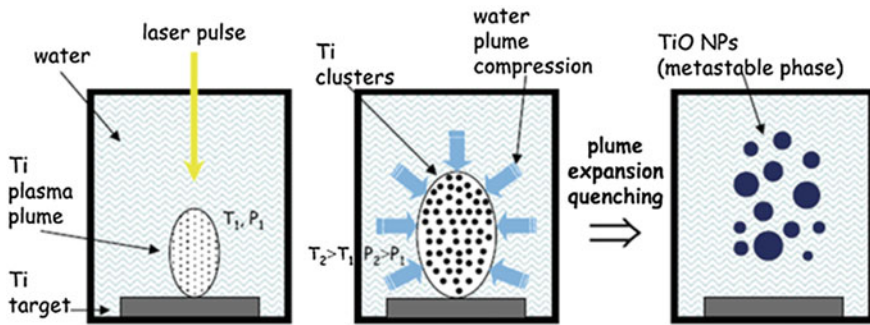
Fig. 40 A schematic diagram of the proposed physical mechanism of formation of TiO NPs in the disordered phase [187]

Fig. 41 Atomic force microscopy image of organic NP obtained by underwater laser ablation of PC at 500 mJ/cm^2, 100 pulses delivered at 1 Hz [190]
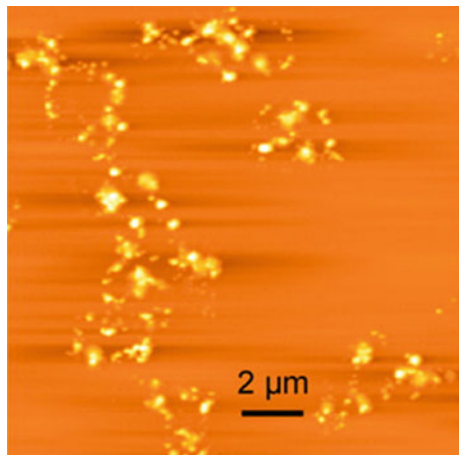
PLA is an effective method to control the size, impurity and minimal chemical waste generation which is the major problem with other wet chemical methods. Huang et al. [193] synthesized titanium nano-particles and nanotubes from pure titanium under PLA processing in the presence of water. Compagnini et al. [194] worked on the formation of Molybdenum disulfide (MoS_2) fullerene-like nano-particles by the laser ablation of crystalline targets in water and found that NP of size 10–15 nm diameter can easily be obtained in a single step.

The laser fluence has a direct influence on the morphology of NPs. However, irrespective to the laser parameters, the shape and composition of NPs also depends on the nature of the liquid used [186]. For example, laser ablation of titanium immersed in ethanol results in cubic structured particles. The immersion of titanium in dichlorethane after laser irradiations build TiC particles instead of solely titanium particles. Finally, the water immersion allows to produce TiO NPs having the composition of non-stoichiometric oxides. Among these fluids the size of NPs is found to be smallest in case of water [195]. In general terms, the aqueous environments have the ability to alter the chemical composition of NPs compared to the bulk material due to the high chemical reactivity of water at elevated temperature gained during ablation. For instance, the ablation of Cu immersed in water produces Cu+ ionic states instead of pure Cu particles [196]. Modifications in chemical composition can also be found for ablation of Si. The water immersion produces amorphous SiO_2 while ablation in ethanol results in the formation of Si nano-particles having an outside shell of oxide. This oxide shell can also be observed in some other metals as well. However, there are certain materials which does not react with the surrounding environments and retain their stoichiometry after laser ablation. This concern, for example, NPs of CdS or CdSe obtained via laser ablation of semiconductor under water, acetone and other liquids. NPs of CdS showed a strong crystallinity while processing in different liquids. Similarly, ZnSe fabricated through laser ablation under different liquid environments revealed almost perfect stoichiometry [197].

6.5 Conclusions and Remarks

The inspirations of UWLA on ablation performance are undeniable. This confining process looks favorable for various real-world applications in surface treatment aided by laser. The following list of conclusion can be drawn from this section:

1. This hybrid process has the potential to significantly control the core drawbacks of dry laser ablation.
2. In terms of ablation rate, a mix of results are published by numerous researchers.

   (a) Most of the research outcomes favor the high ablation in the presence of water compared to dry laser ablation.
   (b) There are many authors who claimed low ablation rate by UWLA in comparison with air atmosphere.

    (c) The common reason behind this conflict is stated as the particular behavior of the target material or the specific experimental conditions.

3. The work position relative to laser beam contributes a significant role in the ablation mechanism, material ejection and ablation rate. The configuration of vertically oriented work target and horizontally oriented laser beam gives improved results.
4. Water layer thickness above specimen surface is one of the key parameter in UWLA. In general, a 1–4 mm layer thickness is demonstrated to achieve high MRR.
5. With respect to UWLA machining characteristics drilling, milling and crater formation have been found the main research themes resulting in good surface morphologies and less thermal damage as compare to laser ablation in air atmosphere.
6. In another highly positive aspect the process is greatly promising and simple to achieve nano-particles from a wide range of materials under different liquid environments. Although, most of the NPs are not pure as the bulk target material. The chemical composition of the particles changes depending upon the environment and compel to propagate some carbides and oxides.

7 Micro-channels Applications and Fabrication

Microchannel heat exchangers have applications in several important and diverse fields including: aerospace; automotive; bioengineering; cooling of gas turbine blades, power and process industries; refrigeration and air conditioning; infrared detectors and powerful laser mirrors and superconductors; microelectronics; and thermal control of film deposition. The advantages of microchannel heat exchangers include high volumetric heat flux, compactness for space-critical applications, robust design, effective flow distribution, and modest pressure drops. This section will cover selected industrial examples for microchannel heat exchangers, microchannel heat pipes, and microchannel heat plates [198].

7.1 Microchannel Heat Exchangers

7.1.1 Automotive and Aerospace

Microchannel heat exchangers have at least one fluid flow passage with typical dimensions between 10 and 1000 µm and have great potential in process intensification of various industrial areas [199]. There are many possible channel geometries for microchannel heat exchangers, two types of which are the most widely used in compact heat exchanger designs for automotive and aerospace

applications. These are shown in Figs. 42 and 43. High-temperature and compact micro heat exchangers can be manufactured using ceramic tape technology which uses fused ceramic layers to create channels with dimensions below 1 mm [200]. Metal-based microchannel heat exchangers are also of current interest because of the combination of high heat transfer performance and improved mechanical integrity [201]. Figure 44 shows a manufactured, flat extruded multichannel aluminum heat exchanger.

In recent years major progress in microchannel heat exchangers has been made by the automotive, aerospace, chemical reactor, and cryogenic industries. Thermal duty and energy efficiency requirements have increased during this period, while space constraints have become more restrictive. The trend has been toward greater heat transfer rates per unit volume. The hot side of the evaporators in these applications is generally air, gas, or a condensing vapor. With advances in the airside fin geometry, heat transfer coefficients have increased, as have surface area densities. As the air-side heat transfer resistance has decreased, more aggressive heat transfer designs have been sought on the evaporating side, resulting in the use of microchannel flow passages on the liquid side (evaporating or condensing or single-phase regimes). The major changes in recent evaporator and condenser designs for automotive and other compact heat exchanger applications involve the use of individual, small-hydraulic-diameter flow passages arranged in a multi-channel configuration on the liquid side. The ability to efficiently transfer heat between fluids using lightweight, compact heat exchangers is important in a variety of applications, such as automobile radiators, air conditioning, and aerospace applications. Microchannel heat exchangers are well suited to these applications due to the micro-channels' compactness, lightness, and high heat transfer performance.
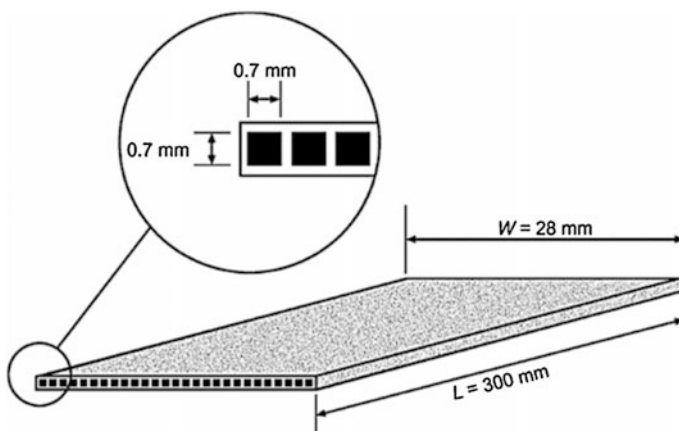
Fig. 42 Typical dimensions of a rectangular microchannel for compact heat exchanger applications [198]
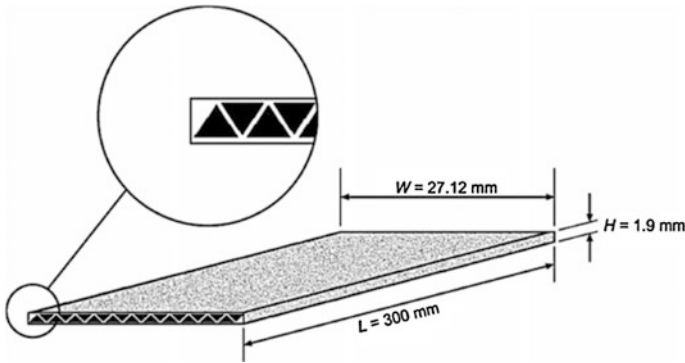
Fig. 43 Typical dimensions of a triangular microchannel for compact heat exchanger applications [198]
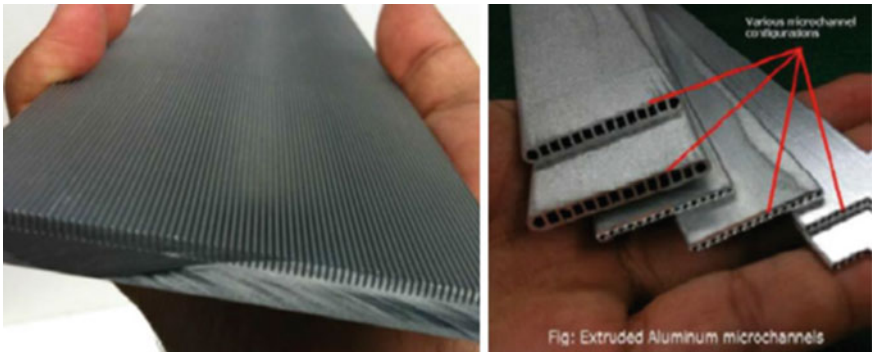
Fig. 44 View of a microchannel heat exchanger [198]

Car radiators employ a cross flow design that allows a sufficient mass flow rate of air through the radiator while using only the stagnation pressure associated with the motion of the automobile. The common measure of performance for car radiators is the heat transfer/frontal area normalized by the difference in inlet temperatures of the coolant (water–glycol) and the air. For conventional car radiators, 0.31 W/K cm^2 of heat transfer/frontal area can be obtained between the air and the coolant. The cross flow microchannel heat exchanger can transfer more heat/volume or mass than existing conventional heat exchangers within the design constraints. This can be important in a wide range of applications (automotive, home heating, and aerospace).

A review by Sommers et al. [202] discussed numerous applications that particularly benefit from ceramic heat exchangers. Ceramic materials offer potentially significant advantages compared to metal alternatives, including significantly higher operating temperatures, improved tolerance of harsh chemical environments, improved bonding with ceramic-based catalyst and significant cost savings in

materials and manufacturing methods. Although there are numerous possible applications, the effort reported here is motivated by the need for low-cost, high-performance fuel reformers, and the need to effectively integrate unit processes in solid-oxide fuel cell systems. The microchannel reactor integrates the upstream fuel heating and reforming with downstream recuperation to harness the high-quality heat exiting the tail-gas combustor. Such process intensification can improve system efficiency. It is feasible to further combine processes by catalytically activating both sides of the microchannel reactor, using one set of layers for upstream fuel reforming and the opposite set for tail-gas combustion.

7.1.2 Chemical Reactors

Microchannel chemical processing technology is an emerging field with applications in most industrial processes due to its excellent mixing capabilities, controlled reaction environment, and energy efficiency. This technology offers improvements in existing processes and will enable new processes to become cost effective. The basic microchannel reactor design is based on the flow between parallel platelets coated with a catalyst. The large aspect ratio of the channel provides extensive surface area in a small volume. Microchannel reactors have been developed based on ceramic substrates as well as metal substrates. In both types of reactors, multiple layers coated with catalytic material are bonded, forming a monolithic structure. An added benefit of a layered pattern is the ability to easily scale up or down by adjusting the number of layers. This provides great flexibility in the design, since if the production capacity needs to be changed, there is no need to redesign the reactor. Figure 45 shows a manufactured micro-reactor.
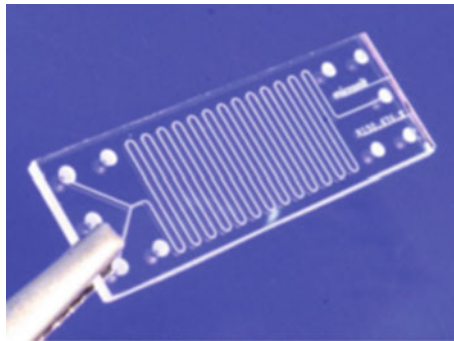
Fig. 45 Glass micro-reactor: the channels of the chip in the picture are 150 μm wide and 150 μm deep [198]
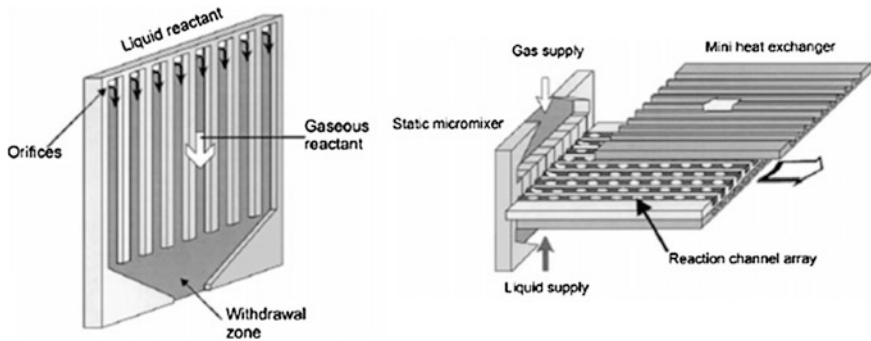
Fig. 46 Falling film and micro-bubble reactors [205]

7.1.3 Falling-Film Micro-reactors

Falling-film micro-reactors work in the same way as macro-scale absorbers. Microchannel falling-film absorbers have been reported in the open literature by Goel and Goswami [203], Hessel et al. [204] and Jähnisch et al. [205]. The central part of the micro-reactor is a stainless steel plate containing 64 vertically positioned micro-channels (300 μm wide and 100 μm deep). Liquid spreads to form a thin film among the micro-channels and flows further downward to the withdrawal zone at the bottom. Gas flows in a large gas chamber positioned above the microchannel section, facilitating concurrent or countercurrent operation mode. Figure 46 shows a schematic of a falling-film and microbubble reactor.

7.1.4 Membrane Separation Technology

In membrane separation technology, gas and liquid flow in two different channels, separated by some physical structure, such as a mesh, selective membrane, or micro-porous plate [206]. Oak Ridge National Laboratory and Velocys Inc. separated liquid and vapor phases in micro-channels by membrane in a traditional counter-flow arrangement. The membrane prevents the liquid from bridging the microchannel and maintains stable phase separation. However, it significantly decreases the surface area of the liquid–gas interface. Figure 47 shows the opening area of the membrane comprising just about 10 % of total surface area.

7.1.5 Co-current Micro-channel Absorption

In the co-current configuration, gas, and liquid flow concurrently in the same microchannel, creating various types of flow patterns similar to that of two-phase flow in a tube. The liquid film is maintained by shear stress of the moving gas phase, and film thickness can be ultimately small. The channel hydraulic diameter
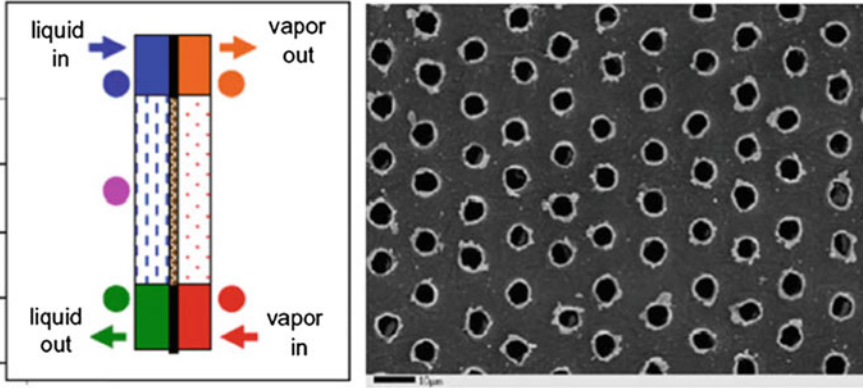
Fig. 47 Counter-flow absorber and phase separating membrane (Velosys Inc.)
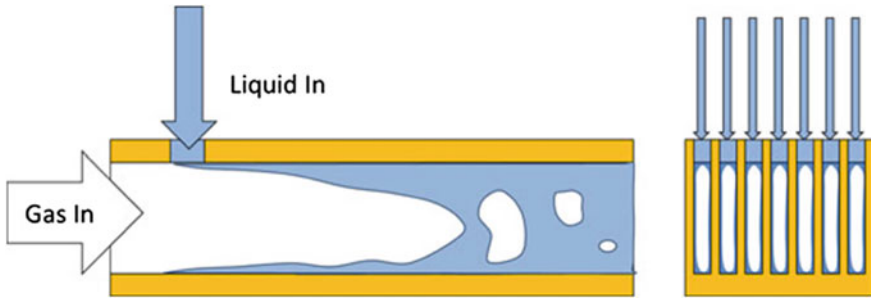
Fig. 48 Co-current micro-channel absorption process [207]

can be significantly smaller, limited only by the desired fouling characteristics. With co-current flow, films of a few microns thick can be arranged on the channel wall, and associated with this thickness very high mass transfer coefficients can be obtained [207]. Figure 48 shows a schematic of the concurrent microchannel absorption process.

7.1.6 Cryogenic Systems

Microchannel heat exchangers are used in cryosurgical probes for ablating tumors or treating heart arrhythmia [208], as shown in Fig. 49a. The Joule–Thomson cryocooler is most widely used for the cryosurgical probe. The advantages of the Joule–Thomson cryocooler include its simple structure and compactness and the lack of electrical interference. The heat exchanger of the subminiature Joule–Thomson refrigerator used in the cryosurgical probe has channel diameters from tens of microns to hundreds of microns, according to space limitations. Figure 49b, c shows
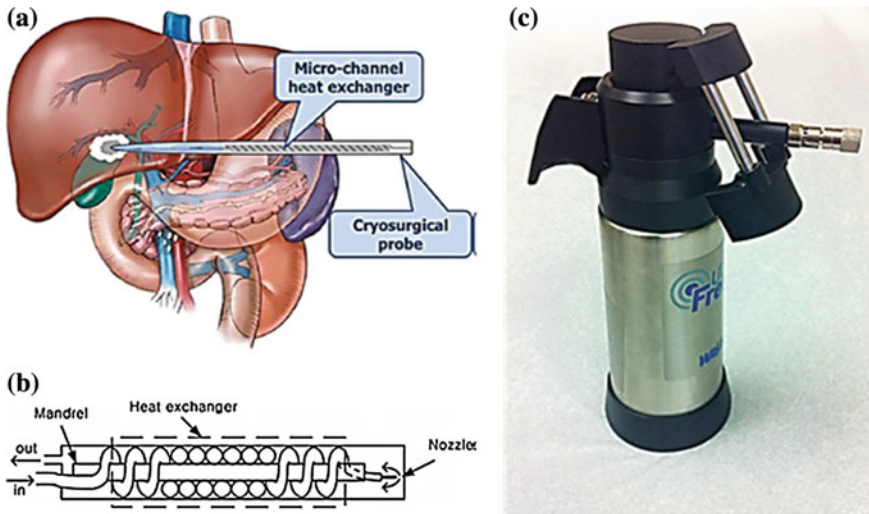
Fig. 49 Micro-channels in cryosurgery; **a** treatment of a cancer by cryosurgery, **b** schematic diagram of a cryosurgical probe and **c** cryosurgical system for surgery of cancer [208]

schematic diagrams of a cryosurgical probe and a cryosurgical system for use in cancer surgery. In many cryogenic applications, the desired heat transfer, which is the refrigeration load, is a small fraction of the heat transferred within the heat exchanger. In this case, the ineffectiveness of the heat exchanger must be an even smaller number, and the effect of axial heat conduction and parasitic heat transfer can dominate the performance of the device. Furthermore, the large absolute temperature change within the heat exchanger produces correspondingly large variations in the properties of the fluids and metal that can also affect performance.

7.2 Laser Diode Applications

Microchannel cooling is now a mature technology, over 30 years old and widely used on a commercial basis in the high-power laser diode industry. Microchannel coolers are also now being used in commercial systems to cool LEDs in UV curing systems and photovoltaic cells in concentrated solar power systems. The present commercial cooling technologies, however, will not be adequate as power levels of semiconductor devices increase. Since laser diodes have stringent performance requirements and are by far the largest commercial market share of microchannel coolers, the remainder of this discussion will focus on laser diode applications. Commercial coolers generally employ water-cooled copper micro-channels to dissipate up to 1 kW/cm^2 from semiconductor heat sources ranging from 0.1 to 2 cm^2

Fig. 50 CVD diamond microchannel cooler with 250×300 μm rectangular ducts [209]

in size. These coolers use rectangular ducts with widths from 25 to 200 μm, duct aspect ratios up to $15\times$, and flow rates ranging from 10 to 30 g/cm^2/W (based on heated area). These parameters result in thermal resistances of 30–75 K-cm^2/kW, with pressure losses between 10 and 50 psi. There are four main ways future commercial microchannel systems can be improved: (1) reducing the cooler thermal resistance; (2) reducing package thermal resistance through use of reduced thermal expansion coolers; (3) reducing flow rate to minimize system costs of cooling; and (4) increasing operating lifetime. Reducing channel width is promising: for water-cooled systems, reducing the channel width of a copper microchannel cooler to ~ 12.5 μm results in thermal resistances in the 15–20 K-cm^2/kW range with reasonable pressure losses. Secondary features can offer performance improvements for larger channels (channel width >100 μm), but they cannot be economically fabricated in smaller channels. Diamond is well known for its outstanding thermal conductivity, but it is difficult to machine with micro-passages. Figure 50 shows a prototype diamond microchannel cooler fabricated by laser etching thin (100 μm thick) diamond sheets and brazing the sheets together. This approach was not able to create passages narrower than 250 μm [209].

7.3 Micro-channel Heat Pipes

Because advanced electronic equipment is decreasing in size, the circuit integration per unit area must increase, which in turn contributes to a rapid increase of heat generation rates. As a consequence, the operating temperatures of electronic components may exceed the desired temperature level, and if heat is not sufficiently removed, the failure rate of the equipment will cause an accelerated system failure. Due to the compactness of most modern electronic components, cooling devices also need to be small but highly effective in heat transport. Wicked heat pipes (or capillary-force-driven heat pipes) evaporate and condense the working. Recently,

microchannel technology has been applied to the fabrication of micro heat pipes. Many experiments have been conducted on microchannel heat pipes. Cotter [210] first introduced the concept of a micro heat pipe that did not include a complicated wick structure. Kang and Huang [211] and Berre et al. [212] have studied silicon micro heat pipes with a polygonal cross-section. The silicon micro heat pipes use the sharp edges of the polygonal groove for return of the condensate to the evaporator. Although silicon micro heat pipes are small and can overcome the thickness limitations of wicked heat pipes, they cannot handle a large amount of heat, and their performance has yet to be improved.

7.4 Micro-pulsating Heat Pipes

Youn and Kim [213] developed a micro-pulsating heat pipe that did not have a wick structure and instead contained rectangular micro-channels forming a meandering closed loop. The heat was transferred from an evaporator to a condenser by means of the axial oscillation of liquid slugs and vapor slugs. This micro-pulsating heat pipe has progressed beyond research laboratories and is now under mass production. As shown in Fig. 51, micro-pulsating heat pipes with looped micro-channels were fabricated by MEMS or micro-machining technology. The fabrication of the micro-pulsating heat pipe was completed by bonding the top cover plate and filling the pipe with a working fluid. Then the heat input and output were connected at the evaporation and the condensation sections, respectively. A total of 10 parallel,
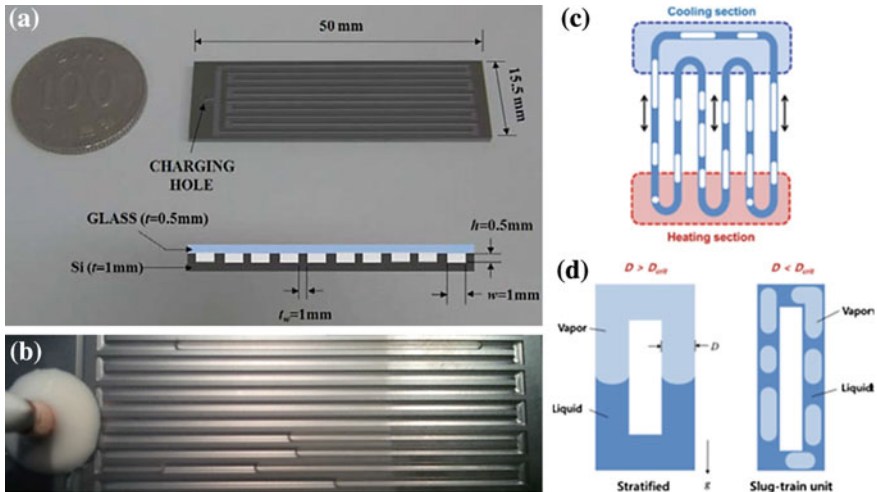
Fig. 51 Micro-pulsating heat pipe; **a** CAD model with dimensions, **b** *top view* of the micro-pulsating heat pipe with filling ratio of 50 %, **c** working principle of micro-pulsating heat pipe and **d** vapor and liquid arrangement according to tube diameter [213]

interconnected rectangular channels forming a meandering closed loop were engraved on the silicon wafer with a thickness of 1 mm. The top of the silicon wafer was covered by a transparent glass plate with a thickness of 0.5 mm to allow visualization of the internal thermos-hydrodynamic behavior in the micro-pulsating heat pipes. The silicon wafer and glass plate were bonded together using anodic bonding. A hole of 1 mm diameter was drilled on the top of the glass plate to evacuate the micro-pulsating heat pipes and fill the micro-pulsating heat pipes with working fluid. Figure 51 represents the fabricated micro-pulsating heat pipes and dimensions of the heat pipe. The overall micro-pulsating heat pipes had a length of 50 mm, width of 15.5 mm, and thickness of 1.5 mm. The width and height of the engraved rectangular channel were 1 and 0.6 mm, respectively, and the hydraulic diameter was 0.75 mm. Ethanol was used as a working fluid. The micro-pulsating heat pipes achieved maximum effective thermal conductivity of 600 W/m K and a maximum heat transport capability of 4 W.

The heat is transported from the evaporator to the condenser by means of local axial oscillations and phase changes in the working fluids. A manufactured micro-pulsating heat pipe is shown in Fig. 51b, in which the boundary between the liquid slugs and the vapor slugs is distinguishable. The micro-pulsating heat pipe has many advantages, including high thermal performance and a maximum effective thermal conductivity of about 600 W/mK, which is 3.5 times higher than that of silicon (k = 162 W/mK) and 1.5 times that of copper (k = 400 W/mK). It is possible to make a small, thin, and flat structure, and if a flexible material is used for the base and cover materials, it is possible to make a flexible micro-pulsating heat pipe because there is no wick structure.

As shown in Fig. 51c, the heat was transferred from the evaporator to the condenser sections by means of the axial oscillation of liquid slugs and vapor slugs. The micro-pulsating heat pipe is different from conventional heat pipes in design and working principle. There is no wick structure to return the condensed working fluid back to the evaporator section. The micro-pulsating heat pipe is made from a long meandering continuous capillary tube bent into many turns. The diameter of the tube is made sufficiently small that vapor plugs can be formed by capillary action as shown in Fig. 51d.

7.5   Micro-channel Flat Heat Pipes

The potential devices for which the flat micro heat pipes fabricated may be applied are mobile electronics such as small notebook PCs, PDAs, or cellular phones. Although conventional heat pipes use either wire mesh or sintered metal for the wick structure that is attached to the inner surface of a sealed metal housing, it is difficult to adopt the same approach in micro flat heat pipes, as MHP size cannot be reduced below a certain limit, for instance of 2–3 mm in thickness, due to the volume of the wick structure itself. Thus, the flat micro flat heat pipes should occupy as little space as possible to fit in the already small mobile device. Also, since the main heat source

Fig. 52 Micro-channel flat heat pipe; **a** structure of microchannel grooves and **b** *top view* of the micro flat heat pipe [214]
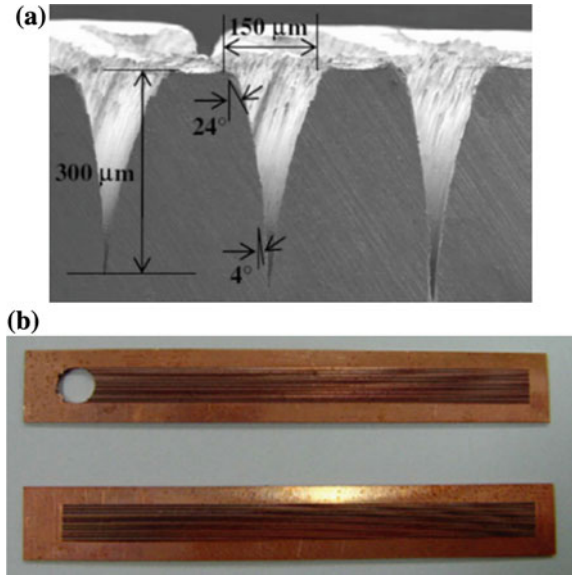
in an electronic device is a chip, and the sides of most chips are flat, the flat micro flat heat pipes are designed in a flat rectangular shape with a thickness of 1.5 mm. Recently, Lim et al. [214] developed a micro heat pipe with a microchannel groove wick structure using laser micro-machining technology. The structure of the microchannel grooves of a micro flat heat pipe is shown in Fig. 52a.

A manufactured micro-pulsating heat pipe is shown in Fig. 52b. The working principle of the micro flat heat pipe is the same as that of a conventional heat pipe with a porous wick structure. The heat is transferred from an evaporator to a condenser. When one end of the heat pipe is heated, the working fluid inside the pipe at that end evaporates and increases the vapor pressure inside the cavity of the heat pipe. The latent heat of evaporation absorbed by the vaporization of the working fluid reduces the temperature at the hot end of the heat pipe. The heated vapor moves to the condensation section and condenses back into a liquid at the cold interface, releasing the latent heat. The liquid then returns to the hot interface through the capillary action of the microchannel grooves, where it evaporates once more and repeats the cycle. The micro flat heat pipe has many advantages, including its small, thin, and flat structure. It also has high thermal performance, with a maximum heat transfer rate of 8 W under stable operation and 13 W at the dryout point.

7.6 Micro-channel Heat Plates

A microchannel plate (MCP) is a planar component used to detect particles (electrons or ions) and impinging radiation (ultraviolet radiation and X-rays).

A typical MCP consists of about 10,000,000 closely packed channels of common diameter, formed by drawing, etching, or firing in hydrogen, forming a lead glass matrix. Typically, the diameter of each channel is 10 microns. Each channel acts as an independent, continuous dynode photomultiplier. The MCPs are widely used to intensify low-light signal inside various image detectors. Industries for MCP applications range from astronomy to aerospace, machine-building, experimental physics, chemistry, biology, medicine, and ecology.

7.7 Micro-channel Fabrication Techniques, Materials, Sizes and Shapes

7.7.1 Fabrication Techniques

There are many techniques to produce above said sizes and shapes of micro-channels including both the conventional as well as non-conventional techniques. But every manufacturing process has its own limitations. For example, the conventional micro-milling process using micro-tools are commonly used but the high tooling cost, burr formation, material constraints offered by difficult-to-machine materials, chip adhesion, high thrust forces, heat affected zone and striation marks are the obvious drawbacks of conventional micro-milling and consequently restrict the process for precise micro-featuring especially in hard-to-machine materials such as titanium and nickel alloys [215–219]. Fabrication of micro-channels in Ti-6Al-4V has been realized by Vazquez et al. [220] with the help of tungsten carbide micro-tools using CNC machining center. Micro-hot embossing is another potential candidate among the available technique of micro-channel production. The process of micro-hot embossing was utilized by the researchers of [221] while manufacturing an array of micro-channels of size 5–100 μm in aluminum target material. Gau et al. [222] proposed a flexible die forming process to form micro channels in aluminum foils (foil thickness 50 and 75 μm). They produced micro-channels of width size less than 1000 μm. Vacuum die-casting is another cost effective method if the objective is to produce array of micro-channels on large areas such as required in components used in proton exchange membrane fuel cells. Jin and Kang [223] fabricated such arrays of micro-channels on both sides of bipolar plates of aluminum alloys by vacuum die-casting. Among non-traditional machining process electric discharge machining (EDM) is considered as relatively good alternative having no material hardness and channel shape restrictions [224, 225]. But there are also number of problems linked with EDM and wire-EDM such as low productivity, high tool wear rate, lack of precision due to tool wear, unsuitable for batch production or multi-channels [226], thick recast layer (from 2.5 to 30 μm) [227], heat affected layer of 40–100 um [227], thick white layers (6–8 μm) with micro-cracks [228], poor surface integrity [229] and necessary post processing requirements [230]. Chemical etching is another alternative for the

fabrication of micro-channels but it offers troubles of having high aspect-ratio micro-channels [231]. The comparison of different machining methods in terms of advantages and shortfalls is shown in Table 7.

Laser beam micro-milling (LBMM) is considered as among the competent techniques used for micro-fabrications. It is well suited for machining of a wide range of materials; from ductile to hard-to-machine materials. LBMM using Nd: YVO_4 nano-second laser can be found to produce circular cross-sectional micro-channels on soda lime glass [232]. Similarly, femtosecond laser has been utilized by a research team of Suriano et al. [233] where they generated micro-features on different polymeric samples. Selection of channel size is also important and should be considered alongside the laser parameters. Wider sized channels with relatively good dimensional accuracy can be more flexibly produced in by Nd:YAG pulsed laser compared to the accuracy in narrow sized micro-channels [51]. Different sized micro-channels machined through Nd:YAG pulsed laser are shown in Fig. 53. Likewise, the processing of metals (aluminum and titanium) by laser milling has been documented in [234] where width and depth of micro-features were studied. Aluminum and steel based alloys dealt under nano-second pulsed fiber laser are presented in [235] where the authors examined the effect of laser based parameters on the formation of micro-notches. As per their conclusions the micro-notches vary in sizes and the machined width and depth mainly depend on laser power and pulse repetition rate. Another study stated that laser milling is a complex process due to which a variation in depth and width of micro-channel can be soundly observed [236]. They applied Nd:YAG laser to machine micro-channels of size 200×50 µm. In general, for polymeric materials, the micro-channel's geometry (width and depth) primarily relies on laser power and scanning speed under linear relationship. However, the frequency of laser pulses does not severely affects the channel's depth and width [237]. Malhotra et al. [65] produced micro-channels on transparent alumina ceramic, shiny silicon wafer, sialon, and polycarbonate with laser-induced plasma micro-machining (LIPMM) process and direct laser ablation as shown in Fig. 54. The micro-channel grooves can be fabricated by laser micro-machining, MEMS, or LIGA technologies. The micro-grooves of the micro flat heat pipe were fabricated on copper foil using a femtosecond laser micro-machining technique. A commercial chirped pulse amplification laser system and a translation *XYZ*-stage were used to fabricate the grooves under normal atmospheric air. The laser beam was focused on the work-piece using a $10\times$ objective lens, and the workpiece was firmly attached on the translation stage using tape. The microgrooves, which serve to facilitate liquid passage during operation, were machined on the top and bottom plates. The width, depth, and length of each microgroove were about 150, 300, and 50 mm, respectively, and 16 grooves were produced on each plate.

Table 7 Different machining processes; advantages and shortfalls

Process/operation	Geometry/tools	Advantages	Shortfalls	References
Conventional drilling	Holes through modified twist drills Holes by gun-drilling	High aspect ratio 50 % increase in tool life by coating	Drill damage High wear High heat generation Tool degradation Poor straightness Burrs at edges High tool cost	[248, 249]
Conventional milling	Diamond-like coated micro-end mill (Ø 760 µm) WC–Co micro milling tools Micro-grooves by diamond tool	High material removal rate ($3401 \ mm^3/min$) [215] Smaller cutting forces Better surface finish	High cost of micro-tools Chip adhesion High thrust forces Heat affected zone Striations	[215–219]
Conventional turning	Coated tools uncoated tools	Improves hardness Work hardening layer (around 100 µm)	Surface tearing Cavities, cracking Metallurgical recrystallization Plastic deformation Residual stresses	[250–253]
EDM/WEDM (cutting, milling and drilling)	Fir tree slots by brass wire Coated high speed cutting wire [254] Flat bottomed tool [255] Powder metallurgy processed CuW electrode [256]	Material removal efficiency in W-EDM [228] Reduced machining stresses Improved micro-hardness (from 380.9 to 496.7 HV) [256] Lesser metallurgical damage Complex features Less heat affected layer	Low productivity ($0.47 \times 10^{-8} \ mm^3/min$) Tool wear rate ($5.6 \times 10^{-9} \ mm^3/min$) Suitable for small batch size [226] Lack of precision due to tool wear Poor cylindericity Thick recast layer (from 2.5 to 30 µm) [227] Heat affected layer 40–100 µm [227]	[226–230, 254–260]

Table 7 (continued)

Process/operation	Geometry/tools	Advantages	Shortfalls	References
			Thick white layers (6–8 μm) with micro-cracks [228], Micro-cracks [257, 258], Poor surface integrity [229], Post processing requirements [230], Less fatigue life [259]	
ECM		High material removal rates [261], Good surface integrity [261], Less heat affected zone [262]	High tooling cost, Suitable for large batch sizes [226], Salt film on machined surface [261], Selective corrosion due to the formation of a porous salt film [263], Current density ($<5A\ cm^2$) results undesirable dissolution [263]	[226, 261–265],
Air/abrasive/water jet (cutting and milling)	3D pockets (20 × 20 mm) [264]	No tool required, Very less thermal effects	Surface striations, Waviness [265], Surface waviness (Wa = 7.53–10.37 μm for NiTi shape memory alloy) [266], Undercut to the designed geometry [264], Surface roughness (R_a = 2–8 μm for Inconel) [267], Surface residual stress, Compressive stresses [268, 269]	[266–269]
Ultrasonic/vibration assisted (cutting, turning, milling, drilling and grinding)		Improve surface roughness by 9.10–51.61 %, Decrease cutting force by 32.34–24.47 % [270]	Large vibration amplitudes lowers drill life [271], Greater wheel wear (30–60 %), Increase roughness (up to 24 %) [272]	[270–274]

(continued)

Table 7 (continued)

Process/operation	Geometry/tools	Advantages	Shortfalls	References
		Improve drill life [271] Decrease working time [271] Reductions in vertical and horizontal forces [272] Less stresses in the tools [273]	Overlapping grit marks [272]	
Laser/plasma assisted (cutting, drilling and surface modification)		30 % reduction in cutting force [114] Improved surface roughness 40 % [115, 275] Increase in tool life [275, 276] No micro-crack during laser surface melting [277] Increase in hardness by laser surface treatment [278]	Compressive residual stresses [115] Thicker compressive zone (40–70 μm) [279] Hardness reduction [276] Heat affected zone [280] Striation formation Micro-cracking Oxide layers [281] Kerf taper Recast layer [282] Residual stresses [278]	[114, 115, 117]
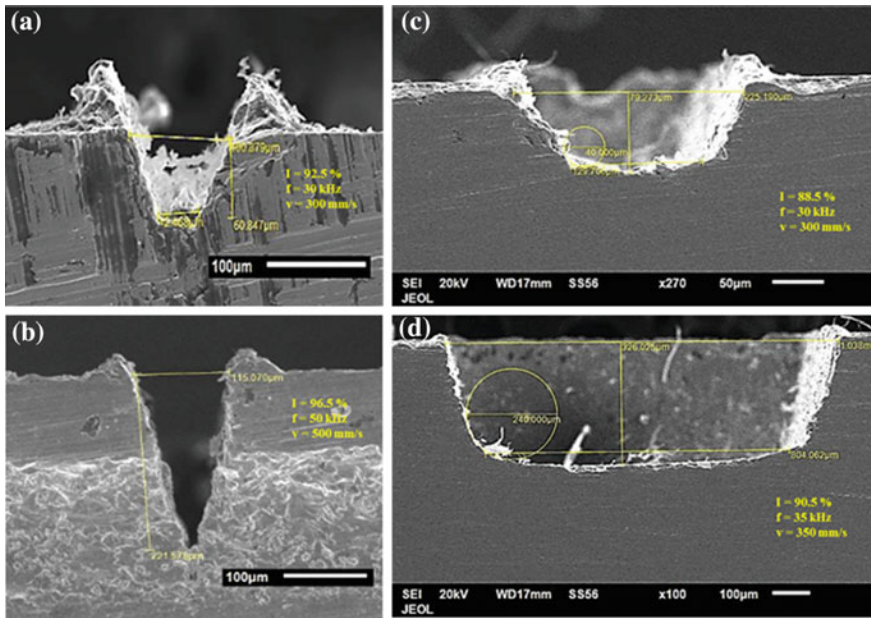
Fig. 53 Micro-channels of different sizes fabricated by Nd:YAG pulsed laser [51]

7.7.2 Micro-channel Materials

Several materials on which the micro-channel fabrication is required are used in different kinds of applications. The choice of material depends on the requirements and systems where the micro-channels have to serve for cooling applications. For example, copper micro-channels are used for heat sinks cooling [224] and silicon micro-channels for particle physics detectors [238, 239]. Micro-channels in aluminum alloy can be found in [221, 223, 225]. Very less study is done on fabrication of micro-channels in hard-to-machine materials like titanium and nickel alloys. The fabrication of micro-channels in non-metallic can be found in various studies showing micro-channels produced in Polycarbonate (PC) [240], polymethyl methacrylate (PMMA) [241], Polydimethylsiloxane (PDMS) [242] and boro-aluminosilicate glass [243].

7.7.3 Micro-channel Shapes and Sizes

In terms of micro-channel's cross-sectional shapes, different shapes are reported in literature including rectangular [244], triangular [239], trapezoidal [245] and circular cross-section micro-channels [246]. In one of the study, a unique Ω-shaped

cross section was seen where the researchers study the effect of micro-channel shape on flow boiling performance of fluids passing through micro-passages of the channels [224]. They also compared the performance of Ω-shaped micro-channels with rectangular shaped micro-channels. The most common type of micro-channel cross section found in literature is the open ended v-shaped or u-shaped square/rectangular cross section. The shape and size of micro-channel directly influence the fluid flow characteristics, heat transfer process, pressure drop characteristics and two-phase flow instabilities. For example, 100 parallel micro-channels having equal sizes of $100 \times 680 \ \mu m$ have been fabricated in multichannel heat sink used for cooling of micro-electronic central processing unit to study the two-phase flow boiling of R134a refrigerant [247]. In another similar study, the air and water (two-phase) flow performance is studied in hybrid
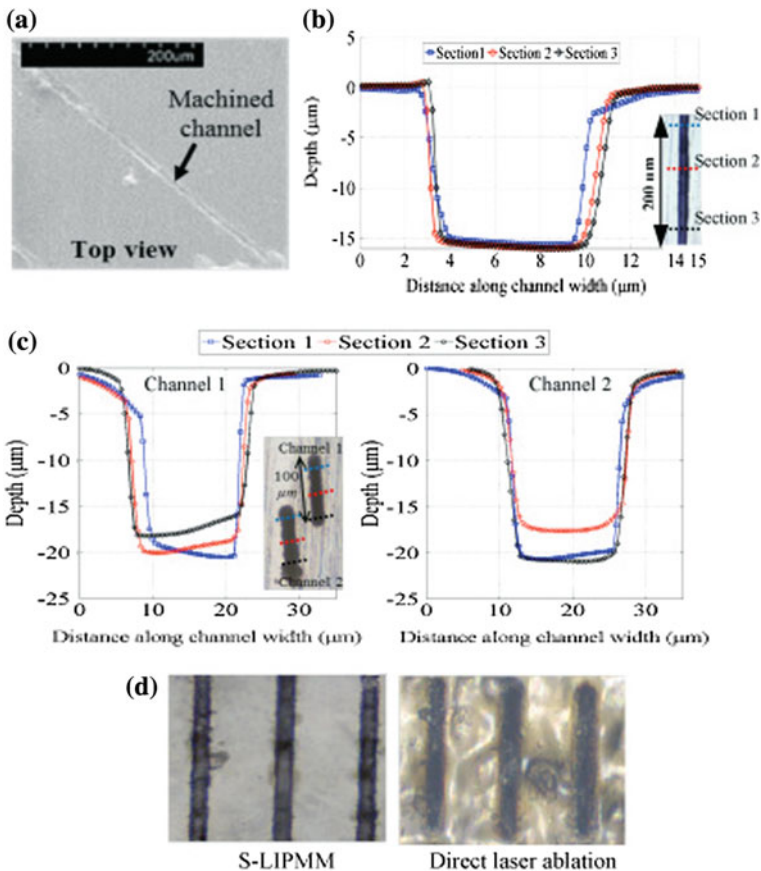
Fig. 54 Channels machined on: **a** transparent alumina ceramic, **b** shiny silicon wafer, **c** sialon, and **d** polycarbonate with laser-induced plasma micro-machining (LIPMM) process and direct laser ablation [65]

micro-channel solar cell by fabricating an array of rectangular micro-channels with a hydraulic diameter of 667 µm. To meet a similar objective, the authors of [244] used three high-aspect-ratio rectangular shaped micro-channels having the hydraulic diameters of 571, 762 and 1454 µm.

7.8 Conclusions and Remarks

Micro-channels have proven tremendous applications in several engineering and biomedical fields. From the brief literature reviewed with respect to the micro-channels applications and fabrication techniques, following conclusions may possibly be drawn:

1. The micro-channels are extensively used in various fields including engineering, aerospace, automotive, and biomedical applications. The micro-channels are utilized in the form of micro-heat exchangers, micro-reactors, micro-channel heat plates, and micro-pulsating heat pipes etc.
2. Fluid flow dynamics inside the micro-channels plays an important role to design the precise process where the micro-channels are required. The flow boiling performance of fluids passing through micro-passages of the micro-channels is widely attempted. About the fluid flow dynamics, a common inference can be established that the flow boiling performance inside the micro-channels depends on the shape and size of micro-channels.
3. There are several techniques to produce micro-channels on different materials, such as micro-CNC machining, micro-hot embossing, micro-forming, micro-die casting, chemical etching, electric discharge machining (EDM) and laser beam machining (LBM). Among these techniques, laser beam machining is considered as the most flexible micro-channel fabrication process in terms of flexibility in material and production, quality, size, and shape.
4. Depending on the application requirements, almost all kinds of materials including metals and non-metals are used for the fabrication of micro-channels of several sizes. Selection of micro-channel size solely depends on the fluid flow requirements. That is why, a number of micro-channel sizes can be found in several researches and thus, the literature is dense in this regard. In terms of micro-channel's cross-sectional shapes, different shapes are reported in literature including rectangular, triangular, trapezoidal and circular cross-section micro-channels. However, the rectangular shaped micro-channels are most widely attempted and required.

8   Future Directions of Research

The discussion in the previous sections is about the overview of recent developments in LBM and the widely used hybrid processes associated with laser LBM. Researchers have contributed in many directions of pure LBM and hybrid-LBM. The following recommendations could be assumed as the future research areas in LBM and its hybrid tree especially fluidic LBM.

- Hypothetically, the ablation mechanism of LBM is well addressed by many researchers showing that large number of factors contribute to ablation such as laser features, laser parameters, material's properties (thermal, chemical, mechanical), absorptivity, reflectivity, assist gas and much more. Effects of laser parameters and assist gas are deeply investigated but, the researchers have excluded many important material based factors such as absorptivity, reflectivity, latent heats and thermal conductivity of work material which otherwise would surely affect the performance characteristics differently. The consideration of material based properties and the interaction of effects on machining characteristics could be a bright research area.
- Physics based phenomenon (absorption, reflection, thermal reaction, chemical dissolution and many more) get involved when laser radiations strike and interact with the work material. The explanations of such phenomena is although quoted by some authors but in randomized order. The identification of such phenomena is need to be addressed in a more categorical viewpoint. The evaluation and validation in scientific manner is additionally more tedious and requires further research to understand the actual mechanisms involved in laser ablation.
- Similarly, the type of laser (nanosecond, picosecond and femtosecond) involves varying physics based facts. For example, much complicated physics involved in picosecond laser ablation as compared to other types. Therefore, more detailed experimental and theoretical work is still needed to further clarify the ablation mechanism for each type of laser.
- The logical reasoning of force reduction and high MRR in LAM is well presented but the clarifications of tool life and surface integrity improvements are not properly disclosed. This is due to the non-standardized evaluation procedures adopted especially for tool life. That is why there is conflict among the results. Employing the standard procedures for tool wear may generate even different results than quoted which leads towards a new research direction in LAM.
- HAZ is always there in LBM as well as in LAM. It is, almost all the time, a usual and unwanted characteristic. Temperature distribution and its measurement (in LAM and LBM) is essential to determine HAZ. This measurement is relatively easier during LAM than in LBM. There is much liberty for positioning thermocouples or an infrared camera during LAM but LBM offers more restrictions due to confined place. For thin sheets (wafers) the temperature can easily be captured by thermocouples mounted at the backside of the sheet but

does not give the actual heat values. Thus, we need estimations and some assumptions. Furthermore, dealing with thick plates, the use of thermocouples becomes inefficient. Modern thermal cameras are promising in this regard but offer high resistance for their installations in between the laser head and work station. Therefore, the actual temperature measurements in LBM and their scientific validations might be a future research area. Particularly, measurements of thermal distributions for thick sheets and plates requires more research in the future. The temperature measurements ultimately rivet with thermal models. Thus, thermal modeling would become more relied for thick plates.

- During LCM/E there are laser based and chemical etchant based parameters that in combine governs the high precise and good quality ablation. The laser based and etching based parameters closely interconnect with each other. The impact of each set of parameters is researched individually. The optimization of the combined parametric window needs to be explored in the future research that would serve more effectively to understand the interacting behaviors of laser and etchant. In addition, as the etching mechanism is a complex in the presence of laser energy, thus, controlling the etching process to obtain structures of desired shape, size, and surface quality is still an issue to be resolved for micromachining applications

- Low MRR and short aspect ratio are still two iconic drawbacks of LCM/E that should be addressed in future research. Although, the etch rate is widely evaluated by many research teams with a fixed ratio of etchant and varying conditions of laser parameters. Experimentation with varying etchant concentrations is very rarely reported. It may yield more improved results especially for high aspect ratio and MRR. The effects of varying chemical concentrations on machined geometries and microstructural modifications is suggested as an upcoming research direction.

- Again, the ablation mechanism of UWLA processes involves a lot of factors that is why a mix of inferences are found especially related to the ablation rate. The common reason behind this conflict is reported as the particular behavior of the target material. This leads to a wide research gap that could be filled up in future by fine tuning the understanding of ablation phenomenon. This could be achieved by the real time measurements (of temperatures, chemical reactions, phase transformations, plasma pressure, shock wave and many more) and post analysis. One of the possible ways to obtain the ablation rate in real time is to measure the acoustic wave at the laser-work-interaction zone by some microphone as experienced by Zhu et al. [175].

- Under the category of UWLA, there is a dense study available to synthesize nano-particles (NPs) of various metals. The process is very commonly attributed to yield NPs of metals with some oxides or carbides due to the presence of water. The future research could be directed to restrict the process for producing pure metal NPs instead of oxides.

- In terms of micro-channels fabrication through laser beam machining (LBM), the produced micro-channels are either undersized or oversized for some geometrical characteristics. It has not been addressed in open literature. The

variation is micro-channel sizes disturbs the fluid flow dynamics and performance during operation. Therefore, the variations in micro-channel geometries caused by LBM can be chosen as a fresh research area.

- The laser beam machining (LBM) produces micro-channels with taperness along channel's sidewalls. Many factors involve in resulting the taperness of sidewalls. However, the taperness is mainly due to Gaussian shape of laser beam. The fabrication of micro-channels with straight sidewalls having 90° angle is very difficult to produce through LBM. The future research in this direction may be carried out to produce vertical sidewalls of micro-channels.

References

1. Dubey, A.K., Yadava, V.: Laser beam machining—a review. Int. J. Mach. Tools Manuf. **48** (6), 609–628 (2008)
2. Yilbas, B.S.: 9.02—Laser heating and the phase change process. In: Hashmi, S., Batalha, G. F., Tyne, C.J.V., Yilbas, B. (eds.) Comprehensive Materials Processing, pp. 5–24. Elsevier, Oxford (2014)
3. Willis, D.A., Xu, X.: Heat transfer and phase change during picosecond laser ablation of nickel. Int. J. Heat Mass Transf. **45**(19), 3911–3918 (2002)
4. Chryssolouris, G., Anifantis, N., Karagiannis, S.: Laser assisted machining: an overview. J. Manuf. Sci. Eng. **119**(4B), 766–769 (1997)
5. Nakashima, S., Sugioka, K., Midorikawa, K.: Fabrication of microchannels in single-crystal GaN by wet-chemical-assisted femtosecond-laser ablation. Appl. Surf. Sci. **255**(24), 9770–9774 (2009)
6. Dong, C., Gu, Y., Zhong, M., Li, L., Sezer, K., Ma, M., Liu, W.: Fabrication of superhydrophobic Cu surfaces with tunable regular micro and random nano-scale structures by hybrid laser texture and chemical etching. J. Mater. Process. Technol. **211**(7), 1234–1240 (2011)
7. Nowak, R., Metev, S.: Thermochemical laser etching of stainless steel and titanium in liquids. Appl. Phys. A **63**(2), 133–138 (1996)
8. Park, J.-K., Yoon, J.-W., Cho, S.-H.: Vibration assisted femtosecond laser machining on metal. Opt. Lasers Eng. **50**(6), 833–837 (2012)
9. Park, J.-K., Yoon, J.-W., Kang, M.-C., Cho, S.-H.: Surface effects of hybrid vibration-assisted femtosecond laser system for micro-hole drilling of copper substrate. Trans. Nonferrous Met. Soc. China **22**(Supplement 3), s801–s807 (2012)
10. Li, L., Diver, C., Atkinson, J., Giedl-Wagner, R., Helml, H.J.: Sequential laser and EDM micro-drilling for next generation fuel injection nozzle manufacture. CIRP Ann. Manuf. Technol. **55**(1), 179–182 (2006)
11. Lu, J., Xu, R.Q., Chen, X., Shen, Z.H., Ni, X.W., Zhang, S.Y., Gao, C.M.: Mechanisms of laser drilling of metal plates underwater. J. Appl. Phys. **95**(8), 3890–3894 (2004)
12. O'Malley, S.M., Amin, M., Borchert, J., Jimenez, R., Steiner, M., Fitz-Gerald, J.M., Bubb, D.M.: Formation of rubrene nanocrystals by laser ablation in liquids utilizing MAPLE deposited thin films. Chem. Phys. Lett. **595–596**, 171–174 (2014)
13. Taniguchi, N.: Current status in, and future trends of, ultraprecision machining and ultrafine materials processing. CIRP Ann. Manuf. Technol. **32**(2), 573–582 (1983)

14. Meijer, J., Du, K., Gillner, A., Hoffmann, D., Kovalenko, V.S., Masuzawa, T., Ostendorf, A., Poprawe, R., Schulz, W.: Laser machining by short and ultrashort pulses, state of the art and new opportunities in the age of the photons. CIRP Ann. Manuf. Technol. **51**(2), 531–550 (2002)

15. Meijer, J.: Laser beam machining (LBM), state of the art and new opportunities. J. Mater. Process. Technol. **149**(1–3), 2–17 (2004)

16. Chen, X., Liu, X.: Short pulsed laser machining: how short is short enough? J. Laser Appl. **11**(6), 268–272 (1999)

17. Ready, J.F.: Fundamentals of lasers (Chapter 1). In: Ready, J.F. (ed.) Industrial Applications of Lasers, 2nd edn, pp. 1–30. Academic Press, San Diego (1997)

18. Samant, A.N., Dahotre, N.B.: Three-dimensional laser machining of structural ceramics. J. Manuf. Process. **12**(1), 1–7 (2010)

19. Meijer, J.: Laser beam machining (LBM), state of the art and new opportunities. J. Mater. Process. Technol. **149**(1–3), 2–17 (2004)

20. Pham, D.T., Dimov, S.S., Petkov, P.V.: Laser milling of ceramic components. Int. J. Mach. Tools Manuf. **47**(3–4), 618–626 (2007)

21. Bäuerle, D.: Laser Processing and Chemistry. Springer, Heidelberg (2011)

22. Vogel, A., Noack, J., Nahen, K., Theisen, D., Busch, S., Parlitz, U., Hammer, D.X., Noojin, G.D., Rockwell, B.A., Birngruber, R.: Energy balance of optical breakdown in water at nanosecond to femtosecond time scales. Appl. Phys. B **68**(2), 271–280 (2014)

23. Liu, X., Du, D., Mourou, G.: Laser ablation and micromachining with ultrashort laser pulses. IEEE J. Quantum Electron. **33**(10), 1706–1716 (1997)

24. Sola, D., Peña, J.I.: Laser machining of Al_2O_3–ZrO_2 (3 %Y_2O_3) eutectic composite. J. Eur. Ceram. Soc. **32**(4), 807–814 (2012)

25. Cejnar, M., Kobler, H., Hunyor, S.N.: Quantitative photoplethysmography: Lambert-Beer law or inverse function incorporating light scatter. J. Biomed. Eng. **15**(2), 151–154 (1993)

26. Weber, R., Hafner, M., Michalowski, A., Graf, T.: Minimum damage in CFRP laser processing. Phys. Procedia **12**(Part B), 302–307 (2011)

27. Yilbas, B.S., Shuja, S.Z., Arif, A., Gondal, M.A.: Laser-shock processing of steel. J. Mater. Process. Technol. **135**(1), 6–17 (2003)

28. Zweig, A.D., Deutsch, T.F.: Shock waves generated by confined XeCl excimer laser ablation of polyimide. Appl. Phys. B **54**(1), 76–82 (1992)

29. Mishra, S., Yadava, V.: Modeling and optimization of laser beam percussion drilling of nickel-based superalloy sheet using Nd:YAG laser. Opt. Lasers Eng. **51**(6), 681–695 (2013)

30. Yue, L., Wang, Z., Li, L.: Material morphological characteristics in laser ablation of alpha case from titanium alloy. Appl. Surf. Sci. **258**(20), 8065–8071 (2012)

31. Milovanović, D.S., Petrović, S.M., Shulepov, M.A., Tarasenko, V.F., Radak, B.B., Miljanić, Š.S., Trtica, M.S.: Titanium alloy surface modification by excimer laser irradiation. Opt. Laser Technol. **54**, 419–427 (2013)

32. Cheng, J., Perrie, W., Wu, B., Tao, S., Edwardson, S.P., Dearden, G., Watkins, K.G.: Ablation mechanism study on metallic materials with a 10 ps laser under high fluence. Appl. Surf. Sci. **255**(18), 8171–8175 (2009)

33. Le Harzic, R., Breitling, D., Weikert, M., Sommer, S., Föhl, C., Valette, S., Donnet, C., Audouard, E., Dausinger, F.: Pulse width and energy influence on laser micromachining of metals in a range of 100 fs to 5 ps. Appl. Surf. Sci. **249**(1–4), 322–331 (2005)

34. Khosroshahi, M.E., Mahmoodi, M., Tavakoli, J.: Characterization of Ti6Al4V implant surface treated by Nd:YAG laser and emery paper for orthopaedic applications. Appl. Surf. Sci. **253**(21), 8772–8781 (2007)

35. Cunha, A., Serro, A.P., Oliveira, V., Almeida, A., Vilar, R., Durrieu, M.-C.: Wetting behaviour of femtosecond laser textured Ti–6Al–4V surfaces. Appl. Surf. Sci. **265**, 688–696 (2013)

36. Balla, V.K., Soderlind, J., Bose, S., Bandyopadhyay, A.: Microstructure, mechanical and wear properties of laser surface melted Ti6Al4V alloy. J. Mech. Behav. Biomed. Mater. **32**, 335-344 (2014)

37. Amaya-Vazquez, M.R., Sánchez-Amaya, J.M., Boukha, Z., Botana, F.J.: Microstructure, microhardness and corrosion resistance of remelted TiG2 and Ti6Al4V by a high power diode laser. Corros. Sci. **56**, 36–48 (2012)

38. Al-ahmari, A., Saied, D., Naveed, A.: Laser beam micro-milling (LBMM) of selected aerospace alloys. Int. J. Adv. Manuf. Technol. (2016, Jan)

39. Ahmed, N., Darwish, S., Alahmari, A.M., Shar, M.A.: Micro-channels by Nd:YAG laser beam machining: fabrication, microstructures, and micro-hardness profiles. Int. J. Adv. Manuf. Technol. 1–14 (2015, May)

40. Ahn, D.-G., Byun, K.-W.: Influence of cutting parameters on surface characteristics of cut section in cutting of Inconel 718 sheet using CW Nd:YAG laser. Trans. Nonferrous Met. Soc. China **19**(Supplement 1), s32–s39 (2009)

41. Ahn, D.G., Kim, M.S., Yoo, Y.T., Park, H.J.: Effects of process parameters on surface characteristics in cutting of cold rolled steel sheets using a high-power CW Nd: YAG laser. Mater. Sci. Forum **580–582**, 455–458 (2008)

42. Ahn, D.G., Byun, K.W., Kang, M.C.: Thermal characteristics in the cutting of inconel 718 superalloy using CW Nd:YAG laser. J. Mater. Sci. Technol. **26**(4), 362–366 (2010)

43. Hasçalık, A., Ay, M.: CO_2 laser cut quality of Inconel 718 nickel—based superalloy. Opt. Laser Technol. **48**, 554–564 (2013)

44. Wolynski, A., Herrmann, T., Mucha, P., Haloui, H., L'huillier, J.: Laser ablation of CFRP using picosecond laser pulses at different wavelengths from UV to IR. Phys. Procedia, **12** (Part B), 292–301 (2011)

45. Jiao, J., Wang, X.: Cutting glass substrates with dual-laser beams. Opt. Lasers Eng. **47**(7–8), 860–864 (2009)

46. Emmelmanna, C., Petersen, M., Goeke, A., Canisius, M.: Analysis of laser ablation of CFRP by ultra-short laser pulses with short wavelength. Phys. Procedia **12**(Part A), 565–571 (2011)

47. Ghosal, A., Manna, A.: Response surface method based optimization of ytterbium fiber laser parameter during machining of Al/Al_2O_3-MMC. Opt. Laser Technol. **46**, 67–76 (2013)

48. Ulutan, D., Ozel, T.: Machining induced surface integrity in titanium and nickel alloys: a review. Int. J. Mach. Tools Manuf. **51**(3), 250–280 (2011)

49. Cicală, E., Soveja, A., Sallamand, P., Grevey, D., Jouvard, J.M.: The application of the random balance method in laser machining of metals. J. Mater. Process. Technol. **196**(1–3), 393–401 (2008)

50. Perry, T.L., Werschmoeller, D., Li, X., Pfefferkorn, F.E., Duffie, N.A.: Pulsed laser polishing of micro-milled Ti6Al4V samples. J. Manuf. Process. **11**(2), 74–81 (2009)

51. Ahmed, N., Darwish, S., Alahmari, A.M., Salik, K.: Laser ablation process competency to fabricate microchannels in titanium alloy. Mater. Manuf. Process. **30**(11), 1290–1297 (2015)

52. Dehmas, M., Lacaze, J., Niang, A., Viguier, B.: TEM study of high-temperature precipitation of delta phase in Inconel 718 alloy. Adv. Mater. Sci. Eng. **2011**, e940634 (2011)

53. Kuo, C.-M., Yang, Y.-T., Bor, H.-Y., Wei, C.-N., Tai, C.-C.: Aging effects on the microstructure and creep behavior of Inconel 718 superalloy. Mater. Sci. Eng. A **510–511**, 289–294 (2009)

54. Aliou Niang, B.V.: Some features of anisothermal solid-state transformations in alloy 718. Mater. Charact. **61**(5), 525–534 (2010)

55. Ghosh, S., Yadav, S., Das, G.: Study of standard heat treatment on mechanical properties of Inconel 718 using ball indentation technique. Mater. Lett. **62**(17–18), 2619–2622 (2008)

56. Chester, T.S., Norman, S.S., William, C.H.: Wiley: superalloys II: high-temperature materials for aerospace and industrial power [Online]. Available: http://eu.wiley.com/WileyCDA/WileyTitle/productCd-0471011479.html. Accessed: 26 Apr 2015

57. Yang, X., Richard Liu, C.: Machining titanium and its alloys. Mach. Sci. Technol. **3**(1), 107–139 (1999)

58. Yilbas, B.S., Akhtar, S.S., Karatas, C.: Laser surface treatment of Inconel 718 alloy: thermal stress analysis. Opt. Lasers Eng. **48**(7–8), 740–749 (2010)

59. Reissig, L., Völkl, R., Mills, M.J., Glatzel, U.: Investigation of near surface structure in order to determine process-temperatures during different machining processes of Ti6Al4V. Scr. Mater. **50**(1), 121–126 (2004)

60. Choi, H., Li, X.: Fabrication and application of micro thin film thermocouples for transient temperature measurement in nanosecond pulsed laser micromachining of nickel. Sens. Actuators Phys. **136**(1), 118–124 (2007)

61. Semaltianos, N.G., Perrie, W., French, P., Sharp, M., Dearden, G., Watkins, K.G.: Femtosecond laser surface texturing of a nickel-based superalloy. Appl. Surf. Sci. **255**(5, Part 2), 2796–2802 (2008)

62. Fauchet, P.M.: Gradual surface transitions on semiconductors induced by multiple picosecond laser pulses. Phys. Lett. A **93**(3), 155–157 (1983)

63. Fournier, I., Marinach, C., Tabet, J.C., Bolbach, G.: Irradiation effects in MALDI, ablation, ion production, and surface modifications. Part II: 2,5-dihydroxybenzoic acid monocrystals. J. Am. Soc. Mass Spectrom. **14**(8), 893–899 (2003)

64. Li, L., Kim, J.H., Shukor, M.H.A.: Grit blast assisted laser milling/grooving of metallic alloys. CIRP Ann. Manuf. Technol. **54**(1), 183–186 (2005)

65. Malhotra, R., Saxena, I., Ehmann, K., Cao, J.: Laser-induced plasma micro-machining (LIPMM) for enhanced productivity and flexibility in laser-based micro-machining processes. CIRP Ann. Manuf. Technol. **62**(1), 211–214 (2013)

66. Lee, S.W., Shin, H.S., Chu, C.N.: Fabrication of micro-pin array with high aspect ratio on stainless steel using nanosecond laser beam machining. Appl. Surf. Sci. **264**, 653–663 (2013)

67. Samant, A.N., Dahotre, N.B.: Differences in physical phenomena governing laser machining of structural ceramics. Ceram. Int. **35**(5), 2093–2097 (2009)

68. Samant, A.N., Dahotre, N.B.: An integrated computational approach to single-dimensional laser machining of magnesia. Opt. Lasers Eng. **47**(5), 570–577 (2009)

69. Girardot, J., Schneider, M., Berthe, L., Favier, V.: Investigation of delamination mechanisms during a laser drilling on a cobalt-base superalloy. J. Mater. Process. Technol. **213**(10), 1682–1691 (2013)

70. Voisey, K.T., Clyne, T.W.: Laser drilling of cooling holes through plasma sprayed thermal barrier coatings. Surf. Coat. Technol. **176**(3), 296–306 (2004)

71. Yilbas, B.S., Akhtar, S.S., Karatas, C.: Laser trepanning of a small diameter hole in titanium alloy: temperature and stress fields. J. Mater. Process. Technol. **211**(7), 1296–1304 (2011)

72. Tam, S.C., Yeo, C.Y., Jana, S., Lau, M.W.S., Lim, L.E.N., Yang, L.J., Noor, Y.M.: Optimization of laser deep-hole drilling of Inconel 718 using the Taguchi method. J. Mater. Process. Technol. **37**(1–4), 741–757 (1993)

73. Mishra, S., Yadava, V.: Modeling and optimization of laser beam percussion drilling of thin aluminum sheet. Opt. Laser Technol. **48**, 461–474 (2013)

74. Low, D.K.Y., Li, L., Byrd, P.J.: The effects of process parameters on spatter deposition in laser percussion drilling. Opt. Laser Technol. **32**(5), 347–354 (2000)

75. Yan, Y., Ji, L., Bao, Y., Jiang, Y.: An experimental and numerical study on laser percussion drilling of thick-section alumina. J. Mater. Process. Technol. **212**(6), 1257–1270 (2012)

76. Low, D.K.Y., Li, L., Corfe, A.G., Byrd, P.J.: Spatter-free laser percussion drilling of closely spaced array holes. Int. J. Mach. Tools Manuf. **41**(3), 361–377 (2001)

77. Choudhury, I.A., Chong, W.C., Vahid, G.: Hole qualities in laser trepanning of polymeric materials. Opt. Lasers Eng. **50**(9), 1297–1305 (2012)

78. He, D., Shinshi, T., Nakai, T.: Development of a maglev lens driving actuator for off-axis control and adjustment of the focal point in laser beam machining. Precis. Eng. **37**(2), 255–264 (2013)

79. Lendraitis, V., Brikas, M., Snitka, V., Mizarienė, V., Raciukaitis, G.: Fabrication of actuator for nanopositioning using laser micro-machining. Microelectron. Eng. **83**(4–9), 1212–1215 (2006)

80. Ng, G.K.L., Crouse, P.L., Li, L.: An analytical model for laser drilling incorporating effects of exothermic reaction, pulse width and hole geometry. Int. J. Heat Mass Transf. **49**(7–8), 1358–1374 (2006)

81. Beno, T., Hulling, U.: Measurement of cutting edge temperature in drilling. Procedia CIRP **3**, 531–536 (2012)

82. Ashkenasi, D., Kaszemeikat, T., Mueller, N., Dietrich, R., Eichler, H.J., Illing, G.: Laser trepanning for industrial applications. Phys. Procedia **12**(Part B), 323–331 (2011)

83. Jahns, D., Kaszemeikat, T., Mueller, N., Ashkenasi, D., Dietrich, R., Eichler, H.J.: Laser trepanning of stainless steel. Phys. Procedia **41**, 630–635 (2013)

84. Fornaroli, C., Holtkamp, J., Gillner, A.: Laser-beam helical drilling of high quality micro holes. Phys. Procedia **41**, 661–669 (2013)

85. Man, H.C., Wang, Q., Guo, X.: Laser surface microdrilling of Ti and laser gas nitrided Ti for enhancing fixation of dental implants. Opt. Lasers Eng. **48**(5), 583–588 (2010)

86. Jiao, J., Wang, X.: A numerical simulation of machining glass by dual CO_2-laser beams. Opt. Laser Technol. **40**(2), 297–301 (2008)

87. Wan, D., Liu, H., Wang, Y., Hu, D., Gui, Z.: CO_2 laser beam modulating for surface texturing machining. Opt. Laser Technol. **40**(2), 309–314 (2008)

88. Tsai, C.-H., Chen, H.-W.: Laser milling of cavity in ceramic substrate by fracture-machining element technique. J. Mater. Process. Technol. **136**(1–3), 158–165 (2003)

89. Biswas, R., Kuar, A.S., Sarkar, S., Mitra, S.: A parametric study of pulsed Nd:YAG laser micro-drilling of gamma-titanium aluminide. Opt. Laser Technol. **42**(1), 23–31 (2010)

90. Chang, C.-W., Kuo, C.-P.: An investigation of laser-assisted machining of Al_2O_3 ceramics planing. Int. J. Mach. Tools Manuf. **47**(3–4), 452–461 (2007)

91. Germain, G., Dal Santo, P., Lebrun, J.L.: Comprehension of chip formation in laser assisted machining. Int. J. Mach. Tools Manuf. **51**(3), 230–238 (2011)

92. Pfefferkorn, F.E., Incropera, F.P., Shin, Y.C.: Heat transfer model of semi-transparent ceramics undergoing laser-assisted machining. Int. J. Heat Mass Transf. **48**(10), 1999–2012 (2005)

93. Tagliaferri, F., Leopardi, G., Semmler, U., Kuhl, M., Palumbo, B.: Study of the influences of laser parameters on laser assisted machining processes. Procedia CIRP **8**, 170–175 (2013)

94. Chang, C.-W., Kuo, C.-P.: Evaluation of surface roughness in laser-assisted machining of aluminum oxide ceramics with Taguchi method. Int. J. Mach. Tools Manuf. **47**(1), 141–147 (2007)

95. Bejjani, R., Shi, B., Attia, H., Balazinski, M.: Laser assisted turning of titanium metal matrix composite. CIRP Ann. Manuf. Technol. **60**(1), 61–64 (2011)

96. Attia, H., Tavakoli, S., Vargas, R., Thomson, V.: Laser-assisted high-speed finish turning of superalloy Inconel 718 under dry conditions. CIRP Ann. Manuf. Technol. **59**(1), 83–88 (2010)

97. García Navas, V., Arriola, I., Gonzalo, O., Leunda, J.: Mechanisms involved in the improvement of Inconel 718 machinability by laser assisted machining (LAM). Int. J. Mach. Tools Manuf. **74**, 19–28 (2013)

98. Rahman Rashid, R.A., Sun, S., Wang, G., Dargusch, M.S.: An investigation of cutting forces and cutting temperatures during laser-assisted machining of the Ti–6Cr–5Mo–5V–4Al beta titanium alloy. Int. J. Mach. Tools Manuf. **63**, 58–69 (2012)

99. Rahman Rashid, R.A., Sun, S., Wang, G., Dargusch, M.S.: The effect of laser power on the machinability of the Ti-6Cr-5Mo-5V-4Al beta titanium alloy during laser assisted machining. Int. J. Mach. Tools Manuf. **63**, 41–43 (2012)

100. Dumitrescu, P., Koshy, P., Stenekes, J., Elbestawi, M.A.: High-power diode laser assisted hard turning of AISI D2 tool steel. Int. J. Mach. Tools Manuf. **46**(15), 2009–2016 (2006)

101. Zamani, H., Hermani, J.-P., Sonderegger, B., Sommitsch, C.: 3D simulation and process optimization of laser assisted milling of Ti6Al4V. Procedia CIRP **8**, 75–80 (2013)

102. Masood, S.H., Armitage, K., Brandt, M.: An experimental study of laser-assisted machining of hard-to-wear white cast iron. Int. J. Mach. Tools Manuf. **51**(6), 450–456 (2011)

103. Skvarenina, S., Shin, Y.C.: Laser-assisted machining of compacted graphite iron. Int. J. Mach. Tools Manuf. **46**(1), 7–17 (2006)

104. Kim, D.-H., Lee, C.-M.: A study of cutting force and preheating-temperature prediction for laser-assisted milling of Inconel 718 and AISI 1045 steel. Int. J. Heat Mass Transf. **71**, 264–274 (2014)

105. Dandekar, C.R., Shin, Y.C., Barnes, J.: Machinability improvement of titanium alloy (Ti–6Al–4V) via LAM and hybrid machining. Int. J. Mach. Tools Manuf. **50**(2), 174–182 (2010)

106. Melkote, S., Kumar, M., Hashimoto, F., Lahoti, G.: Laser assisted micro-milling of hard-to-machine materials. CIRP Ann. Manuf. Technol. **58**(1), 45–48 (2009)

107. Bermingham, M.J., Palanisamy, S., Dargusch, M.S.: Understanding the tool wear mechanism during thermally assisted machining Ti-6Al-4V. Int. J. Mach. Tools Manuf. **62**, 76–87 (2012)

108. Ding, H., Shin, Y.C.: Laser-assisted machining of hardened steel parts with surface integrity analysis. Int. J. Mach. Tools Manuf. **50**(1), 106–114 (2010)

109. Yang, J., Sun, S., Brandt, M., Yan, W.: Experimental investigation and 3D finite element prediction of the heat affected zone during laser assisted machining of Ti6Al4V alloy. J. Mater. Process. Technol. **210**(15), 2215–2222 (2010)

110. Singh, R., Alberts, M.J., Melkote, S.N.: Characterization and prediction of the heat-affected zone in a laser-assisted mechanical micromachining process. Int. J. Mach. Tools Manuf. **48** (9), 994–1004 (2008)

111. Yilbas, B.S., Davies, R., Yilbas, Z.: Study into penetration speed during CO_2 laser cutting of stainless steel. Opt. Lasers Eng. **17**(2), 69–82 (1992)

112. Rozzi, J.C., Incropera, F.P., Shin, Y.C.: Transient, three-dimensional heat transfer model for the laser assisted machining of silicon nitride: II. Assessment of parametric effects. Int. J. Heat Mass Transf. **43**(8), 1425–1437 (2000)

113. Tian, Y., Shin, Y.C.: Thermal modeling for laser-assisted machining of silicon nitride ceramics with complex features. J. Manuf. Sci. Eng. **128**(2), 425–434 (2005)

114. Venkatesan, K., Ramanujam, R., Kuppan, P.: Analysis of cutting forces and temperature in laser assisted machining of Inconel 718 using Taguchi method. Procedia Eng. **97**, 1637–1646 (2014)

115. Attia, H., Tavakoli, S., Vargas, R., Thomson, V.: Laser-assisted high-speed finish turning of superalloy Inconel 718 under dry conditions. CIRP Ann. Manuf. Technol. **59**(1), 83–88 (2010)

116. Rebro, P.A., Shin, Y.C., Incropera, F.P.: Design of operating conditions for crackfree laser-assisted machining of mullite. Int. J. Mach. Tools Manuf. **44**(7–8), 677–694 (2004)

117. Venkatesan, K., Ramanujam, R., Kuppan, P.: Laser assisted machining of difficult to cut materials: research opportunities and future directions—a comprehensive review. Procedia Eng. **97**, 1626–1636 (2014)

118. Stephen, A., Sepold, G., Metev, S., Vollertsen, F.: Laser-induced liquid-phase jet-chemical etching of metals. J. Mater. Process. Technol. **149**(1–3), 536–540 (2004)

119. Zhu, D., Qu, N.S., Li, H.S., Zeng, Y.B., Li, D.L., Qian, S.Q.: Electrochemical micromachining of microstructures of micro hole and dimple array. CIRP Ann. Manuf. Technol. **58**(1), 177–180 (2009)

120. Ali, S., Hinduja, S., Atkinson, J., Pandya, M.: Shaped tube electrochemical drilling of good quality holes. CIRP Ann. Manuf. Technol. **58**(1), 185–188 (2009)

121. Jo, C.H., Kim, B.H., Chu, C.N.: Micro electrochemical machining for complex internal micro features. CIRP Ann. Manuf. Technol. **58**(1), 181–184 (2009)

122. Curtis, D.T., Soo, S.L., Aspinwall, D.K., Sage, C.: Electrochemical superabrasive machining of a nickel-based aeroengine alloy using mounted grinding points. CIRP Ann. Manuf. Technol. **58**(1), 173–176 (2009)

123. Kelly, J.J., Philipsen, H.G.G.: Anisotropy in the wet-etching of semiconductors. Curr. Opin. Solid State Mater. Sci. **9**(1–2), 84–90 (2005)

124. Stephen, A.: Mechanisms and applications of laser chemical machining. Phys. Procedia **12** (Part B), 261–267 (2011)

125. Ting, H.T., Abou-El-hossein, K.A., Chua, H.B.: Review of micromachining of ceramics by etching. Trans. Nonferrous Met. Soc. China **19**(Supplement 1), s1–s16 (2009)

126. Dausinger, F.: Femtosecond technology for precision manufacturing: fundamental and technical aspects. **50** (2003)

127. Yamamura, K., Shimada, S., Mori, Y.: Damage-free improvement of thickness uniformity of quartz crystal wafer by plasma chemical vaporization machining. CIRP Ann. Manuf. Technol. **57**(1), 567–570 (2008)

128. Stephen, A., Vollertsen, F.: Mechanisms and processing limits in laser thermochemical machining. CIRP Ann. Manuf. Technol. **59**(1), 251–254 (2010)

129. Kurita, T., Kasashima, N., Yamakiri, H., Ichihashi, N., Kobayashi, N., Ashida, K., Sasaki, S.: Development of the new IC decapsulation technology. Opt. Lasers Eng. **49**(9–10), 1216–1223 (2011)

130. Li, L., Achara, C.: Chemical assisted laser machining for the minimisation of recast and heat affected zone. CIRP Ann. Manuf. Technol. **53**(1), 175–178 (2004)

131. Mehrafsun, S., Vollertsen, F.: Disturbance of material removal in laser-chemical machining by emerging gas. CIRP Ann. Manuf. Technol. **62**(1), 195–198 (2013)

132. Matsuo, S., Sumi, H., Kiyama, S., Tomita, T., Hashimoto, S.: Femtosecond laser-assisted etching of Pyrex glass with aqueous solution of KOH. Appl. Surf. Sci. **255**(24), 9758–9760 (2009)

133. Luo, S.-W., Tsai, H.-Y.: Fabrication of 3D photonic structure on glass materials by femtosecond laser modification with HF etching process. J. Mater. Process. Technol. **213** (12), 2262–2269 (2013)

134. Lin, D., Zhang, M.Y., Ye, C., Liu, Z., Liu, C.R., Cheng, G.J.: Large scale, highly dense nanoholes on metal surfaces by underwater laser assisted hydrogen etching near nanocrystalline boundary. Appl. Surf. Sci. **258**(10), 4254–4259 (2012)

135. Näth, O., Stephen, A., Rösler, J., Vollertsen, F.: Structuring of nanoporous nickel-based superalloy membranes via laser etching. J. Mater. Process. Technol. **209**(10), 4739–4743 (2009)

136. Al-Khazraji, K.K., Rasheeda, B.G., Ibrahem, M.A., Mohammed, A.F.: Effect of laser-induced etching process on porous structures. Procedia Eng. **38**, 1381–1390 (2012)

137. Kumar, R., Mavi, H.S., Shukla, A.K.: Macro and microsurface morphology reconstructions during laser-induced etching of silicon. Micron **39**(3), 287–293 (2008)

138. Nayak, B.K., Gupta, M.C., Kolasinski, K.W.: Ultrafast-laser-assisted chemical restructuring of silicon and germanium surfaces. Appl. Surf. Sci. **253**(15), 6580–6583 (2007)

139. Dai, Y.-T., Xu, G., Tong, X.-L.: Deep UV laser etching of GaN epilayers grown on sapphire substrate. J. Mater. Process. **212**(2), 492–496 (2012)

140. Zhang, F., Duan, J., Zeng, X., Cao, Y.: UV laser microprocessing and post chemical etching on ultrathin Al_2O_3 ceramic substrate. J. Eur. Ceram. Soc. **31**(9), 1631–1639 (2011)

141. Zimmer, K., Böhme, R., Pissadakis, S., Hartwig, L., Reisse, G., Rauschenbach, B.: Backside etching of fused silica with Nd:YAG laser. Appl. Surf. Sci. **253**(5), 2796–2800 (2006)

142. Oh, K.H., Park, J.B., Cho, S.I., Im, H.D., Jeong, S.H.: Investigation of sidewall roughness of the microgrooves manufactured with laser-induced etching technique. Appl. Surf. Sci. **255** (24), 9835–9839 (2009)

143. Luo, S.-W., Chang, T.-L., Tsai, H.-Y.: Fabrication of diffractive microlens array by femtosecond laser-assisted etching process. Microelectron. Eng. **98**, 448–452 (2012)

144. Luo, S.-W., Chang, T.-L., Tsai, H.-Y.: Fabrication of glass micro-prisms using ultra-fast laser pulses with chemical etching process. Opt. Lasers Eng. **50**(2), 220–225 (2012)

145. Datta, M., Landolt, D.: Fundamental aspects and applications of electrochemical microfabrication. Electrochim. Acta **45**(15–16), 2535–2558 (2000)

146. Park, B.J., Kim, B.H., Chu, C.N.: The effects of tool electrode size on characteristics of micro electrochemical machining. CIRP Ann. Manuf. Technol. **55**(1), 197–200 (2006)

147. Kasashima, N., Kurita, T.: Laser and electrochemical complex machining of micro-stent with on-machine three-dimensional measurement. Opt. Lasers Eng. **50**(3), 354–358 (2012)

148. Pajak, P.T., Desilva, A.K.M., Harrison, D.K., Mcgeough, J.A.: Precision and efficiency of laser assisted jet electrochemical machining. Precis. Eng. **30**(3), 288–298 (2006)

149. Long, Y., Shi, T., Xiong, L.: Excimer laser electrochemical etching n-Si in the KOH solution. Opt. Lasers Eng. **48**(5), 570–574 (2010)
150. Kikuchi, T., Wachi, Y., Takahashi, T., Sakairi, M., Suzuki, R.O.: Fabrication of a meniscus microlens array made of anodic alumina by laser irradiation and electrochemical techniques. Electrochim. Acta **94**, 269–276 (2013)
151. Shin, H.S., Park, M.S., Chu, C.N.: Electrochemical etching using laser masking for multilayered structures on stainless steel. CIRP Ann. Manuf. Technol. **59**(1), 585–588 (2010)
152. Shin, H.S., Chung, D.K., Park, M.S., Chu, C.N.: Analysis of machining characteristics in electrochemical etching using laser masking. Appl. Surf. Sci. **258**(5), 1689–1698 (2011)
153. Zhang, H., Xu, J., Wang, J.: Investigation of a novel hybrid process of laser drilling assisted with jet electrochemical machining. Opt. Lasers Eng. **47**(11), 1242–1249 (2009)
154. Hua, Z., Jiawen, X.: Modeling and experimental investigation of laser drilling with jet electrochemical machining. Chin. J. Aeronaut. **23**(4), 454–460 (2010)
155. De Silva, A.K.M., Pajak, P.T., McGeough, J.A., Harrison, D.K.: Thermal effects in laser assisted jet electrochemical machining. CIRP Ann. Manuf. Technol. **60**(1), 243–246 (2011)
156. Pajak, P.T., De Silva, A.K.M., McGeough, J.A., Harrison, D.K.: Modelling the aspects of precision and efficiency in laser-assisted jet electrochemical machining (LAJECM). J. Mater. Process. Technol. **149**(1–3), 512–518 (2004)
157. Tangwarodomnukun, V., Wang, J., Huang, C.Z., Zhu, H.T.: An investigation of hybrid laser–waterjet ablation of silicon substrates. Int. J. Mach. Tools Manuf. **56**, 39–49 (2012)
158. Yang, G.W.: Laser ablation in liquids: applications in the synthesis of nanocrystals. Prog. Mater Sci. **52**(4), 648–698 (2007)
159. Darwish, S., Ahmed, N., Alahmari, A.M., Mufti, N.A.: A comparison of laser beam machining of micro-channels under dry and wet mediums. Int. J. Adv. Manuf. Technol. 1–17 (2015)
160. Dupont, A., Caminat, P., Bournot, P., Gauchon, J.P.: Enhancement of material ablation using 248, 308, 532, 1064 nm laser pulse with a water film on the treated surface. J. Appl. Phys. **78**(3), 2022–2028 (1995)
161. Yan, Y., Li, L., Sezer, K., Wang, W., Whitehead, D., Ji, L., Bao, Y., Jiang, Y.: CO_2 laser underwater machining of deep cavities in alumina. J. Eur. Ceram. Soc. **31**(15), 2793–2807 (2011)
162. Choo, K.L., Ogawa, Y., Kanbargi, G., Otra, V., Raff, L.M., Komanduri, R.: Micromachining of silicon by short-pulse laser ablation in air and under water. Mater. Sci. Eng. A **372**(1–2), 145–162 (2004)
163. Dolgaev, S.I., Lyalin, A.A., Shafeev, G.A., Voronov, S.: Fast etching and metallization of SiC ceramics with copper-vapor-laser radiation. Appl. Phys. A **63**(1), 75–79 (1996)
164. Kruusing, A., Leppävuori, S., Uusimäki, A., Petrêtis, B., Makarova, O.: Micromachining of magnetic materials. Sens. Actuators Phys. **74**(1–3), 45–51 (1999)
165. Geiger, M., Becker, W., Rebhan, T., Hutfless, J., Lutz, N.: Increase of efficiency for the XeCl excimer laser ablation of ceramics. Appl. Surf. Sci. **96–98**, 309–315 (1996)
166. Geiger, M., Roth, S., Becker, W.: Microstructuring and surface modification by excimer laser machining under thin liquid films. 200–208 (1998)
167. Ren, J., Kelly, M., Hesselink, L.: Laser ablation of silicon in water with nanosecond and femtosecond pulses. Opt. Lett. **30**(13), 1740–1742 (2005)
168. Dowding, C.F., Lawrence, J.: Impact of open de-ionized water thin film laminar immersion on the liquid-immersed ablation threshold and ablation rate of features machined by KrF excimer laser ablation of bisphenol A polycarbonate. Opt. Lasers Eng. **47**(11), 1169–1176 (2009)
169. Daminelli, G., Krüger, J., Kautek, W.: Femtosecond laser interaction with silicon under water confinement. Thin Solid Films **467**(1–2), 334–341 (2004)
170. Bärsch, N.: Improving laser ablation of zirconia by liquid films: multiple influence of liquids on surface machining and nanoparticle generation. J. Laser Micro/Nanoeng **4**(1), 66–70 (2009)

171. Kruusing, A.: Underwater and water-assisted laser processing: Part 2—Etching, cutting and rarely used methods. Opt. Lasers Eng. **41**(2), 329–352 (2004)

172. Patel, D.N., Singh, R.P., Thareja, R.K.: Craters and nanostructures with laser ablation of metal/metal alloy in air and liquid. Appl. Surf. Sci. **288**, 550–557 (2014)

173. Stephan Roth, M.G.: Novel technique for high-quality microstructuring with excimer lasers (2000)

174. Alahmari, A.M., Ahmed, N., Darwish, S.: Laser beam micro-machining under water immersion. Int. J. Adv. Manuf. Technol. 1–11 (2015)

175. Zhu, S., Lu, Y.F., Hong, M.H., Chen, X.Y.: Laser ablation of solid substrates in water and ambient air. J. Appl. Phys. **89**(4), 2400–2403 (2001)

176. Dowding, C., Lawrence, J.: Effects of closed immersion filtered water flow velocity on the ablation threshold of bisphenol A polycarbonate during excimer laser machining. Appl. Surf. Sci. **256**(12), 3705–3713 (2010)

177. Peyre, P., Berthe, L., Scherpereel, X., Fabbro, R.: Laser-shock processing of aluminium-coated 55C1 steel in water-confinement regime, characterization and application to high-cycle fatigue behaviour. J. Mater. Sci. **33**(6), 1421–1429 (1998)

178. Voronov, V.V., Dolgaev, S.I., Lyalin, A.A., Shafeev, G.A.: Laser-assisted etching of the surface of polycrystalline silicon carbide by copper-vapour laser radiation. Quantum Electron. **26**(7), 621 (1996)

179. Ohara, M.N.O.J.: High aspect ratio etching by infrared laser induced micro bubbles. 175–179 (1997)

180. Kaakkunen, J.J.J., Silvennoinen, M., Paivasaari, K., Vahimaa, P.: Water-assisted femtosecond laser pulse ablation of high aspect ratio holes. Phys. Procedia **12**(Part B), 89–93 (2011)

181. Morita, N., Ishida, S., Fujimori, Y., Ishikawa, K.: Pulsed laser processing of ceramics in water. Appl. Phys. Lett. **52**, 1965 (1988)

182. Mahdieh, M.H., Nikbakht, M., Eghlimi Moghadam, Z., Sobhani, M.: Crater geometry characterization of Al targets irradiated by single pulse and pulse trains of Nd:YAG laser in ambient air and water. Appl. Surf. Sci. **256**(6), 1778–1783 (2010)

183. Li, Y., Itoh, K., Watanabe, W., Yamada, K., Kuroda, D., Nishii, J., Jiang, Y.: Three-dimensional hole drilling of silica glass from the rear surface with femtosecond laser pulses. Opt. Lett. **26**(23), 1912–1914 (2001)

184. Tsai, C.-H., Li, C.-C.: Investigation of underwater laser drilling for brittle substrates. J. Mater. Process. Technol. **209**(6), 2838–2846 (2009)

185. Makridis, S.S., Gkanas, E.I., Panagakos, G., Kikkinides, E.S., Stubos, A.K., Wagener, P., Barcikowski, S.: Polymer-stable magnesium nanocomposites prepared by laser ablation for efficient hydrogen storage. Int. J. Hydrog. Energy **38**(26), 11530–11535 (2013)

186. Kazakevich, P.V., Simakin, A.V., Voronov, V.V., Shafeev, G.A.: Laser induced synthesis of nanoparticles in liquids. Appl. Surf. Sci. **252**(13), 4373–4380 (2006)

187. Semaltianos, N.G., Logothetidis, S., Frangis, N., Tsiaoussis, I., Perrie, W., Dearden, G., Watkins, K.G.: Laser ablation in water: a route to synthesize nanoparticles of titanium monoxide. Chem. Phys. Lett. **496**(1–3), 113–116 (2010)

188. Zhang, J., Lan, C.Q.: Nickel and cobalt nanoparticles produced by laser ablation of solids in organic solution. Mater. Lett. **62**(10–11), 1521–1524 (2008)

189. Piriyawong, V., Thongpool, V., Asanithi, P., Limsuwan, P.: Effect of laser pulse energy on the formation of alumina nanoparticles synthesized by laser ablation in water. Procedia Eng. **32**, 1107–1112 (2012)

190. Elaboudi, I, Lazare, S., Belin, C., Bruneel, J.L., Servant, L.: Organic nanoparticles suspensions preparation by underwater excimer laser ablation of polycarbonate. Appl. Surf. Sci. **253**(19), 7835–7839 (2007)

191. Mahfouz, R., Cadete Santos Aires, F.J., Brenier, A., Jacquier, B., Bertolini, J.C.: Synthesis and physico-chemical characteristics of nanosized particles produced by laser ablation of a nickel target in water. Appl. Surf. Sci. **254**(16), 5181–5190 (2008)

192. Gondal, M.A., Saleh, T.A., Drmosh, Q.A.: Synthesis of nickel oxide nanoparticles using pulsed laser ablation in liquids and their optical characterization. Appl. Surf. Sci. **258**(18), 6982–6986 (2012)

193. Huang, C.-N., Bow, J.-S., Zheng, Y., Chen, S.-Y., Ho, N.J., Shen, P.: Nonstoichiometric titanium oxides via pulsed laser ablation in water. Nanoscale Res. Lett. **5**(6), 972–985 (2010)

194. Compagnini, G., Sinatra, M.G., Messina, G.C., Patanè, G., Scalese, S., Puglisi, O.: Monitoring the formation of inorganic fullerene-like MoS_2 nanostructures by laser ablation in liquid environments. Appl. Surf. Sci. **258**(15), 5672–5676 (2012)

195. Dolgaev, S.I., Simakin, A.V., Voronov, V.V., Shafeev, G.A., Bozon-Verduraz, F.: Nanoparticles produced by laser ablation of solids in liquid environment. Appl. Surf. Sci. **186**(1–4), 546–551 (2002)

196. Kazakevich, P.V., Voronov, V.V., Simakin, A.V., Shafeev, G.A.: Production of copper and brass nanoparticles upon laser ablation in liquids. Quantum Electron. **34**(10), 951–956 (2004)

197. Anikin, K.V., Melnik, N.N., Simakin, A.V., Shafeev, G.A., Voronov, V.V., Vitukhnovsky, A.G.: Formation of ZnSe and CdS quantum dots via laser ablation in liquids. Chem. Phys. Lett. **366**(3–4), 357–360 (2002)

198. Ohadi, M., Choo, K., Dessiatoun, S., Cetegen, E.: Emerging applications of microchannels. In: Next Generation Microchannel Heat Exchangers, pp. 67–105. Springer, New York (2013)

199. Wang, Z., Fan, J., Luo, K.: Combined multi-direct forcing and immersed boundary method for simulating flows with moving particles. Int. J. Multiph. Flow **34**(3), 283–302 (2008)

200. Ponyavin, V., Chen, Y., Mohamed, T., Trabia, M., Wilson, M., Hechanova, A.E.: Modeling and parametric study of a ceramic high temperature heat exchanger and chemical decomposer. 1013–1020 (2006, Jan)

201. Mei, D., Qian, M., Liu, B., Jin, B., Yao, Z., Chen, Z.: A micro-reactor with micro-pin-fin arrays for hydrogen production via methanol steam reforming. J. Power Sources **205**, 367–376 (2012)

202. Sommers, A., Wang, Q., Han, X., T'Joen, C., Park, Y., Jacobi, A.: Ceramics and ceramic matrix composites for heat exchangers in advanced thermal systems—a review. Appl. Therm. Eng. **30**(11–12), 1277–1291 (2010)

203. Goel, N., Goswami, D.Y.: A compact falling film absorber. J. Heat Transf. **127**(9), 957 (2005)

204. Hessel, V., Ehrfeld, W., Golbig, K., Haverkamp, V., Löwe, H., Storz, M., Wille, C., Guber, A.E., Jähnisch, K., Baerns, M.: Gas/liquid microreactors for direct fluorination of aromatic compounds using elemental fluorine. In: Ehrfeld, P.D.W. (ed.) Microreaction Technology: Industrial Prospects, pp. 526–540. Springer, Heidelberg (2000)

205. Jähnisch, K., Baerns, M., Hessel, V., Ehrfeld, W., Haverkamp, V., Löwe, H., Wille, C., Guber, A.: Direct fluorination of toluene using elemental fluorine in gas/liquid microreactors. J. Fluor. Chem. **105**(1), 117–128 (2000)

206. Abdallah, B., Chao, T.-C., Fromme, P., Ros, A.: Size based nanoparticle separation using dielectrophoretic focusing for femtosecond nanocrystallography of membrane proteins. In: Proceedings of Mu TAS International Conference on Miniaturized Chemistry and Biochemical Analysis System, vol. 2012, pp. 458–460 (2012)

207. Jenks, J., Narayanan, V.: Effect of channel geometry variations on the performance of a constrained microscale-film ammonia-water bubble absorber. J. Heat Transf. **130**(11), 112402 (2008)

208. Marquardt, E.D., Radebaugh, R., Dobak, J.: A cryogenic catheter for treating heart arrhythmia. In: Kittel, P. (ed.) Advances in Cryogenic Engineering, pp. 903–910. Springer, US (1998)

209. Campbell, G.O., Fryer, J.M.: Microchannel cooling device for small heat sources. US7836940 B2, 23 Nov 2010

210. Cotter, T.P.: Principles and prospects for micro heat pipes. NASA STIRecon Technical Report N, **84** (1984, Apr)

211. Kang, S.-W., Huang, D.: Fabrication of star grooves and rhombus grooves micro heat pipe. J. Micromech. Microeng. **12**(5), 525 (2002)

212. Berre, M.L., Launay, S., Sartre, V., Lallemand, M.: Fabrication and experimental investigation of silicon micro heat pipes for cooling electronics. J. Micromech. Microeng. **13**(3), 436 (2003)

213. Youn, Y.J., Kim, S.J.: Development of a compact micro pulsating heat pipe, p. T10133 (2011, Jan)

214. Lim, H.T., Kim, S.H., Im, H.D., Oh, K.H., Jeong, S.H.: Fabrication and evaluation of a copper flat micro heat pipe working under adverse-gravity orientation. J. Micromech. Microeng. **18**(10), 105013 (2008)

215. Klocke, F., Zeis, M., Klink, A., Veselovac, D.: Technological and economical comparison of roughing strategies via milling, sinking-EDM, wire-EDM and ECM for titanium- and nickel-based blisks. CIRP J. Manuf. Sci. Technol. **6**(3), 198–203 (2013)

216. Aramcharoen, A., Mativenga, P.T., Yang, S., Cooke, K.E., Teer, D.G.: Evaluation and selection of hard coatings for micro milling of hardened tool steel. Int. J. Mach. Tools Manuf. **48**(14), 1578–1584 (2008)

217. Ucun, İ., Aslantas, K., Bedir, F.: The performance Of DLC-coated and uncoated ultra-fine carbide tools in micromilling of Inconel 718. Precis. Eng. **41**, 135–144 (2015)

218. Ucun, İ., Aslantas, K., Bedir, F.: An experimental investigation of the effect of coating material on tool wear in micro milling of Inconel 718 super alloy. Wear **300**(1–2), 8–19 (2013)

219. Dornfeld, D., Min, S., Takeuchi, Y.: Recent advances in mechanical micromachining. CIRP Ann. Manuf. Technol. **55**(2), 745–768 (2006)

220. Vazquez, E., Gomar, J., Ciurana, J., Rodríguez, C.A.: Analyzing effects of cooling and lubrication conditions in micromilling of Ti6Al4V. J. Clean. Prod. **87**, 906–913 (2015)

221. Xu, J., Shi, L., Wang, C., Shan, D., Guo, B.: Micro hot embossing of micro-array channels in ultrafine-grained pure aluminum using a silicon die. J. Mater. Process. Technol. **225**, 375–384 (2015)

222. Gau, J.-T., Gu, H., Liu, X., Huang, K.-M., Lin, B.-T.: Forming micro channels on aluminum foils by using flexible die forming process. J. Manuf. Process. **19**, 102–111 (2015)

223. Jin, C.K., Kang, C.G.: Fabrication by vacuum die casting and simulation of aluminum bipolar plates with micro-channels on both sides for proton exchange membrane (PEM) fuel cells. Int. J. Hydrog. Energy **37**(2), 1661–1676 (2012)

224. Deng, D., Wan, W., Tang, Y., Wan, Z., Liang, D.: Experimental investigations on flow boiling performance of reentrant and rectangular microchannels—a comparative study. Int. J. Heat Mass Transf. **82**, 435–446 (2015)

225. Jahan, M.P., Kakavand, P., Kwang, E.L.M., Rahman, M., Wong, Y.S.: An experimental investigation into the micro-electro-discharge machining behaviour of aluminium alloy (AA 2024). Int. J. Adv. Manuf. Technol. **78**(5–8), 1127–1139 (2014)

226. Rajurkar, K.P., Sundaram, M.M., Malshe, A.P.: Review of electrochemical and electrodischarge machining. Procedia CIRP **6**, 13–26 (2013)

227. Izquierdo, B., Plaza, S., Sánchez, J.A., Pombo, I., Ortega, N.: Numerical prediction of heat affected layer in the EDM of aeronautical alloys. Appl. Surf. Sci. **259**, 780–790 (2012)

228. Li, L., Wei, X.T., Li, Z.Y.: Surface integrity evolution and machining efficiency analysis of W-EDM of nickel-based alloy. Appl. Surf. Sci. **313**, 138–143 (2014)

229. Tsai, H.C., Yan, B.H., Huang, F.Y.: EDM performance of Cr/Cu-based composite electrodes. Int. J. Mach. Tools Manuf. **43**(3), 245–252 (2003)

230. Wang, C.-C., Chow, H.-M., Yang, L.-D., Lu, C.-T.: Recast layer removal after electrical discharge machining via Taguchi analysis: a feasibility study. J. Mater. Process. Technol. **209**(8), 4134–4140 (2009)

231. Beach, R., Benett, W.J., Freitas, B.L., Mundinger, D., Comaskey, B.J., Solarz, R.W., Emanuel, M.: Modular microchannel cooled heatsinks for high average power laser diode arrays. IEEE J. Quantum Electron. **28**(4), 966–976 (1992)

232. Nieto, D., Delgado, T., Flores-Arias, M.T.: Fabrication of microchannels on soda-lime glass substrates with a Nd:YVO4 laser. Opt. Lasers Eng. **63**, 11–18 (2014)

233. Suriano, R., Kuznetsov, A., Eaton, S.M., Kiyan, R., Cerullo, G., Osellame, R., Chichkov, B. N., Levi, M., Turri, S.: Femtosecond laser ablation of polymeric substrates for the fabrication of microfluidic channels. Appl. Surf. Sci. **257**(14), 6243–6250 (2011)
234. Vázquez, E., Ciurana, J., Rodríguez, C.A., Thepsonthi, T., Özel, T.: Swarm intelligent selection and optimization of machining system parameters for microchannel fabrication in medical devices. Mater. Manuf. Process. **26**(3), 403–414 (2011)
235. Kumar, A., Gupta, M.C.: Laser machining of micro-notches for fatigue life. Opt. Lasers Eng. **48**(6), 690–697 (2010)
236. Teixidor, D., Ferrer, I., Ciurana, J., Özel, T.: Optimization of process parameters for pulsed laser milling of micro-channels on AISI H13 tool steel. Robot. Comput. Integr. Manuf. **29**(1), 209–218 (2013)
237. Teixidor, D., Thepsonthi, T., Ciurana, J., Özel, T.: Nanosecond pulsed laser micromachining of PMMA-based microfluidic channels. J. Manuf. Process. **14**(4), 435–442 (2012)
238. Francescon, A., Mapelli, A., Nuessle, G., Petagna, P., Pezous, A., Renaud, P., Romagnoli, G.: Application of micro-channel cooling to the local thermal management of detectors electronics for particle physics. Microelectron. J. **44**(7), 612–618 (2013)
239. Xu, J., Gan, Y., Zhang, D., Li, X.: Microscale boiling heat transfer in a micro-timescale at high heat fluxes. J. Micromech. Microeng. **15**(2), 362 (2005)
240. Gómez, D., Goenaga, I.: On the incubation effect on two thermoplastics when irradiated with ultrashort laser pulses: broadening effects when machining microchannels. Appl. Surf. Sci. **253**(4), 2230–2236 (2006)
241. Prakash, S., Kumar, S.: Fabrication of microchannels on transparent PMMA using CO_2 laser (10.6 µm) for microfluidic applications: an experimental investigation. Int. J. Precis. Eng. Manuf. **16**(2), 361–366 (2015)
242. Wu, Z., Yan, H., Chen, H., Huang, H.: One-stage fabrication of sub-micron hydrophilic microchannels on PDMS. Appl. Surf. Sci. **255**(8), 4702–4704 (2009)
243. Holmberg, P., Pasiskevicius, V., Fokine, M.: Study of incubation effects during surface ablation using picosecond pulses at a wavelength of 800 nm. Phys. Status Solidi C **8**(9), 2862–2865 (2011)
244. Wang, Y., Sefiane, K., Harmand, S.: Flow boiling in high-aspect ratio mini- and micro-channels with FC-72 and ethanol: experimental results and heat transfer correlation assessments. Exp. Therm. Fluid Sci. **36**, 93–106 (2012)
245. Wu, H.Y., Cheng, P.: Boiling instability in parallel silicon microchannels at different heat flux. Int. J. Heat Mass Transf. **47**(17–18), 3631–3641 (2004)
246. Yang, L.-J., Chen, Y.-T., Kang, S.-W., Wang, Y.-C.: Fabrication of SU-8 embedded microchannels with circular cross-section. Int. J. Mach. Tools Manuf. **44**(10), 1109–1114 (2004)
247. Madhour, Y., Olivier, J., Costa-Patry, E., Paredes, S., Michel, B., Thome, J.R.: Flow boiling of R134a in a multi-microchannel heat sink with hotspot heaters for energy-efficient microelectronic CPU cooling applications. IEEE Trans. Compon. Packag. Manuf. Technol. **1** (6), 873–883 (2011)
248. Beer, N., Özkaya, E., Biermann, D.: Drilling of Inconel 718 with geometry-modified twist drills. Procedia CIRP **24**, 49–55 (2014)
249. Woon, K.S., Chaudhari, A., Kumar, A.S., Rahman, M.: The effects of tool degradation on hole straightness in deep hole gundrilling of Inconel-718. Procedia CIRP **14**, 593–598 (2014)
250. Sharman, A.R.C., Hughes, J.I., Ridgway, K.: An analysis of the residual stresses generated in Inconel 718^{TM} when turning. J. Mater. Process. Technol. **173**(3), 359–367 (2006)
251. Madariaga, A., Esnaola, J.A., Fernandez, E., Arrazola, P.J., Garay, A., Morel, F.: Analysis of residual stress and work-hardened profiles on Inconel 718 when face turning with large-nose radius tools. Int. J. Adv. Manuf. Technol. **71**(9–12), 1587–1598 (2014)
252. Devillez, A., Le Coz, G., Dominiak, S., Dudzinski, D.: Dry machining of Inconel 718, workpiece surface integrity. J. Mater. Process. Technol. **211**(10), 1590–1598 (2011)
253. Choudhury, I.A., El-Baradie, M.A.: Machinability of nickel-base super alloys: a general review. J. Mater. Process. Technol. **77**(1–3), 278–284 (1998)

254. Klocke, F., Welling, D., Klink, A., Veselovac, D., Nöthe, T., Perez, R.: Evaluation of advanced wire-EDM capabilities for the manufacture of fir tree slots in Inconel 718. Procedia CIRP **14**, 430–435 (2014)
255. Manohar, M., Selvaraj, T., Sivakumar, D., Gopinath, S., George, K.M.: Experimental study to assess the effect of electrode bottom profiles while machining Inconel 718 through EDM process. Procedia Mater. Sci. **6**, 92–104 (2014)
256. Beri, N., Maheshwari, S., Sharma, C., Kumar, A.: Surface quality modification using powder metallurgy processed CuW electrode during electric discharge machining of Inconel 718. Procedia Mater. Sci. **5**, 2629–2634 (2014)
257. Ekmekci, B.: Residual stresses and white layer in electric discharge machining (EDM). Appl. Surf. Sci. **253**(23), 9234–9240 (2007)
258. Aspinwall, D.K., Soo, S.L., Berrisford, A.E., Walder, G.: Workpiece surface roughness and integrity after WEDM of Ti–6Al–4V and Inconel 718 using minimum damage generator technology. CIRP Ann. Manuf. Technol. **57**(1), 187–190 (2008)
259. Jeelani, S., Collins, M.R.: Effect of electric discharge machining on the fatigue life of Inconel 718. Int. J. Fatigue **10**(2), 121–125 (1988)
260. Lin, M., Tsao, C., Hsu, C., Chiou, A., Huang, P., Lin, Y.: Optimization of micro milling electrical discharge machining of Inconel 718 by Grey-Taguchi method. Trans. Nonferrous Met. Soc. China **23**(3), 661–666 (2013)
261. Huang, C.A., Chen, Y.C., Chang, J.H.: The electrochemical polishing behavior of the Inconel 718 alloy in perchloric–acetic mixed acids. Corros. Sci. **50**(2), 480–489 (2008)
262. Klocke, F., Zeis, M., Herrig, T., Harst, S., Klink, A.: Optical in situ measurements and interdisciplinary modeling of the electrochemical sinking process of Inconel 718. Procedia CIRP **24**, 114–119 (2014)
263. Wang, D., Zhu, Z., Wang, N., Zhu, D., Wang, H.: Investigation of the electrochemical dissolution behavior of Inconel 718 and 304 stainless steel at low current density in $NaNO_3$ solution. Electrochim. Acta **156**, 301–307 (2015)
264. Escobar-Palafox, G.A., Gault, R.S., Ridgway, K.: Characterisation of abrasive water-jet process for pocket milling in Inconel 718. Procedia CIRP **1**, 404–408 (2012)
265. Çaydaş, U., Hasçalık, A.: A study on surface roughness in abrasive waterjet machining process using artificial neural networks and regression analysis method. J. Mater. Process. Technol. **202**(1–3), 574–582 (2008)
266. Axinte, D.A., Karpuschewski, B., Kong, M.C., Beaucamp, A.T., Anwar, S., Miller, D., Petzel, M.: High energy fluid jet machining (HEFJet-Mach): from scientific and technological advances to niche industrial applications. CIRP Ann. Manuf. Technol. **63**(2), 751–771 (2014)
267. Hashish, M.: Optimization factors in abrasive-waterjet machining. J. Manuf. Sci. Eng. **113**(1), 29–37 (1991)
268. Sadasivam, B., Hizal, A., Park, S., Arola, D.: An evaluation of abrasive waterjet peening with elastic prestress. J. Manuf. Sci. Eng. **131**(1), 011010 (2009)
269. Yünlü, L., Çolak, O., Kurbanoğlu, C.: Taguchi DOE analysis of surface integrity for high pressure jet assisted machining of Inconel 718. Procedia CIRP **13**, 333–338 (2014)
270. Hsu, C.Y., Lin, Y.Y., Lee, W.S., Lo, S.P.: Machining characteristics of Inconel 718 using ultrasonic and high temperature-aided cutting. J. Mater. Process. Technol. **198**(1–3), 359–365 (2008)
271. Liao, Y.S., Chen, Y.C., Lin, H.M.: Feasibility study of the ultrasonic vibration assisted drilling of Inconel superalloy. Int. J. Mach. Tools Manuf. **47**(12–13), 1988–1996 (2007)
272. Bhaduri, D., Soo, S.L., Novovic, D., Aspinwall, D.K., Harden, P., Waterhouse, C., Bohr, S., Mathieson, A.C., Lucas, M.: Ultrasonic assisted creep feed grinding of Inconel 718. Procedia CIRP **6**, 615–620 (2013)
273. Brehl, D.E., Dow, T.A.: Review of vibration-assisted machining. Precis. Eng. **32**(3), 153–172 (2008)

274. Mitrofanov, A.V., Ahmed, N., Babitsky, V.I., Silberschmidt, V.V.: Effect of lubrication and cutting parameters on ultrasonically assisted turning of Inconel 718. J. Mater. Process. Technol. **162–163**, 649–654 (2005)
275. Leshock, C.E., Kim, J.-N., Shin, Y.C.: Plasma enhanced machining of Inconel 718: modeling of workpiece temperature with plasma heating and experimental results. Int. J. Mach. Tools Manuf. **41**(6), 877–897 (2001)
276. García Navas, V., Arriola, I., Gonzalo, O., Leunda, J.: Mechanisms involved in the improvement of Inconel 718 machinability by laser assisted machining (LAM). Int. J. Mach. Tools Manuf. **74**, 19–28 (2013)
277. Abdul Aleem, B.J., Hashmi, Yilbas, B.S.: Laser controlled melting of pre-prepared Inconel 718 alloy surface. Opt. Lasers Eng. **49**(11), 1314–1319 (2011)
278. Yilbas, B.S., Akhtar, S.S., Karatas, C.: Laser surface treatment of Inconel 718 alloy: thermal stress analysis. Opt. Lasers Eng. **48**(7–8), 740–749 (2010)
279. Pusavec, F., Hamdi, H., Kopac, J., Jawahir, I.S.: Surface integrity in cryogenic machining of nickel based alloy—Inconel 718. J. Mater. Process. Technol. **211**(4), 773–783 (2011)
280. Tam, S.C., Yeo, C.Y., Jana, S., Lau, M.W.S., Lim, L.E.N., Yang, L.J., Noor, Y.M.: Optimization of laser deep-hole drilling of Inconel 718 using the Taguchi method. J. Mater. Process. Technol. **37**(1–4), 741–757 (1993)
281. Ahn, D.-G., Byun, K.-W.: Influence of cutting parameters on surface characteristics of cut section in cutting of Inconel 718 sheet using CW Nd:YAG laser. Trans. Nonferrous Met. Soc. China **19**(Supplement 1), s32–s39 (2009)
282. Hasçalık, A., Ay, M.: CO_2 laser cut quality of Inconel 718 nicklel—based superalloy. Opt. Laser Technol. **48**, 554–564 (2013)

Erratum to: Laser Beam Machining, Laser Beam Hybrid Machining, and Micro-channels Applications and Fabrication Techniques

Saied Darwish, Naveed Ahmed and Abdulrahman M. Alahmari

Erratum to:
Chapter 17 in: A. Öchsner and H. Altenbach (eds.),
Machining, Joining and Modifications of Advanced Materials, **Advanced Structured Materials 61,**
DOI 10.1007/978-981-10-1082-8_17

In Chapter 17, the authors missed to acknowledge that the corresponding project was financially supported by King Saud University, Vice Deanship of Research Chairs. The erratum chapter and the book has been updated with the change.

The updated original online version for this chapter can be found at
10.1007/978-981-10-1082-8_17

S. Darwish (✉) · N. Ahmed · A.M. Alahmari
Princess Fatima Alnijiris's Research Chair for Advanced Manufacturing Technology (FARCAMT), King Saud University, Riyadh, Saudi Arabia
e-mail: darwish@ksu.edu.sa

N. Ahmed
e-mail: anaveed@ksu.edu.sa

A.M. Alahmari
e-mail: alahmari@ksu.edu.sa

S. Darwish · N. Ahmed · A.M. Alahmari
Industrial Engineering Department, King Saud University, Riyadh, Saudi Arabia

S. Darwish · N. Ahmed · A.M. Alahmari
Advanced Manufacturing Institute, King Saud University, Riyadh, Saudi Arabia

N. Ahmed
Department of Industrial and Manufacturing Engineering, University of Engineering and Technology, Lahore, Pakistan

Erratum to: Laser Polishing of Additive Manufactured AlSi10Mg Parts with an Oscillating Laser Beam

Jochen Schanz, Markus Hofele, Leonhard Hitzler, Markus Merkel and Harald Riegel

Erratum to:
Chapter "Laser Polishing of Additive Manufactured AlSi10Mg Parts with an Oscillating Laser Beam"
in: A. Öchsner and H. Altenbach (eds.), *Machining, Joining and Modifications of Advanced Materials*,
Advanced Structured Materials 61,
DOI 10.1007/978-981-10-1082-8_16

The affiliations of two authors: Markus Merkel and Harald Riegel were modified from Chapter "Laser Polishing of Additive Manufactured AlSi10Mg Parts with an Oscillating Laser Beam" post-publication. The erratum chapter and the book have been updated with correct affiliation of the authors in Chapter "Laser Polishing of Additive Manufactured AlSi10Mg Parts with an Oscillating Laser Beam".

The updated original online version for this chapter can be found at
10.1007/978-981-10-1082-8_16

J. Schanz (✉) · M. Hofele · M. Merkel · H. Riegel
Aalen University of Applied Sciences, Beethovenstraße 1, 73430 Aalen, Germany
e-mail: jochen.schanz@hs-aalen.de

M. Hofele
e-mail: markus.hofele@hs-aalen.de

M. Merkel
e-mail: markus.merkel@hs-aalen.de

H. Riegel
e-mail: harald.riegel@hs-aalen.de

L. Hitzler
School of Engineering, Griffith University, Gold Coast Campus, Southport 4222, Australia
e-mail: leonhard.hitzler@griffithuni.edu.au